Investigating the Structure of Collagen using Surface-enhanced Raman Spectroscopy and X-ray Scattering

by

Yi Zhang

A thesis

submitted to the Victoria University of Wellington

in fulfilment of the requirements for the degree of

Doctor of Philosophy

in Chemistry

Victoria University of Wellington

2023

Abstract

Collagen is the most abundant protein in mammals, comprising a variety of tissues including skin, tendon, and pericardium where it exhibits a hierarchical structure at molecular and fibrillar levels. The structure of collagen in native tissues can be modified by chemical processing which imparts desired properties to collagenous materials ranging from bioprostheses to leathers. However, conventional processing technologies involve intense chemical use and are under much scrutiny due to their undesirable environmental and health impacts.

Herein, investigations of three interrelated research questions were undertaken to provide an insightful mechanistic understanding of the binding and crosslinking of collagen with metallic species and organic crosslinkers. This work facilitated the design of chemically benign and efficient processing technologies to circumvent the environmental and health-related concerns existing with the current processing technologies. Surface-enhanced Raman spectroscopy (SERS) and X-ray scattering (in particular, small-angle X-ray scattering (SAXS)) were used during the investigations: SERS probed side chain interactions with metallic species, whereas SAXS provided information on the intermolecular packing of collagen.

The binding of chromium(III) (Cr(III)) to collagen in bovine skin was investigated using a combination of SAXS and SERS, focussing on the competition between covalent and electrostatic binding, as regulated by the anions in the system. Two counterions of Cr(III) were assessed: sulfate (SO_4^{2-}) and chloride (Cl^-). It was found that both covalent and electrostatic binding mechanisms occur concurrently in the collagen matrix under the conditions investigated. Higher kosmotropicity of the anion (*e.g.*, sulfate (SO_4^{2-})) and weaker acidity (specifically, at pH = 4.5) facilitated the covalent binding of Cr(III) with side chain carboxylate ($-COO^-$) groups (Cr–OOC) in collagen. In contrast, when a more chaotropic anion (*e.g.*, chloride (Cl^-)) was present or at stronger acidity (pH = 2.5), the electrostatic binding mechanism between $Cr(H_2O)_6^{3+}$ complex ions and side chain carboxylate ($-COO^-$) groups dominate. The findings from this study highlight that the conventional high Cr use to exhaust covalent binding sites ($-COO^-$) in collagen during the processing of skin into leather, is unnecessary. It also supports a potential correlation between the electrostatically bound Cr species and the health concerns related to Cr leaching and allergic contact dermatitis. Both re-emphasise the urgency to replace excess chromium salts in collagen treatments with benign chemicals.

Following the SERS measurements on collagen fibres in skins, the SERS measurements of collagen molecules in solution using citrate-reduced silver nanoparticles (AgNPs) led to the revealing of coadsorption phenomena on the surface of the AgNPs. When chloride ions (Cl^-) were introduced to the AgNPs, citrate (Cit) species desorbed and were replaced by its thermal decomposition product, acetoacetate (AAc), which was produced during the synthesis of AgNPs. Protonated AAc was readily decomposed when acidified, giving a SERS spectrum of only the silver-halide bond and water peaks. The use of bromide (Br^-) and iodide (I^-) led to

the displacement of AAc from the surface of AgNPs, but allowed the surface to adsorb and reveal the residual anionic surfactant (AS) in water. The residual was proposed to be a polyoxyethylene alkyl ether carboxylate. A mechanism was proposed to explain the variations in binding modes and affinities of the coadsorbed species based on the surface coverage of AgNPs by the strong ligands introduced, such as halides. Instead of forming a complete coating layer, the Cl ligand layer has minor gaps that repel Cit anions but allows AAc to bind to the exposed silver (Ag) atoms. The Br and I ligands are bulkier and thus leave larger gaps that allow the AS to fit into and directly bind to exposed Ag atoms.

The phenomena were then explored for potential interference with the SERS signals of collagen. The introduction of acidic collagen into Cl or Br-coated AgNPs gave clear SERS signals corresponding to collagen, whereas a remarkable persistence of AS on the I ligand layer was found to lead to overlapping SERS signals of AS and collagen. The strong persistence could be due to the deeper gaps in the ligand layer due to the larger radius of I^- ions, which stabilise the binding of AS on the surface. The findings from this study highlight the importance of recording the background spectra of halide-coated AgNPs (especially after aggregation with salts or proteins) to examine any interference and avoid potential misinterpretation in SERS bioanalysis.

The effects of organic covalent crosslinking on the structure of collagen were also investigated using SAXS to reveal how the structural changes confer the corresponding enzymatic and thermal stability on bovine pericardia. Knowing the cytotoxicity of glutaraldehyde (GA) and its propensity to promote the calcification of pericardia, GA was chosen to be a candidate alongside 1-ethyl-3-(3-dimethylaminopropyl) carbodiimide (EDC) as an alternative crosslinker. Concentrations from as low as 50 times dilution of the conventional usage were investigated. A mechanism was proposed to highlight the preferred formation of telopeptidyl-helical intermolecular linkages at low concentrations, which led to major changes in the D-period and the denaturation temperature (T_d) of collagen. Full collagenase resistance was observed at low concentrations, showing the key role of telopeptidyl-helical linkages in stabilising collagen. Higher concentrations were less efficient, as the crosslinkers mainly create helical-helical linkages with side reactions forming monovalent binding and self-polymerising in GA and hydrolysis in EDC. An optimal set of conditions was postulated to maximise crosslinking efficiency. The optimised reaction pathway directs future research to devise alternative methods that use more benign chemistries and minimise the level of adverse effects.

Acknowledgements

List of Publications

Three first-authored publications were generated from this thesis. The preliminary work in Chapter 3 was published with Wiley in the journal *Biopolymers* in 2020 and featured as the cover image of the small issue [1]. The findings in Chapter 4 were published with the American Chemical Society (ACS) in *The Journal of Physical Chemistry C* in 2022 as part of a virtual special issue, "*Nanophotonics for Chemical Imaging and Spectroscopy*" [2]. The work in Chapter 5 was published with Elsevier in the journal *Acta Biomaterialia* in 2022 [3].

(1) Zhang, Y.; Mehta, M.; Mansel, B. W.; Ng, H. W.; Liu, Y.; Holmes, G.; Le Ru, E. C.; Prabakar, S., Anion-regulated binding selectivity of Cr (III) in collagen. *Biopolymers* **2020,** e23406. (https://doi.org/10.1002/bip.23406)

(2) Zhang, Y.; Prabakar, S.; Le Ru, E. C., Coadsorbed Species with Halide Ligands on Silver Nanoparticles with Different Binding Affinities. *The Journal of Physical Chemistry C* **2022,** *126* (20), 8692-8702. (https://doi.org/10.1021/acs.jpcc.2c01092)

(3) Zhang, Y.; Zhang, W.; Snow, T.; Ju, Y.; Liu, Y.; Smith, A. J.; Prabakar, S., Minimising Chemical Crosslinking for Stabilising Collagen in Acellular Bovine Pericardium: Mechanistic Insights via Structural Characterisations. *Acta Biomaterialia* **2022,** *152,* 113-123. (https://doi.org/10.1016/j.actbio.2022.08.057)

Table of Contents

List of Figures

List of Tables

List of Abbreviations

AAc	acetoacetate (including protonated variations)
ABP	acellular bovine pericardium
ADC	acetonedicarboxylate (including protonated variations)
AgNPs	citrate-reduced silver nanoparticles
APS	ammonium persulfate
AS	anionic surfactant (including protonated variations)
b-AgNPs	borohydride-reduced silver nanoparticles
BP	bovine pericardium
CC	chromium chloride
CCD	charge-coupled device
Cit	citrate (including protonated variations)
Coll	collagen
Cr(III)	trivalent chromium
CS	chromium sulfate
DAWN	Data Analysis Workbench (data analysis software at Diamond)
DF	dilution factor
DFT	density functional theory
DI	deionised
Diamond	Diamond Light Source
DSC	differential Scanning calorimetry
EDC	1-ethyl-3-(3-dimethylaminopropyl) carbodiimide
FT-IR	Fourier transform infrared
GA	glutaraldehyde
h-AgNPs	hydroxylamine-reduced silver nanoparticles
ILP	intermolecular lateral packing
LSP	localised surface plasmon
LSPR	localised surface plasmon-polaritons resonances
MES	2-(morpholino) ethane sulfonic acid
NHS	N-hydroxysuccinimide
OD	optical density
PBS	phosphate-buffered saline
pI	isoelectric point
PSPP	propagating surface plasmon-polaritons
PVP	polyvinylpyrrolidone
SAED	selected area electron diffraction
SAXS	small-angle X-ray scattering
SDS	sodium dodecyl sulfate
SDS-PAGE	sodium dodecyl sulfate-polyacrylamide gel electrophoresis
SEM	scanning electron microscope
SERS	surface-enhanced Raman spectroscopy
SPR	surface plasmon resonance
SS	sodium sulfate
T_d	denaturation temperature
TEM	transmission electron microscope
TEMED	tetramethylethylenediamine
TLS	Taiwan Light Source

Tris	tris(hydroxymethyl)aminomethane
VSH	vector spherical harmonic
WAXS	wide-angle X-ray scattering

Chapter 1   Introduction

Collagen is a protein found in all animals and is the most abundant in mammals. The structure of collagen is one of the determinative factors for the properties of collagenous biological tissues and collagen-based biomaterials [4-6]. Around a century ago, research on collagen structure emerged as a field of interest [7], and in the 1950s, the helix era began with the discovery of the α helix in proteins and the double helix in DNA [8]. Around the same time, the molecular structure of collagen was proposed as a triple helix consisting of three polypeptide chains [9], and later a primitive model was introduced for the intermolecular packing of collagen with a periodic arrangement [10]. Since then, the research on collagen structure has continued to be active and branched into many subtopics, particularly in elucidating the native collagen structures in tissues for biomedical interests and monitoring the structural changes during the processing of collagen for versatile applications [6, 11-14]. Although it has been heavily investigated, collagen remains far from well-understood in many aspects due to its intrinsic complexity: the 28 different types with 46 distinct polypeptide chains, the pseudo-random arrangement of amino acid residues in the polypeptide, the triple helical nature, the staggered intermolecular packing, as well as the chemical binding and crosslinking during and after its biosynthesis [5]. Its application growth also widens the scope for mechanistic studies; the number of new applications of collagen grows at a comparable pace to that of the fundamental breakthroughs[1], showing the expansion of the scope of knowledge around collagen over time. The work in this thesis builds upon the extensive previous knowledge of collagen structures and applications and clarifies several unresolved research questions surrounding the processing and characterisation techniques for collagen-based materials. A thorough literature review of the relevant mechanisms and findings is provided in this introductory chapter and the following chapter of theoretical background, with suitable figures reprinted from corresponding references.

This chapter introduces the hierarchical structure of collagen from amino acid residues to molecules and fibrils, followed by the multiple aspects that affect collagen structure. It is then followed by a brief highlight of the advanced techniques that will benefit collagen structural studies, which leads toward the motivations of the three research questions investigated in this thesis. All three questions in this thesis centre around how the structure of collagen changes when it binds or crosslinks with chemicals, to understand the relationship between the structure and properties of the collagenous materials.

1.1   Hierarchical Structure of Collagen

Researchers have identified 28 types of collagens in which types I, II, III, V, and XI are fibrillar, giving rise to collagen fibrils in tissues following a strictly long-range ordered structural

---

[1] There were 7987 and 13149 results on the Web of Science website when searching the topic for the keywords "collagen + application" and "collagen + mechanism" in the recent 5 years, respectively. Results were acquired on 29 Aug 2022.

hierarchy [5, 15]. Type I collagen is found in various tissues, including skin, tendon, bone, cornea, lung and vasculature. Type II collagen is only abundant in cartilage, while type III collagen is found in elastic tissues such as embryonic skin, lung and blood vessels. Type V and XI collagens are minor and only relatively rich in cornea and cartilage, respectively. The work presented in this thesis involves collagen in bovine skins (or, colloquially, "bovine hides", with the word "hide" originating from the German word "haut", which means skin) and pericardia; both are mainly composed of type I collagen. Therefore, for simplicity, the word "collagen" in this thesis implies that it is "type I collagen" unless specified otherwise.

The actual structural hierarchy of collagen starts from the triple-helical collagen molecules; the triple helix motif defines the protein as collagen. However, chemical reactions often occur at submolecular levels between specific amino acid residues in the three polypeptide chains in collagen molecules. Hence, this section will begin with a brief introduction of the primary structure, from amino acids into procollagen and its post-translational modifications into collagen molecules [15]. Collagen molecules assemble into microfibrils, fibrils, fibril bundles, fibres, and higher levels of organisations, such as the interwoven networks of collagen fibres (Figure 1.1) [15-17].
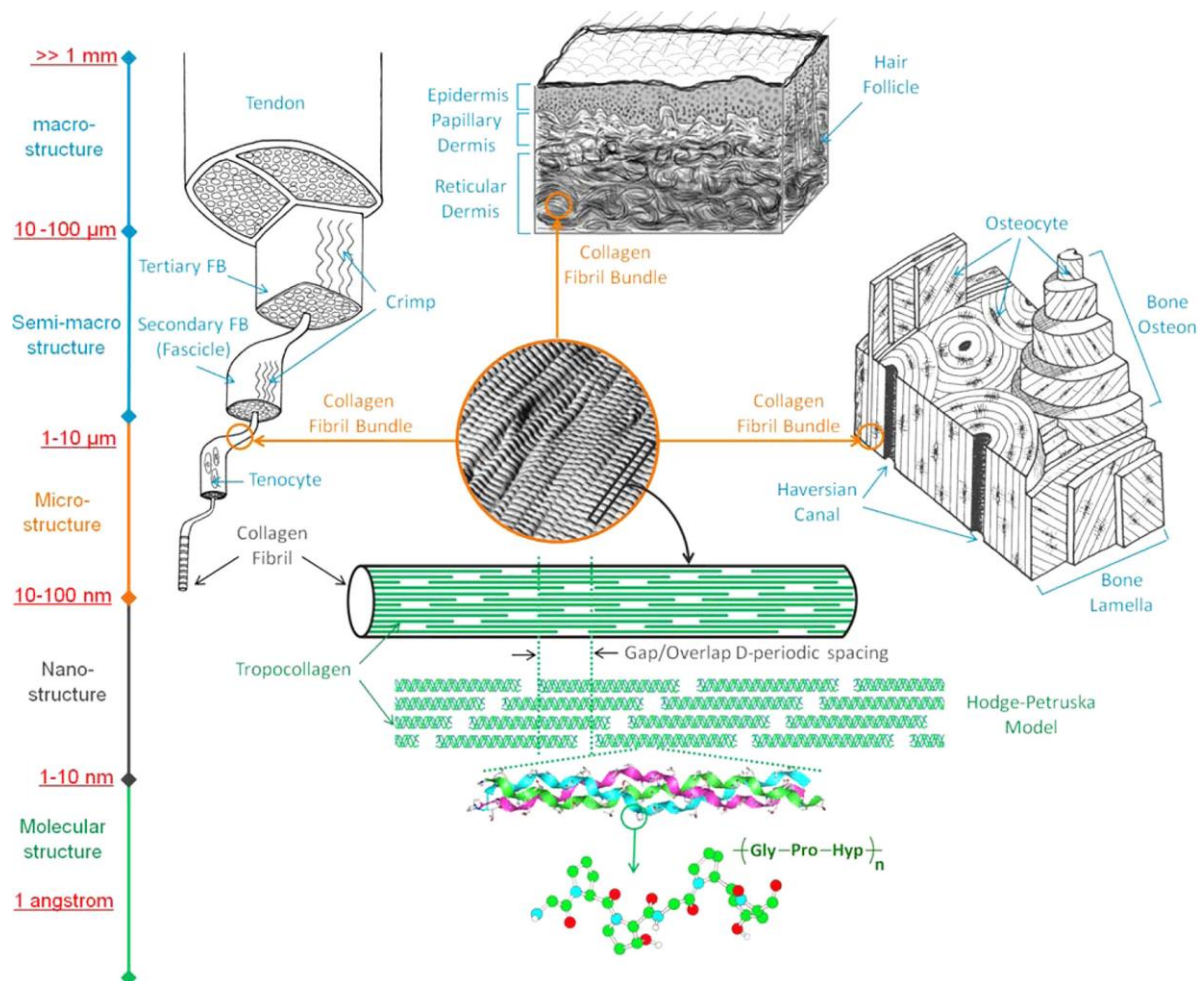
Figure 1.1: Hierarchical structure of collagen in biological tissues. (Reprinted with permission from Ref. [17]. Copyright (2012) American Chemical Society.)

1.1.1 Molecular Structure

The primary structure of collagen is determined by the process of biosynthesis (elaborated on in greater detail in Ref. [15]). The process begins with the construction of amino acids into procollagen α chains on the ribosome, followed by the partial prolyl hydroxylation of proline (Pro) to hydroxyproline (Hyp), the selective lysyl hydroxylation of lysine (Lys) to hydroxylysine (Hyl) and further the O-linked glycosylation of Hyl [15]. The Hyp residues play critical roles in stabilising the collagen triple helix via stereoelectronic effects and hydrogen bonding [5, 14, 18]. The Hyl residues are responsible for the enzymatic covalent crosslinking *in vivo* that supports fibril formation and stabilises the collagen molecules [15].

The modified procollagen α chains then coil into triple-helical procollagen molecules in the endoplasmic reticulum (Figure 1.2) [15, 19]. Type I collagen is a heterotrimeric triple helix that consists of two α_1(I) chains and one α_2(I) chain. The common structural motif in the polypeptide α chains is the repeating triplet, Gly-Xaa-Yaa, where Gly stands for glycine and the Xaa and Yaa are arbitrary amino acids [4], giving the pseudo-random arrangement of amino acid residues in collagen. The presence of Gly as every third residue is mandatory for forming the left-handed polyproline II (PPII) triple helix due to its low steric hindrance present in the core of the triple helix [5, 20]. In contrast, the Xaa and Yaa are often exposed to the surface of the triple helix, allowing them to interact with adjacent molecules [5].

The procollagen molecules are then trimmed at the N- and C-terminus to remove propeptides by metalloproteinases and convertases in the Golgi apparatus, leaving about 20 amino acid residues on each end called "telopeptides", which remain non-helical (Figure 1.2) [15, 19, 21-23]; thus forms a "collagen molecule" (also called "tropocollagen"[2]). In a collagen molecule, the most frequently found amino acid residues in Xaa and Yaa positions are (2*S*)-proline (Pro, 28%) and (2*S*,4*R*)-4-hydroxyproline (Hyp, 38%), respectively, which makes the Gly-Pro-Hyp the most frequent triplet (10.5%) in collagen [5, 24]. Apart from Gly, Pro and Hyp, other amino acid residues are also found in collagen with irregular distributions; the charged and non-charged residues are subjected to electrostatic and hydrophobic interactions, respectively [25]. Detailed composition analysis of amino acid residues in bovine skin collagen is presented in Table 1.1 [26].

---

[2] "Collagen molecule" is also known as "tropocollagen" to highlight its triple helically winding nature and as a monomeric unit. However, in a general context, it could be confusing if use "tropocollagen" to highlight the triple helical nature of collagen, as the "procollagen" trimer molecule is also triple helical, and so is the "atelocollagen" extracted using pepsin. Therefore, the generic expression "collagen molecule" is preferred to represent the intact and, by default, triple-helical, monomeric molecule.
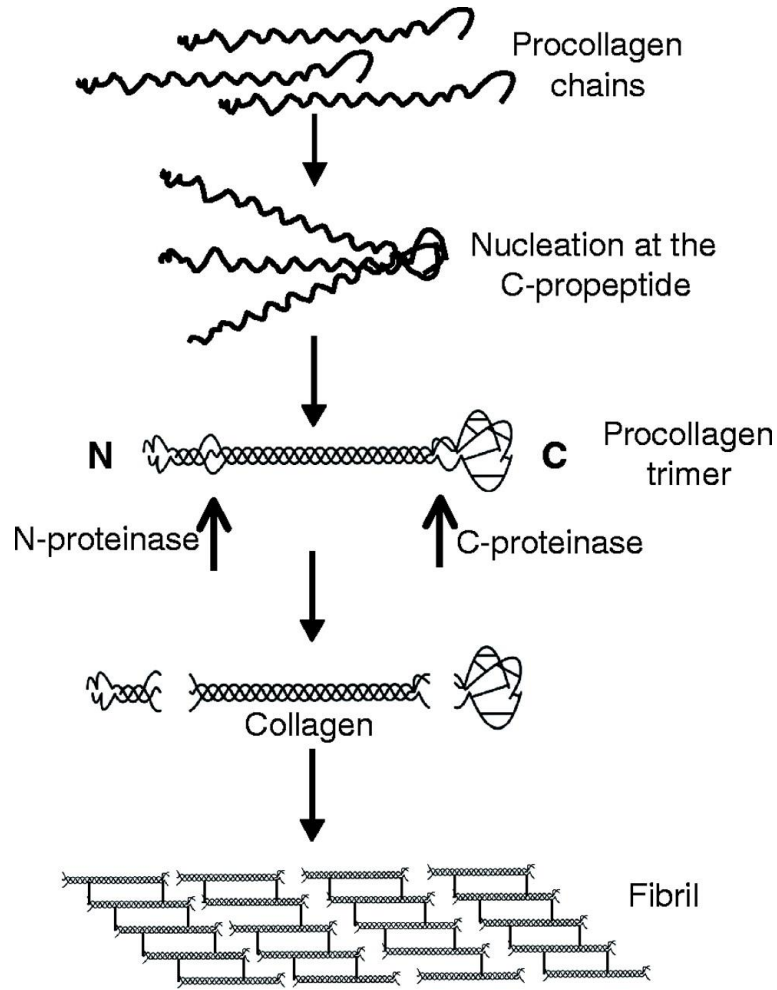
Figure 1.2: Collagen biosynthesis from procollagen α chains to triple-helical procollagen molecules, collagen molecules (propeptides are removed, but telopeptides remain) and collagen fibrils. (Reprinted with permission of The Company of Biologists Ltd., from Ref. [19]; permission conveyed through Copyright Clearance Centre, Inc.)

Table 1.1: Amino acid composition of collagen extracted from bovine skins [26].

Amino acid	Collagen (mmol/g)
Alanine (Ala)	1.158
Glycine (Gly)	3.540
Valine (Val)	0.210
Leucine (Leu)	0.284
Isoleucine (Ile)	0.143
Proline (Pro)	1.252
Phenylalanine (Phe)	0.142
Tyrosine (Tyr)	0.054
Serine (Ser)	0.406
Threonine (Thr)	0.190
Methionine (Met)	0.065
Arginine (Arg)	0.472
Histidine (His)	0.045

Lysine (Lys)	0.271
Aspartic acid (Asp)	0.522
Glutamic acid (Glu)	0.756
Hydroxyproline (Hyp)	0.978
Hydroxylysine (Hyl)	0.062

As the Pro and Hyp residues facilitate the triple helix formation by pre-organising individual polypeptide chains into left-handed polyproline II-type (PPII) helices, they also counterpoise that with the need for the tertiary amide bonds to undergo conformational changes from *cis* to *trans* isomers as to fold into a triple helix [5, 27]. The subsequent helical structure along each α chain was found to vary with Pro and Hyp contents, leading to an intermediate between two characteristic structures [5, 7, 14, 28, 29]. Proline-rich regions adhere to a 7/2-helix (seven residue units in two 360° turns) with an axial repeat of 20.0 Å along the *c*-axis, whereas proline-poor regions prefer a 10/3-helix with a different axial repeat of 28.6 Å [7, 30].

Apart from the variations in the helical symmetry, the collagen triple helix also twists to result in a distorted rope-like molecule instead of a straight cylinder [31, 32]. As shown in Figure 1.3, a distorted collagen molecule is divided into five segments (each between two horizontal grid lines), with full segments 1 to 4 and a short segment 5. Each segment among numbers 1 to 4 contains a tilted section and a near-parallel section to the *c*-axis, while the short segment number 5 only contains the tilted section leaving a "gap" in the horizontal repeating unit along the *c*-axis [32].
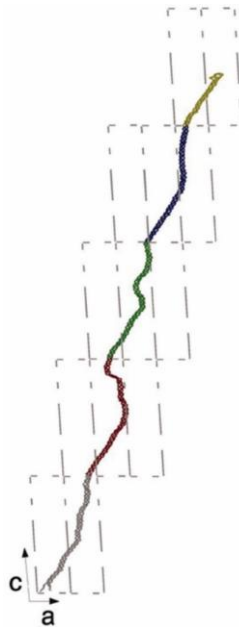
Figure 1.3: A 2D view on the ac plane of the shape of a triple helical collagen molecule in a fibril through successive unit cells. The *c*-axis has been compressed to a scale of 1/5 of the *a*-axis. Each segment is coloured differently: segments 1 to 4 = grey, red, green and blue; segment 5 = yellow. (Reprinted in part with permission from Ref. [32]. Copyright (2006) National Academy of Sciences, U.S.A.)

1.1.2 Intermolecular Packing into Microfibrils and Fibrils

The collagen molecules start to assemble into fibrils in the Golgi apparatus at the same time as the N- and C-propeptides are removed. The newly formed fibrils are then transported through the plasma membrane carriers (*i.e.*, fibropositors) towards the extracellular matrix (ECM) and join existing fibril bundles produced by neighbouring cells [19, 33].

In each fibril, collagen molecules pack laterally against each other in a quasi-hexagonal pattern with near-parallel lengthways but stagger axially[3] with a periodicity D called the "D-stagger" or "D-period" [11, 34]. A unit cell of the packing is shown in Figure 1.4 as a triclinic lattice, with each alpha carbon (the central carbon atom to which both the amino and carboxyl groups are covalently linked) in the amino acid residues rendered as spheroids. The length of the unit cell along the c-axis equals $1D$.
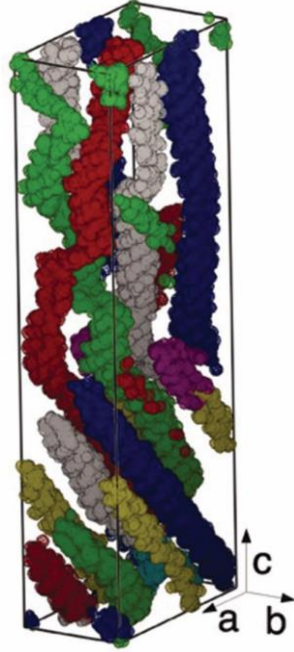
Figure 1.4: A 3D model shows a single unit cell in a collagen fibril. Alpha carbons in the amino acid residues are rendered as spheroids showing the conformation of collagen molecules within a single unit cell (cell axis shown). The c-axis has been compressed to a scale of 1/5 of the a and b-axes. Each segment is coloured differently: segments 1 to 4 = grey, red, green and blue; segment 5 = yellow. (Reprinted in part with permission from Ref. [32]. Copyright (2006) National Academy of Sciences, U.S.A.)

The typical D-period in a native rat tail tendon is $D = 67$ nm, while the overall length (L) of a collagen molecule is approximately $L = 300$ nm, giving $L = 4.4D$ (therefore called "quarter-staggered") and leading to a $0.6D$ axial gap between two collagen molecules [10]. A

---

[3] The term "axial" is used interchangeably with "longitudinal", as the length of collagen is referred to as the axis. Another term is "meridional", but it is more commonly used in pair with "equatorial" for describing X-ray scattering features.

simplified longitudinal view (ignoring the twists) shows a $0.6D$ gap and a $0.4D$ overlap in each axial repeating unit (Figure 1.5); the gap/overlap ratio could vary across different collagenous tissues. The "overlap" indicates that the quasi-hexagonal lateral packing is complete on a lateral plane, with each molecule surrounded by six neighbouring molecules. In contrast, the "gap" highlights the situations in which at least one of the hexagonal lattice points is absent of collagen molecule on a lateral plane. This model explains the repeating light and dark banding pattern ("D-banding") observed from a negatively stained collagen fibril under a transmission electron microscope (TEM) (Figure 1.5) [35].
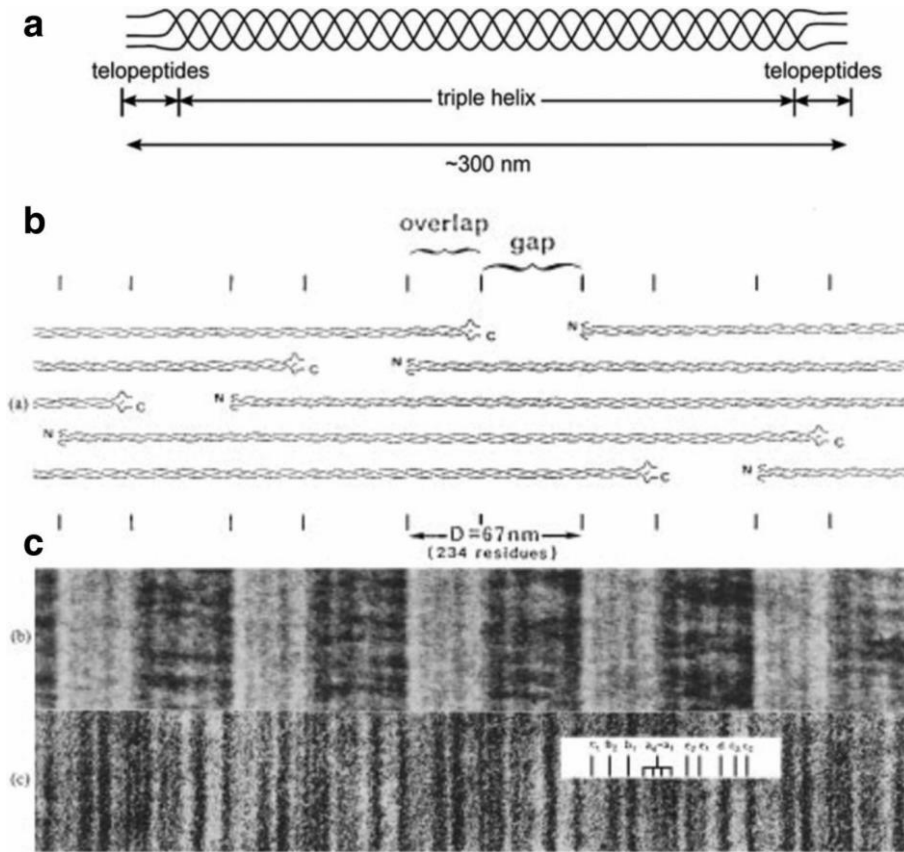
Figure 1.5: Simplified schematics of (a) a triple-helical collagen molecule highlighting the telopeptides on the N- and C-terminus (not shown to scale) and (b) intermolecular arrangement of collagen molecules in a fibril showing overlap and gap regions. (c) TEM images of a negatively stained collagen fibril using sodium phosphotungstate (1%, pH 7) and a positively stained collagen fibril with phosphotungstic acid (1%, pH 3.4) and then uranyl acetate (1%, pH 4.2). The dark bands in the negatively stained fibril highlight the position of the gap regions filled with phosphotungstate ions. (Figure (a) is reprinted in part with permission of the Royal Society of Chemistry, from Ref. [34]; permissions conveyed through Copyright Clearance Centre, Inc. Figures (b) and (c) are reprinted with permission of the Portland Press, Ltd., from Ref. [35]; permission conveyed through Copyright Clearance Centre, Inc.)

Considering a single collagen molecule (Figure 1.3), the axial rise (not the length of the molecule) is $1D$ for each full segment, of which $0.6D$ is near-parallel to the c-axis and $0.4D$ is

tilted. The shorter segment (segment 5) only contains the $0.4D$ tilted section, leaving the $0.6D$ gap. The switch between the tilted and the near-parallel conformation is attributed to the intermolecular interactions [32]. A longitudinal view of the electron density map shows that collagen molecules tilt in the overlap regions against the c-axis of the unit cell, unlike in the gap regions in which they are essentially parallel to the c-axis (Figure 1.6) [31].
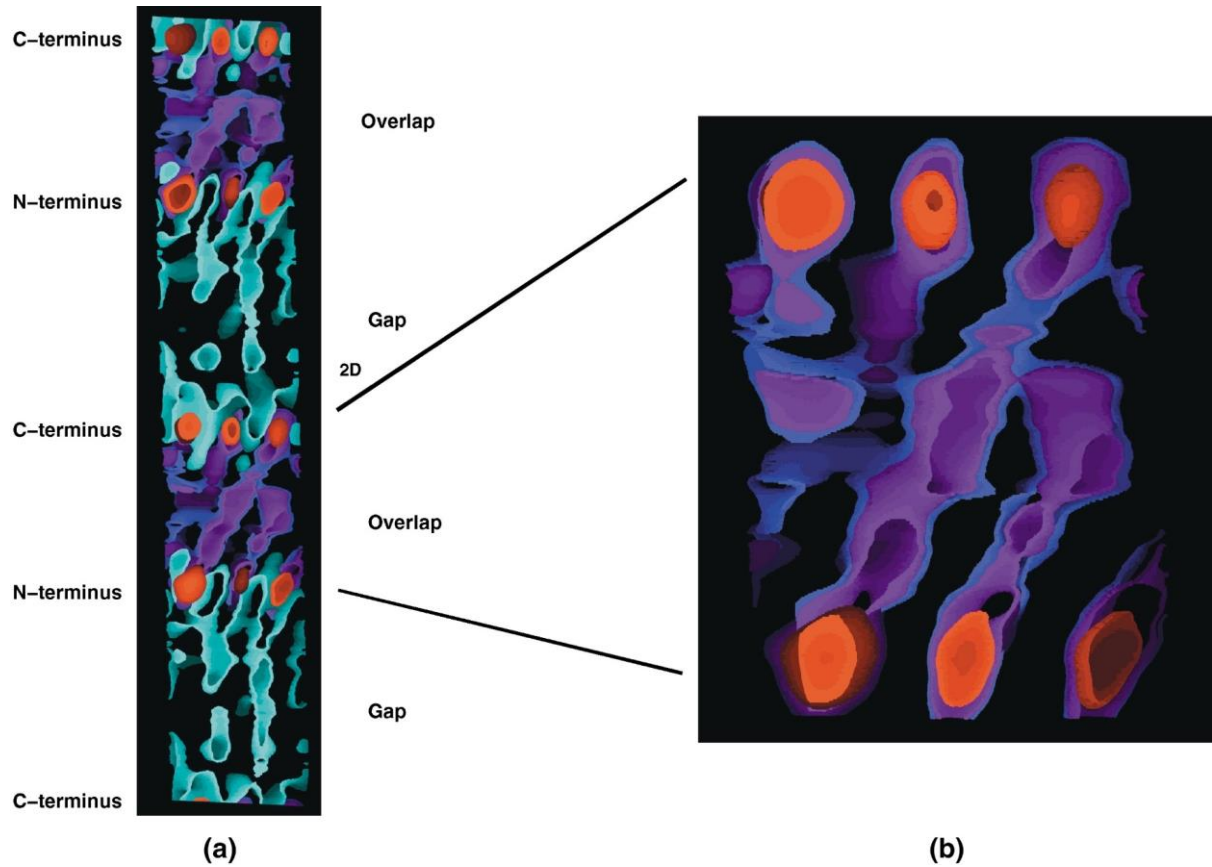
Figure 1.6: An electron density map of a longitudinal view of unit cells highlighting the tilted conformation in the overlap regions and the near-parallel conformation in the gap regions. The c-axis has been compressed to a scale of $1/5$ of the a-axis. (Reprinted from Ref. [31] with permission from Elsevier.)

Further analysis based on the calculation of overall intermolecular forces revealed a determinative mechanism for the specific axial staggering (Figure 1.7) [36]. When collagen molecules are placed at a series of axial offsets, $0D$, $1D$, $2D$, $3D$ and $4D$ (here, $D = 234$ residues out of the 1011 residues in one α chain), both the attraction between oppositely charged residues and the aggregation tendency between hydrophobic side chains are peaked, thus favouring the D-staggered arrangement [36]. The intactness of N- and C-telopeptides is also essential for initiating fibrillogenesis by forming metastable nuclei at the correct $4D$-staggered position [15]. Lacking telopeptides could affect fibril formation and result in abnormal shapes [37].
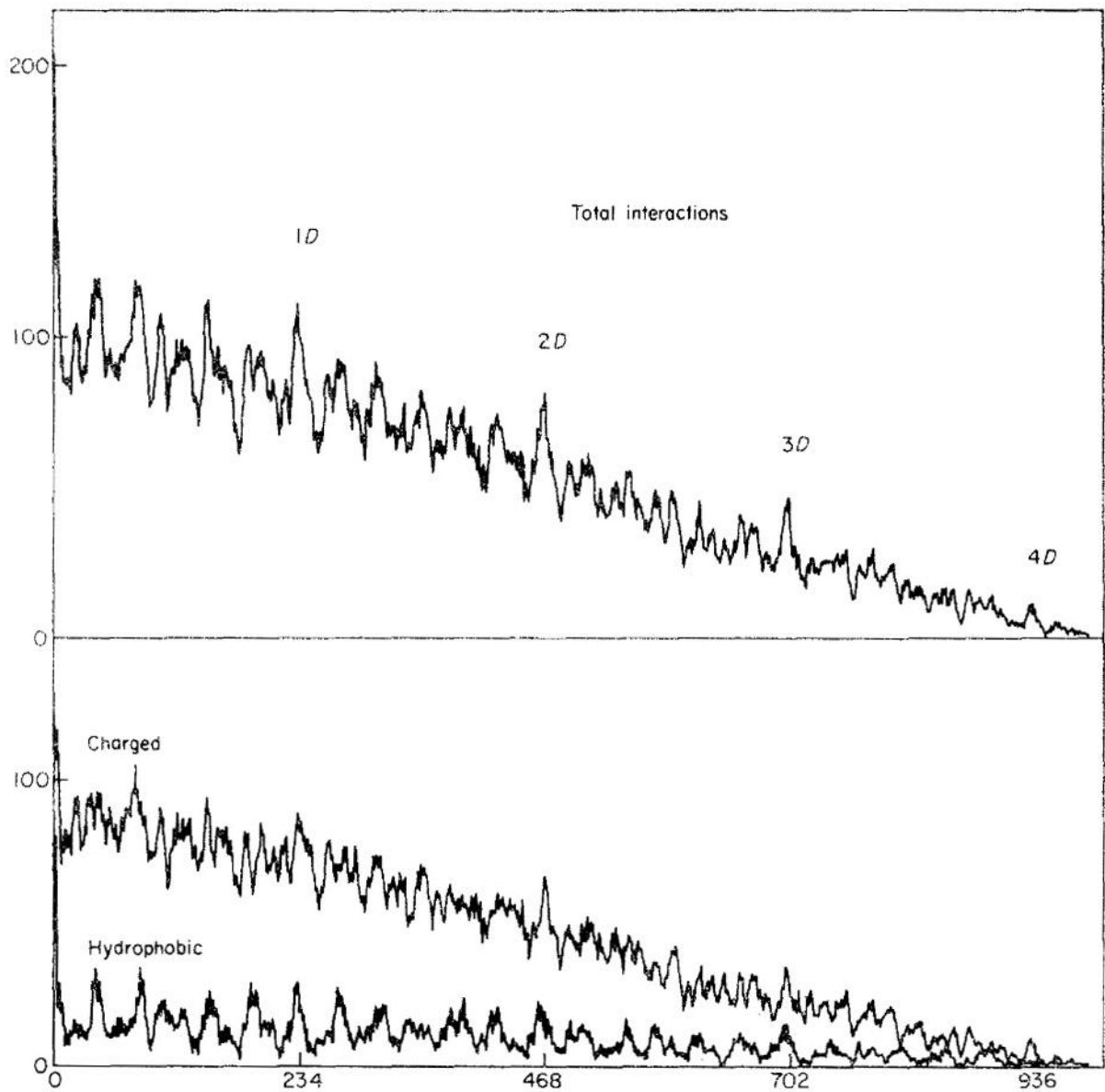
Figure 1.7: The total number of interactions (the y-axes) between two collagen molecules and the contributions of charged and hydrophobic interactions (total interactions = charged interactions + hydrophobic interactions). Both charts are presented as a function of the stagger (the x-axis). The staggering distance is measured in the number of residues. (Reprinted from Ref. [36] with permission from Elsevier.)

For the lateral packing, a simplified cross-sectional view reveals the relative positioning of the collagen molecules in a specific lateral plane (Figure 1.8) [38], numbered as 1 to 5 for different segments as above. In the quasi-hexagonal lateral arrangement, each five $1D$-staggered triple-helical collagen molecules are posited as a group winding around each other with a right-handed supertwist and is described as a "microfibril" (Figure 1.8, highlighted by orange polygons) [32]. Adjacent microfibrils are further interdigitated to form fibrils [32]. The lateral centre-to-centre spacing between collagen triple-helical molecules in the quasi-hexagonal lattice (d, also called intermolecular lateral packing distance (d_{ILP})) usually falls in the range of 1 to 2 nm, with a native state typically showing around 1.5 nm [39, 40].

9
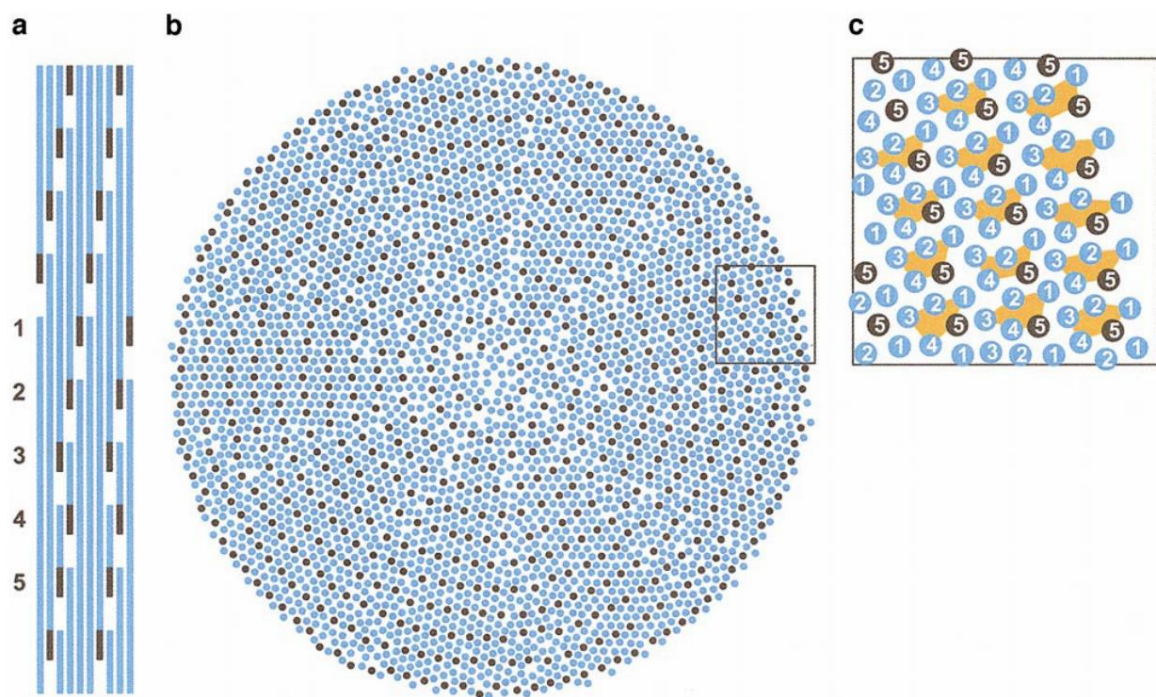
Figure 1.8: (a) Schematic of axial packing of collagen molecules (not to scale); (b) Cross-sectional view of a collagen fibril showing the radial packing of collagen molecules; (c) Enlarged view of the boxed area showing collagen molecules grouped in the form of microfibrils (orange polygons). The numbers 1 to 5 match the molecular segment numbering. (Reprinted from Ref. [38] with permission from Elsevier.)

Nevertheless, the intermolecular packing of collagen into fibrils is also stabilised (but not initiated) by the natural covalent crosslinks formed along with the assembly [41]. The formation of the crosslinks is associated chiefly with the lysyl oxidases. For each crosslink, an ε-amino group of a Lys residue in the telopeptide region is first converted to an aldehyde group which then links with another ε-amino group in a Hyl posited in a Hyl-Gly-His-Arg sequence in the triple-helical region. The relative amount of the so-formed divalent telopeptidyl-helical crosslinks is low, with up to one per collagen molecule; however, the divalent crosslinks could become more stable as they derive into multivalent crosslinks as the age of the animal grows [41].

1.1.3 Fibrillar Structure and Suprafibrillar Architecture

The growths of early fibrils to their target morphologies are generally determined by the anatomical location [25, 42], which involves the interplay of heterotypic collagens, the effects of extracellular macromolecules such as proteoglycans (PGs) and glycosaminoglycans (GAGs), and the functions of cellular processes [43, 44]. Briefly, fibrils can be categorised into two classes with distinct sizes and distributions [42]. Fibrils of the first class are usually narrow (25 to 100 nm) and have a relatively low polydispersity in diameter with a unimodal distribution (Figure 1.9, left). This class includes various collagenous tissues such as fetal tissues, corneas, nerve sheaths, blood vessels and interstitial connective tissues of parenchymatous organs [42].

The second class comprises tissues from locomotor systems (*e.g.*, tendons, ligaments, aponeuroses) and the sclera. Fibrils of the second class are widely distributed in diameter (near 0 to 500 nm) with multimodal distributions (Figure 1.9, right); some are even visible under light microscopy as large, straight fibres [25, 42, 45].

The two distinctive classes of fibrils behave dramatically differently when they form suprafibrillar architecture in a fibre network in the tissues [42, 46]. The morphology of the fibrils of the first class may vary from straight to wavy; however, they tend to spread widely apart, resulting in more hydrated interfibrillar matrices [42]. An excellent example of a parallel assembly of straight fibrils is the cornea (Figure 1.9, left); the large lateral spacing between the fibrils imparts the cornea with transparency and water retention properties. The connective stroma of the small intestine provides another example of a well-spaced fibrillar assembly but from wavy fibrils and forms an interwoven matrix (Figure 1.10, left) [42]. This structure would allow the tissues to have both flexibility and stiffness to withstand strain and stress in any direction during frequent bowel movements. On the other hand, the fibrils in the second group usually gather into thick and straight fibres, such as tendons (Figure 1.10, right). Also, with the multimodal size distribution, thinner fibrils can fit themselves into the lateral gaps of the thicker fibrils as in the sclera (Figure 1.9, right), increasing the packing density and thereby providing opacity and stronger resistance to strain and stress in the axial direction.
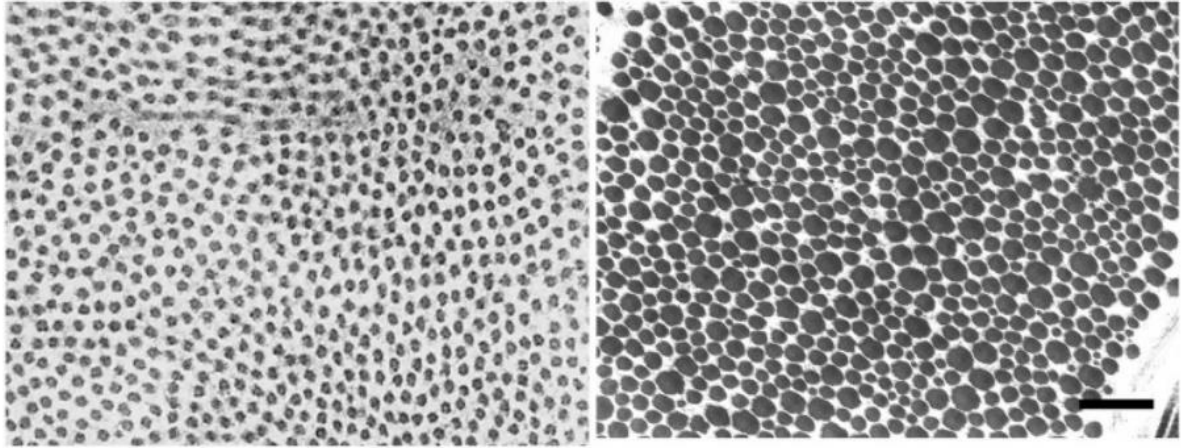
Figure 1.9: TEM images of the cross-sections of collagen fibrils in the cornea (*left*) and the sclera (*right*). Scale bar = 50 nm. (Reprinted by permission from Springer Nature Customer Service Centre GmbH from Ref. [25].)
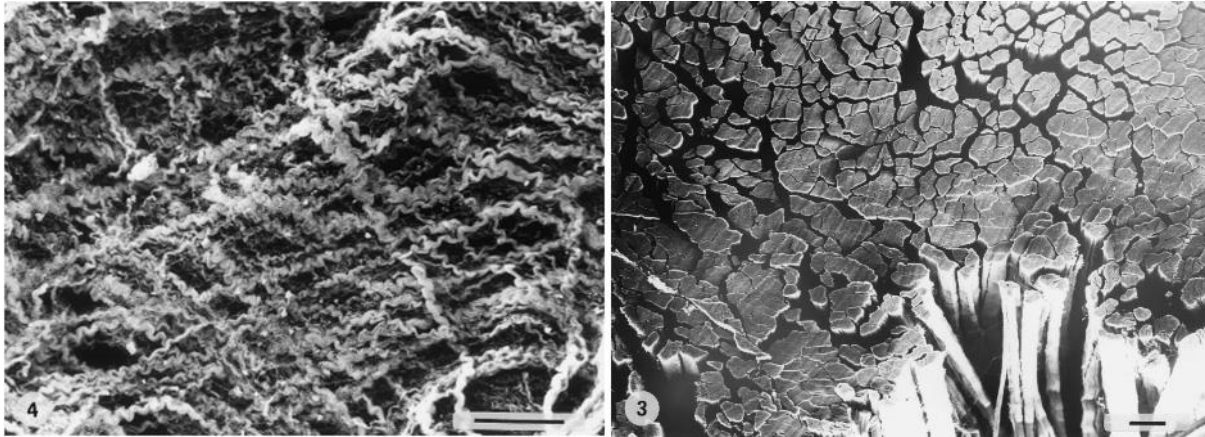
Figure 1.10: Scanning electron microscope (SEM) images of collagen fibrils in the connective stroma of the small intestine (*left*) and the transect tendon (*right*). Scale bar = 50 μm. (Reprinted from Ref. [42] with permission from Elsevier.)

1.2 Structural Changes in Collagen

Many external factors could trigger changes in collagen structure at multiple levels of the hierarchy. The changes can be categorised into two types: top-down and bottom-up. In a top-down structural change, the structure at the highest level (such as the fibrillar network) is affected first, and the impacts are passed on to lower levels. In contrast, a bottom-up structural change affects the lowest level (usually the amino acid residues) and sequentially affects higher levels and macroscopic properties. The top-down and bottom-up processes are mechanistically different and should be accounted for separately, considering that the latter is more relevant to the topic of this thesis.

1.2.1 Top-down Structural Changes

Top-down structural changes are mostly studied on native tissues, as such changes are frequently found in physical and biological processes. Air drying and stretching are two common physical processes to be considered [47, 48], whilst enzymatic digestion and demineralisation are the main focuses of biological process studies [49, 50]. Such processes have limited direct relevance to the scope of this thesis, but the concepts should be introduced to help understand the collagen structural changes in the bottom-up manner discussed in the next section.

Air drying of a collagenous tissue involves the loss of water from the pores of the collagen fibre network, the interfibrillar spacing, and the intermolecular gaps but probably does not affect the bound water at the lowest levels; a brief introduction of the hydration structure of collagen is therefore needed to explicate the dehydration process. Figure 1.11 shows the hydration shell of a collagen model peptide at different hydration levels: the first shell directly binds to the triple helix, the second shell forms hydrogen bonding to the first shell, and the third shell may be loosely bound to the surface of the hydration shell [18]. In an actual collagen molecule, detailed categorising can be complicated due to the numerously different combinations of adjacent triplets, however similar in the mechanisms of the model peptide. Each triplet in collagen has an average of 1.7 amide groups bound via hydrogen bonding to acquire extra stability than bare ones. One forms a direct hydrogen bond with another amide group, whereas the rest 0.7 part is stabilised via a "water bridge" that links two amide groups. Such water bridges comprise the first shell, which is also called the "structural water", to underline its importance in the local stability of the triple helix to maintain its conformation in regions lacking imino acids (Hyp and Pro) [14, 51]. Changes associated with the structural water can result in irreversible changes to the native triple helical structure; however, the impact on thermal stability is as yet debatable.[52, 53] Then water fills into the grooves of the polypeptides forming the second shell, so-called "cleft water", that binds to the bridging structural water molecules [14, 51, 54]. The last and loosest type of bound water is also called "surface water", which completes the interfacial monolayer of water on the collagen molecule [54]. Besides the three types of bound water, unbound water (or "free water") fills the intermolecular gaps, interfibrillar spacing and collagen fibre network rapidly exchangeable with

solvent water molecules. Also, the bound water is called "unfreezable water", highlighting that it is stably binding to collagen, and the unbound water is called "freezable water" or "bulk water".
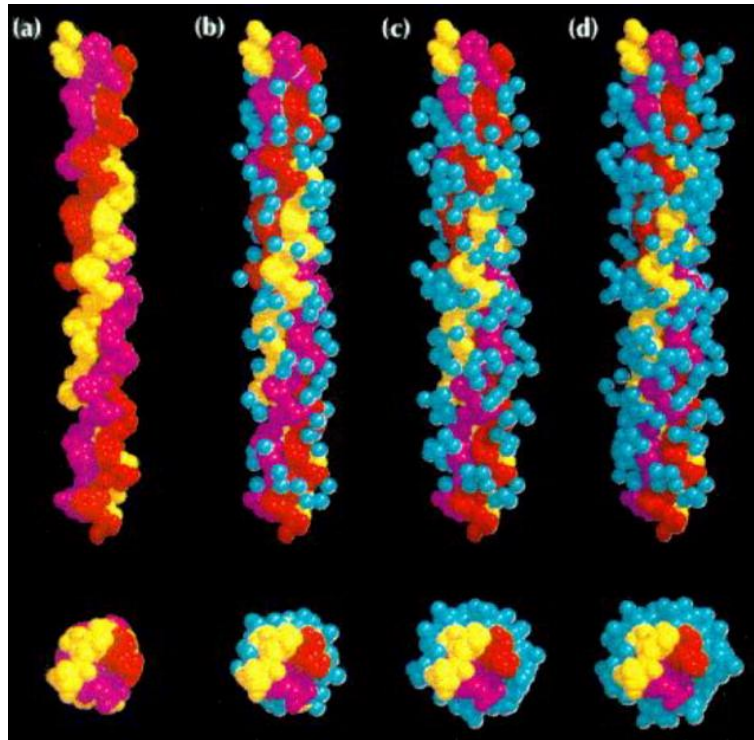
Figure 1.11: Model of the hydration shells of a Gly→Ala model peptide, (Pro-Hyp-Gly)$_4$-Pro-Hyp-Ala-(Pro-Hyp-Gly)$_5$. (a) "naked" triple helix; (b) the first shell of water molecules directly bound to the collagen; (c) the second shell of water molecules that are hydrogen-bonded to the first shell; (d) the third shell of water molecules. (Reprinted from Ref. [18] with permission from Elsevier.)

When a collagenous tissue is air-dried, unbound water can be removed, which shows a decrease in length macroscopically, dissipates down to reduce the fibrillar molecular axial and lateral packing spacing, and is also observed as contractions in the helix pitch of collagen molecules [47, 48, 51]. However, when physically constrained lengthways, dehydration causes lesser decreases in the D-period of collagen fibrils but similar contraction laterally [47].

Extension of tissues (*e.g.*, tendon, zonular filament, and pericardium) under uniaxial stretching is also found to rearrange the interfibrillar structure and expand the intermolecular spacing (Figure 1.12) [55-58]. During the stretching, each structural compartment has various rigidity and responds to the external force and strain differently through a dissipation chain at all hierarchical levels, from straightening the fibrils, rotating towards the tension axis, sliding between fibrils and molecules, and finally delamination before cracks form.
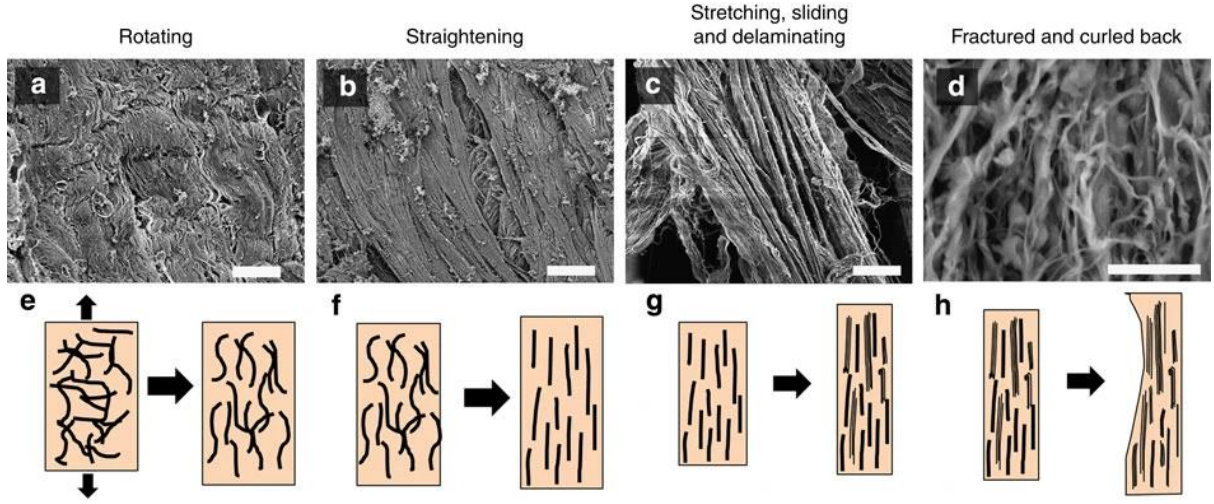
Figure 1.12: Schematic model of different stages of tensile loading of collagenous tissue. The black lines are collagen fibrils. Scale bars for SEM images are 20, 20, 20 and 50 µm, respectively. (Reprinted from [57] under the Creative Commons CC BY licence terms.)
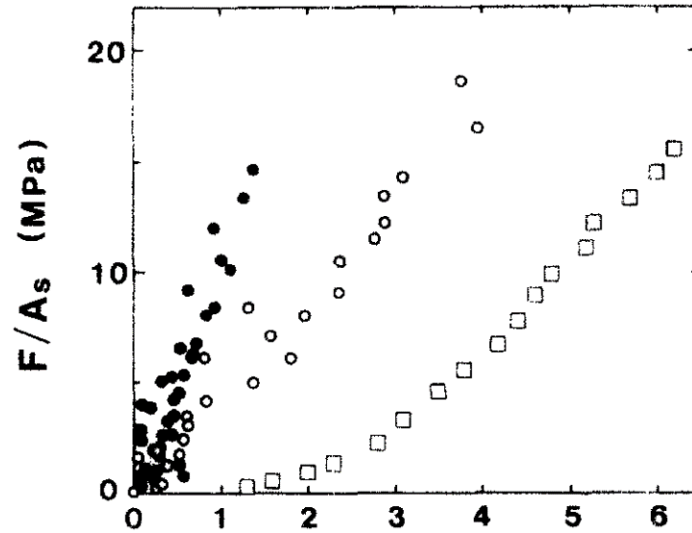
Figure 1.13: Comparison of the force-strain curves of a collagen molecule (●), a collagen fibril (○), and a tendon (□). Small-angle X-ray scattering measurements were conducted to determine the strain in the fibril structure. (Reprinted from Ref. [58] with permission from Elsevier.)

1.2.2 Bottom-up Structural Changes

Bottom-up structural changes are associated with molecular interactions during material processing, including extraction, stabilisation and functionalisation. Collagen extraction involves acid or base treatments and usually enzymes to assist the process [6, 59]. Enzymatically assisted processes using endopeptidase such as pepsin will remove the N- and C-telopeptides from the collagen, affecting its performance in assembly into fibrils and fibre networks [15, 60]. For stabilising and functionalising native tissues, one would aim to maintain the intrinsic collagen structure while (chemically) modifying the amino acid side chains; thus,

numerous binding and crosslinking chemistry variations are to be investigated thoroughly [6]. Specifically, many processing technologies of collagenous tissues face a common challenge of adverse effects due to the unknowingly excess usage of chemicals (elaborated in Chapter 3 and Chapter 5). Herein, three chemicals are introduced to represent the distinctive reaction mechanisms with collagen and the bits of knowledge around the bottom-up impacts on the collagen structure.

Glutaraldehyde (GA) is one of the most widely used covalent crosslinkers in collagenous materials [61]. As a dialdehyde, the reaction mechanism of GA with collagen starts from the formation of a Schiff base between the aldehyde (–CHO) group of GA and the amino (–NH₂) group in the Lys residues in collagen (Figure 1.14) [62]. Other amino acid residues containing –NH₂ (such as Arg) are much less favoured in crosslinking with GA than Lys, therefore negligible in the discussion, yet the rare occurrence is not completely excluded [63-66]. The Schiff base intermediate can also react with more GA molecules before being terminated by a –NH₂ group, forming polymerised long chains [61, 62]. Some novel crosslinkers like dialdehyde starch share a similar reaction mechanism to GA. The reaction of GA with collagen rapidly occurs at neutral pH at room temperature, leaving a slightly yellow shade on the crosslinked material at a typical concentration of 0.25%–1% (w/w) [62, 67, 68]. However, issues around GA-crosslinked collagen were revealed progressively during clinical practices, including its structural degradation, calcification and immune responses after implantation. Most of these issues were proposed to be connected to the use of GA [69].
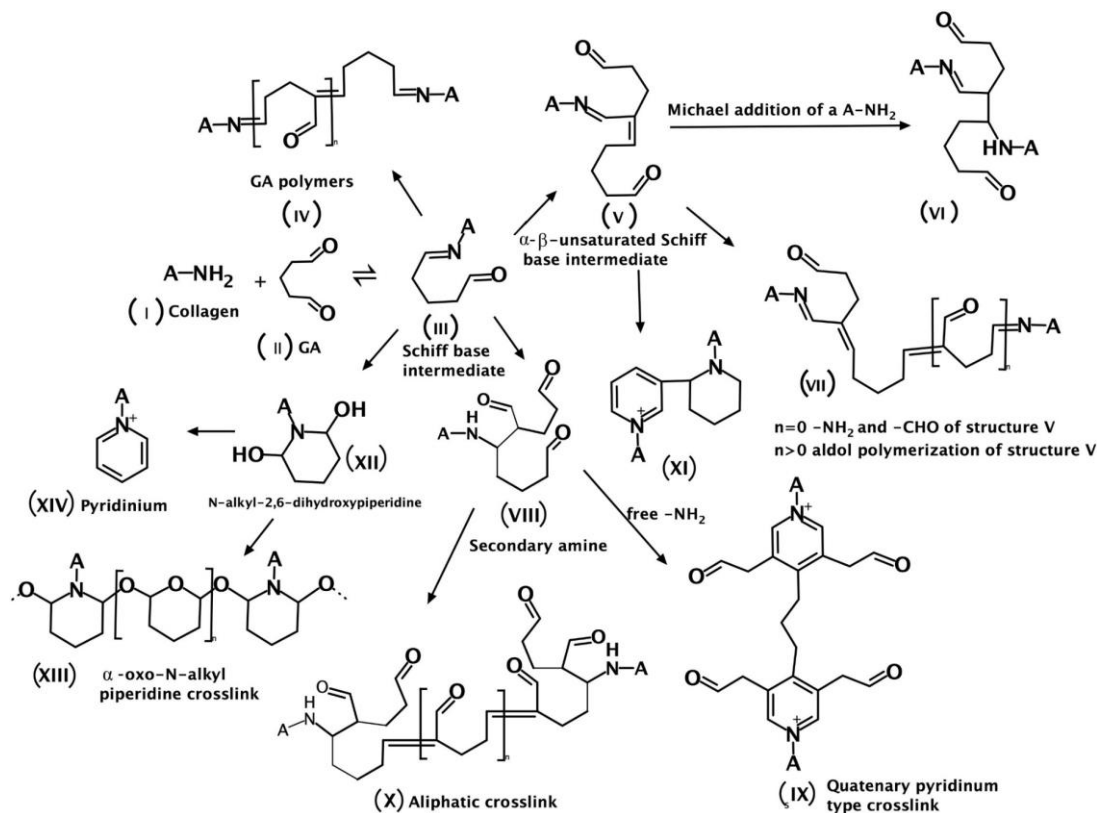
Figure 1.14: Proposed reaction pathways of glutaraldehyde (GA) with collagen (the "A" in "A–NH₂"). (Reprinted from Ref. [61] with permission from Elsevier.)

In addition to dialdehydes, carbodiimides also link the collagen molecules covalently yet with a completely different mechanism called "zero-length" crosslinking (*i.e.*, peptide bond formation) [70]. An example here shows the reaction mechanism of the well-known EDC (1-ethyl-3-(3-dimethyl aminopropyl)carbodiimide) with collagen Glu (or Asp) and Lys (or Hyl) residues (Figure 1.15) [70]. N-hydroxysuccinimide (NHS) is often added to form a relatively stable intermediate to suppress the side reaction, *i.e.*, a rearrangement followed by the hydrolysis back into the original carboxyl (–COOH) group. The reaction is usually undertaken at pH 5.0-5.5 in 2-(morpholino) ethane sulfonic acid (MES) buffer. It provides a low cytotoxic product due to its non-participation during crosslinking while maintaining the original colour of the tissue and potentially improving cell attachment and proliferation [71, 72]. However, the urea derivates formed as by-products exhibit cytotoxicity to a certain degree [70].
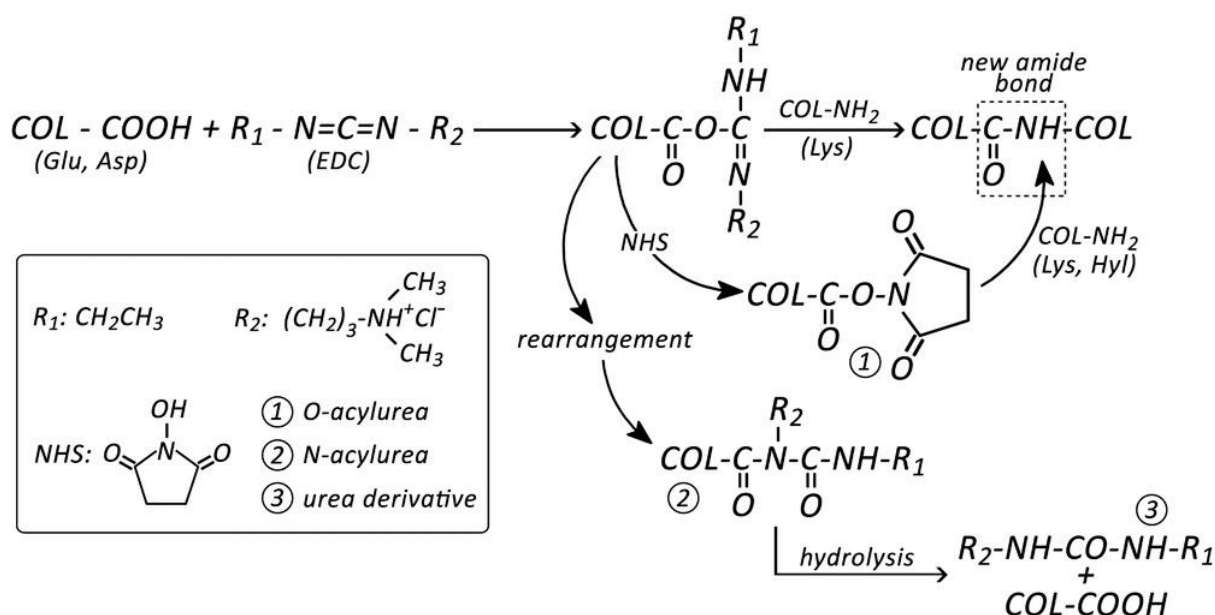
Figure 1.15: EDC crosslinking mechanism with collagen between Glu (or Asp) and Lys (or Hyl) residues. The NHS-mediated pathway is also displayed. (Reprinted from Ref. [70] with permission from John Wiley and Sons.)

Apart from organic crosslinkers, metallic salts have been used as fixatives to stabilise collagen in tissues, leading to extensive uses in the leather processing industry for almost two centuries [45]. Leather processing starts with raw animal skins and involves intense chemical treatments to remove non-collagenous proteins and fats [45, 73]. Then, the skins undergo a process called "tanning", historically using bark tannins, but nowadays, more commonly using metallic salts such as chromium sulfate, which is involved in 90% of the modern tanning processes. Like chrome tanning [4], many leather tanning technologies are long-established but lack molecular-level understandings, limiting their further development to keep up with the times.

The mechanism of the binding reaction of chromium sulfate with collagen has been shown as predominantly covalent while having minor electrostatic interactions (when used excessively)

---

[4] "Chrome" is a colloquial term used in leather tanning representing trivalent chromium (Cr(III)).

[74]. The coordinate covalent bonds form between the carboxylate (–COO⁻) groups in Asp and Glu residues of collagen, preferentially initiating in the telopeptides. Once the covalent binding sites are fully occupied, electrostatic interactions allow further absorption of chromium species (charged aquo complex or deposited clusters) into the collagen matrix [74]. However, its potentially leachable ionic forms have raised health concerns about allergic contact dermatitis [75]. The chromium-bound collagen tends to have a blue or green shade, and gives a much higher thermal resistance with a typical increase in denaturation temperature (T_d) from 50 °C to 100 °C, probably due to a combination of constraints by covalent bonds and spatial confinements due to occupancy [74]. A series of metallic species, such as aluminium and zirconium, could also be used to stabilise collagen but prefers to bind to collagen through electrostatic interactions [76].

Although having completely different reaction mechanisms with collagen molecules, the three chemicals, GA, EDC and chromium sulfate, share similar impacts on collagen structure in a bottom-up manner. At the molecular level, species binding to collagen on specific side chains can disrupt the intermolecular structure, causing a change in the axial packing *D*-period and the lateral packing distances [74]. The binding was suggested to also physically (or spatially) hinder the entering of water molecules while chemically reducing their affinity to collagen functional groups via hydrogen bonds, shown as dehydration and thus increments in T_d [77]. Dehydration also seems to link with physical constraints or shrinkages in fibrillar diameters, resulting in increases in porosity in collagen materials, which might be beneficial to biomedical applications [78].

1.3　Techniques for Collagen Structural Studies

Many techniques have been employed to characterise collagen properties and hierarchical structure [79-82]. A few of the frequently used techniques are listed, following a sequence from the finest structural unit to macroscopic morphologies:

(1) Sodium dodecyl sulfate-polyacrylamide gel electrophoresis (SDS-PAGE) displays the molecular weight (intactness of the polypeptide chain);

(2) Raman and infrared spectroscopies decipher the structure of the amide bonds in the polypeptide;

(3) Circular dichroism (CD) spectroscopy reveals the triple helicity of the collagen molecule;

(4) Microscopies (*e.g.*, transmission electron microscopy (TEM), scanning electron microscopy (SEM), atomic force microscopy (AFM)) visualise the *D*-periodic banding structure of the collagen fibril and the macroscopic morphologies of the fibrillar network;

(5) Small- and wide-angle X-ray scattering (SAXS and WAXS) techniques provide rich information about the helical structure (by WAXS) as well as the molecular and fibrillar structures of collagen in tissues (by SAXS).

Since the 1920s, X-ray scattering has been used to study collagen molecular and fibrillar structure [83-85]. As an *in situ* technique, samples can be exposed to the X-ray in their native states without requiring heavy metal staining or drying prior to the measurements, giving accurate information about the native states. The recent development in synchrotron radiation techniques allows researchers to achieve sufficient resolution with a very short exposure (typically a few seconds for skin samples), extending the advantage of X-ray scattering techniques. However, X-ray measures the electron density contrast between collagen and the background, so the observations are indirect and are limited to high contrast variations (theories to be introduced in Chapter 2). Also, orderliness is needed to give constructive interference between the diffracted X-rays. Therefore, X-ray scattering results would primarily be used to postulate rather than firmly identify changes in amino acid side chains during chemical binding reactions unless complemented with other techniques.

On the other hand, Raman and infrared spectroscopies have been used widely to identify and resolve collagen structural changes as the spectra have distinctive peaks[5] showing amino acid residues and the secondary structure of peptide bonds [81, 86-88]. While infrared (or Fourier transform infrared, FT-IR) spectroscopy prefers dry samples due to the extremely high infrared absorption of water molecules, Raman spectroscopy can cope with hydrated samples that better represent the native state in the tissues [81]. Moreover, the discovery and development of surface-enhanced Raman spectroscopy (SERS) in the past few decades allows us to probe the site-specific interactions of proteins with reagents, due to its enhancement of Raman signals

---

[5] In Raman spectroscopy studies, "peak" is often interchangeably referred to as "band". In an archaic setup, a photo is generated with bands. However, since modern setups generate digitised spectra with peaks in curves, the term "peak" is preferred in this thesis. Also, using "band" for Raman studies may confuse the reader with the dark and light bands in TEM images of collagen fibrils.

by manifold to resolve the subtle changes [89-91]. The advantages of SERS over conventional Raman spectroscopy attract increasing research interest in its bioanalytical applications, which is particularly interesting for us as we could employ this technique to identify collagen and analyse its structural changes during reactions; in fact, the SERS bioanalysis of collagen was performed but only briefly explained until the work in this thesis (elaborated in Chapter 3 and Chapter 4).

Combining X-ray scattering and SERS techniques allows us to cover the scale of interest of collagen structures and reaction mechanisms from the macroscopic levels down to amino acid residues. A brief history of the applications of the two techniques in collagen studies should reveal the state-of-the-art in collagen structural studies and also lead to the motivation of the work in this thesis.

1.3.1 X-ray Scattering in Collagen Structural Studies

The use of X-ray scattering to investigate collagen structure has a long history starting around two decades after the discovery of the X-ray itself. Figure 1.16 displays one of the earliest X-ray scattering images of collagen fibrils in tendons [83]. Depending on the sample-to-detector distance (the "specimen-to-film" distance, in an archaic setup) and the collected scattering angle, X-ray scattering techniques can be roughly categorised into wide-angle X-ray scattering (WAXS) and small-angle X-ray scattering (SAXS). WAXS provides information at finer scales in real space and vice versa. As labelled in the figure, the WAXS image of the tendon resolves three features: the meridional diffraction lines (L), equatorial scattering arcs (ES) and meridional scattering arcs (MS). The diffraction lines can be closely investigated in the SAXS region to give the well-known axial D-period of the collagen fibrils in native tendons (around 67 nm). The largely ordered lateral packing (the "quasi-hexagonal" structure, or "liquid crystal" to highlight its variability across the lengthways) is indicated by the equatorial scattering arcs, of which the smeariness shows the variations in the intermolecular lateral packing distance (d_{ILP}) with an average falling in the range of 1–2 nm.
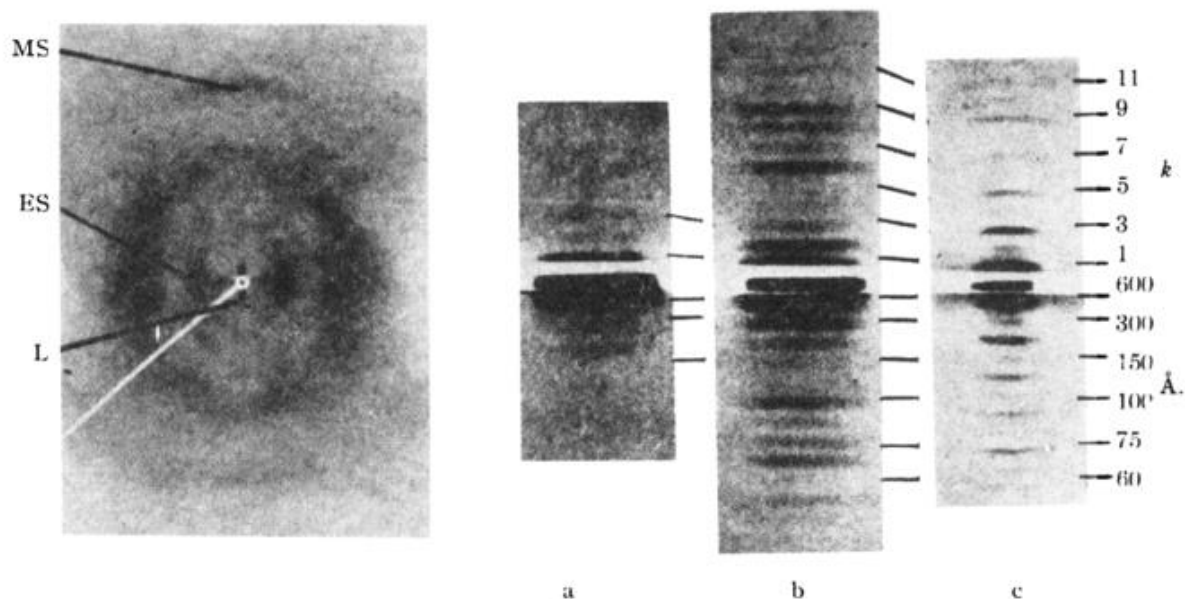
Figure 1.16: (*Left*) The WAXS image of a bovine Achilles tendon. Three features are labelled the diffraction lines (L), equatorial scattering arcs (ES) and meridional scattering arcs (MS). (*Right*) The SAXS images of (a) formaldehyde-treated rat tail tendon, (b) dried bovine Achilles tendon, and (c) hydrated kangaroo tail tendon. k indexes the order of the diffraction while the angstrom values are the corresponding scale in the real space. (Reprinted with permission from Ref. [83]. Copyright (1944) American Chemical Society.)

The "meridional" scattering arc was not explained until a better resolution was achieved to show that the "meridional" scattering arc is not a true meridional scattering but rather a superposition of two non-meridional reflections [92]. Based on this observation, the first helical symmetry of collagen was proposed as containing three residues per turn in a repeating unit cell of a = 12.0–16.0 Å, c = 9.0–9.5 Å with a 3_1 symmetry (3/1-helix) about the c-axis; the two non-meridional arcs are from the diffraction of Miller indices of the (113) lattice planes with the spacing of 2.82–2.86 Å [92]. A detailed analysis of the WAXS pattern suggested that both 7/2-helix and 10/3-helix models fit the pattern well (Figure 1.17, as shown by the lines on each side of the pattern), implying that the actual collagen structure is an intermediate of the two [29, 93]. WAXS images acquired nowadays have much higher resolution showing well-defined features (Figure 1.18), which could be used to calculate the finer helical structural information in collagen molecules. The distance from the centre to the four scattering arcs at the diagonal corners can be decomposed into two components. The meridional component represents the helical pitch, which allows us to estimate the length of the axial repeating units within a collagen molecule. The equatorial component signifies the diameter of the triple helix, typically around 1–1.5 nm in the native state [47].

21
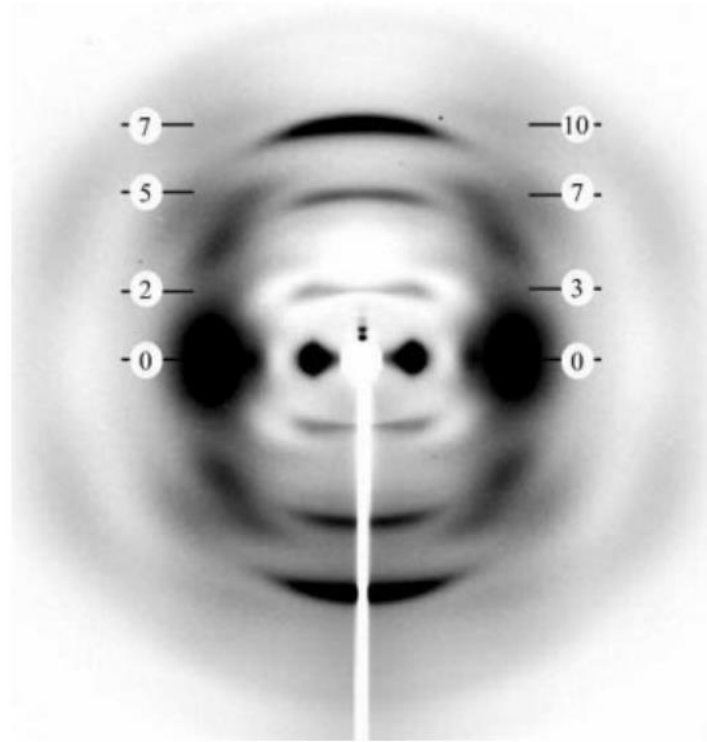
Figure 1.17: WAXS pattern from a kangaroo tail tendon with indices for 10/3 and 7/2-helical models. The layer indices on the left correspond to a 10/3-helical model with a repeating period of 28.6 Å, and the ones on the right correspond to a 7/2-helical modal with a repeating period of 20.0 Å. (Reprinted from Ref. [93] with permission from John Wiley and Sons.)
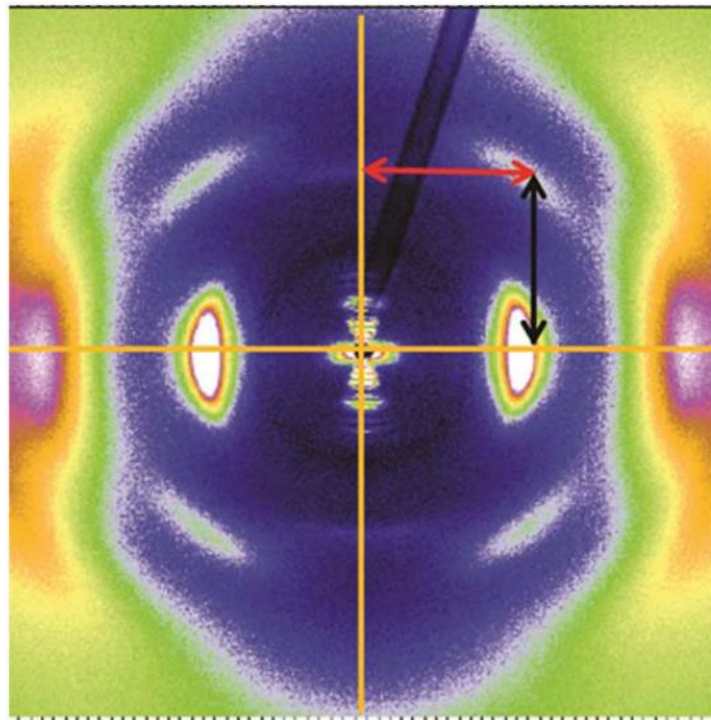
Figure 1.18: Collagen structure hierarchy corresponds to features from X-ray scattering (SAXS and WAXS). (Reprinted from [47] under the Creative Commons CC BY licence terms.)

The WAXS patterns are usually broad and diffused in contrast to the narrow SAXS patterns, which focus on the series of meridional diffraction lines, or if collagen fibrils are not aligned perfectly, they become diffraction rings as the sum of diffraction lines in all directions. Figure 1.19 displays a set of SAXS patterns with the corresponding radially integrated one-dimensional (1D) scattering profile [94]. The diffraction peaks are not isolated from each other; they originate from the long-range ordered axial packing of collagen and hence can be used to estimate the D-period of collagen [94]. The odd-order peaks (*e.g.*, 3rd and 5th) are usually sharp and well resolved, giving accurate estimations of the D-period and the subtle shifts even at subnanometer levels. However, since collagen packing distances (D-period and d_{ILP}) can inevitably be affected by the moisture content, a subtle change in hydration level could significantly affect the results [47, 48, 51]. Therefore, strict sampling and measurement conditions must be carefully followed during the SAXS operation.
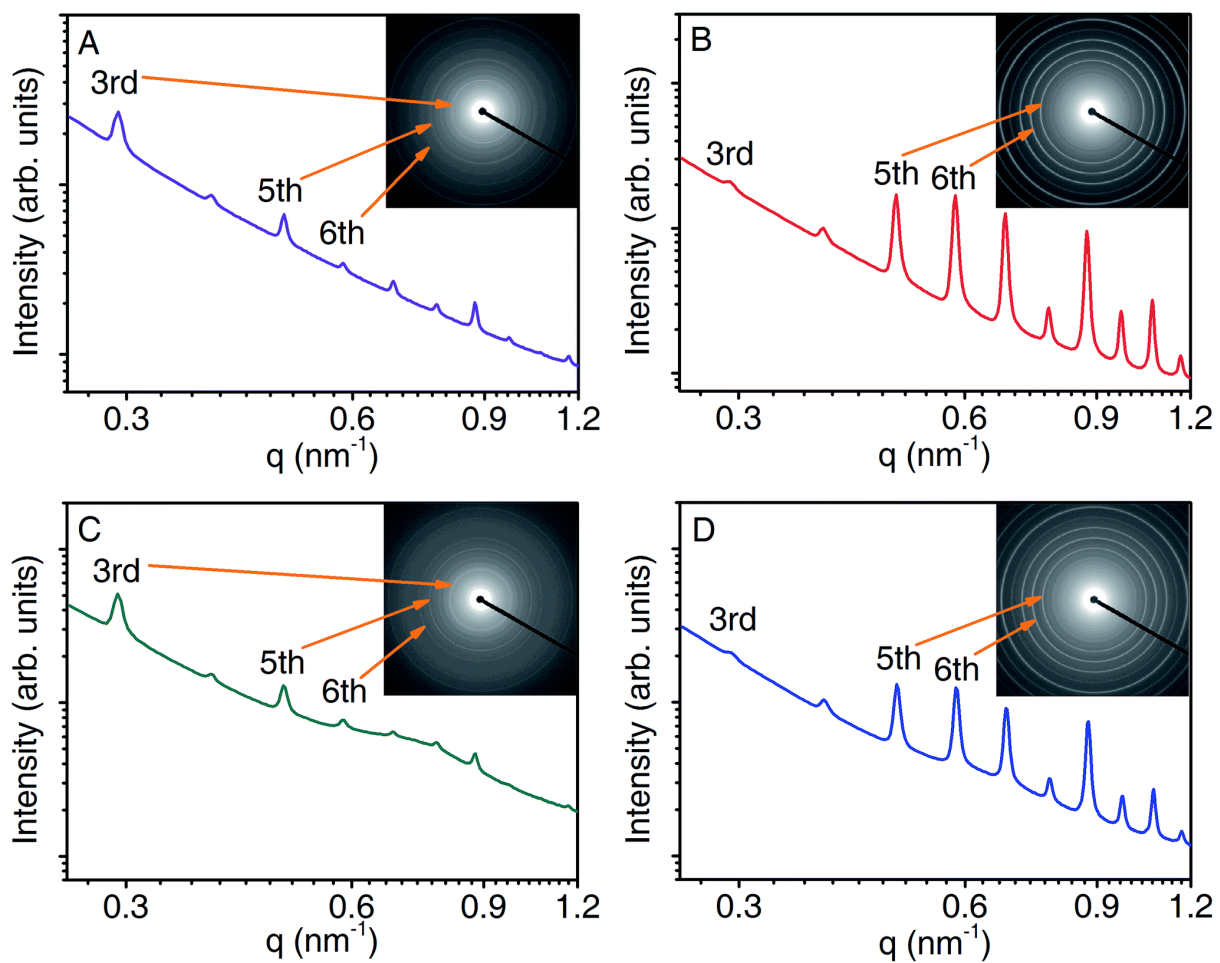
Figure 1.19: SAXS 2D diffraction pattern and the corresponding radially integrated 1D profile of ovine skins reacted with (a) oxazolidine and followed by (b) chromium sulfate. Peak orders 3rd, 5th, and 6th are denoted. (Reprinted from [94] under the Creative Commons CC BY licence terms.)

Apart from the shifts, the fluctuations in peak intensities also give rich information on the collagen structure [45]. One typical example is the changes in hydration level. When

dehydration occurs, the changes in peak intensity of a tendon sample were found to separate into two groups: the even-order peaks increases relative to the odd-order peaks [95, 96]. Similarly, when collagen fibril is air-dried without strain to maintain its macroscopic length, the intensities of the 3rd and 5th peaks decrease while the 2nd and 6th peaks increase relatively [47, 96]. In contrast, when stretched or extended from the native state, collagen fibrils showed decreases in the 3rd to 2nd order ratio [55, 97].

While dehydration solely changes the molecular arrangement to reflect in the SAXS diffraction peaks, chemical reactions affect the arrangement and the electron density contrast of the collagen molecule to its surroundings, similar to the concept of metallic staining used in TEM for biological samples [35]. As exemplified in Figure 1.19, the intensities of the peaks from the 5th order onwards increase significantly, while the 3rd order peak decreases upon the binding of collagen with chromium species [74, 94]. Likewise, an "asymmetry value" was introduced, calculated as the sum of the integrated peak intensities of all even-order peaks (from the 4th) divided by the sum of all odd-order peaks (from the 3rd); it was used to represent the structural changes in the *in vitro* glycation of collagen in the bovine pericardium [98]. Conversion of peak intensities to a real-space electron density map of collagen can be realised based on collagen models to reveal the folding in telopeptides [99, 100], yet it relies heavily on molecular models and is beyond our scope of this investigation.

1.3.2 Raman Spectroscopy and SERS in Collagen Structural Studies

In contrast to the decades of Raman spectroscopic investigations into collagen [81] and the SERS analyses of biological molecules [101], the use of the SERS technique in collagen studies is unexpectedly scarce [102-104]. A full, characteristic Raman spectrum of collagen from bone is shown in Figure 1.20 (Raman shift ranging from 100 cm^{-1} to 3700 cm^{-1}), with distinct peaks labelled by referring to theoretical bond vibration frequency and previous studies on hydroxyapatite (HAp) and peptides [105]. One of the earliest comprehensive Raman peak assignments of collagen was reported in the 1970s and is hitherto well-recognised in modern collagen studies (Table 1.2) [86].
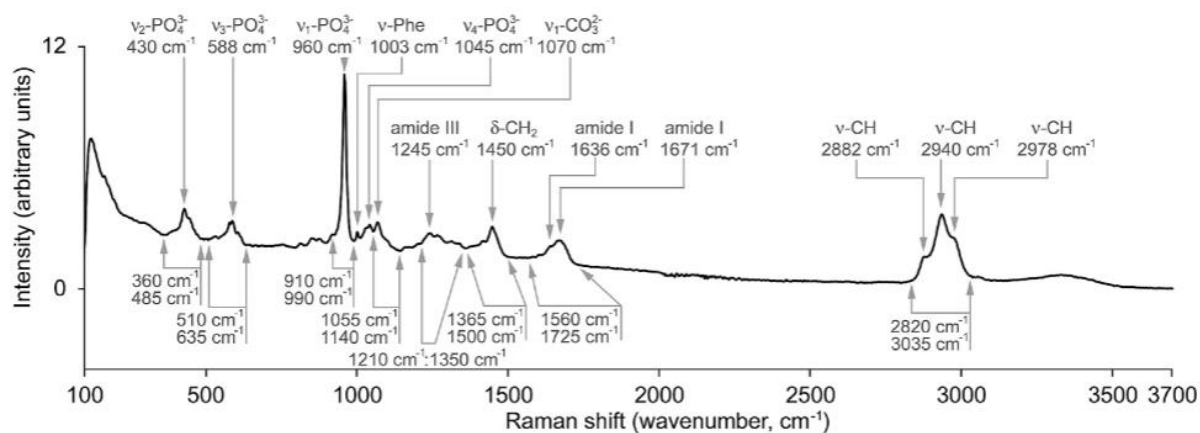
Figure 1.20: The full Raman spectrum of a historic human metatarsal bone showing collagen and hydroxyapatites (HAp). (Reprinted from Ref. [105] with permission from Elsevier.)

Table 1.2: Raman peaks in the spectra of collagen and related molecules. (B.A.T. = bovine Achilles tendon.) General notations refer to Appendix A. (Reprinted from Ref. [86] with permission from John Wiley and Sons.)

TABLE I   Raman Lines in Collagen and Related Spectra

Collagen (B.A.T.)	Gelatin (10% Aqueous Solution)	Mixture of All Amino Acids pH 13	Mixture of All Amino Acids pH 2	Mixture of Aromatic Amino Acids pH 13	Mixture of Nonaromatic Amino Acids pH 13	Gelatin (10% in D_2O)	Assignment
			1746 s				ν(C=O)
1670 s	1668 s					1664 s	Amide I
1642 s sh	1636 s sh					1645 s sh?	Amide I
					1601 m		
	1608 w	1611 m	1611 m	1604 m		1611 w	Phe, Tyr
		1589 m	1589 m	1585 m			Pro., Hypro
	1566 w				1576 m		
				1483 w			
1464 s sh	1464 s sh		1460 s		1457 s	1464 s	δ(CH_3, CH_2)
1451 s	1451 s	1450 s		1451 s			δ(CH_3, CH_2)
			1438 s				in. pl. bend of carboxyl OH
1422 m	1422 m	1415 vs			1408 s	1415 m	ν_s(COO^-)
	1399 m			1396 s			
1392 m	1389 m						
1343 m	1347 m	1353 s	1353 m	1330 m	1350 m	1347 m	γ_w(CH_3, CH_2),
1314 m	1320 m	1323 m	1324 m	1320 m	1320 m	1330 m	γ_t(CH_3, CH_2), δ(C_a—H)
		1271 w	1274 w				
1271 s	1271 s					1274 w	Amide III
		1245 w	1235 m	1238 w			
1248 s	1248 s					1247 w	Amide III
1211 w	1211 w	1211 w	1211 m	1211 m		1211 δ(D_2O)	Hypro, Tyr
	1198 w						
1178 w	1182 w	1188 w	1188 w	1188 m		1185 w	Tyr
					1178 w		
1161 w	1165 w						
					1145 w	1135 w	NH_3^+
1128 w	1128 w						
			1118 m		1111 m		ν(C—N)
1101 w	1101 w	1111 m				1105	
1087 w	1084 w	1088 m	1091 w	1091 m	1088 m		ν(C—N)
1067 w	1064 w					1057 w	
	1051 w			1051 w			
			1044 s				o. pl. bend of carboxyl OH
1037 m	1037 m	1037 w		1034 m			Pro
					1024 w		
1006 m	1006 m	1006 m	1006 m	1006 s		1006 s	Phe
		986 w		982 m		993 m	Amide III'
966 w	969 sh		969 m			966 m	Amide III'
					942 s		ν(C—C) of residues
938 m	942 s					942 s	ν(C—C) of protein backbone
921 m	925 s					925 s	ν(C—C) of Pro ring
918 m			918 m	918 s			
		907 vs			908 s		
890 w	890 w						
876 m	880 s			873 s		884 s	ν(C—C) of Hypro ring
		856 vs	870 vs		866 s		ν(C—C) of residues
856 m	863 s			859 s		856 s	ν(C—C) of Pro ring
			825 vs				ν(C—C) of residues
821 w	818 m					814 m	ν(C—C) of backbone
		783 m					
769 w	769 w			786 w	783 w		
			741 s		668 w	759 w Br	
			650 m	646 w			
622 w	625 w	629 w	629 m	629 w			Phe
		593 w	593 w		593		
568 w	572 w		575 w			575 w	
533 w	536 w	543 s	522 m		540 w	540 w	
		518 m	504 s		522 w		
		447 w					
	425 w			479 m			Pro
			414 m	447 m			Hypro
396 w						407 w	Pro
				345 w			Pro

Key to abbreviations: s(strong), m(medium), w(weak), sh(shoulder), vw(very weak), ν(stretching coordinate), δ(deformation coordinate), γ_w(wagging coordinate), γ_t(twisting coordinate), Tyr(tyrosine), Phe(phenylalanine), Trp(tryptophan), Pro(proline), Hypro(hydroxyproline), B.A.T. (Bovine Achilles tendon).

The characteristic amide I peaks are observed at 1670 cm^{-1} and 1640 cm^{-1}, mainly corresponding to C=O bond stretching (ν(C=O)) modes, with minor contributions from the C–N bond stretching (ν(C–N)) and the N–H bond bending (δ(N–H)) modes [86, 103, 106]. The peak around 1450 cm^{-1} shows the scissoring bending vibration of the aliphatic C–H bonds (δ_s(C–H)) in methylene groups (–CH$_2$–) or methyl groups (–CH$_3$) [86, 107]. The minor peak at 1424 cm^{-1} could be related to the δ(C–OH) in the carboxyl groups (–COOH) in Asp and Glu residues [108]. The amide III peaks observed at 1275 cm^{-1} and 1245 cm^{-1} originate from δ(NH$_2$) and ν(C–N), respectively [86, 102, 109, 110]. One suggested that the 1270 cm^{-1} peak could be assigned to the helical structures in protein, the 1245 cm^{-1} peak to a random-coil structure, and the peak in 1230–1240 cm^{-1} to a β-pleated sheet [111]; the ratio of those peaks may be useful for determining the structural integrity of collagen. Besides that, a distinct peak at 1005 cm^{-1} represents the ring breathing mode (ν_{12}, Wilson's notation for modes of benzene ring vibration [112]) of Phe residues [86, 103, 107, 113]. Peaks below 1000 cm^{-1} are mostly related to ν(C–C) of collagen, including the backbone, Pro, Hyp and other aliphatic or aromatic residues (such as Tyr) [86, 110].

The peak shifts and intensity variations usually imply a specific structural change in collagen [106, 114]. When a rat tail tendon is under tension, the Raman spectrum could give a blueshift of the 822 cm^{-1} backbone ν(C–C) peak and a redshift of the 879 cm^{-1} carbonyl δ(C=O) peak; shifts are attributed to the extension in the backbone skeleton and the resulting contraction of the amide C=O bonds [114]. Similar observations on peak shifts were also reported in amide I and amide III regions of the Raman spectra from human skins [106]. However, studies using polarised lasers suggested that Raman peak intensity can change with the relative orientation of the collagen fibrils and the laser polarisation (Figure 1.21). Therefore, if a peak is sensitive to polarisation (e.g., 1670 cm^{-1}) and the orientation of the collagen sample is not controlled during the measurements, the peak is not suitable for determining the integrity of the collagen structures [110, 115, 116].
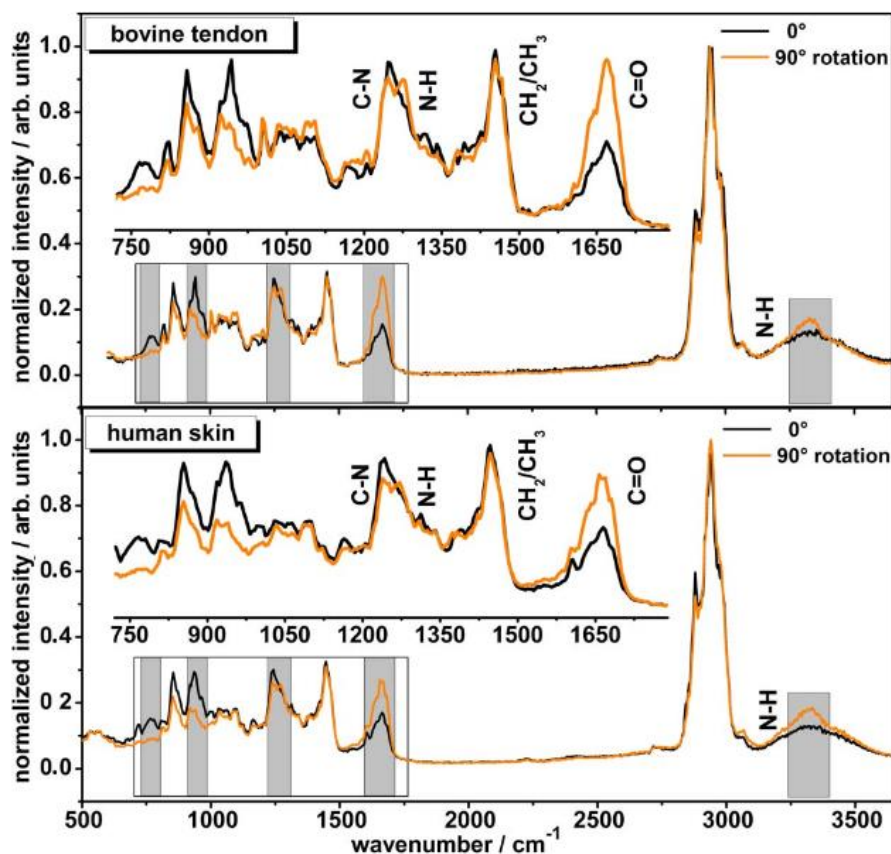
Figure 1.21: Normalized Raman spectra of collagen fibrils oriented parallel and perpendicular to the incident laser beam. The grey squares indicate the peaks that show the most substantial anisotropic Raman scattering. The inset outlines the fingerprint region of collagen. (Reprinted from [115] under the Creative Commons CC BY terms.)

Applying the SERS technique provide strong enhancements of the Raman scattering signal to resolve subtle changes in the structure of proteins (the theories of surface enhancement will be introduced in Section 2.1.1.2). A few attempts were reported to analyse collagen or gelatin structures in intact tissues and solutions [102-104], in which all three attempts chose hydrated approaches using either roughened electrodes or cast nanoparticle aggregates. Dry approaches are also reported in protein SERS detections [117], but none are focused on collagen or gelatin. The hydrated approach in solution allows better reproducibility due to the averaging effect from the Brownian motions. The dry approach may sacrifice signal uniformity due to variations in the location where the nanoparticles aggregate (which is where the SERS enhancement locate) and the composition of each measuring spot. Multiple measurements are commonly required to generate representative results. However, due to the high concentrations (as pure solid) of the analyte, a much higher signal intensity can often be produced [118, 119].

The earliest reported SERS measurement of gelatin was based on a roughened copper (Cu) electrode submerged in a solution of gelatin and acids at −600 mV (Figure 1.22) [102]. Agreeing with the FT-Raman spectrum, common gelatin features were identified such as the amide I modes, δ_s(C–H), and amide III modes at around 1670 cm^{-1}, 1410–1450 cm^{-1}, and 1270 cm^{-1}

[102]. It is worth noting that gelatin was described as only weakly adsorbed on the Ag surface compared with the SERS probes (usually dye molecules, *e.g.*, Rhodamine 6G, brilliant cresyl blue), therefore having negligible interference with the target molecules [120, 121]. It also indicates that impurities with strong affinities to copper (Cu), silver (Ag), or gold (Au) should be carefully assessed or eliminated to enable the accurate analysis of gelatin or collagen using SERS.
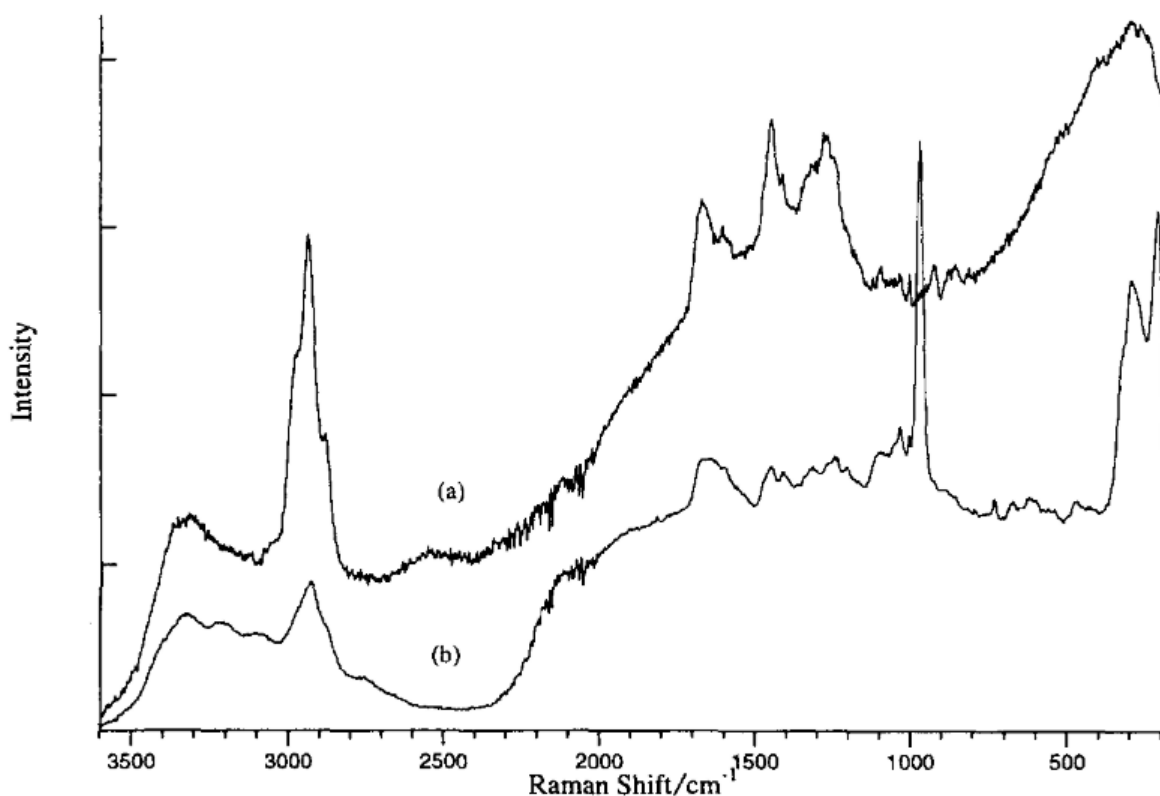
Figure 1.22: (a) FT-Raman spectrum of solid gelatin and (b) SERS spectrum of gelatin adsorbed at a Cu electrode polarised at −600 mV in 2 M H_2SO_4 solution containing 50 ppm of gelatin. (Reprinted from Ref. [102] with permission from Elsevier.)

The first-ever reported SERS measurement on collagen fibrils [103] was based on the controlled self-assembly of collagen with citrate-stabilised silver or gold nanoparticles (AgNPs or AuNPs). The bright dots in the differential interference contrast microscopy (Figure 1.23) indicate the distribution of AgNPs alongside the collagen fibrils. As a result of the aggregation of AgNPs (mechanisms to be explained in Chapter 2), strong SERS hot spots are formed, and peaks are observed with enhanced intensity (Figure 1.23). Many distinct peaks from the SERS measurements do not match the non-SERS spectrum of solid collagen (Figure 1.20 and Figure 1.21) nor the electrode-based gelatin SERS spectrum in solution (Figure 1.22). The differences are attributed to the strong binding of amino acid residues with the NPs, which highlights the potential of this technique in investigating chemical reactions on specific amino acid side chains. Moreover, the variations in the SERS spectrum across a collagen fibril are also significant,

probably due to the uncontrolled distribution of AgNPs to collagen fibrils and the non-uniform assembly at each measured spot [103].

Based on a brief comparison of the SERS spectrum of collagen with amino acid solutions, one can assign those distinct features to specific amino acid residues (Table 1.3 and Table 1.4) [103, 104]. Although the two experiments demonstrated entirely different spectra (Figure 1.23 and Figure 1.24), the common observations of –COO⁻ groups are underlined, as these modes are generally weak and thus hard to resolve in non-SERS conditions [103, 104].
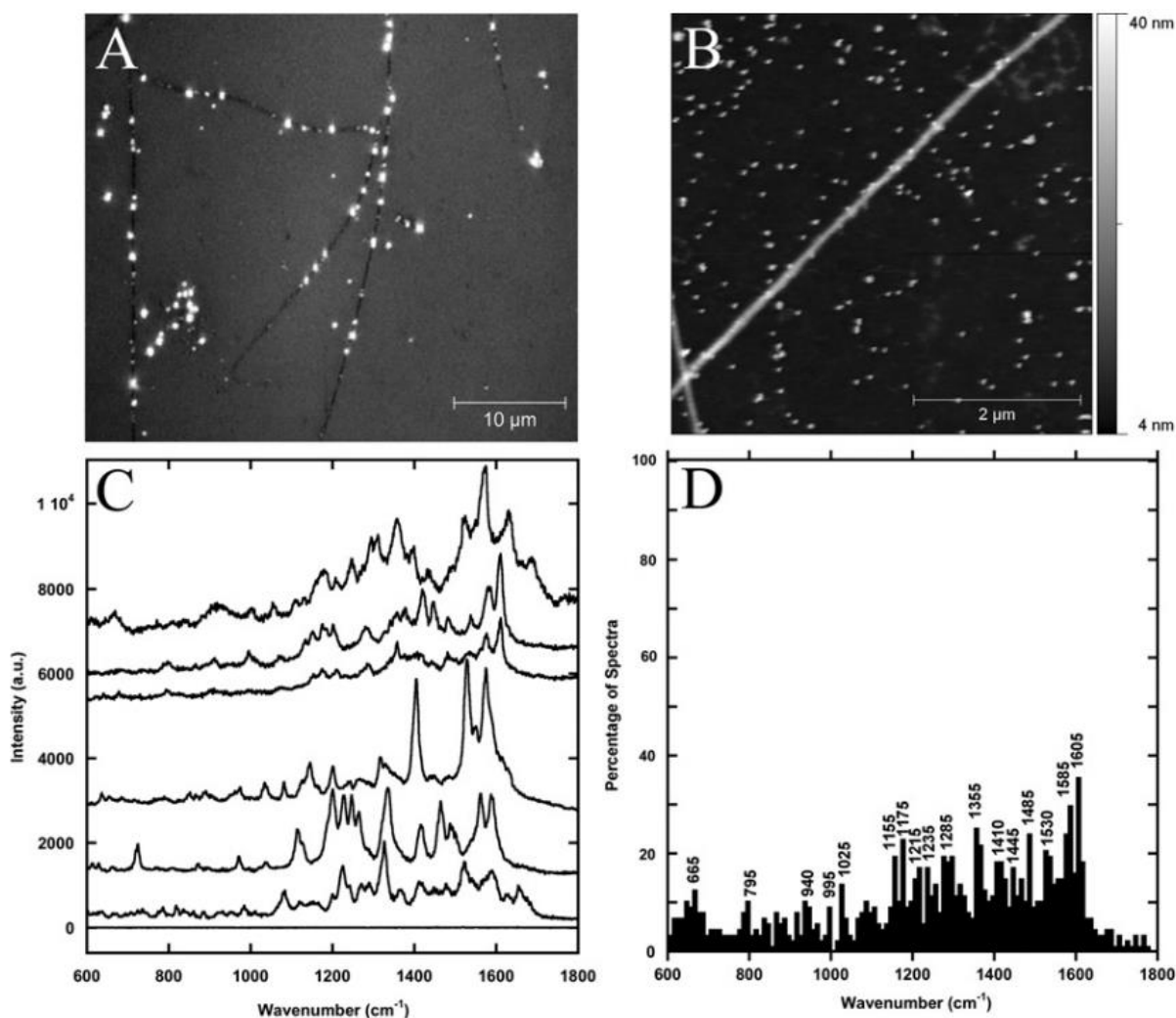
Figure 1.23: (A) Differential interference contrast (DIC) microscopy of collagen fibril with deposited AgNPs. (B) Atomic force microscopy (AFM) contact mode height image of 30 nm AgNPs attached to collagen fibrils. (C) Ag SERS of Collagen type I fibrils compared with a non-SERS spectrum of collagen fibrils (the bottom spectrum). (D) Histogram of peak positions observed in 89 spectra of collagen fibrils. (Reprinted from Ref. [103] with permission from Elsevier.)

Table 1.3: Assignment of Ag and Au SERS and TERS (tip-enhanced Raman spectroscopy[6]) peaks based on the proposed attachments of Phe and Tyr side chains, the amide bonds, aliphatic C–H bonds and carboxylate (–COO⁻) groups. General notations refer to Appendix A. (Reprinted from Ref. [103] with permission from Elsevier.)

				Proposed assignment			
Far field	Gold SERS	Silver SERS	Silver TERS	Phenylalanine ring (Wilson vibration number, group, and range) (22,29,34–37,39)	Tyrosine ring (Wilson vibration number, group, and range) (22,29,34–37,39)	Amide (27,28,40,42,43)	Other (22,27,28,34–36)
	645	665	—		6b, B_{3g} (630 ± 20)		COO⁻ wag.
	685		—	4, B_1 (690 ± 10)	4, B_{2g} (700 ± 35)		
	765		—				
		795	—	A_1 (725 ± 75)	A_g (820 ± 50)		
	835		—	10a, A_2 (835 ± 25)	10a, B_{1g} (820 ± 30)		CH
	945	940	—	17a, A_1 (960 ± 20)	17a, A_u (960 ± 30)		C-COO⁻
1002	995		—	12, A_1 (1000 ± 10)			
	1025	1025	—	18a, A_1 (1024 ± 6)	18a, B_{1u} (1012 ± 9)		
	1065		—	18b, B_2 (1074 ± 8)			
	1165	1155		15, B_2 (1156 ± 5)	9a, A_g (1166 ± 24)		
	1195	1175		9a, A_1 (1175 ± 5)			
		1215		A_1 (1205)	A_g (1210 ± 15)		
	1245	1235			B_{1u} (1250 ± 15)	Amide III	
1246 1289						Amide III	CH
	1265	1285	1275	3, B_2 (1275 ± 20)	3, B_{3g} (1286 ± 26)	Amide III	CH
		1355	1335		14, B_{2u} (1310 ± 70)		CH
	1405	1410	1415		19b, B_{2u} (1420 ± 50)		COO⁻ sym. (1390 ± 50)
1445 1449	1445	1445	1460	19b, B_2 (1455 ± 16)			CH
	1485	1485	1515	19a, A_1 (1492 ± 22)	19a, B_{1u} (1495 ± 35)		
		1530					
		1565	1565			Amide II	
	1585	1585	1585	8b, B_2 (1579 ± 18)	8b, B_{3g} (1578 ± 26)		COO⁻ asym.
		1605	1605	8a, A_1 (1594 ± 20)	8a, A_g (1600 ± 29)		COO⁻ asym.
1627	1632*					Amide I (3_{10}-helix)	COO⁻ asym.† (1620 ± 70)
1649	1656					Amide I (α-helix)	COO⁻ asym.
1675	1675					Amide I (β-sheet)	COO⁻ asym.

Values and vibration numbers are given by Dollish et al. (34).
*Amide I values are from the histogram including all enhancement methods (Fig. 7 B).
†A COO– asymmetric stretch is very weak in Raman.

---

[6] TERS results were reported in the referenced work as a comparison to SERS, but it is not used in this thesis. TERS is a technique that combines SERS with scanning probe microscopy that allows SERS measurements at the location where the tip (coated with SERS active material) points at.
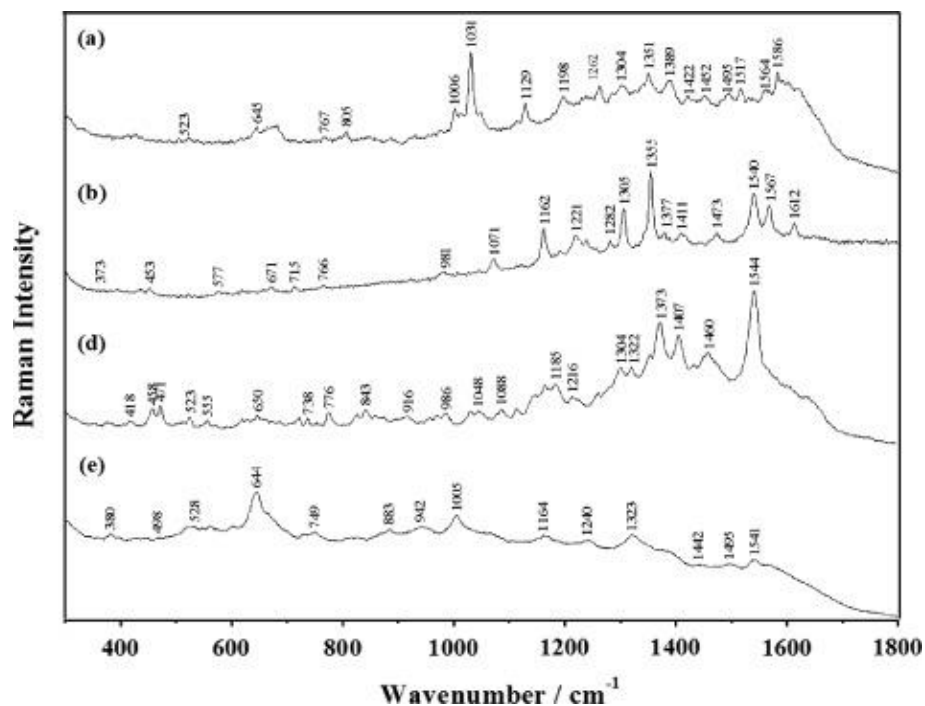
Figure 1.24: SERS spectra from *top* to *bottom*: Ala, Gly, Pro, and type III collagen from rat tissue. (Reprinted from Ref. [104] with permission from John Wiley and Sons.)

Table 1.4: Raman and Ag SERS peaks of Ala, Gly, Pro, and collagen of rat tissue and SERS peaks of human tissues before (HT) and after shockwave treatments (HTSW). General notations refer to Appendix A. (Reprinted from Ref. [104] with permission from John Wiley and Sons.)

Raman Ala	SERS Ala	Raman Gly	SERS Gly	Raman Pro	SERS Pro	Raman collagen I	Raman collagen III	SERS collagen III	SERS HT	SERS HTSW	Assignment
		1670 vw				1682 m	1674 s				Amide I
		1631 wb	1612 m	1622 mw					1631 m	1635 w	δNH_3^+, δNH_3^+
1595 m	1586 ms	1568 w	1567 ms	1550 m	1544 s			1541 mw	1545 sh	1544 ms	$\nu_{as}COO^-$, Lys
1497 w	1517 m	1513 m							1523 vs	1521 w	δNH, δNH_3^+ Lys
1481 s	1495 m							1495 vw		1502 w	δCH_3
1460 m	1452 w	1454 m	1473 mw	1450 md	1460 ml	1459 s	1451 s	1442 vw	1446 vw	1448 vs	δCH_3, δCH_2
	1422 w	1438 w									δCH_2
					1407 ms						νC-OH Pro
	1389 m								1387 w	1375 vs	δCH_3
1376 w	1351 m		1377 w	1373 m	1373 s			1323 ms	1365 wm	1348 m	$\nu_s COO^-$, Lys
1358 m		1324 s	1355 vs								ωCH_2 Gly
1304 m	1304 m		1305 ms	1319 vw	1322 w		1307 s			1316 w	δCH
			1282 w	1285 m	1304 w				1299 wm		δCH
	1262 m			1264 m		1278 sh	1276 md			1281 vw	ΔNH Amide III
1237 vw			1221 mt	1237 m		1250 vs	1251 m	1240 vw	1252 s	1227 w	δNH Amide III
1147 wb	1129 m	1138 w	1162 m	1174 md		1171 wm	1166 w	1164 dw	1161 mw	1153 vw	ωCH_2, tNH_2, rNH_3^+, OH-Lys.
1111 m		1105 vw		1117					1132 w	1127 vw	ΔNCH
			1071 m	1081 m	1088 w	1084 m			1074 vw		νCN Pro
1018 m	1031 s	1032 m		1033 m						1031 w	NCCN
	1006 w					1009 m	1008 w	1005 s			Phe
			981 w	983 m	986 wt				997 m		νCCN, NCC
				951 m		942 sh	941 vw	942 m		964 ms	νCC skeletal Pro
918 w				919 s	916 w	925 s	924 vw		926 mb	931 w	νC-COO$^-$
850 vs		890 s		898 vs		879 m	896 sh	883 vw		888 w	NCC Gly
				840 s	843 w	859 m	858 sd				NCC ring Pro
	805 w					822 m	819 vw			813 m	νCC skeletal
771 w	767 vw		766 vw	790 w	776 wm	763 wb	762 vwb			794 w	δCOO^-
		696 vw	671 w							668 ms	δ, ω COO$^-$
651 w	645 w	601 w		641 m	650 w	644 w		644 m	634 vw	631 wm	$r, \delta, \omega COO^-$
530 s	523 vw				523 w	532 m		528 wm		534 w	δCCN, COO$^-$ Ala
479 w		486 wb	453 w	447 m	471 md			498 wm		506 bw	Skeletal deformation
283 m				296 vw		297 vw	296 vw				Skeletal deformation

1.4 Thesis Motivation

Bearing in mind the three key elements of this thesis introduced above (*i.e.*, collagen structure, X-ray scattering, and SERS), it is now straightforward to reify the rather non-specific thesis title into the detailed research work. The work in this thesis is dedicated to three interrelated research questions centred around how the structure of collagen changes when it binds or crosslinks with chemicals, and to provide a better understanding of the structure-property relationship of collagenous materials.

The first body of work aimed to resolve a long-standing doubt about the reaction mechanism of Cr(III) with collagen molecules in bovine skins during chrome tanning in leather manufacturing. The binding to collagen was assumed covalent for most of the Cr species; however, more recent studies revealed the deposition of Cr species that bind to collagen electrostatically at a non-negligible amount. The underlying mechanism of the switching between covalent and electrostatic binding paradigms was not understood until the work in this thesis, which elaborates the crucial roles of the counter ions using a combination of SAXS and SERS techniques.

The second part of the work focused on the reliability and reproducibility of the protein SERS methods in colloidal solutions, which was an obstacle to the correct interpretations of collagen SERS spectra. Previously when researchers conducted SERS of protein or dye solution using the most popular citrate-capped AgNPs, they tended to add "activation agents", which are commonly halide salts, yet ignoring the potential impacts of halides on the coadsorbed species on the surface of AgNPs. In reality, the SERS spectra of halide-coated AgNPs are not featureless as opposed to the widely accepted assumptions. The coadsorbed species that compose the SERS spectra were either unnoticed or misinterpreted until this study was conducted. The background signals are significant, which, unless accounted for, will drastically interfere with collagen or other protein signals.

The third part of the work considered the mechanistic question of how organic covalent crosslinking affects the structure and the corresponding stability of collagen in the bovine pericardium. The excess usage of chemicals has adverse impacts on the environment and, more importantly, on the patients who will be implanted with those processed collagenous materials. Utilising our knowledge of the SAXS technique, with the support of thermal and colourimetric analyses, we revealed more insightful collagen crosslinking and stabilisation mechanisms, highlighted the excess usage, and proposed an optimal condition for crosslinking bovine pericardium.

An overarching goal interconnects and motivates the above research works: to fill in the knowledge gaps between the well-established native collagen structure and the advanced development of industry-focused processing technologies. This goal supports the continuing interest in developing a novel collagen processing technology and a toolbox for characterising various collagen materials.

1.5   Thesis Layout

The following chapters in this thesis are structured as follows:

Chapter 2 presents the necessary knowledge for carrying out the work of this thesis, including the theoretical background of the techniques, the experimental setups and the method for data analyses relevant to the experimental results in the later chapters. The techniques of choice are dedicated to the niche research topic serving the characterisation of collagen, AgNPs and the combination of the two.

Chapter 3 elaborates on the Cr(III)-collagen interactions. A mechanism for the selectivity of covalent and electrostatic binding of the Cr(III) to collagen is revealed as mediated by the kosmotropicity of the counter ions (*i.e.*, anions). Although covalent bindings do occur, a considerable proportion of Cr(III) interacts with collagen electrostatically; the latter is more favoured when a less kosmotropic anion is present. This study is also the first time SERS has been employed in analysing the binding mechanisms in collagen, confirming the effectiveness of the drop-casting SERS method on solid samples.

Chapter 4 discusses the variations in SERS spectra from citrate-capped AgNPs when treated using different halide salts and the associated collagen spectra considering the interference. The assignments of the features are sophisticated, which evolved into the major proportion of this work. When AgNPs are mixed with collagen, the backgrounds are not indifferent, which adds another level of complexity to the surface coadsorption of species. The underlying mechanisms governing these phenomena are carefully inspected and explicated.

Chapter 5 demonstrates the multi-aspect investigation of the structural changes in bovine pericardia during chemical crosslinking. The characterisation using SAXS adds an essential element to understanding the relationship between structure and stability, revealing a reverting trend in the axial packing of collagen in fibrils as crosslinking occurs. The mechanism behind this phenomenon is postulated to be the preferred formations of telopeptidyl-helical linkages followed by helical-helical linkages.

Chapter 2 Theoretical Background and Experimental Setup

This chapter introduces the theoretical background of the characterisation techniques of choice dedicated to this research topic, in addition to the experimental setups and the analyses of the acquired data.

The introduction begins with the basics of Raman spectroscopy, followed by the electromagnetic theory governing the SERS effect. Then it continues onto the X-ray scattering section, in which it briefly describes the principles as well as the scattering and diffraction models.

Other techniques relevant to this thesis are also introduced, namely, UV-Vis spectroscopy for the changes in AgNPs under ligand exchanges and the aggregation of AgNPs with collagen, differential scanning calorimetry (DSC) for collagen thermal analysis, transmission electron microscopy (TEM) for the morphology of AgNPs, and a series of protein assays for collagen characterisations.

2.1 Surface-enhanced Raman Spectroscopy (SERS)

2.1.1 Theoretical Background

The theory behind the SERS technique should be elaborated from the basics as per the three indispensable cornerstones in its name to highlight the essences of this technique: a "surface" phenomenon on metallic nanostructures that "enhances" the "Raman spectroscopy" signal; the name explicates its multi-disciplinary nature. A fraction of these basic theories is also supportive of other light-matter interactions, such as in UV-Vis spectroscopy. Extensive information beyond the scope of this thesis can be found in greater detail in Ref. [122, 123].

2.1.1.1 Raman Scattering

When a photon encounters a molecule, it can be absorbed, in which case the photon energy is transferred to the molecule, resulting in electronic state changes which can be probed using IR spectroscopy (Figure 2.1). Alternatively, it can be scattered to carry the same or different energy as the incident photon (Figure 2.2). If the energy of the scattered photon is the same as the incident photon, the process is called "elastic scattering" or "Rayleigh scattering", which also leaves the vibrational state of the molecule unaffected. Otherwise, the scattered photon can carry less energy than the incident photon, with the difference in energy associated with the excitation of the molecule from its ground vibrational state ($v = 0$) to the first excited vibrational state ($v = 1$); or vice versa, for a scattered photon carrying extra energy imparted by a molecular relaxation from the excited state back to the ground state. This phenomenon is called "inelastic scattering" or the well-known "Raman scattering", discovered in 1928 by Sir Chandrasekhara Venkata Raman [124]. The energy change is commonly expressed as the corresponding wavenumber, or the "Raman shift" (in the unit of [cm^{-1}]):

$$\Delta\bar{\nu}_R = \Delta E_R/hc = (E_L - E_S)/hc$$

where E_L [J] is the incident (laser) photon energy, E_S [J] is the scattered photon energy, h [J s^{-1}] is the Planck constant, and c [m s^{-1}] is the speed of light.
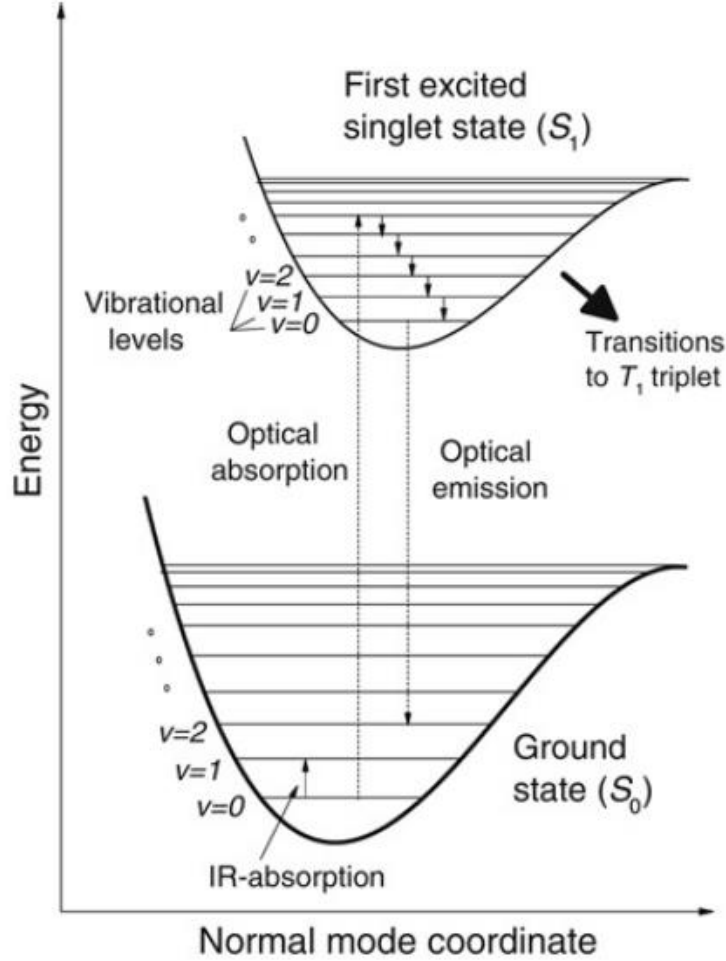
Figure 2.1: Schematic diagram ("Jablonski diagram") of the electronic states (bold lines, S_0 and S_1) and vibrational energy levels within each electronic state (thin lines, $v = 0, 1, 2, ...$). Possible transitions are indicated by arrows, with the dotted ones radiative and the solid ones non-radiative. (Reprinted from Ref. [122] with permission from Elsevier.)
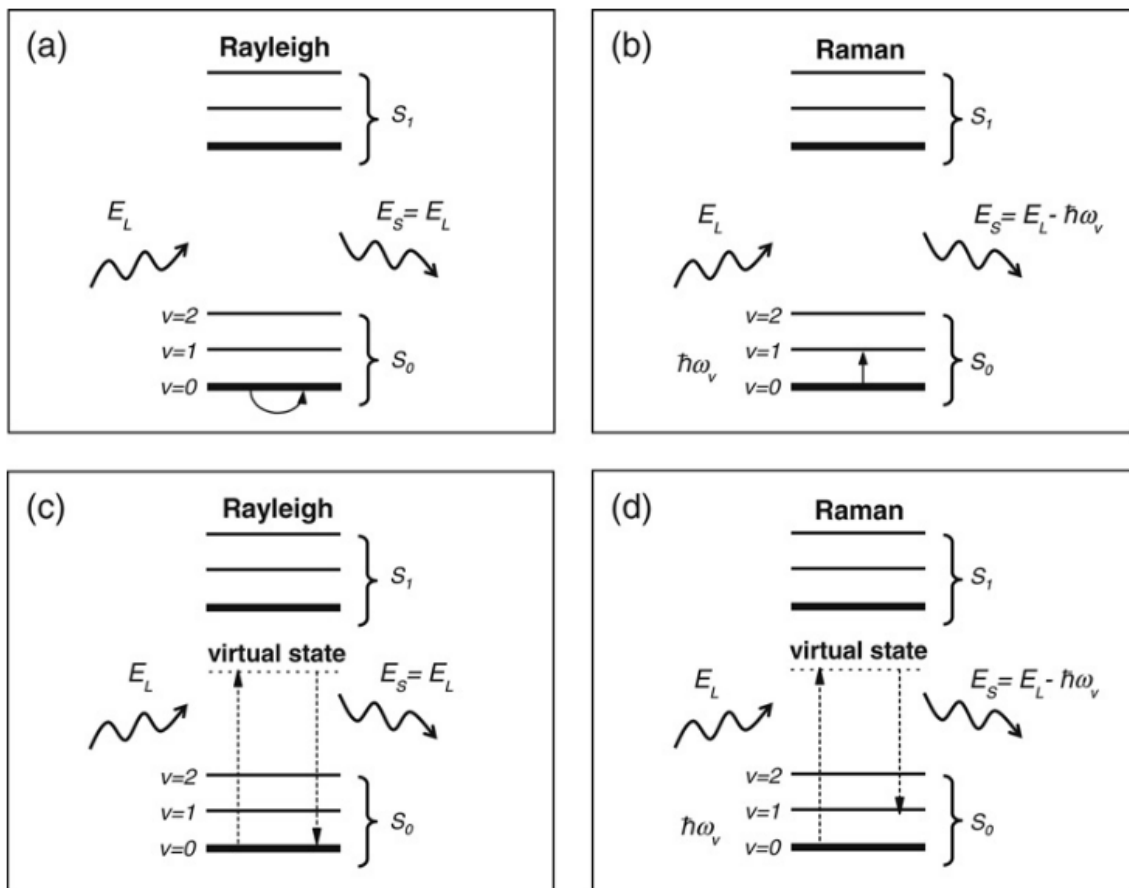
Figure 2.2: The Rayleigh (elastic) and the Raman (inelastic) scattering processes. The scattering may be viewed as two simultaneous processes: absorption of a photon through a transition to a virtual state, from where recombination back to S_0 follows. (Reprinted from Ref. [122] with permission from Elsevier.)

When $\Delta\bar{\nu}_R > 0$, the Raman shift is called a Stokes shift; otherwise, it is called an anti-Stokes shift (Figure 2.3). As there are a variety of vibrational modes in a molecule, the scattered light becomes a spectrum that includes many narrow lines and broad bands, which evolves into the Raman spectroscopic technique dedicated to analysing the vibrational energy changes based on the unique scattering spectrum of the molecule. Usually, molecules at the ground vibrational state compose the majority, making the Stokes Raman scattering much stronger than the anti-Stokes counterpart. Hence, by convention, speaking of Raman scattering without specifications implies the Stokes process.
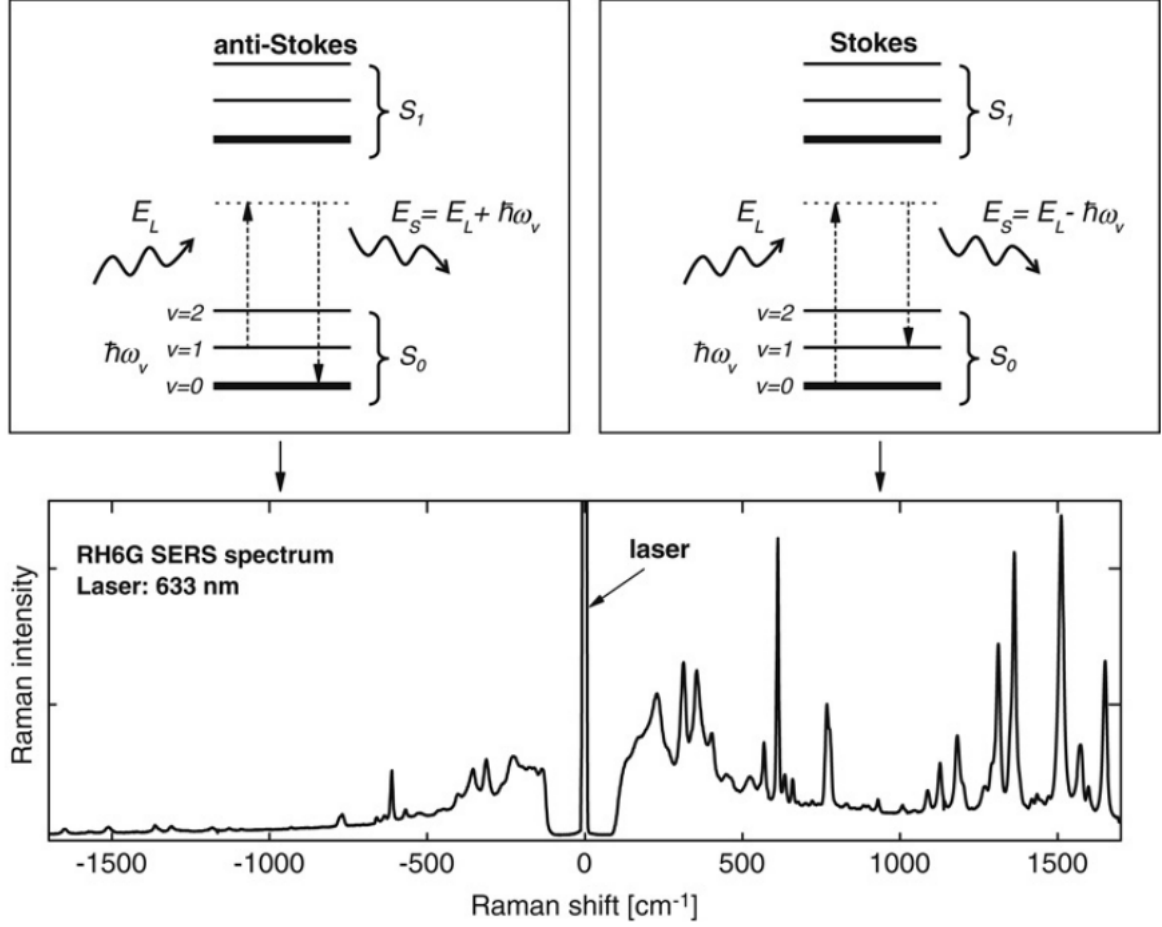
Figure 2.3: The Stokes and the anti-Stokes Raman scattering processes. The result (not the process) of the former case is an excitation process of the molecule to a higher vibrational state, while the latter is equivalent to a relaxation process. A typical Raman spectrum shows the intensity on the Stokes side and their anti-Stokes counterparts (Reprinted from Ref. [122] with permission from Elsevier.)

The relative intensity of each Raman peak arises from the scattering characteristic of a particular vibrational mode in the molecule. Each vibrational mode has a unique Raman scattering cross-section at a certain excitation wavelength, σ_{Sca} [m^2], and its Raman depolarisation ratio, ρ_{R} [a.d.].

The Raman cross-section (σ_{Sca}) can be phenomenologically considered as the "strength" of the Raman scattering effect, which is responsible for the Raman scattered power P_{Sca} [W] within the detection angle:

$$P_{\text{Sca}} = S_{\text{Inc}} \int \frac{d\sigma_{\text{Sca}}}{d\Omega}(\Omega)d\Omega$$

where S_{Inc} [W m^{-2}] is the power density of the incident light. The Raman scattering power could vary when observed in different scattering configurations such as 90°-, forward- or back-scattering.

On the other hand, the depolarisation ratio (ρ_R) is associated with the symmetry of the vibrational mode and, therefore, is closely related to the Raman tensor ($\hat{R}_k(\omega_L)$) [ϵ_0 m^2 kg$^{-1/2}$], in which $k = 1, 2, \ldots, (3N - 6)$ (or up to $(3N - 5)$ for linear molecules) to designate a normal vibrational mode, and ω_L [m^{-1}] is the angular frequency of the incident light. The relationship of $\hat{R}_k(\omega_L)$ with the linear optical polarisability $\hat{\alpha}_L(\omega_L)$ [ϵ_0 m^3], can be defined as:

$$\hat{R}_k(\omega_L) = \left(\frac{\partial \hat{\alpha}_L(\omega_L)}{\partial Q_k} \right)_{Q_k = 0}$$

where Q_k [kg$^{1/2}$ m] is the normal mode coordinates (*i.e.*, the positions of the atoms in a molecule). If the linear polarisability tensor ($\hat{\alpha}_L(\omega_L)$) does not depend on the normal mode coordinates (Q_k) (usually when the molecule is highly symmetrical), then $\hat{R}_k(\omega_L) = 0$, and the corresponding vibrational mode k is called "Raman inactive". Otherwise, the induction of a Raman dipole in the vibration by the incident light can produce Raman scattered light, *i.e.*, "Raman active". The occurrences are related not only to the symmetry of the molecule but also to the vibrational modes (*e.g.*, stretching, bending, and incorporated breathing modes in rings). The discussions around such phenomena are summarised as the "Raman selection rules", with more details described in Ref. [125-127]. Although the work in this thesis does not involve any quantum chemistry calculations (*e.g.*, density functional theory (DFT)) for the prediction of Raman spectra and vibrational analyses, the basic understanding of Raman selection rules here serves as a supportive foundation for further discussions around the surface selection rules in SERS conditions.

2.1.1.2 Surface Enhancement

A simplified phenomenological approach is presented to clarify the origin of the SERS effect (detailed theoretical explanations are presented in Ref. [122, 128]): the SERS effect arises from the "local field enhancement" on metal surfaces, on which numerous free electrons "oscillate" to result in "plasmon resonances" or, more precisely, "localised surface plasmon-polaritons resonances" (LSPR)[7]. The naming highlights the "localised" nature which typically occurs in small objects, *i.e.*, metallic nanoparticles (NPs), to differentiate from the "surface plasmon resonance" (SPR) in planar metal surfaces based on the coupling of light to the propagating surface plasmon-polaritons (propagating SPP, or PSPP). The LSPR response, as opposed to PSPP, is radiative, showing strong scattering that leads to the SERS effect. In one sentence, it is the localised resonating optical response of a non-planar metal surface that makes the SERS effect.

---

[7] The term "plasmon" stands for a quantum quasi-particle that quantifies the excitations, waves, or modes of the charge density oscillations in a plasma. When the electromagnetic wave propagates in an optically responsive medium (other than a vacuum), the plasmon excites the oscillations of the internal polarisation and magnetisation with which it then couples. Such oscillation modes can be quantified as another quasi-particle, "polariton". In the case of surface plasmon, the incident light causes resonance on the metal surface; thus, the mixed modes are called "surface plasmon-polaritons".

The optical response of metal regarding the contribution from a free electron can be described by a dielectric function (or permittivity, in the unit of $[A^2\ s^4\ kg^{-1}\ m^{-3}]$) following the Drude model (which is the Lorentz model for classical harmonic oscillators under the assumptions of free electrons and constant optical response of cations):

$$\epsilon(\omega) = \epsilon_\infty \left(1 - \frac{\omega_p^2}{\omega^2 + i\gamma_0\omega}\right)$$

$$\omega_p = \sqrt{\frac{ne^2}{m\epsilon_0\epsilon_\infty}}$$

$$\lambda_p = \frac{2\pi c}{\omega_p}$$

where ϵ_0 is the permittivity of vacuum, and ϵ_∞ is the background real dielectric function when $\omega \to \infty$ [rad s^{-1}] ($\epsilon_\infty \geq 1$). γ_0 [rad s^{-1}] is a damping term for the electrical resistivity in this model, which has a smaller value than ω for the common wavelengths of interest. ω_p [rad s^{-1}] is a natural oscillation frequency of the charges in the plasma or, concisely, "plasma frequency", and λ_p is the corresponding wavelength. n [m^{-3}] is the number of free electrons per unit volume, and m [kg] is the mass of the electrons. Since $\epsilon(\omega)$ is a complex, the real and imaginary parts of $\epsilon(\omega)$ can be expressed separately as:

$$\text{Re}\big(\epsilon(\omega)\big) = \epsilon_\infty \left(1 - \frac{\omega_p^2}{\omega^2 + \gamma_0^2}\right)$$

$$\text{Im}\big(\epsilon(\omega)\big) = \epsilon_\infty \frac{\gamma_0}{\omega} \left(\frac{\omega_p^2}{\omega^2 + \gamma_0^2}\right)$$

For metals, $\text{Re}\big(\epsilon(\omega)\big)$ decay monotonously from small positive values in the UV region to negative values in the visible region (for SERS, ideally, $-20 \leq \text{Re}\big(\epsilon(\omega)\big) \leq -1$). On the other hand, $\text{Im}\big(\epsilon(\omega)\big)$ of metals usually has a small positive value in the visible region and is associated with absorption.

For a sufficiently small (radius < 10 nm) metallic sphere (*i.e.*, NPs) in an external electromagnetic field of a laser beam, the electric field inside the sphere can be calculated under the electrostatics approximation (ESA) as:

$$\mathbf{E}_{\text{Internal}} = \frac{3\epsilon_M}{\epsilon(\omega) + 2\epsilon_M}\mathbf{E}_{\text{Inc}} = (1 - \beta_S)\mathbf{E}_{\text{Inc}}$$

$$\beta_S = \frac{\epsilon(\omega) - \epsilon_M}{\epsilon(\omega) + 2\epsilon_M}$$

where ϵ_M is the dielectric constant of the medium, which is commonly air or water, and $\mathbf{E}_{\text{Inc}}$ is the incident electric field of the laser. Similarly, the external electric field outside (or on the surface of the sphere can be written as:

$$\mathbf{E}_{External} = \mathbf{E}_{Inc} + \mathbf{E}_{Sca}$$

where $\mathbf{E}_{Sca}$ is the scattered electrostatic field. When the scattered field is much stronger than the incident field (due to enhancement under resonance), the polarised small metal sphere (with rearranged surface charges) can be simplified to an induced electrostatic dipole. This dipole leads to an external field outside the sphere sharing the same denominator as the internal field. The resonance condition of the system is therefore closely related to the wavelength-dependent denominator $(\epsilon(\omega) + 2\epsilon_M)$.

When the incident wavelength meets $Im\big(\epsilon(\omega)\big) \approx 0$ and $Re\big(\epsilon(\omega)\big) \approx -2\epsilon_M$, the system approximately reaches a resonance condition. Strong absorption would occur when metals are excited under such conditions, resulting in distinct decreases in reflectivity and/or increases in scattering at certain wavelengths, thus showing characteristic colours in the NPs. However, when $Re\big(\epsilon(\omega)\big)$ is positive as in non-metallic materials or if $Im\big(\epsilon(\omega)\big)$ is large, then the resonance will hardly be achievable. Amongst the metallic elements on the periodic table, Ag and Au are two metals that fit the above criteria. They also show a certain degree of inertness at nanoscales against chemical dissociations, making them suitable for "SERS substrates".

Under the resonance conditions, the SERS enhancement can be categorised into two major components, *i.e.*, electromagnetic enhancement and chemical enhancement, based on their different mechanisms of interacting with the metal surface. Electromagnetic enhancement occurs when the molecule is physisorbed onto the metal surface through electrostatic bonding or Van der Waals forces. In contrast, chemical enhancement involves a change in polarisability in the molecule due to a chemical bonding between the molecule and the metal surface, which always comprises charge transfer. Electromagnetic enhancement always occurs, whereas chemical enhancement is secondary and could as well be electromagnetic in origin.

The electromagnetic enhancement is coupled from two aspects: the local field enhancement and radiation enhancement. The former originates from the response of metal under the incident field, while the latter represents the radiation of a molecule modified by the total external field near a metal. Each of them contributes to the enhancement effect by a factor of $|\mathbf{E}_{Loc}|^2/|\mathbf{E}_{Inc}|^2$ (under a series of approximations, see Ref. [122]), combining into an overall $|E|^4$ relationship which gives the large SERS enhancement phenomena.

Although electrostatics approximation (ESA) gives a simple estimation of the resonance wavelength, it relies on the approximate energy conservation that only considers absorption and energy propagation within the surface and assumes minimal radiation from the surface into the dielectric medium. In larger NPs that are more than 25 nm in radius, scattering radiation takes an extensive part in the extinction of incident light, leading to deviations in the predicted resonance wavelength to the experimental results.

When two resonant SPPs are coupled by entering the vicinity of each other, an additional aspect of the SPPs ("gap SPPs") emerges, giving prominent local field enhancement in the gaps between two metal spheres, which are conventionally called "hot spots". The detailed analytic

solution can be expressed using generalised Mie theory and will not be covered in this thesis. The coupling of LSPR also affects the visual colour of AgNPs and AuNPs, which provides a simple way of characterising the clustering (aggregation) of the NPs using the optical spectra (discussed in Section 2.3).

For an experimental observation of the LSPR through the corresponding SERS effect, a probe (from a physical phenomenon point of view) or a target analyte (from an analytical chemistry point of view) is needed near the surface of the SERS substrate ("near-field"). The "near-field" does not always mean the "first layer" on the metal surface; the latter is a common misunderstanding of the distance dependence of the SERS effect. For a molecule at a distance d from the surface of a metal sphere with a radius a, the amplitude of the electric field changes as $1/(a+d)^3$ and the SERS enhancement would decrease as $1/(a+d)^{12}$. For AgNPs with $a \approx 30\,\text{nm}$, even with a distance $d \approx 6\,\text{nm}$, the SERS enhancement would only attenuate by a factor of around 10. Therefore, practically speaking, the SERS enhancements (typically those via electromagnetic mechanism) can extend to about 10 nm away from the metal surface, allowing a good average of the molecular structural information of the surface-bound target analytes during spectroscopic measurements.

2.1.2 Experimental Setup and Data Processing

The SERS and conventional Raman measurements in this thesis were carried out using the Horiba-Jobin Yvon LabRam HR spectrometer in the Raman Lab at VUW (Figure 2.4 and Figure 2.5). The laser used in the studies is the Melles-Griot argon-ion laser at 514 nm. The laser is delivered towards the sample through mirrors, irises, an interference filter, an attenuation filter, a notch filter, and an LM Plan FI Olympus air objective ($\times$50, NA $=$ 0.50). The scattered light is collected in a backscattering configuration, and the notch filter rejects the Rayleigh scattered light and allows Raman scattered light to pass through into a Symphony CCD (charge-coupled device) detector cooled with liquid N_2 at -130 °C.

Before each set of measurements, the spectrometer is aligned and calibrated with a silicon substrate using its distinct peak at 520.5 cm^{-1}. During a typical measurement, a sample is placed on the stage under the objective; solid samples are directly placed on a glass slide, whereas liquid samples are contained in the cap cut off from an Eppendorf Protein LoBind tube (the same type of Eppendorf tube was used throughout this thesis).
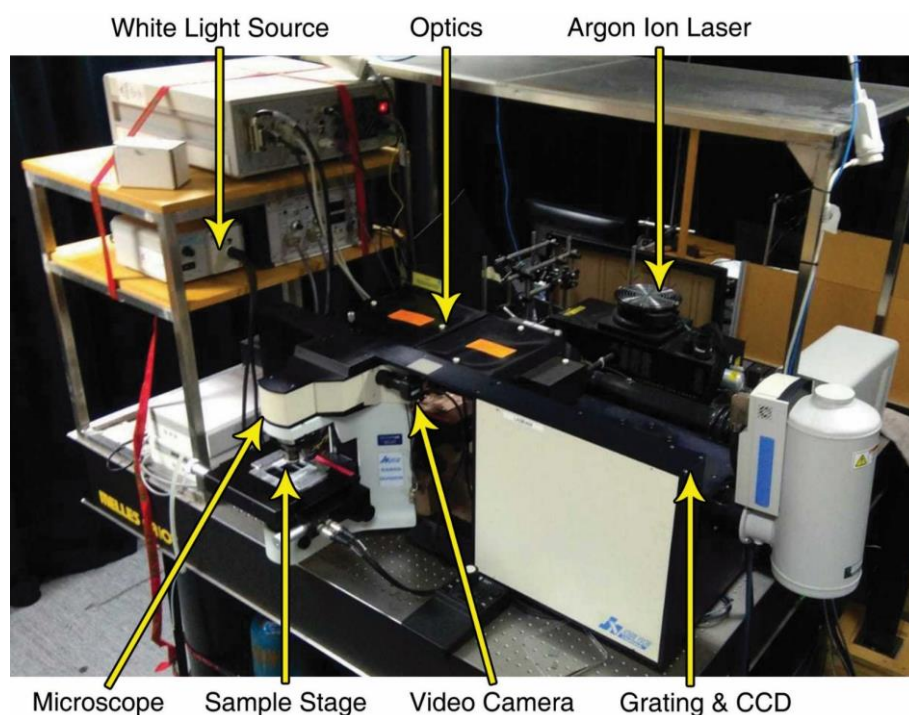
Figure 2.4: A photo of the Horiba-Jobin Yvon LabRam HR spectrometer in the Raman Lab at VUW.
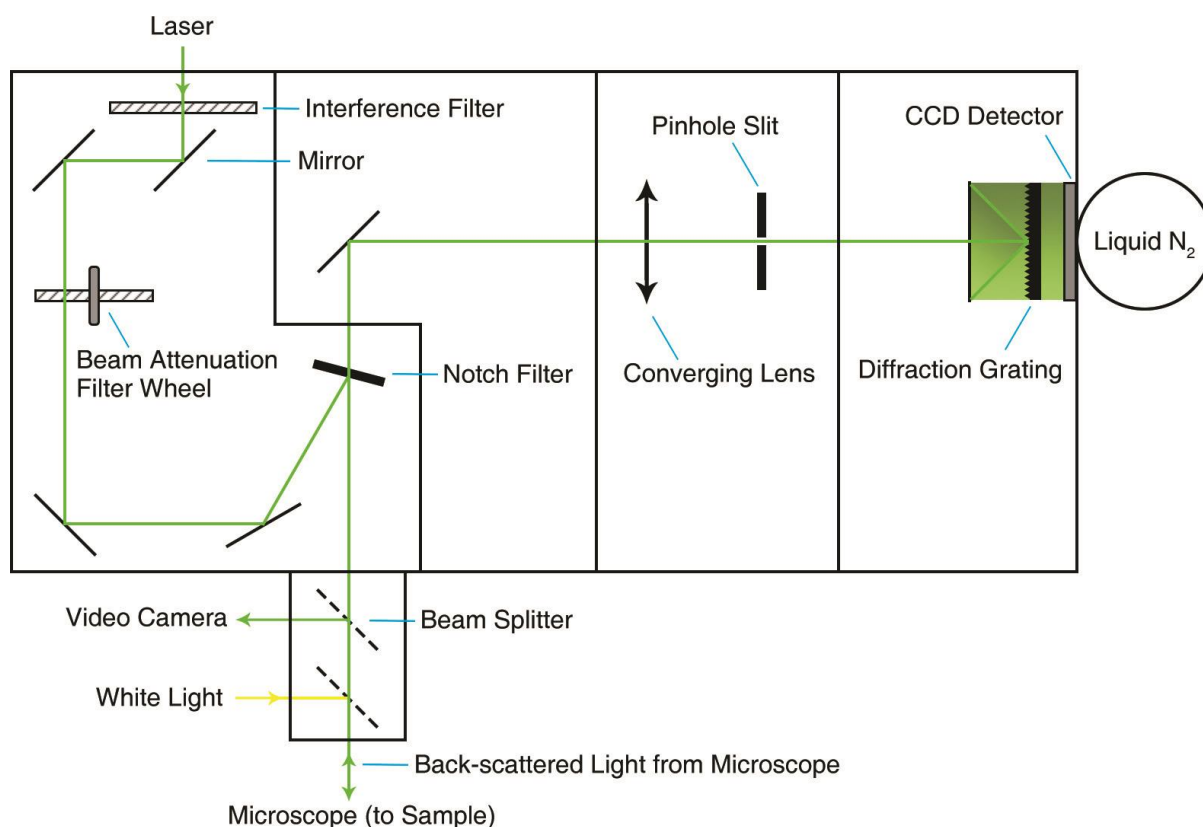
Figure 2.5: Schematic illustration of the internal optics of the LabRam HR showing the path of the 514 nm laser.

The collected spectra were analysed with a generic focus on the position and intensity of the peaks (*i.e.*, the molecular fingerprints). When the peaks are weak (such as the solution SERS results in Chapter 4), the signal-to-noise ratio is poor, which brings up the need to precisely remove the noises from the notch filter and the CCD. Note that the CCD response depends on pixel position, while the notch filter response is wavelength-dependent. It is possible to disentangle these two types of noises by recording the same spectrum at different grating positions. In principle, a well-characterized calibrated source should be required, but instead, we use a broadband white-light halogen source here. Its spectrum is smooth and slow-varying, so it can be approximated as a polynomial function. Any deviation from the smooth curve can be attributed to either the CCD response (pixel-to-pixel variation in efficiency) or the notch response (often appearing as small wavelength-dependent oscillations in its transmission).

The following data correction steps are carried out to identify and suppress the fixed-structure noises from the notch filter and the uneven response of the CCD (see Figure 2.6 for a comparison of a white light spectrum before and after corrections):

(1) Collect spectra of a broadband halogen white light at a series of shifted grating centres.
(2) Convert wavenumbers (Raman shifts) to pixels on the CCD and average the intensity-versus-pixel spectra.
(3) Fit the spectra to a polynomial function (typically, at a degree of 6) to identify the noises in the spectrum, and the ratio is recorded to feature the uneven CCD response.
(4) Correct the group of intensity-versus-wavenumber spectra at shifted grating centres according to the CCD response, and again fit each spectrum to a polynomial function, calculate the ratio between data and fitted curves to highlight the fluctuating notch response across the wavenumbers in the range of interest.
(5) Correct the spectra according to the noise profile of the notch filter.

Through this flat-field correction method, the weak features in the SERS spectra of the SERS substrate and the collagen solutions can be resolved. This method is modified based on Ref. [129], in which the experiments were conducted using a triple subtractive Raman spectrometer that does not involve a notch filter.
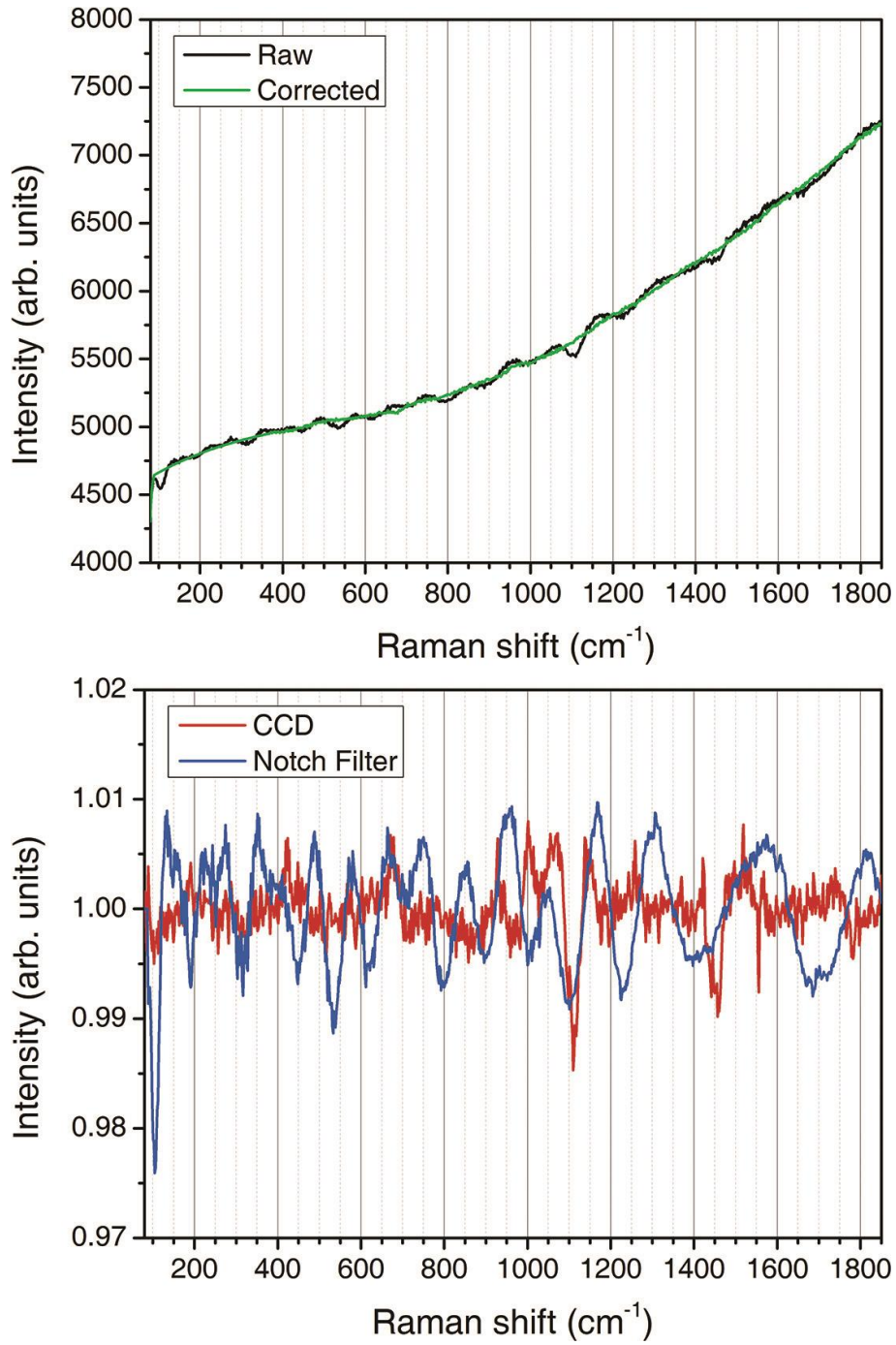
Figure 2.6: A white light spectrum before and after flat-field corrections and the corresponding artificial features from the CCD and the notch filter.

2.2 X-ray Scattering

As a polypeptide with a size of around 300 nm in length and 1–1.5 nm in diameter, collagen can scatter an X-ray beam, while it also has a long-range ordered hierarchical structure, leading to distinct diffraction features (as introduced in Section 1.3.1 and Figure 1.18) [47]. The scattered X-ray commonly leads to "form factor" and "structure factor" scattering patterns (broad oscillations), while the diffracted X-ray leads to diffraction rings or arcs. The theories behind these features will be discussed briefly in this section.

Before introducing the theories, it is always important to clarify the terms "scattering" and "diffraction". As introduced in Section 2.1, "scattering" occurs when light encounters the electrons in atoms. Simultaneously, the scattered lights interfere with each other due to their differences in phases to derive into a regular "diffraction" pattern (typically from a crystalline material). Early studies commonly used "diffraction" for summarising all the phenomena regarding the interaction between X-rays and matter. However, the overall phenomena are recently more commonly summarised as "scattering", which, in a strict sense, describes the initial process that inevitably occurs regardless of the crystallinity of the material. Therefore, in this thesis, the overall process is called "X-ray scattering", and the term "diffraction" is only used when discussing the long-range ordered axial packing of collagen molecules. Comprehensive discussions of X-ray scattering phenomena beyond the scope of this thesis can be found in Ref. [130-132].

2.2.1 Theoretical Background

X-ray is also electromagnetic radiation but has much shorter wavelengths than visible light. When an X-ray beam falls on an atom, the electrons can be accelerated by the incident electromagnetic field, resulting in the scattered radiation of X-ray that has the same frequency as the incident radiation, called the "Thomson scattering". The scattered intensity of light can be calculated as [132, 133]:

$$I_{\text{Sca}}(R) = r_e{}^2 \frac{I_{\text{Inc}}}{R^2} \sin^2 \psi = r_e{}^2 \frac{I_{\text{Inc}}}{R^2} (1 - \cos^2 \varphi \sin^2(2\theta))$$

$$r_e = \frac{Q^2}{4\pi\epsilon_0 mc^2}$$

where R is the distance of the detector to the scattering centre, ψ is the angle between the direction of the polarisation of the incident X-ray and the direction of the scattered X-ray, 2θ is the scattering angle between the incident X-ray and the scattered X-ray (or polar angle, if the direction of incident X-ray is placed on the z-axis), φ is the angle between the x-axis and the projection of the scattered X-ray on the xy-plane (or azimuthal angle) and Q is the charge of the electron. The factor r_e is called Thomson scattering length of the electron.

In a typical measurement (Figure 2.7), since the size of an electron is much smaller than the X-ray beam cross-section, the shape of the X-ray beam is omitted and can be simplified to a

planar wave front travelling along the z-axis when encountering the cloud of electrons. Therefore, the electric field in this sinusoidal electromagnetic wave is expressed as:

$$E(r,t) = E_0 \cos(\mathbf{k} \cdot \mathbf{r} - \omega t) = E_0 \text{Re}\big(\exp(i(\mathbf{k} \cdot \mathbf{r} - \omega t))\big)$$

where $\mathbf{k}$ is the wave vector and $\mathbf{r}$ is a vector that represents the position of one electron with respect to another electron. The scattering vector ($\mathbf{q}$) is therefore defined as $\mathbf{q} = \mathbf{k}_{\text{Sca}} - \mathbf{k}_{\text{Inc}}$. For an elastic scattering event, $k = |\mathbf{k}_{\text{Inc}}| = |\mathbf{k}_{\text{Sca}}| = 2\pi/\lambda$, so the length of the scattering vector is:

$$q = |\mathbf{q}| = 2k\sin\theta = \frac{4\pi\sin\theta}{\lambda}$$
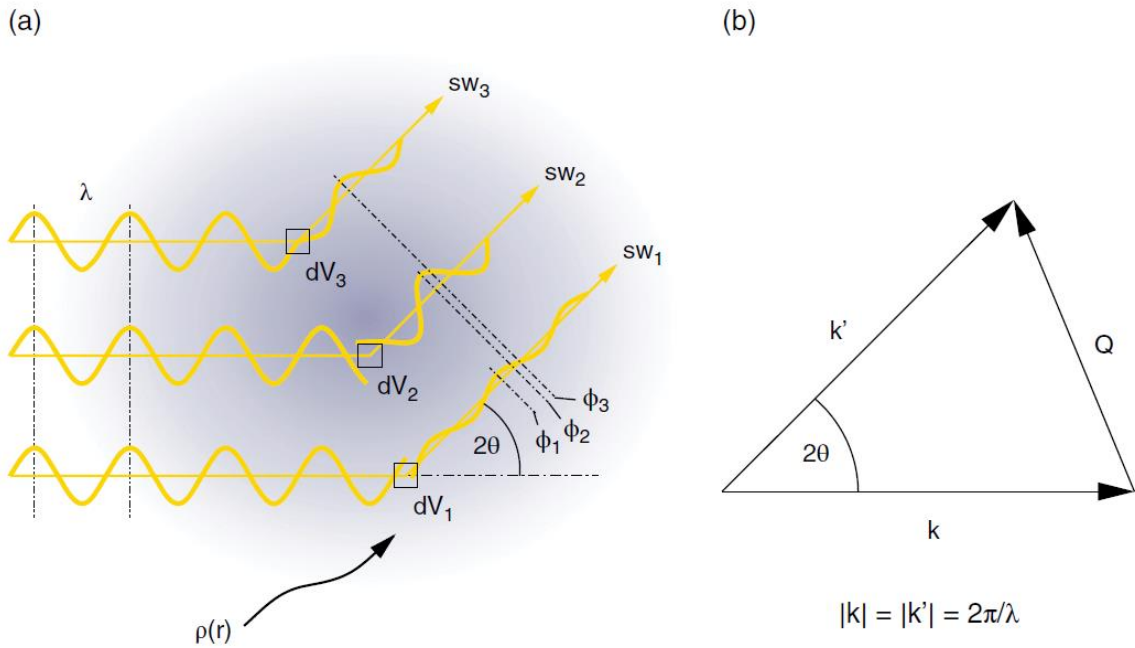
Figure 2.7: (a) A typical X-ray scattering experiment (planar wavefront). (b) scattering vector and scattering angle. (Reprinted from Ref. [134] with permission from John Wiley and Sons.)

2.2.1.1 Form Factor

The phase difference of X-ray before and after scattering by an electron cloud can be expressed as the phase factor, $\exp(i\mathbf{q} \cdot \mathbf{r})$. The scattering factor (*i.e.*, amplitude per atom) can then be expressed as the integration (Fourier transform) of electron density in the whole atom:

$$F^{\text{atom}}(\mathbf{q}) = \int_{\text{atom}} \rho(\mathbf{r})\exp(i\mathbf{q} \cdot \mathbf{r})d\mathbf{r}$$

Now consider an isolated, homogenous, spherical object: this represents a spherical particle in reality with low crystallinity but has almost uniform internal electron density in a very dilute

solution. The radius of the sphere is a. The electron density ($\rho(\mathbf{r})$) can be expressed as an average value $\bar{\rho}$. The phase factor is also averaged based on spherical symmetry. Under this assumption, the scattering factor is therefore written as:

$$F(q) = \int_0^a 4\pi r^2 \rho(r)\langle\exp(i\mathbf{q}\cdot\mathbf{r})\rangle dr = \int_0^a 4\pi r^2 \rho(r)\frac{\sin(qr)}{qr}dr = \frac{4\pi\bar{\rho}}{q^3}\int_0^a qr\sin(qr)\,d(qr)$$

$$= \frac{4\pi\bar{\rho}}{q^3}(\sin(qa) - qa\cos(qa)) = \frac{4\pi\bar{\rho}a^3}{3}\Phi(qa) = n\Phi(qa)$$

Here, $n = 4\pi a^3\bar{\rho}/3 = V\bar{\rho}$ represents the total number of electrons in the scattering object, and the factor $\Phi(qa) = 3(\sin(qa) - qa\cos(qa))/(qa)^3$ is called the "form factor" of the sphere; the naming "form" implies the relationship of this factor to the shape of the scattering object.

The scattering intensity $I(q) = NF^2(q) = NV^2\bar{\rho}^2\,\Phi^2(qa)$ (where N = quantity of spheres) can now be employed to estimate the shape of the target molecule.

In the low q region, the scattering intensity ($I(q)$) can be written as:

$$I(q) = NV^2\bar{\rho}^2\,\Phi^2(qa) = NV^2\bar{\rho}^2\left[1 - \frac{(qR_g)^2}{3} + \cdots\right] \approx I_0\exp\left(-\frac{(qR_g)^2}{3}\right)$$

R_g is the radius of gyration. It represents the equivalent radius of an object with an arbitrary shape. (For instance, for a sphere with a radius a, $R_g = \sqrt{3/5}\,a$, while for a long rod with a length $2l$, $R_g = 2l/\sqrt{12}$.) The above expression indicates a way of calculating the size of the scattering object based on the slope of a $\log[I(q)]$ versus q^2 plot (so-called "Guinier plot").

In the high q region, $\sin(qa)/qa \to 0$. Hence, another approximation is made:

$$I(q) = NV^2\bar{\rho}^2\,\Phi^2(qa) \approx NV^2\bar{\rho}^2\frac{9}{2q^4a^4} = \frac{9}{2}N\bar{\rho}^2\frac{V^2}{q^4a^4}$$

The equation suggests that the intensity is decaying with q^{-4} dependence with a slope related to the ratio of volume and radius (V^2/a^4). A plot of $q^4 I(q)$ versus q (so-called "Porod plot") can thus be used to analyse the shape and surface morphology of the scattering object.

Note that non-spherical objects can be expressed in more sophisticated equations (see Ref. [130, 135]) and can be modelled with dedicated software (*e.g.*, SASView) if prominent.

2.2.1.2 Structure Factor

When the interactions between the scattering objects are taken into consideration, the formula of the overall scattering intensity of a group of spherical objects becomes:

$$I(q) = \sum_j \sum_k F_j(q) \, F_k(q) \, \langle \exp\left(i\mathbf{q} \cdot (\mathbf{r}_k - \mathbf{r}_j)\right)\rangle$$

$$= \sum_j F_j^2(q) + \sum_{j \neq k} \sum_k F_j(q) \, F_k(q) \, \langle \exp\left(i\mathbf{q} \cdot (\mathbf{r}_k - \mathbf{r}_j)\right)\rangle$$

$$= NF^2(q) + F^2(q) \sum_{j \neq k} \sum_k \langle \exp\left(i\mathbf{q} \cdot (\mathbf{r}_k - \mathbf{r}_j)\right)\rangle = NF^2(q)\langle S(\mathbf{q})\rangle$$

The $S(q)$ is called the "structure factor", related to the interactions of multiple scattering centres. If the distribution is continuous, the summation can be converted into integration with a pair distribution function, $g_2(\mathbf{r}_j, \mathbf{r}_k)$. The structure factor is non-negligible when solution concentration increases, making the data interpretation more complicated.

2.2.1.3 Diffraction from Crystalline Structure

When the atoms are ordered in a crystalline material, the scattering factor of the material is then a sum of the scattering factors from a collection of unit cells that are composed of atoms:

$$F^{\text{crystal}}(\mathbf{q}) = \sum_j^{\text{unit cell}} F_j^{\text{atom}}(\mathbf{q}) \exp(i\mathbf{q} \cdot \mathbf{r}_j) \sum_n^{\text{crystal}} \exp(i\mathbf{q} \cdot \mathbf{R}_n)$$

$$= F^{\text{unit cell}}(\mathbf{q}) \sum_n^{\text{crystal}} \exp(i\mathbf{q} \cdot \mathbf{R}_n) = F^{\text{unit cell}}(\mathbf{q})S(\mathbf{q})$$

where $\mathbf{R}_n$ is the translation vector of the lattice, $\mathbf{r}_j$ is the position of the atoms in a unit cell.

The group of scattered X-rays from the same wavefront can be in phase and will show constructive interference with each other, resulting in a diffraction pattern. Bragg's law is therefore applied in this situation as:

$$2d \sin\theta = n\lambda$$

where d is the spacing between lattice planes, and n is the order of the diffraction. Combining the above equation with $q = 4\pi \sin\theta / \lambda$ to get the relationship between q and d:

$$q = \frac{2\pi n}{d}$$

As elaborated in Section 1.1.2, collagen intermolecular packing in a fibril shows a characteristic D-period (repeating gap and overlap regions), which is the origin of the diffraction rings or arcs on the X-ray scattering patterns or converted to diffraction peaks when radially integrated. X-ray scattering analysis can therefore monitor the changes in the D-period of collagen structure under various conditions.

2.2.2 Experimental Setup and Data Processing

The X-ray scattering experiments, specifically the small-angle X-ray scattering (SAXS) experiments (as our research interest is on the intermolecular packing of collagen), were conducted at synchrotron facilities remotely due to the COVID-19 travel restrictions. Here is a brief overview of the principle of synchrotron radiation and the beamlines, whereas more information is available in Ref. [134].

The principal element of synchrotron radiation is the reciprocating motions of high-speed particles (*e.g.*, electrons) guided by bending magnets (wigglers or undulators, that periodically deflect the electrons in the lateral direction of their path) that can generate extremely strong electromagnetic radiation (photon beam). The name "synchrotron" highlights that the increases in the magnetic field are "synchronised" with the increasing kinetic energy of the accelerating particles to regulate them in a closed path [136]. A synchrotron facility generally consists of five main components (Figure 2.8):

(1) An electron source ("e-gun") that regularly feeds electrons into the booster ring (to compensate for the loss) through a linear accelerator (LINAC) to accelerate them to about 100 MeV;

(2) A booster ring that further accelerates the electrons to match the energy in the main storage ring and frequently injects the electrons into the storage ring to maintain its current while allowing uninterrupted user operation;

(3) A storage ring that contains the accelerated electrons, which are maintained in a closed orbit using an array of magnets, focused and corrected using quadrupole and sextupole magnets to reduce divergences and chromatic aberrations;

(4) A radio frequency (RF) cavity, which supplies energy to electrons in the storage rings to maintain their energy when they pass through;

(5) The tangential exits from the storage ring toward the beamlines (also referred to as the "front ends"), which have a series of important functions: they isolate the beamline vacuum from the storage ring vacuum, monitor the position of the photon beam, define angular acceptance via an aperture, block between the X-ray and braking radiation when needed (the latter is also known as its German name "Bremsstrahlung") and the optics and the experimental hutches, as well as filter out the low-energy tail of the synchrotron radiation spectrum (if necessary, to protect optical components).
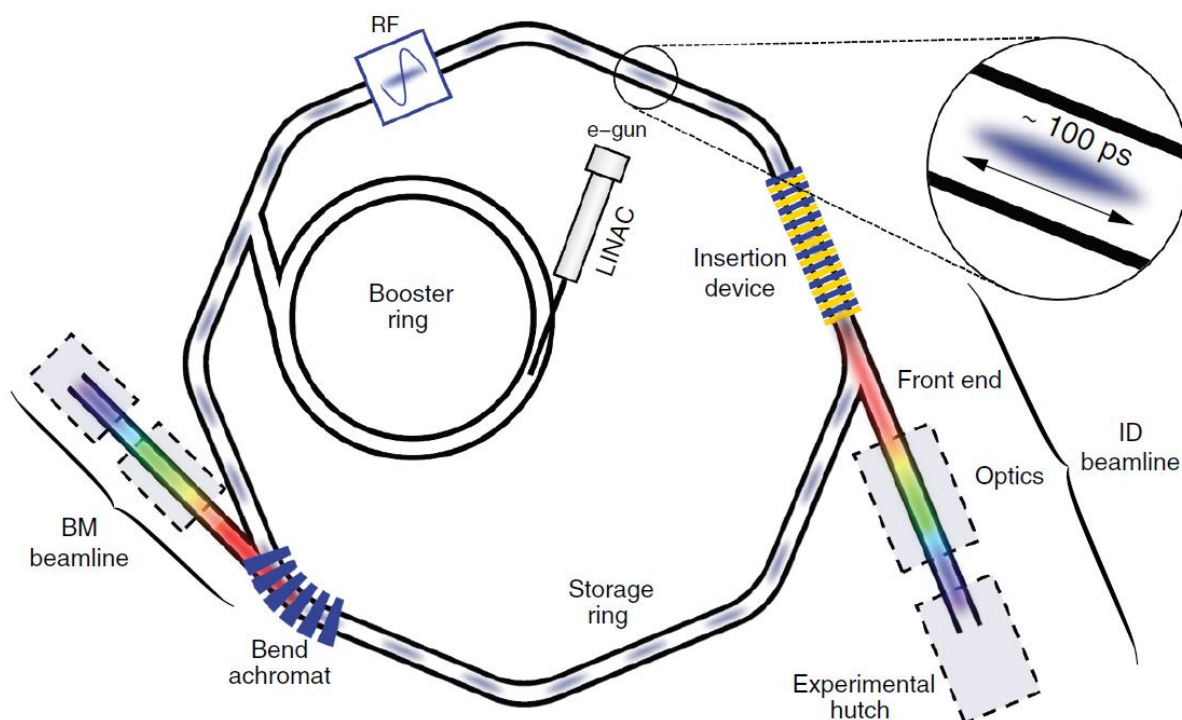
Figure 2.8: A simplified illustration of the most important components of a synchrotron facility. Note that insertion devices (ID) beamlines are typically brighter than bending magnet (BM) beamlines, although the latter remains much brighter than a bench-top setup. (Reprinted from Ref. [134] with permission from John Wiley and Sons.)

When a photon beam leaves the storage ring through the front end, it meets a series of optics and is guided toward the experimental hutch. A typical setup is shown in Figure 2.9. The beamline optics varies in detail at each synchrotron facility. However, it generally includes a beam-defining aperture and a couple of beam-position monitors to determine the height and the tilt angle of the beam, a monochromator, and a series of slits and mirrors before the beam hits the sample.
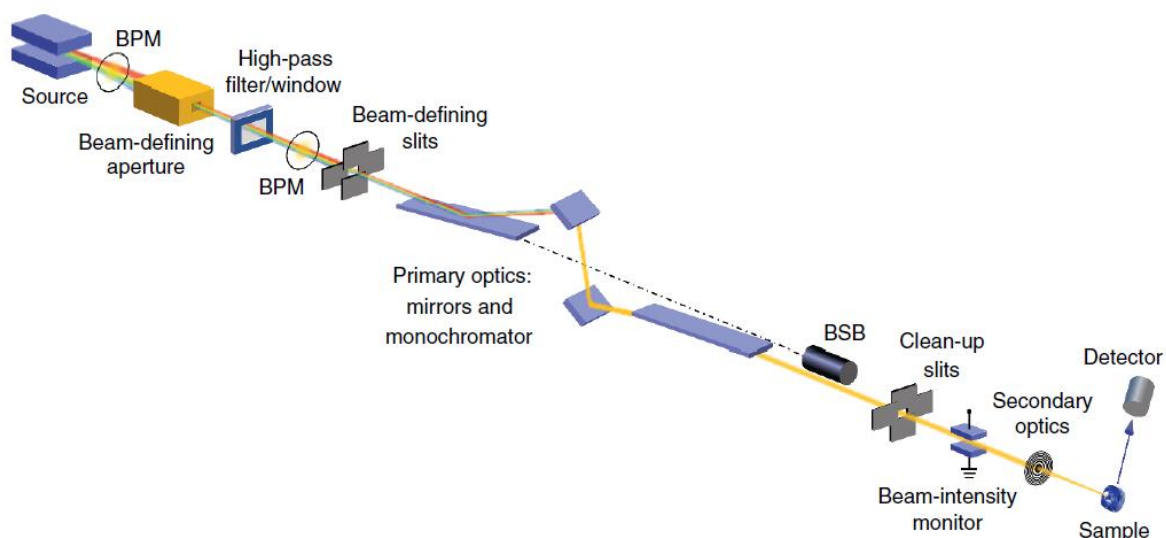
Figure 2.9: A generic illustration of the beamline setup at an X-ray synchrotron beamline. (BPM = beam-position monitor; BSB = Bremsstrahlung blocker.) (Reprinted from Ref. [134] with permission from John Wiley and Sons.)

The SAXS results in Chapter 3 were collected on beamline BL23A1 of the Taiwan Light Source (TLS) at the National Synchrotron Radiation Research Centre (NSRRC) in Hsinchu, Taiwan (ROC). The SAXS results in Chapter 5 were acquired on beamline I22 at the Diamond Light Source (or Diamond, in short), Didcot, UK.

To achieve the typical data curve presenting the scattered intensity $I(q)$ as a function of the scattering vector, q, dedicated data processing procedures were conducted catering to the file systems at each beamline. For the NSRRC BL23A1 beamline, 2D SAXS images were radially integrated (or "reduced") to 1D profiles using in-house software (Figure 2.10). The function of this software includes transmission calculation and data reduction. At BL23A1, the SAXS scattering pattern and the beam transmission of the samples are measured separately; the latter is measured by removing the beam stop (which blocks the non-scattered photon beam to protect the detector) and inserting an attenuator.
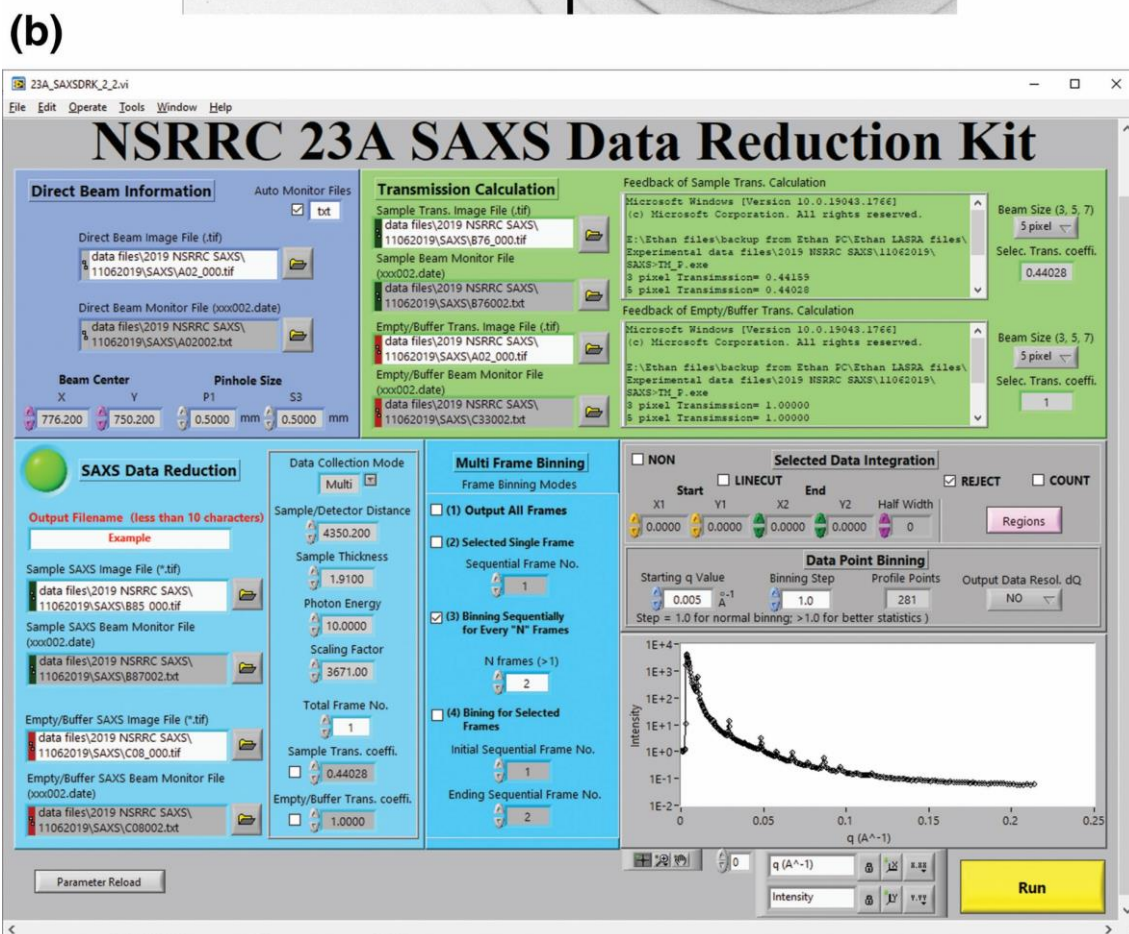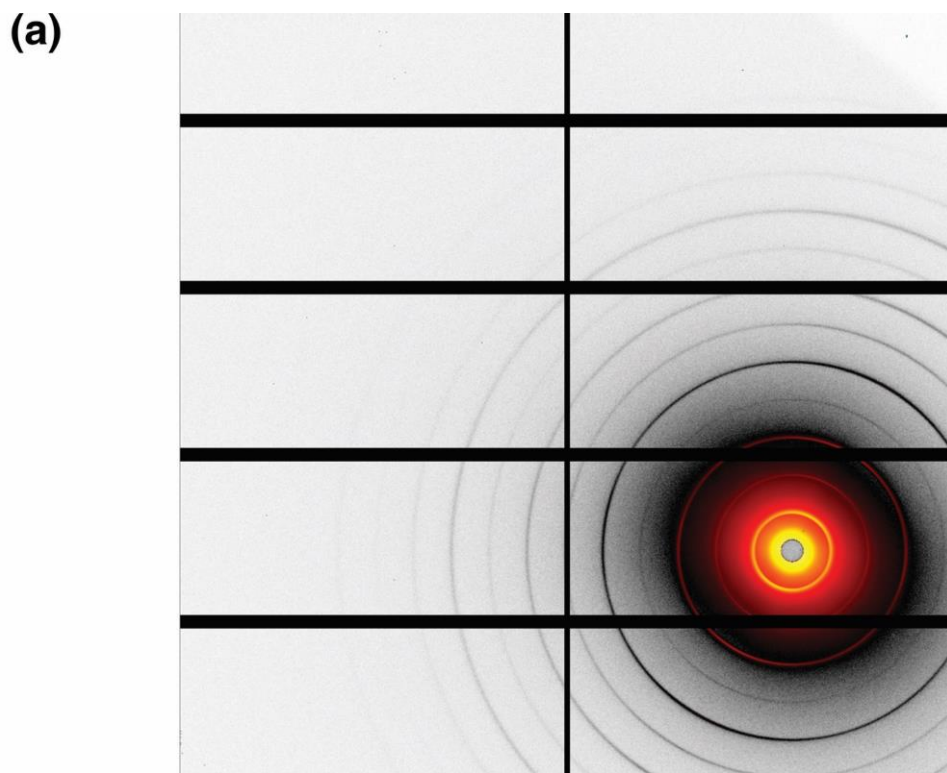
Figure 2.10: (a) A typical 2D SAXS image from a bovine skin collected at BL23A1 (detector: Pilatus 1M); (b) The software "23A_SAXSDRK_2_2.exe" at NSRRC BL23A1 for data reduction.

The converted 1D SAXS profiles were then analysed using an in-house program derived from SAXSFit [137]. This program incorporates a combined form factor and structure factor populations and a power-law function, in addition to a fibre diffraction d-spacing model. The overall equation being fitted comprises three terms:

$$I(q) = I_{\text{pop}}(q) + I_{\text{bkg}}(q) + I_{\text{peaks}}(q)$$

The form and structure factors are not resolvable under the experimental conditions and are treated using the spherical model:

$$I_{\text{pop}}(q) = c \int n(r) \, [f(qr)V(r)]^2 dr$$

where $n(r)$ is a log-normal size distribution, $f(qr) = 3(\sin(qr) - qr\cos(qr))/(qr)^3$ is the form factor of a sphere, and $V(r) = 4\pi r^3/3$ is the volume of a sphere.

The background term $I_{\text{bkg}}(q)$ is modelled as an empirical power-law function as $I_{\text{bkg}}(q) = mq^{-p} + n$.

The diffraction peaks are modelled as a group of Gaussians:

$$I_{\text{peaks}}(q) = \sum_n \frac{A_n}{w(q)\sqrt{\pi/2}} \exp\left(\frac{-2\left(q - \frac{2\pi n}{d}\right)^2}{w(q)^2}\right)$$

where A_n is the area of peak n, d is the D-period [Å], and $w(q)$ is the width [Å^{-1}], expressed as $w(q) = a + bq$ where a and b are fitted parameters.

For the Diamond I22 beamline, the 2D detector images were processed to 1D using Data Analysis Workbench (DAWN) developed at Diamond (Figure 2.11) [138, 139]. Each diffraction peak in the SAXS q range was fitted individually using the embedded Gaussian model and polynomial function in DAWN. The D-period was calculated based on the fitted position of the 3rd order peak as $D = 2n\pi/q$, in which $n = 3$ from the peak order.

Regardless of the fitting method, the ratio of the peak areas was calculated as $R_{n/m} = A_n/A_m$, where A_n and A_m stand for the areas of the peaks of order n and m.
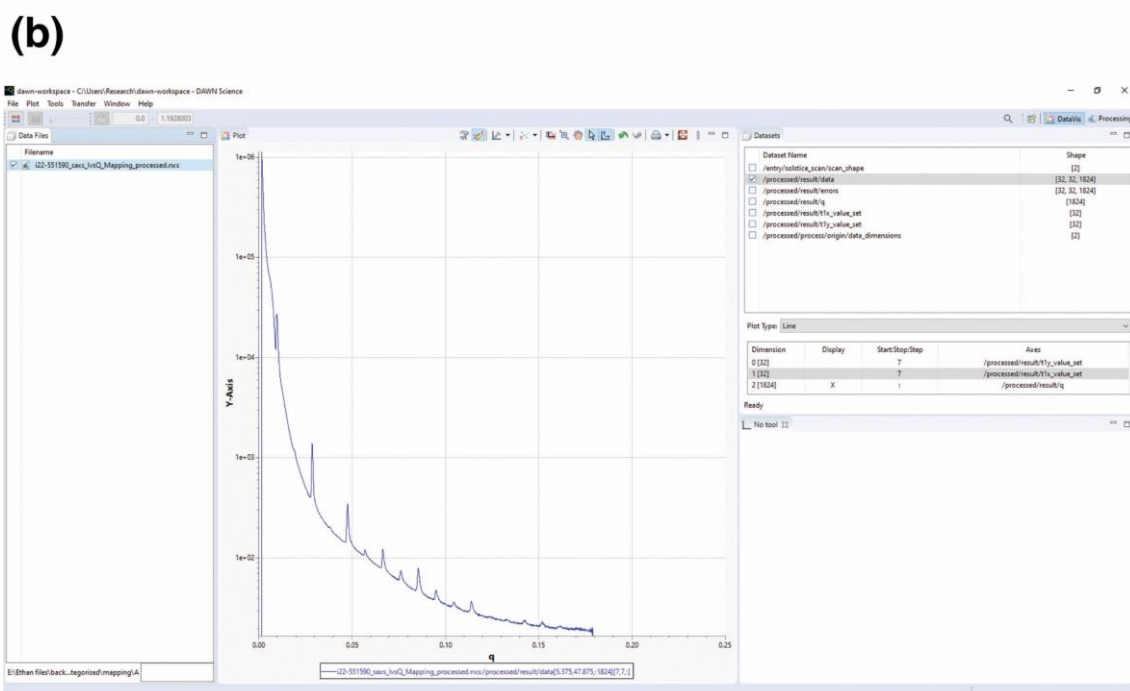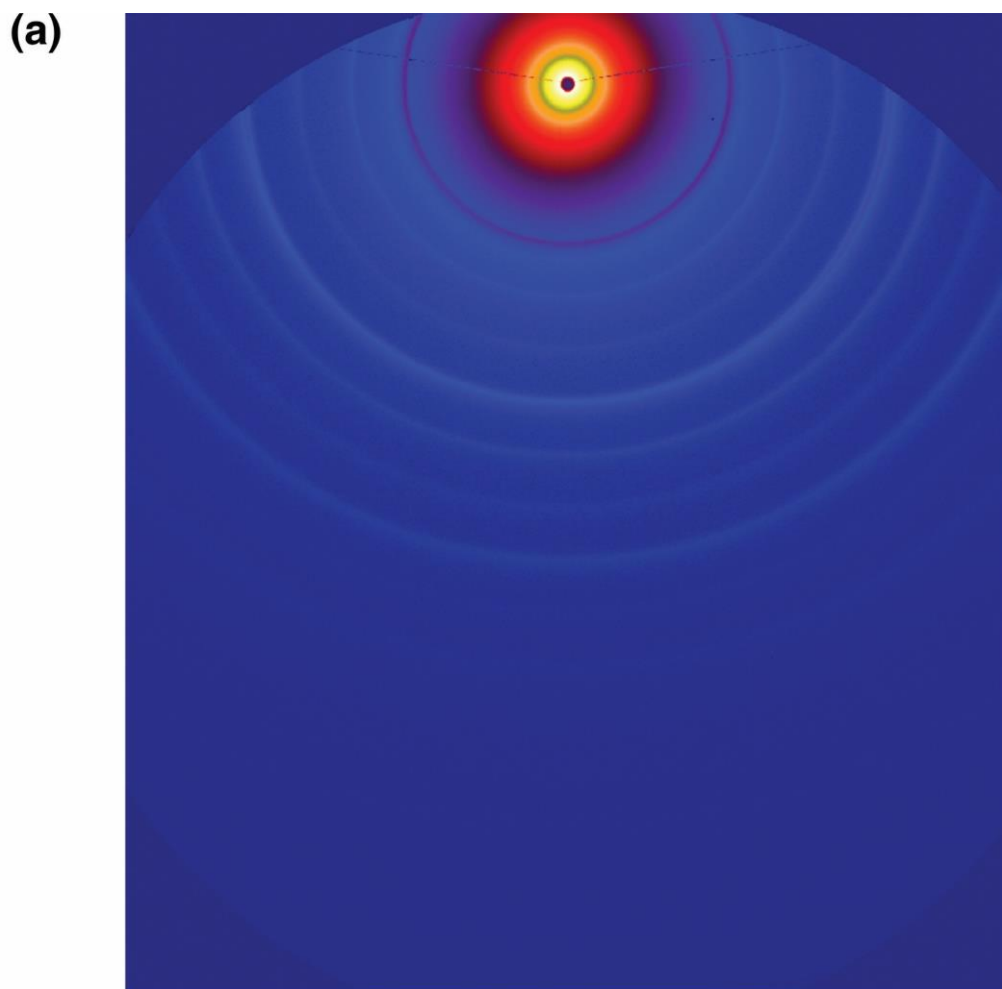
Figure 2.11: (a) A typical 2D SAXS image from a bovine skin collected at I22 (detector: Pilatus P3-2M); (b) A screenshot of DAWN (software version 2.20) for data processing and fitting.

2.3 UV-Vis Spectroscopy

The optical extinction of AgNPs can be regarded as a simple linear combination of two components: absorption and scattering. As discussed in Section 2.1.1.2, both components contribute to the visual colour of AgNPs (certain morphology even provides different transmitted and reflected colours, see "Lycurgus Cup"), while the scattering component is also responsible for the SERS effects. As the "far-field" phenomena in the dielectric medium (such as visual colours) are determined by the "near-field" properties, the UV-visible (or UV-Vis, in short) spectroscopy is thus important for characterising the changes in the surface binding and aggregation of AgNPs when interacting with capping ions or collagen molecules in a colloidal solution (see results in Chapter 4).

The origin of a distinct UV-Vis extinction spectrum of AgNPs is rather complicated to explain fully; under most realistic conditions, it cannot be expressed in analytic forms but estimated numerically. This section will continue introducing (as an extension of Section 2.1.1.2, yet on a conceptual and phenomenological basis) the renowned Mie theory, the effects of the size and shape of AgNPs on the extinction spectroscopy, and a brief touch on the corresponding coupling effects as the interparticle distance varies. Comprehensive theoretical explanations can be found in Ref. [122, 140-142] for further interest in this topic.

2.3.1 Theoretical Background

2.3.1.1 Brief Concept of the Mie Theory

The Mie theory, developed by Gustav Mie, provides the solution to the electromagnetic equations (*i.e.*, Maxwell's equations) that describes the scattering properties of a homogeneous, isotropic, non-magnetic spherical object in a non-absorbing medium excited by an external incident field. A general solution can be written in spherical coordinates as a sum of vector spherical harmonics (VSHs) as:

$$\mathbf{E}(\mathbf{r}) = E_0 \sum_{n=0}^{\infty} \sum_{m=-n}^{m=n} a_{nm} \mathbf{M}_{nm}^{(i)}(k, \mathbf{r}) + b_{nm} \mathbf{N}_{nm}^{(i)}(k, \mathbf{r}), (n > 0, |m| \leq n)$$

where k is the wave vector given by $k^2 = \omega^2 \epsilon(\omega)/c^2$ depending on the optical properties of the medium, a_{nm} and b_{nm} are complex coefficients and E_0 is an electric field amplitude to make the coefficients non-dimensional. The VSHs, $\mathbf{M}_{nm}^{(i)}(k, \mathbf{r})$ and $\mathbf{N}_{nm}^{(i)}(k, \mathbf{r})$, are also called "multipole fields", physically corresponding to the magnetic and electric fields of the multipoles (*e.g.*, $n = 1$ for dipoles, $n = 2$ for quadrupoles).

When considering the external field as a combination of the scattered field and the incident field, $\mathbf{E}_{\text{External}} = \mathbf{E}_{\text{Inc}} + \mathbf{E}_{\text{Sca}}$, the corresponding expanded expressions using VSHs are as follows:

$$\mathbf{E}_{\text{Inc}}(\mathbf{r}) = E_0 \sum_{n,m} a_{nm} \mathbf{M}_{nm}^{(1)}(k_M, \mathbf{r}) + b_{nm} \mathbf{N}_{nm}^{(1)}(k_M, \mathbf{r})$$

$$\mathbf{E}_{\text{Sca}}(\mathbf{r}) = E_0 \sum_{n,m} c_{nm}\mathbf{M}_{nm}^{(3)}(k_M, \mathbf{r}) + d_{nm}\mathbf{N}_{nm}^{(3)}(k_M, \mathbf{r})$$

Note that a_{nm} and b_{nm} are known complex coefficients from the incident light parameters, while c_{nm} and d_{nm} are unknown complex coefficients to be determined. The unknown parameters can be solved with boundary conditions implemented, and the results will allow the computation of the scattered field and, subsequently, the UV-Vis spectra. In particular, absorption, extinction, and scattering cross-sections can be expressed as infinite series involving these coefficients. For small particles, these series can be truncated down to the first ten terms without significant loss of precision.

2.3.1.2 Size Dependence

The absorption, scattering, and extinction spectra of AgNPs in water in the UV-Vis wavelengths are calculated using the Mie theory (Figure 2.12): the major resonance peak of the extinction spectra redshifts from 392 nm to 417 nm and then to 492 nm as the radius of the NPs increases from 10 nm to 50 nm, and the same trend is confirmed by experimental results [143]. The peak maximum also decreases as the size increases due to more radiation losses, indicating a lower local field intensity enhancement factor (LFIEF), thereby associated with a weaker SERS enhancement. A complete loss of enhancement is estimated for spherical AgNPs at a size of over 100 nm.
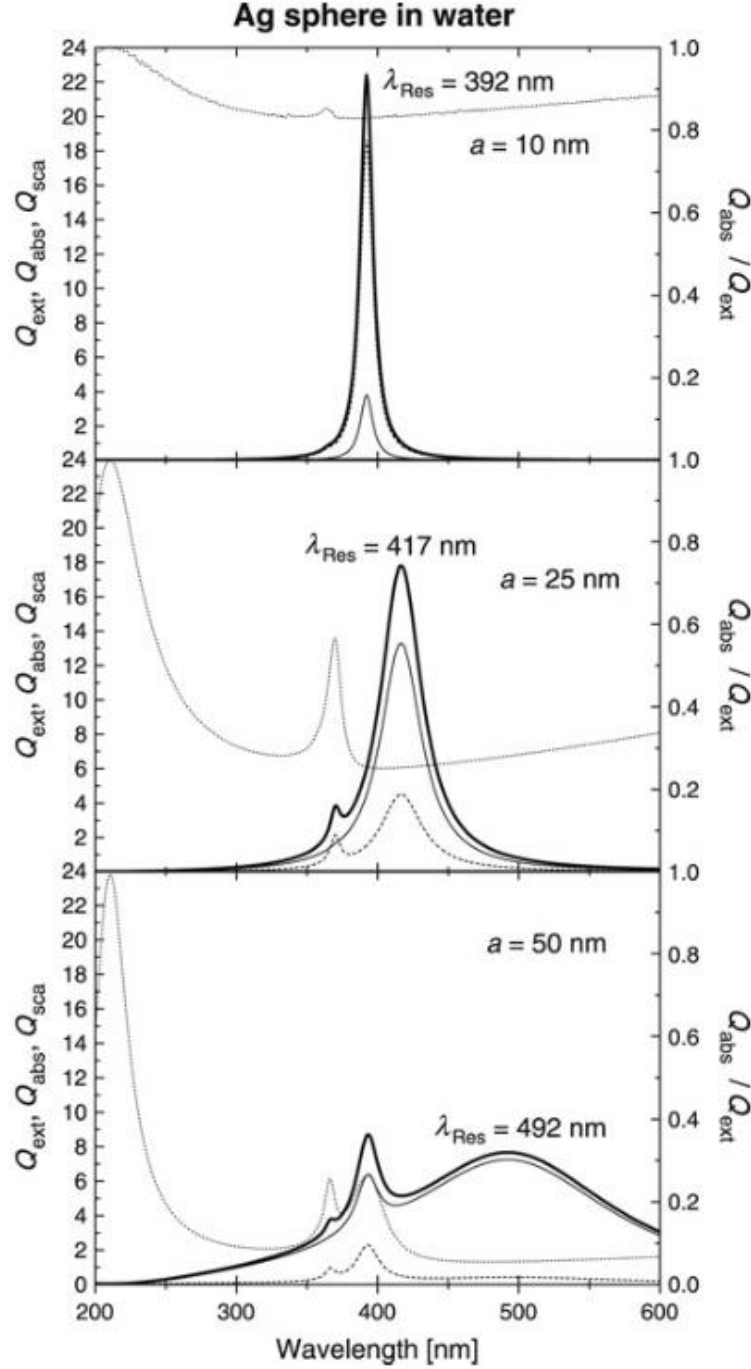
Figure 2.12: Calculated absorption, scattering and extinction coefficient of spherical AgNPs of a series of radii ($a = 10, 25, 50$) in water ($Q_{Abs}^{NP}, Q_{Sca}^{NP}, Q_{Ext}^{NP}$, as dashed lines, thin lines and thick lines, respectively). Dotted lines show the ratio of absorption and extinction with scales on the right y-axis. (Reprinted in part from Ref. [122] with permission from Elsevier.)

2.3.1.3 Shape Dependence

Similarly, through numerical methods (out of the scope of this study, see Ref. [122] for details), the UV-Vis spectra of AgNPs with shapes other than spheres can be calculated based on Maxwell's equations via numerical methods (e.g., finite element method); a series of examples

are presented in Figure 2.13 [144]. As the structural symmetry diminishes, the LSPR shows more anisotropicity and complexity, reflecting onto the UV-Vis spectra. Spherical AgNPs of 40 nm diameter leads to two resonance peaks: a strong dipole resonance at 410 nm and a weak quadrupole resonance at a shoulder at 370 nm. On the contrary, the sharp corners lead to charge accumulation and separation, reducing the restoring force of electron oscillation, and showing a redshift of the strongest peak for about 100 nm in the spectra of nanocubes compared with that of the nanospheres. Likewise, redshifts are found in tetrahedrons, octahedrons, and further nanoplates and discs. Experimental studies also support the theoretical modelling results [143-146].
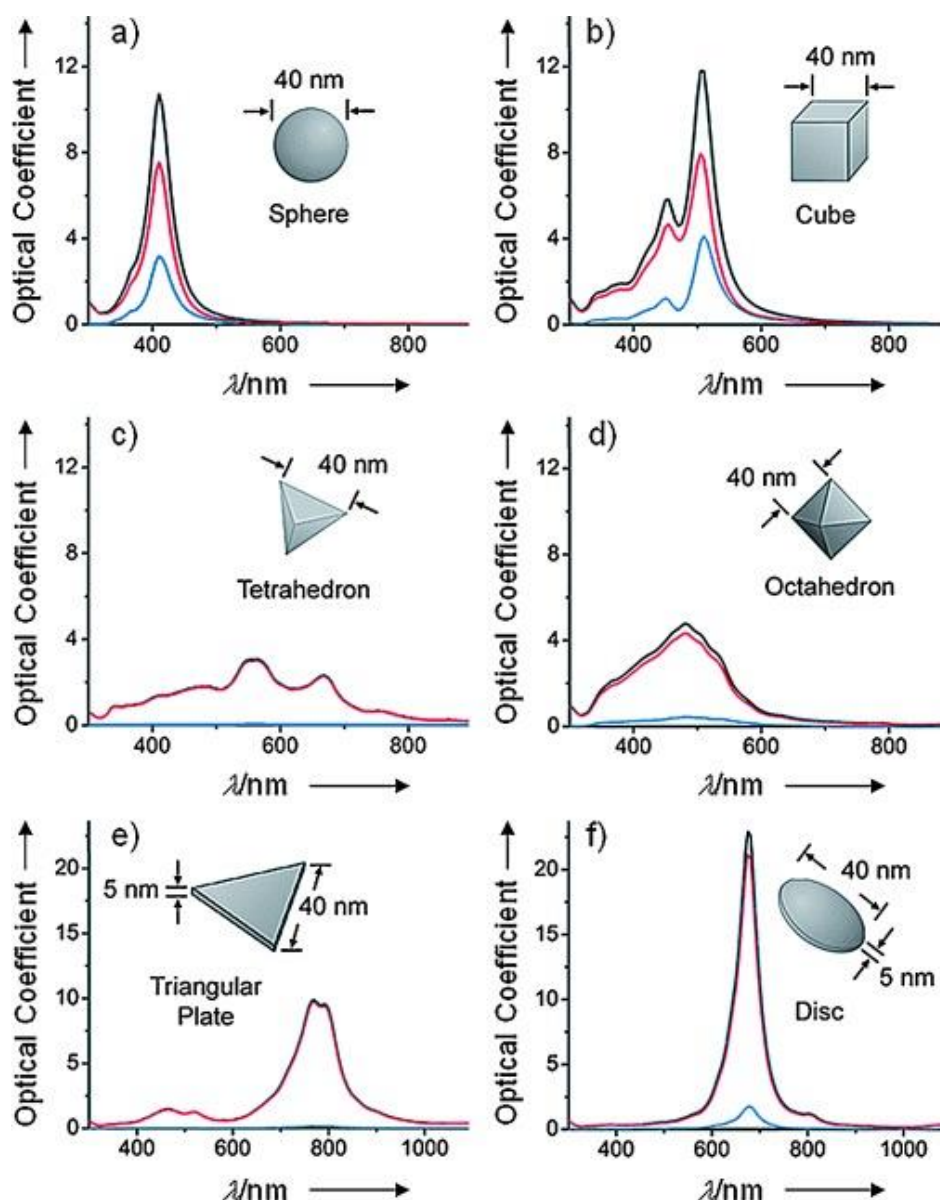
Figure 2.13: Calculated absorption (red), scattering (blue) and extinction spectra (black) of AgNPs in different shapes (with size parameters as labelled): (a) sphere; (b) cube; (c) tetrahedron; (d) octahedron; (e) triangular plate; (f) disc. (Reprinted from Ref. [144] with permission from John Wiley and Sons. Figures were originally from Ref. [147]. Copyright (2006) American Chemical Society.)

The above observations provide a simple way to estimate the size and shape of AgNPs and the suitable excitation wavelength for SERS experiments (although the link between the extinction spectrum and the SERS enhancement is indirect, especially when coupling occurs).

2.3.1.4 Coupling Effects

When two NPs are in the vicinity of each other, the LSPR will experience a coupling effect, creating a new peak on the extinction spectrum calculated from the generalised Mie theory (Figure 2.14)[148].
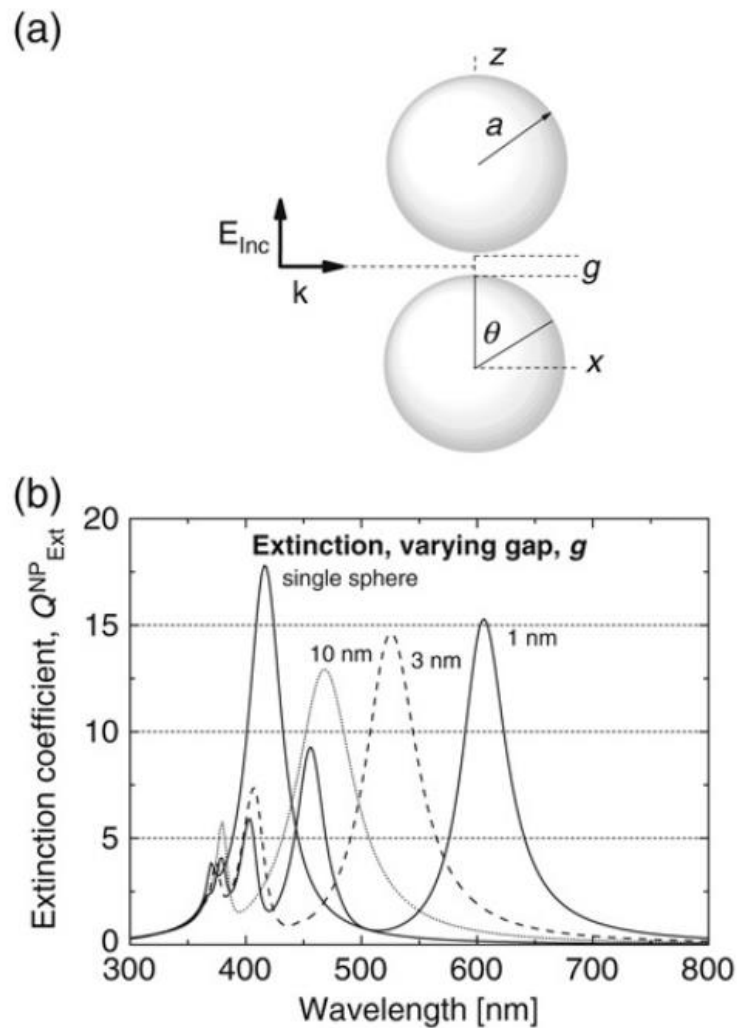
Figure 2.14: (a) Schematic configuration of a dimer along the z-axis with two Ag spheres of radii $a = 25$ nm separated by a gap g. The incident wave is polarised along the z-axis, and the wave vector **k** is along the x-axis. (b) The extinction coefficient of dimer at a distance of 10 nm, 3 nm and 1 nm compared with a single sphere. (Reprinted in part from Ref. [122] with permission from Elsevier.)

The coupling effect can be explained as a "constructive combination" of resonances between the two particles, in analogy with the in-phase and out-of-phase linear combination of atomic orbitals (LCAO) of hydrogen atoms. Therefore, the interaction of a multipolar LSP of one

particle with another particle (or the LSPs of multiple other particles in a cluster) results in a mixed multipolar composition, "bonding" and "anti-bonding" plasmons [149]. Like in the LCAO model, the parallel plasmon modes (or "bonding" plasmons) shift to lower energies (redshifts) with decreasing distance between the two particles, whereas the perpendicular plasmon modes should shift to higher energies (blueshifts) but also become weaker. If more NPs are placed in close proximities within a cluster, the coupled new LSPR peak will increase and redshift further (Figure 2.15) [150].
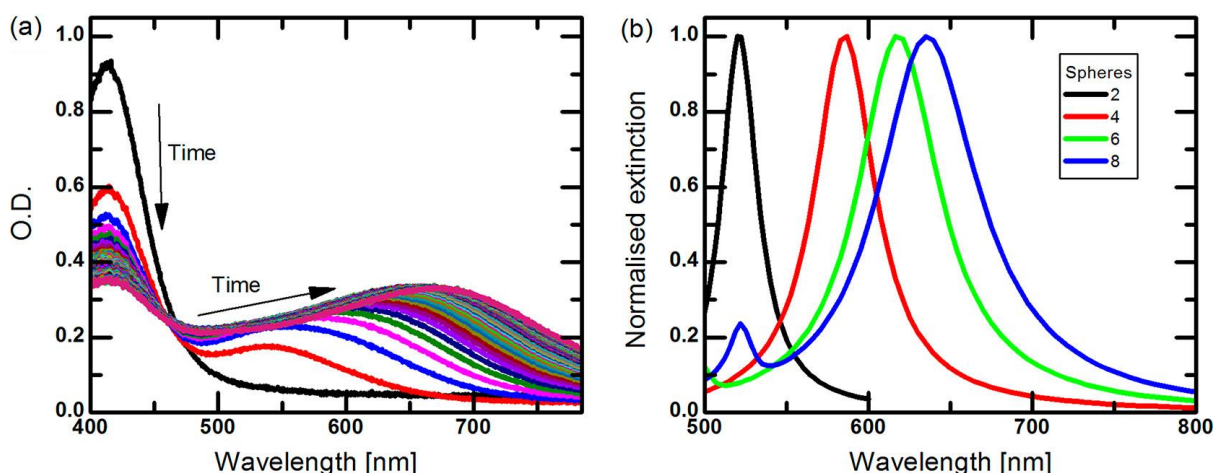
Figure 2.15: (a) UV-Vis extinction optical density (O.D.) of the aggregation of AgNPs over time. (b) Calculated extinction spectra of AgNPs clusters comprised of spheres (radii $a = 17$ nm) with equal spacing of 1.5 nm. (Reprinted with permission from Ref. [150]. Copyright (2012) American Chemical Society.)

2.3.2 Experimental Setup and Data Processing

The UV-Vis spectroscopy measurements were conducted using a Cloudspec spectrophotometer from Marama Labs. The principal design of this equipment is shown in Figure 2.16, a centrally mounted sample cuvette integrating sphere (CMCIS) that allows accurate measurements of the absorption of the sample without interference from scattering. Extinction measurement is also collected simultaneously with embedded normal transmission configurations. Briefly, a white light source is inserted from one point of the integrating cavity, and after a few rounds of diffuse reflections (called "Lambertian reflections"), the remaining flux related to the absorbed light will be collected via a detector placed at another position of the sphere wall.
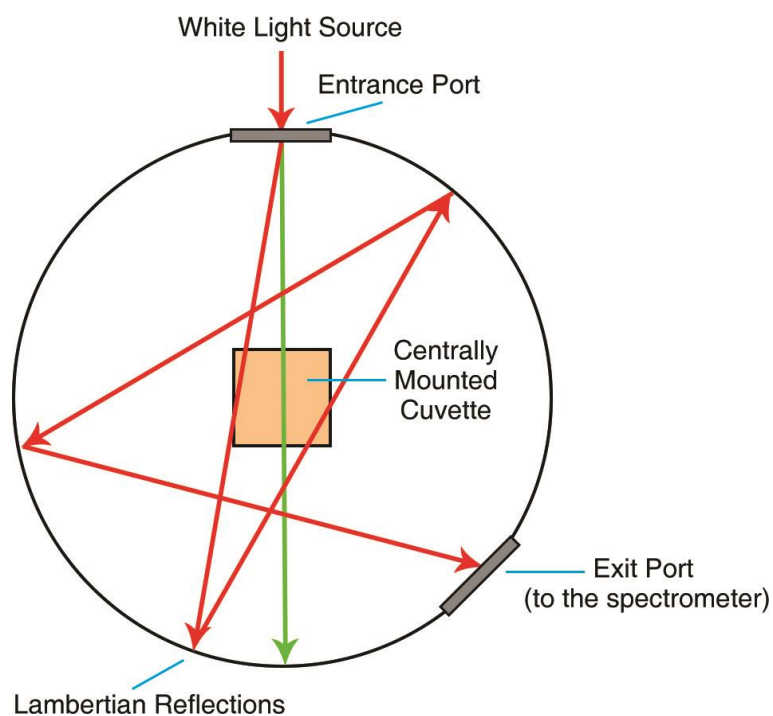
Figure 2.16: Schematic of the centrally mounted sample cuvette integrating sphere (CMCIS) setup showing the light paths for the absorption and extinction measurements embedded in the Cloudspec equipment.

Typically, 1 mL of sample is contained in a Suprasil type 3 quartz cuvette (with all sides transparent), and 2000 runs are accumulated. The raw spectrum is subtracted from a blank H_2O spectrum collected before each sample. This practice is crucial, especially for partially aggregated AgNPs or collagen-AgNPs clusters, to account for the non-trivial accumulation of AgNPs onto the quartz surface over time.

2.4 Differential Scanning Calorimetry (DSC)

The principle of DSC is introduced briefly to cover the required knowledge for understanding and analysing the thermograms of collagen molecules in tissues during heat-induced denaturation events in Chapter 3 and Chapter 5. Extensive discussions around DSC and protein thermal analyses can be found in Ref. [151-154].

2.4.1 Theoretical Background

Proteins fold spontaneously into their native conformations during the synthesis, and when heated, they can also unfold via a highly cooperative process in which very few or no stable intermediate states are involved. The heat-induced unfolding of a specific protein often features a characteristic unfolding temperature and enthalpy, allowing DSC to be a suitable technique to analyse the thermal changes quantitatively.

A generic DSC thermogram is shown in Figure 2.17, with temperature as the x-axis and heat capacity (C_p) as the y-axis, showing two distinct features: a sharp peak and a shift in the baseline. The positive peak represents a surge in heat capacity, indicating an endothermic event during the unfolding of the protein. The baseline shift shows the general heat capacity change (ΔC_p) between folded and unfolded states. From these two features, one can calculate the enthalpy of unfolding, ΔH_{Cal}. Here, "Cal" represents "calorimetric measurement" and is usually noted to differentiate from the indirectly determined enthalpies based on a two-state van't Hoff equilibrium model or a Zimm-Bragg sequential unfolding model (see Ref. [152]); in fact, comparing the enthalpies is a way to verify the predicted unfolding mechanisms of the protein (*e.g.*, intermediate states, reversibility).
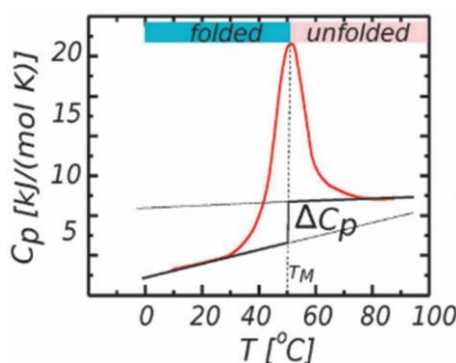
Figure 2.17: A typical thermogram of a protein measured using DSC. (Reprinted in part with permission of the Royal Society of Chemistry, from Ref. [154]; permission conveyed through Copyright Clearance Centre, Inc.)

2.4.2 Experimental Setup and Data Processing

The DSC equipment used for the studies in this thesis is a heat-flux DSC (Q2000, TA Instruments). A comparison between different types of differential thermal instruments is shown in Figure 2.18 [155]. Unlike the differential thermal analyser (DTA) that measures

temperature differences between sample and reference pans, heat-flux DSC measures energy differences and outputs the heat flow, commonly expressed in a unit of [mW]. Instead, the power-compensated DSC has two individual furnaces to adjust the heat "required" to keep the sample and reference pans at the same temperature, rather than measuring the heat "consumed" by sample and reference pans as in a heat-flux DSC.
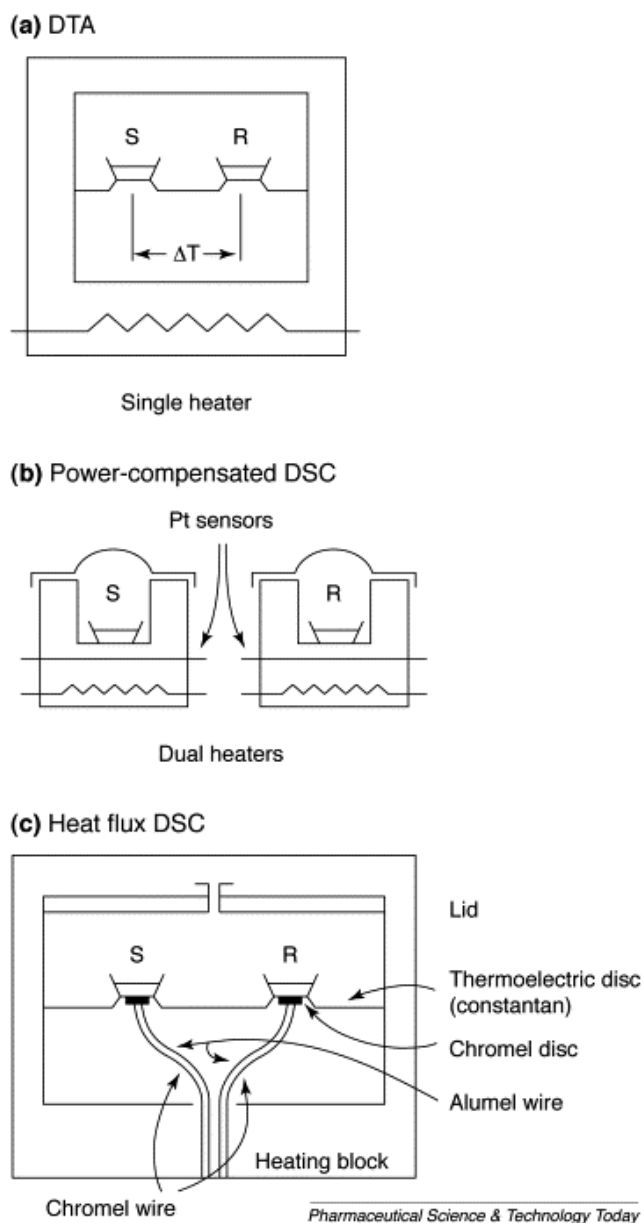
Figure 2.18: Schematic illustrations of (a) DTA, (b) power-compensated DSC and (c) heat-flux DSC. (Reprinted from Ref. [155] with permission from Elsevier.)

For the studies in this thesis, all the collagen tissue samples are sealed in aluminium pans to maintain moisture during heating in the N_2 atmosphere in the DSC instrument because

variations in the hydration levels can largely alter the thermal stability of collagen[8] [67]. The data collected were analysed using TA Universal Analysis; an example is shown in Figure 2.19. The heat capacity values are derived from the heat flow signals and are plotted against the temperature, showing a smooth baseline before the unfolding temperature or the "onset temperature" of collagen (at 79.10 °C in this thermogram). The onset temperature is defined by the temperature value at the intersection of the two tangent lines. The first tangent line represents the baseline, whereas the other is drawn at the point of maximum slope in the first half of the peak. Note that the onset temperature of the peak is commonly referred to as the "denaturation temperature" or "T_d" because, at this point, collagen starts to denature. Its renaturation is extremely slow and likely unable to recoil as in its native state, leaving a permanent (partial) loss of helical structure [156-158]. The peak develops with increasing temperature and reaches the maximum point at which the denaturation (unfolding) rate is maximised (at 84.93 °C). The baseline after the peak is used along with the original baseline to calculate a heat capacity change and the unfolding enthalpy. The medium point in this example graph is estimated to be 83.80 °C, indicating that half of the collagen has converted to the unfolded state. Multiple fitting iterations are carried out to give an accurate baseline for taking the heat capacity changes during the unfolding into consideration. The iteration starts from a straight line connecting the starting and finishing onset points, followed by an integration of the peak area from the starting point to a certain T (based on the straight baseline). Based on the partition of the area, a linear combination of heat capacity before and after the unfolding event is calculated to form the baseline of the next iteration. This method is followed for the integration to calculate the denaturation enthalpy ($\Delta H = 34.02$ mJ).

---

[8] The "thermal stability" of collagen reported in this thesis is also commonly referred to as "hydrothermal stability" due to its measurements at a fully hydrated state. However, the latter can be confused with the resistance to hydrolysis under hydrothermal treatments of zeolites. Therefore, we used the generic term "thermal" instead of "hydrothermal" throughout this thesis for simplicity.
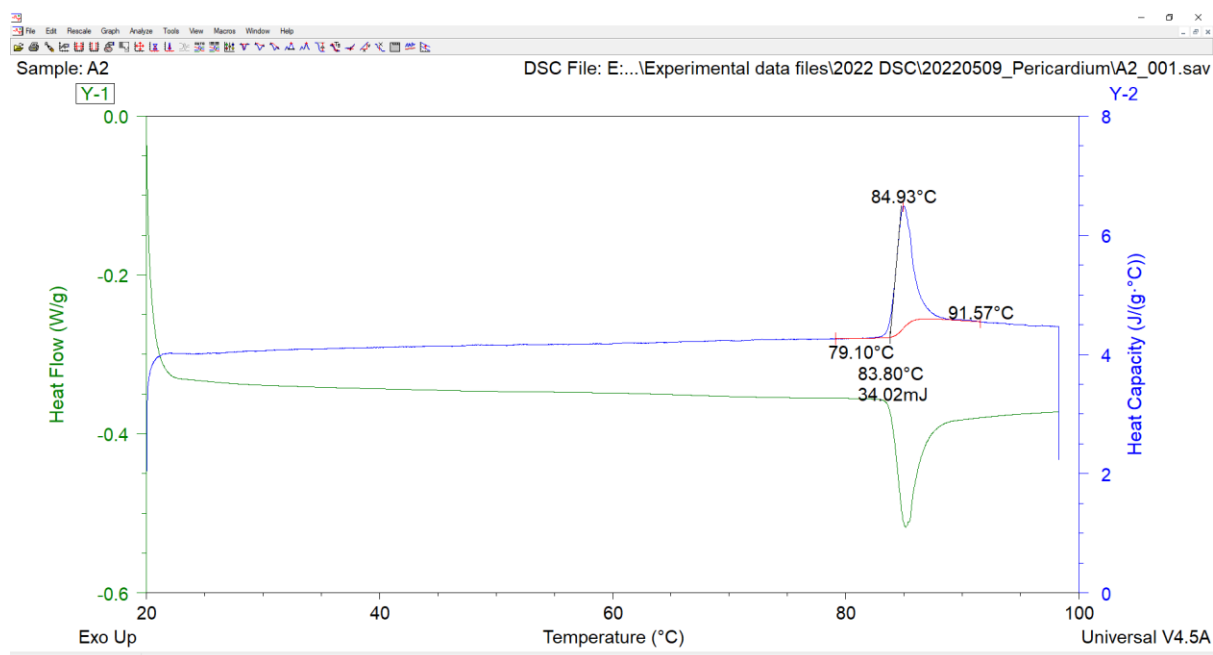
Figure 2.19: An example DSC thermogram of glutaraldehyde-crosslinked bovine pericardium analysed using TA Universal Analysis.

2.5 Other Techniques

Several other techniques applied in this thesis are not of the same level of importance as the above ones but do contribute to the studies supportively. Imaging techniques such as transmission electron microscopy (TEM) are the gold standard for characterising the morphology and crystallinity of NPs, commonly assisted by a selected area electron diffraction (SAED) method. Protein assays are regularly used for collagen for molecular weight and purity assessment (sodium dodecyl sulfate-polyacrylamide gel electrophoresis, SDS-PAGE), concentration assessment (hydroxyproline assay), and free amine content assessment (ninhydrin assay). A detailed account of the techniques could be referred to in Ref. [80, 159, 160].

2.5.1 Transmission Electron Microscopy (TEM) and Selected Area Electron Diffraction (SAED)

Basic principles of TEM and SAED techniques are introduced based on Ref. [159]. Figure 2.20 shows a full cross-sectional view of the JEOL JEM-2100F used in this thesis. An electron microscope contains an electron source (the electron gun) which generates an electron beam. Typically for AgNPs, the applied potential for accelerating the electrons is 200 keV. The beam is then manipulated through a series of magnets and lenses to focus on a suitable position relative to the sample (on the specimen holder). By altering the projector lenses, an image or a diffraction pattern (if focused on the plane of the sample) can be observed on the fluorescent screen or collected by digital cameras.

TEM images give direct information on AgNPs regarding their morphology and size distribution; ImageJ software is employed to estimate these parameters. The diffraction pattern is, in this case, from a selected area rather than the whole collection of the specimen, thus called Selected Area Electron Diffraction (SAED). Based on the pattern, one can distinguish a single crystalline, polycrystalline or amorphous sample; a group of dots indicates a single crystal, while a group of sharp rings originates from a polycrystalline material.
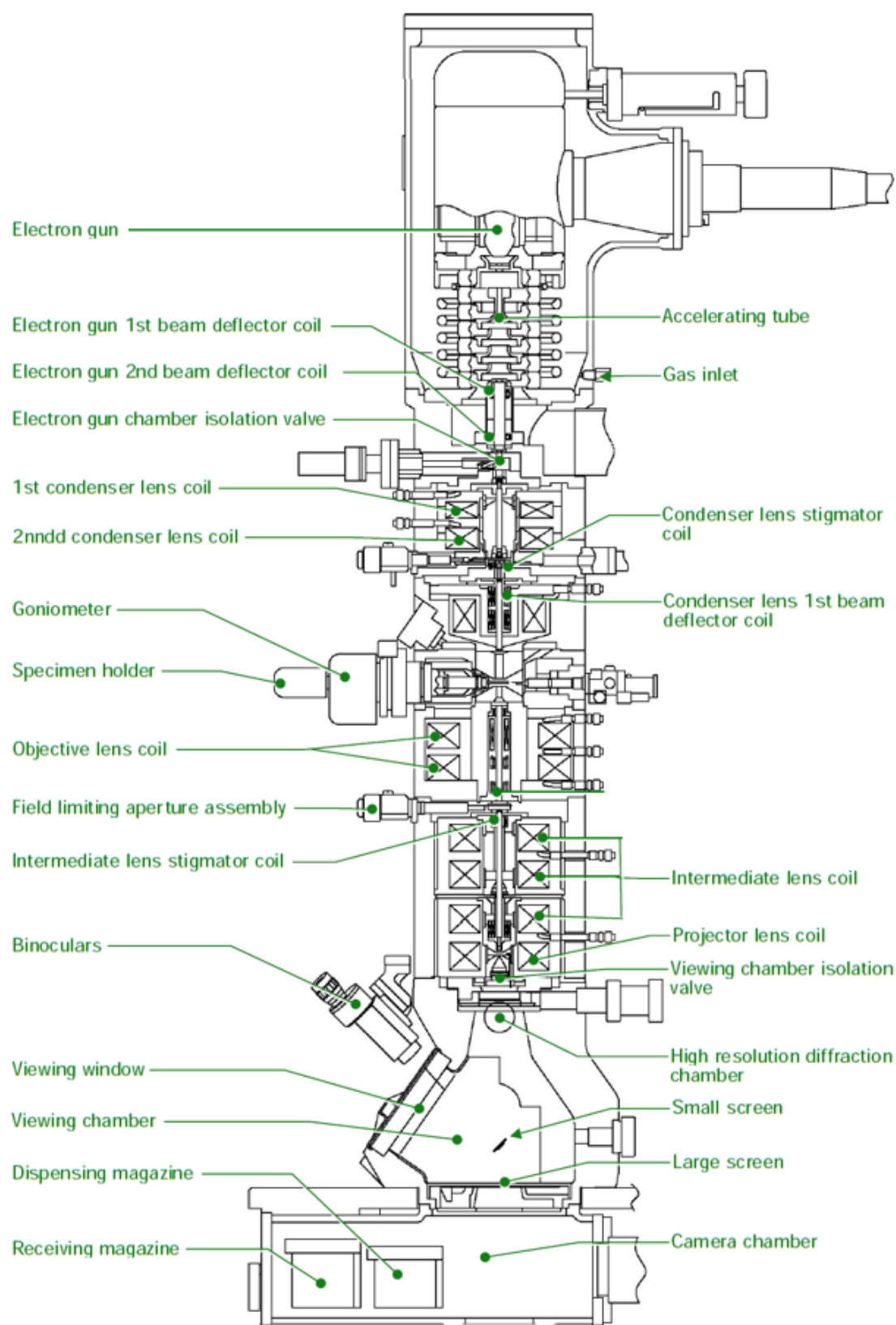
Figure 2.20: a cross-sectional view of the JEOL JEM-2100F TEM column. (Reprinted with permission from the instruction handbook of the JEOL JEM-2100F field emission electron microscope. Copyright (2003) JEOL Ltd.)

2.5.2 Sodium Dodecyl Sulfate-Polyacrylamide Gel Electrophoresis (SDS-PAGE)

Modern gels include a separating gel and a stacking gel on top for sample loading. The separating gel is a crosslinked polyacrylamide gel (typically between 6% to 15%) formed by the polymerisation reaction of acrylamide monomers and the crosslinking reaction using *bis*-acrylamide (*N, N'*-methylene-*bis*-acrylamide) (Figure 2.21). The reaction is initiated using ammonium persulfate (APS), which converts acrylamide monomers to a free radical form, and begins polymerisation. The formation of free radicals is accelerated by tetramethylethylenediamine (TEMED). The stacking gel helps concentrate the protein sample into a sharp band before it enters the separating gel, thereby sharpening the resulting bands for better resolution. A stacking gel is typically shaped into a comb with wells for sample loading and usually has a low concentration for larger pore sizes (4% acrylamide). The solutions for gel preparation are listed in Table 2.1. To confirm the integrity of the extracted collagen, we commonly use 12% gel for its good resolution in the low kDa region.
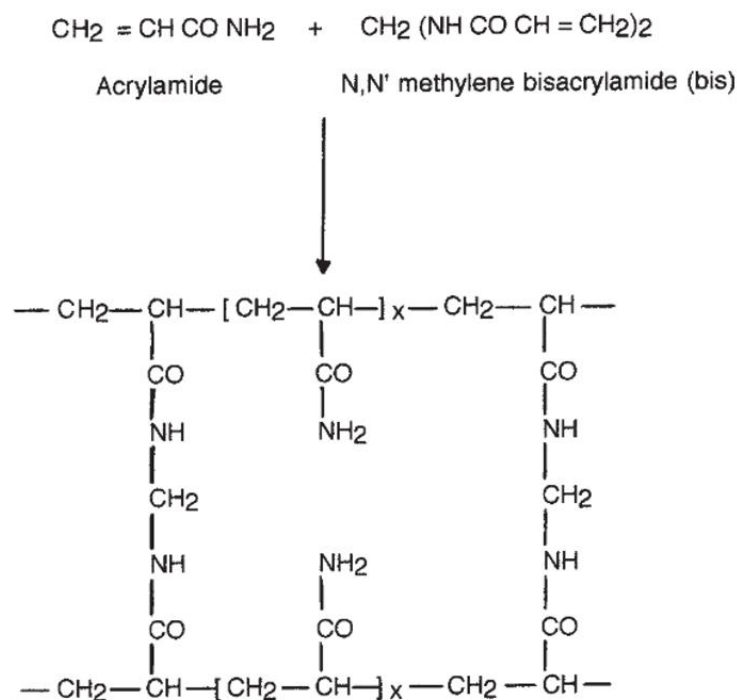
Figure 2.21: The polymerisation reaction of acrylamide with *bis*-acrylamide crosslinking. (Reprinted by permission from Springer Nature Customer Service Centre GmbH from Ref. [161].)

Table 2.1: Solutions for preparing SDS-PAGE gels (4% stacking gel and 7.5% and 12% separating gels).

Component	Volume (mL)
Stacking gel (4%)	**10**
Deionised (DI) water	6.1
Tris(hydroxymethyl)aminomethane hydrochloride (Tris-HCl), 0.5 M (pH = 6.8)	2.5
Sodium dodecyl sulfate (SDS), 10% (*w/v*)	0.2
Mixture of acrylamide and *bis*-acrylamide (29.1 : 0.9), 40% (*v/v*)	1.0
*APS, 10% (*w/v*)	0.2
*TEMED	0.01
Separating gel (7.5%)	**20**
DI water	10.8
Tris-HCl, 1.5 M (pH = 8.8)	5.0
SDS, 10% (*w/v*)	0.2
Mixture of acrylamide and *bis*-acrylamide (29.1 : 0.9), 40% (*v/v*)	3.8
APS, 10% (*w/v*)	0.2
TEMED	0.01
Separating gel (12%)	**20**
DI water	8.7
Tris-HCl, 1.5 M (pH = 8.8)	5.0
SDS, 10% (*w/v*)	0.2
Mixture of acrylamide and *bis*-acrylamide (29.1 : 0.9), 40% (*v/v*)	6.0
APS, 10% (*w/v*)	0.2
TEMED	0.01

*: Before adding APS and TEMED, the mixture of the above solutions is degassed using a water vacuum pump for 15 min.

The electrophoresis is conducted using a Bio-Rad mini-PROTEAN III electrophoresis cell equipped with a Bio-Rad PowerPac Basic power supply (Figure 2.22). The first step is to assemble the gel cassette and the electrophoresis tank, followed by adding the running buffer (Table 2.2). Secondly, the collagen samples are pre-mixed with the sample loading buffer (Table 2.2). Typically, in 2 µL of the loading buffer, add 8 µL of a mixture of the collagen solution and deionised (DI) water to a final total volume of 10 µL. Optionally, the final mixture is heated at 90 °C for 5 min and cooled down to room temperature. Then, the mixture is added to the wells in the stacking gel alongside the protein standards. Lastly, the voltage at 150 V is applied across the electrodes for approximately 50 min at room temperature until the dye front is close to the bottom of the gel. The resulting gel is fixed in a solution of 10% acetic acid and 40% ethanol for 15 min before being stained overnight (Table 2.3), followed by repeated rinsing with DI water until a clear background is observed.

For pure type I collagen, distinct α bands at around 100 kDa and β bands at around 200 kDa should be observed, as shown in Figure 2.23. Any bands lower than the α bands shall be considered impurities (*e.g.*, degraded collagen peptides) [50, 80].
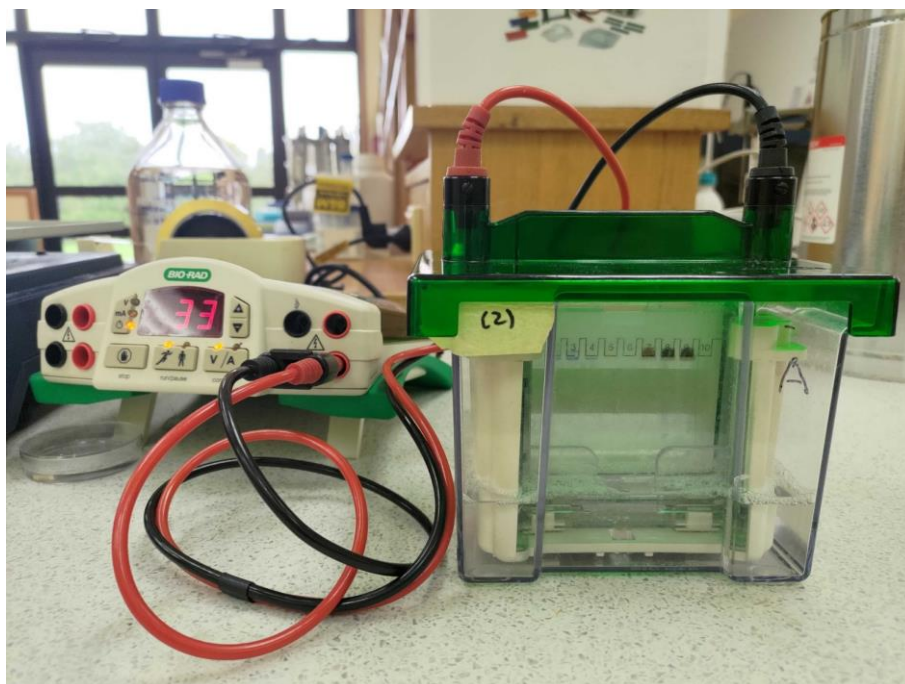
Figure 2.22: A photo of the electrophoresis setup.

Table 2.2: Solutions for electrophoresis (the running buffer and the sample loading buffer).

Component	Concentration
Running buffer	
Glycine	14.4 g L^{-1}
Tris(hydroxymethyl)aminomethane (Tris)	3.0 g L^{-1}
SDS	1.0 g L^{-1}
Sample loading buffer	
SDS	10% (w/v)
Glycerol	50% (v/v)
Dithiothreitol (DTT)	100 mM
Tris-HCl	0.25 M
Bromophenol blue	0.05% (w/v)

Table 2.3: Solutions for gel staining.

Component	Concentration
Stock solution	
Ammonium sulfate	10% (w/v)
Phosphoric acid	1% (w/v)
Coomassie blue G-250 stock	0.1% (w/v)
Working solution	
Stock solution	80% (v/v)
Methanol	20% (v/v)
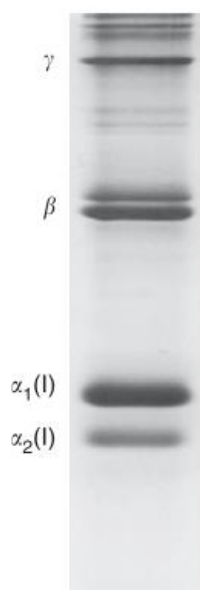
Figure 2.23: The characteristic electrophoretic mobility profile of bovine skin type I collagen, showing distinct bands representing the single polypeptide chains (α_1(I) and α_2(I)), double chains (β) and triple chains (γ). (Reprinted by permission from Springer Nature Customer Service Centre GmbH from Ref. [80].)

2.5.3 Hydroxyproline Assay

The collagen concentration in a solution was estimated through hydroxyproline (Hyp) assay because this amino acid is almost exclusively found in collagen and has a consistent content of around 13.5% in type I collagen in mammals [162, 163].

The procedure and mechanism of the Hyp assay are summarised in Figure 2.24 [80, 164-166]. First, collagenous tissues are hydrolysed in strong acid (or base) into individual amino acids (a mixture including Hyp). The Hyp is then oxidised using chloramine-T into pyrrole-2-carboxylate, which finally reacts with 4-(dimethylamino)benzaldehyde (p-DMAB, or "Ehrlich's reagent"). The final product has a strong absorption at around 555 nm and was quantified using a BioTek absorbance microplate reader ELx800 (Agilent Technologies) at 550 nm.
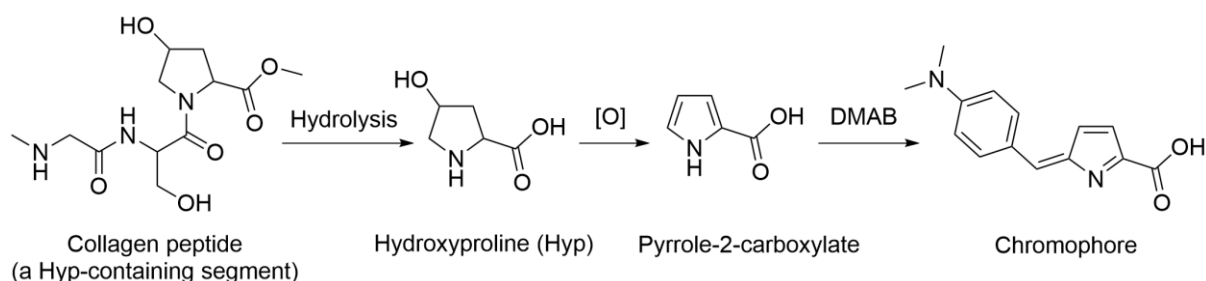
Figure 2.24: Stepwise procedure and mechanism of the Hyp assay [164].

2.5.4 Ninhydrin Assay

The quantitative analysis of the free amino (–NH$_2$) group content in collagen molecules in tissues is conducted based on the chromogenic reaction of ninhydrin with α-amino acids (Figure 2.25) [80, 167]. It allows a direct assessment of the performance of aldehydic crosslinkers on collagen: the reduced number of –NH$_2$ groups is proportional to the degree of crosslinking.

The mechanism begins with the nucleophilic displacement of a hydroxyl (–OH) group in ninhydrin by a –NH$_2$ group in the amino acid. The molecule undergoes a decarboxylation under heat into an imine, which then displaces an –OH group of another ninhydrin molecule to form a dimer chromophore, 2-(1,3-dioxoindan-2-yl)iminoindane-1,3-dione (also called "Ruhemann's purple"). The chromophore has a strong absorption at 570 nm and was quantified using a BioTek absorbance microplate reader ELx800 (Agilent Technologies) at 550 nm.
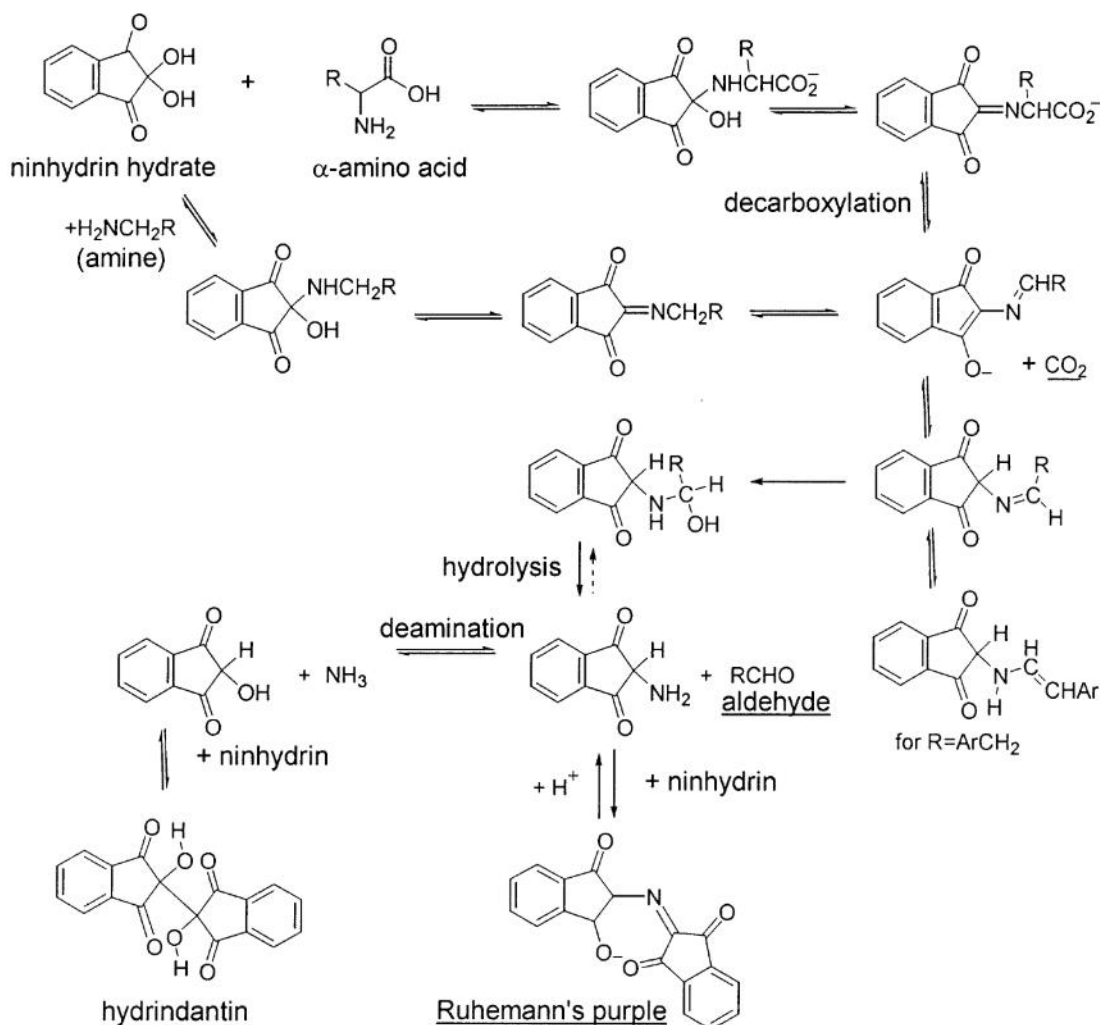
Figure 2.25: Reaction mechanism of ninhydrin with an arbitrary α-amino acid to yield the chromophore. (Reprinted in part with permission from Ref. [167]. Not subject to U.S. Copyright)

Chapter 3   Collagen in Bovine Skin: Binding Mechanisms of Cr(III)

In this chapter, we present the investigations of the binding of Cr(III) species with collagen using several characterisation techniques, including SAXS and SERS, through which we aim to extend the existing knowledge. To explicate this mechanism, we developed a preliminary SERS method for collagen fibres based on the mere report in this field on a collagen fibril cast from solution [103] and largely improved the reproducibility. Results highlight that the Cr(III) do not always bind to collagen covalently, which had been the prevailing belief for more than a century until very recently. A competition between two mechanisms is confirmed to be regulated by the counter ions (*i.e.*, anions) present in the system together with Cr(III). This study sheds light on the seemingly thoroughly developed chrome tanning theories and guides the innovations on more sustainable processing techniques.

Contextually speaking, the SERS method for collagen fibres that we developed in this study led the way toward further SERS measurements in collagen solutions (discussed in Chapter 4). A steady path was followed, starting from native collagen fibre in skins to extracted and dried collagen sponge and ending up with the extracted collagen solution; in the last scenario, we revealed further fundamental knowledge that allowed us to expound on our premature success in this chapter.

Most of the findings in this chapter have been published in Ref. [1] and are reused with permission. Data are reorganised for clarity without modifications to the data themselves; the same practice is carried out in the later result chapters.

3.1   Background

The start of the history of leather tanning dates back to an immemorial time, over 5000 years ago. The word "tanning", which originally refers to the use of polyphenolic tannins to make animal skins into leather, has now been expanded to include a variety of tanning technologies. It is defined in Ref. [73] as the "conversion of putrescible organic material into a stable material capable of resisting biochemical attack" to highlight stabilisation as its main purpose. For the past century, chromium has been the most prevalent element in the periodic table involved in tanning practices; it takes part in 90% of the world's tanning nowadays, and the product is known by its commodity name, "wet blue" [73]. The development of chrome tanning can be traced back to 1858, when Knapp described the use of "chrome alum" (*i.e.*, chromium(III) potassium sulfate) in a single-bath tanning process [168]. Since then, the tanning chemistry of chromium sulfate has been studied with groundbreaking milestones set by Gustavson *et al.* across the 1950s [169, 170] and improved by Covington *et al.* [171, 172] and our group [74] in the recent 30 years.

The binding of chromium with collagen occurs on the side chains of collagen. In each collagen polypeptide chain, the amino acid sequence exists as repeating Gly-Xaa-Yaa triplets. The Xaa

and Yaa residues are exposed to the surface of the collagen triple helix to be available for binding to organic crosslinkers and metallic species [6]. Amongst the amino acid residues, only Asp and Glu have carboxyl (–COOH) groups in the side chains that turn into negatively charged carboxylate (–COO⁻) groups when pH suits. The Cr(III) complex ion can covalently bind to collagen through these –COO⁻ groups forming Cr–O bonds (Figure 3.1) [170], while later studies proposed the deposited Cr(III) species which could be electrostatically bound in the collagen matrix [74, 173, 174]. However, the underlying mechanism for Cr(III) to alter its binding mode in the collagen matrix is yet to be understood.
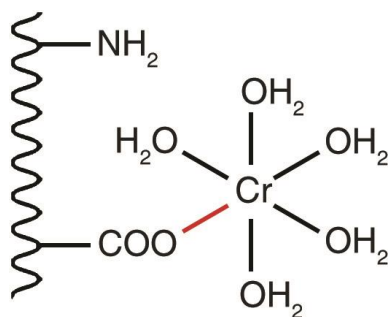
Figure 3.1: Proposed binding of Cr(III) aquo complex with collagen Asp or Glu side chain –COO⁻ group.

If one refers to the literature regarding Cr(III)-related health concerns (e.g., allergic contact dermatitis) [75], it is not hard to find presumptions about chromium species leaching out from the collagen matrix of chrome-tanned leather. While the concerns remain growing, the development of chrome tanning technologies has mostly focused on aspects such as increases in thermal stability, mechanical strength and production turnover [73]. An in-depth study revealing the mechanism of Cr(III) binding to collagen can bridge the gap and benefit both chemistry and health-related research activities.

In this study, the effect of Cr(III) is investigated with consideration of the role of anions and pH on collagen structure. Collagen fibres are treated with chromium sulfate (CS), chromium chloride (CC) and sodium sulfate (SS) at pH = 2.5 and pH = 4.5 for the different availability of the deprotonated form of –COO⁻ groups in collagen. The changes in the hierarchical collagen structure are monitored using SAXS for the intermolecular structure, DSC for the thermal stability, and SERS for probing the secondary structure and the chemical binding of the amino acid residues.

3.2 Experimental Details

3.2.1 Preparation of Collagen Samples

Bovine skins were acquired from a local tannery at the "pickled" stage; skins were soaked in a "pickling"[9] solution at pH = 2.5–3.0, containing HCl and also NaCl to prevent the skins from swelling in acid[10] [73]. The skins were cut into small pieces, air-dried, then ground into fine bovine collagen fibres and collected through a 20-mesh lab sieve.

In each glass vial, dry collagen fibres were weighed at 0.3 g and treated as follows:

(1) Coll-4.5: Dry collagen fibres were rehydrated using 0.6 mL of 0.1 M NaOH. The pH of the sample was 4.0–4.5.

(2) Coll-4.5-CS-x: Dry collagen fibres were rehydrated using 1.2 mL of 0.1 M NaOH, followed by adding chromium sulfate powder to achieve the final Cr concentrations at 29, 86, 171, and 285 in a unit of [mol Cr/mol Coll]. The suffix x indicates the concentration multipliers, $x = 1, 3, 6$, and 10, respectively; same for other chromium-containing samples below. The pH of each sample was 4.0–4.5.

(3) Coll-4.5-CC-x: The procedures were the same as Coll-4.5-CS but replaced chromium sulfate with chromium chloride.

(4) Coll-4.5-SS-x: Rehydrated Coll-4.5 were mixed with Na_2SO_4 at a series of concentrations at 44, 129, 257, and 428 in a unit of [mol SO_4^{2-}/mol Coll] to match the amount of SO_4^{2-} in Coll-4.5-CS. The final pH of each sample was 4.0–4.5.

(5) Coll-2.5: Dry collagen fibres were rehydrated using 0.6 mL of 2.5 M NaCl. The pH of the sample was 2.0–2.5.

(6) Coll-2.5-CS-x: Chromium sulfate powder was weighed and added into rehydrated Coll-2.5 to achieve the final Cr concentrations at 29, 86, 171, and 285. The pH of each sample was 2.0–2.5.

(7) Coll-2.5-CC-x: The procedures were the same as Coll-2.5-CS but replaced chromium sulfate with chromium chloride.

Chemicals:
Chromium sulfate $((Cr(OH)SO_4)_x \cdot (Na_2SO_4)_y \cdot zH_2O)$, 33% basicity, 25% Cr_2O_3 equivalent, LANXESS, Germany;
Chromium chloride hexahydrate $(CrCl_3 \cdot 6H_2O)$, Sigma-Aldrich, USA;
Sodium sulfate (Na_2SO_4), Clark Products Ltd., New Zealand;

---

[9] "Pickling" is an important step during the leather processing for preserving the skins for transport and facilitating the widely used chrome tanning (which usually starts from an acidic pH).

[10] Macroscopic swelling occurs when the pH of the skin is far from the isoelectric point (pI), thereby leading to internal repulsive forces between the collagen molecules that expand the collagen fibres. Swelling is also observed when the skin is strongly basic. However, acid swelling can be suppressed using salt such as NaCl at higher than 1 M.

Sodium chloride (NaCl), Dominion Salt Ltd., New Zealand;

Sodium hydroxide (NaOH), Sigma-Aldrich, USA.

3.2.2 Synchrotron SAXS Measurements

The SAXS measurements were performed on TLS beamline BL23A1 at the NSRRC in Hsinchu, Taiwan (ROC). Collagen samples were loaded into sample cells of size 5 mm × 5 mm × 2 mm (L × W × H) and sealed between polyimide films to prevent dehydration. The samples were kept at around 25 °C and were exposed to X-ray at an energy of 15 keV for 30 s. Scattered radiation was collected using a Pilatus 1 M detector at a distance of 2.602 m from the sample, covering a q range from 0.08 nm^{-1} to 5.2 nm^{-1}. The SAXS profiles of the collagen samples were presented as $I(q)$ versus q plots. The diffraction peaks were fitted for the peak areas for calculating the 5th to 3rd peak area ratios ($R_{5/3}$).

3.2.3 DSC Measurements

The DSC measurements were carried out using the Q2000 DSC (TA Instruments). The as-prepared hydrated collagen samples were encapsulated in hermetically sealed Tzero aluminium pans and measured over a temperature range of 20 °C to 120 °C under N_2 purge at a heating rate of 5 °C/min. The onset temperature of each thermogram was calculated to represent the denaturation temperature of collagen (T_d).

3.2.4 Synthesis of AgNPs

Wan's stepwise seeded growth method [175] was used to synthesise citrate-capped AgNPs. The initial seeds were reduced using $NaBH_4$ and capped using Na_3Cit, while the growths were reduced and capped using Na_3Cit.

(1) Initial seeds: A mixture of 20 mL of 1% (w/v) $Na_3Cit·2H_2O$ and 75 mL of DI water was heated to 70 °C for 15 min, followed by the successive addition of 1.7 mL of 1% (w/v) $AgNO_3$ and 2 mL of freshly prepared 0.1% (w/v) $NaBH_4$. A slight decrease in temperature was observed for less than 1 min before it was rebalanced. The reaction mixture was vigorously stirred at 70 °C for 1 h and cooled down to room temperature. The mixture was topped up with DI water to 100 g. The resulting solution was used as the initial seeds for the following growths.

(2) First growth: To 75 mL of DI water was added 2 mL of 1% (w/v) $Na_3Cit·2H_2O$, and the mixture was boiled for 15 min. To the boiling mixture, 10 mL of the initial seeds and 1.7 mL of 1% (w/v) $AgNO_3$ were added successively. The mixture was then refluxed under vigorous stirring for 1 h. After that, another 2 mL of 1% (w/v) $Na_3Cit·2H_2O$ and 1.7 mL of 1% (w/v) $AgNO_3$ were sequentially added, and the boiling mixture was kept vigorously stirred for another 1 h before being cooled down to room temperature and topped up to 100 g. The resulting solution was used as the secondary seeds for further growth.

(3) Second growth: A mixture of 2 mL of 1% (w/v) $Na_3Cit·2H_2O$ and 80 mL of DI water was heated to 80 °C for 15 min, followed by the consecutive additions of 10 mL of secondary

seeds and 1.7 mL of 1% (w/v) AgNO$_3$. The mixture was kept at 80 °C for 2 h under vigorous stirring before being cooled down to room temperature. The as-prepared AgNPs were stored at 4 °C before being used in SERS experiments.

In addition, Solomon's dropwise addition method [176] was followed to synthesise borohydride-capped b-AgNPs (prefix "b" for borohydride) to rule out the potential interference from the citrate species. Under vigorous stirring in an ice-water bath, 10 mL of 1.0 mM AgNO$_3$ was added dropwise (one drop per second) to 30 mL of 2.0 mM NaBH$_4$ freshly dissolved in 1 mM NaOH. After 5 min, the reaction was stopped, and the b-AgNPs were stored at 4 °C before being used in SERS experiments.

Chemicals:

Silver nitrate (AgNO$_3$), Pure Science Ltd., New Zealand;

Trisodium citrate dihydrate (Na$_3$C$_6$H$_5$O$_7$·2H$_2$O or Na$_3$Cit·2H$_2$O), Sigma-Aldrich, USA;

Sodium borohydride (NaBH$_4$), Sigma-Aldrich, USA;

Sodium hydroxide (NaOH), Sigma-Aldrich, USA.

3.2.5 UV-Vis Spectroscopy Measurements

AgNPs were measured for the extinction optical densities (OD) using the Cloudspec (Marama Labs), covering wavelengths from 300 nm to 800 nm. Proper dilution using DI water was performed to achieve an extinction OD from 0.3 to 1.0. DI water was used as the reference for background subtraction.

3.2.6 TEM Imaging

AgNPs were centrifuged and washed using DI water and sonicated for 30 s before being cast onto a formvar/carbon-coated copper grid (200mesh, ProSciTech, Australia). Images were acquired using the JEOL-2100F (JEOL) electron microscope operated at 200 kV.

3.2.7 Raman and SERS Measurements

The Raman and SERS experiments were carried out using the LabRam HR spectrometer (Horiba-Jobin Yvon) in the Raman Lab at VUW. The laser wavelength was 514 nm, delivered to the sample through an LM Plan FI Olympus air objective ($\times$50, NA = 0.50). The power exiting the objective was approximately 10 mW.

Hydrated collagen samples were placed on a glass plate for Raman measurements. For SERS, around 0.1 mL of AgNPs were loaded onto the sample within 10 min before the measurements. The laser was focused on the air/solid interface of the rehydrated collagen samples. The exposure time was typically 5 s, and five to ten such exposures were collected for each spectrum. A polynomial baseline correction was done to remove the featureless background from AgNPs in the range of interest and the fluorescence of collagen. Note that the Raman/SERS spectra in this study were not refined using the flat-field correction method while presenting sufficiently high signal-to-noise ratios.

3.3 Results and Discussion

3.3.1 SAXS Profiles

A typical SAXS profile of collagen in bovine skin is shown in Figure 3.2, resolving a series of diffraction peaks from the 1st order (centred at around 0.1 nm^{-1}) to the 9th order (centred at around 0.86 nm^{-1}). Diffraction peaks of higher orders than the 9th are poorly resolved as expected from collagen in skins as opposed to the highly uniaxially arranged collagen molecules in tendons [47].

Compared with Coll-2.5, the raw peak intensities diminish when collagen is treated with chromium chloride at the highest concentration (Coll-2.5-CC-10); such a phenomenon is also observed but is less significant when replacing Cl^- with SO_4^{2-} (Coll-2.5-CS-10) (Figure 3.2). The partially basified Coll-4.5 also shows distinct collagen diffraction peaks, with the 2nd order peak weaker than Coll-2.5 (Figure 3.3). The raw peak intensities also fluctuate upon treatments using chromium salts.
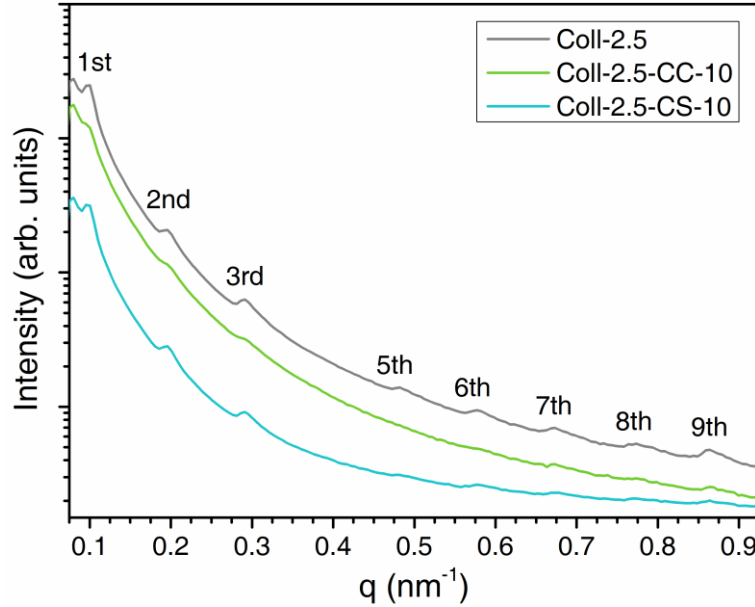
Figure 3.2: Stacked SAXS profiles of Coll-2.5, Coll-2.5-CC-10 and Coll-2.5-CS-10 in the q range from 0.075 nm^{-1} to 0.925 nm^{-1}. Resolvable peaks are denoted according to the peak orders.
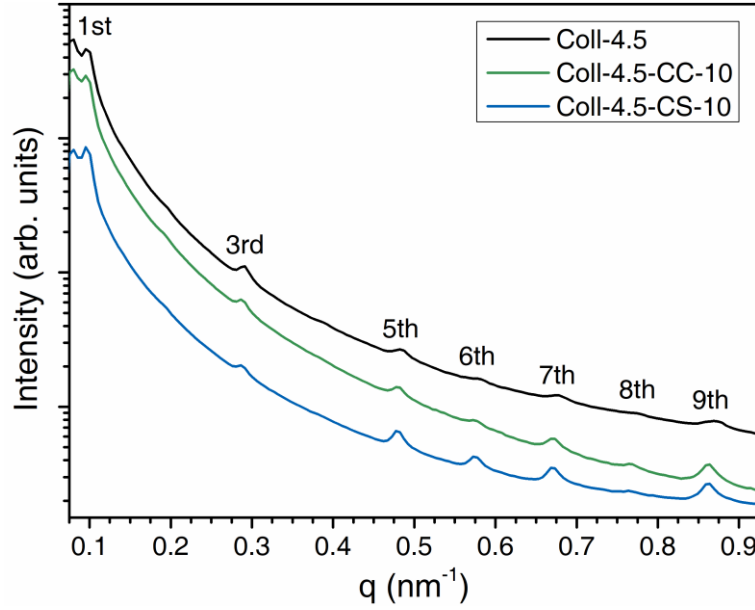
Figure 3.3: Stacked SAXS profiles of Coll-4.5, Coll-4.5-CC-10 and Coll-4.5-CS-10 in the q range from 0.075 nm^{-1} to 0.925 nm^{-1}. Resolvable peaks are denoted according to the peak orders.

Indeed, the changes in raw peak intensities are linked to the altered electron density contrast of collagen in skin fibrils to the surrounding aqueous solution. The X-ray scattering length (a parameter related to the scattering amplitude) of light elements in proteins (commonly H, C, N, O, and S) is lower than that of metallic elements with higher atomic numbers; in our case, chromium [177]. Therefore, if Cr(III) binds to collagen in a site-specific manner, it can contribute to the diffraction peak intensities. Instead, Cr(III) that are not bound to collagen in a regular pattern could only increase the contrast of the background (negligible at low concentrations but should be kept in mind regardless). Such phenomena can be considered in analogy with the positive and negative staining for TEM imaging [178].

However, it is noteworthy that apart from Cr(III), more factors could affect the raw peak intensities and the overall scattering background intensity because the experiment was neither performed *in situ* on the same piece of tissue (as in Ref. [76]) nor in a homogenous solution. The fact that the collagen molecules are "fixed" in individual fibres (that are not intrinsically identical) leads to inevitable variations in the amount of collagen along the beam path (since samples were loaded manually), thereby altering the raw scattering intensity acquired from collagen. For the same reason, the variations in the D-period shall not be overinterpreted in this study; a brief of fitting results are shown in Table 3.1 to highlight the random variations.

Nevertheless, the variations above can be largely ruled out by calculating the relative peak intensities, *i.e.*, the ratio of the fitted peak areas at different orders acquirable from each scattering profile, reflecting collagen intermolecular arrangement regardless of the volume of collagen molecules along the beam path.

Table 3.1: D-period values acquired by fitting the centre of the peaks at orders from the 3rd to the 9th (fitting errors shown).

Sample	D-period (nm)
Coll-2.5	64.63 ± 0.02
Coll-2.5-CC-10	64.82 ± 0.09
Coll-2.5-CS-10	63.79 ± 0.03
Coll-4.5	64.81 ± 0.01
Coll-4.5-CC-10	65.40 ± 0.01
Coll-4.5-CS-10	65.45 ± 0.01

Figure 3.4 shows the SAXS profiles of collagen samples in the full concentration series to highlight the changes in relative peak intensities at different pH, anions and Cr concentrations. For Coll-4.5-CS, with increasing Cr(III) concentrations, noticeable decreases in the 3rd order peak intensity are observed alongside the increases in the 5th to the 9th order peaks. Instead, unchanged peak intensities are found in Coll-2.5-CS at all concentrations. According to the pKa of Asp (3.8) and Glu (4.2), we can estimate the proportion of the –COO⁻ groups in the collagen. At pH = 4.5, the deprotonated percentage $[COO^-]/([COOH] + [COO^-])$ is estimated to be 65%, allowing the binding of Cr(III) to collagen via coordinative covalent bonds [73]. However, at pH = 2.5, the number is merely 3%, resulting in a much lower binding propensity of Cr(III) to affect the collagen structure.

However, comparing Coll-4.5-CS with Coll-4.5-CC, the latter shows no significant changes in relative peak intensities at all Cr concentrations, similar to Coll-2.5-CS. Moreover, an additional set of experiments using Na_2SO_4 confirm the unchanged SAXS profiles when Cr^{3+} is absent, ruling out the direct contribution to the SAXS intensities from solely the SO_4^{2-} anion.

Hence, we could conclude that Cr(III) in the presence of Cl^- does not perform binding in the same manner as in the presence of SO_4^{2-}; in the former case, it is more than likely non-covalent. Cr(III) in a dilute aqueous solution without stronger ligands than H_2O tends to exist in the form of a solvated aquo complex, $Cr(H_2O)_6^{3+}$. This positively charged complex ion may attach to the –COO⁻ groups in collagen via electrostatic forces; this mechanism is also favoured with the abundant –COO⁻ groups at pH = 4.5. Such electrostatic interaction is, in principle, also site-specific as the covalent mechanism but easily disruptable by other cations in the solution (*e.g.*, Na^+), leading to a randomised positioning of the $Cr(H_2O)_6^{3+}$ in the collagen matrix and the unchanged diffraction peak intensities in Coll-4.5-CC.
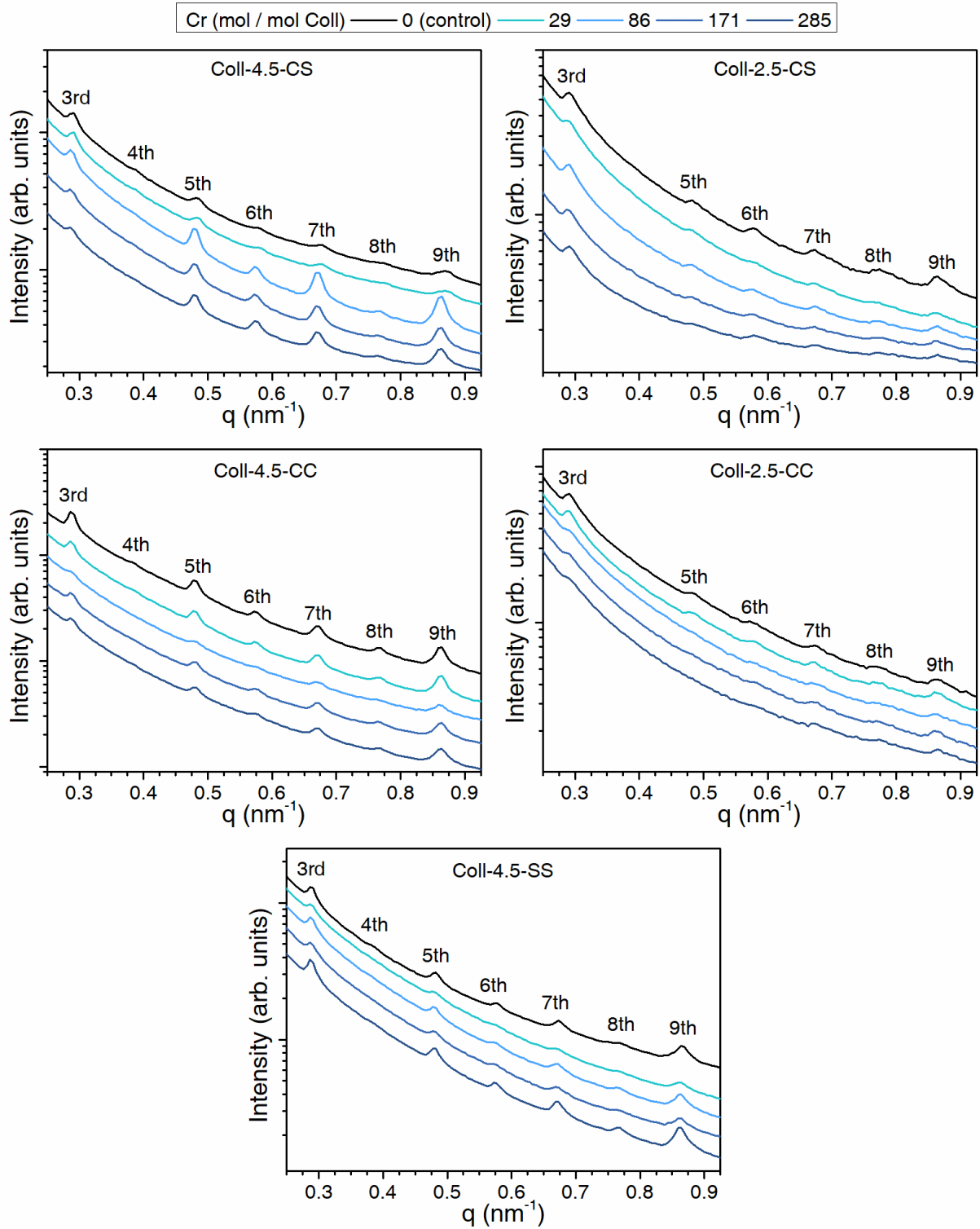
Figure 3.4: Stacked SAXS profiles of Coll-4.5-CS, Coll-2.5-CS, Coll-4.5-CC, Coll-2.5-CC, and Coll-4.5-SS, in the q range from 0.25 nm^{-1} to 0.925 nm^{-1}. Resolvable peaks are denoted according to the peak orders.

However, the question remains: why would altering the anion from SO$_4^{2-}$ to Cl$^-$ cause the differences in the Cr(III) binding mechanism? One could refer to the renowned Hofmeister series of ions for a plausible explanation (extensive knowledge of this series can be found in

Ref. [179, 180]). The anion series has Cl⁻ as the middle point, and the anions to its left (including SO_4^{2-}) are referred to as "kosmotropes", while those to the right are called "chaotropes" (Figure 3.5). The original view of this series is embedded in the naming: the term "kosmos" means "order". Hofmeister proposed that kosmotropic anions such as SO_4^{2-} can form hydrogen bonds with water molecules to "make ordered water structures" and "steal" water from the solute. Such bonding propensity results in the salting-out effect on proteins and macromolecules. Note that the anions do not alter the bulk water properties but only influence the direct vicinity (or the first hydration shell water molecules).

In our case, the high kosmotropicity of the SO_4^{2-} anion may counteract the formation of fully coordinated aquo complex $Cr(H_2O)_6^{3+}$ in the vicinity of the collagen molecules, increasing the availability of under-coordinated Cr cores to bind to ligands (–COO⁻ groups) in collagen. In contrast, Cl⁻ is more chaotropic and thus less solvated than SO_4^{2-}, leading to an increase in the proportion of water favouring the formation of $Cr(H_2O)_6^{3+}$ [181, 182]. As a result, the electrostatic interactions of Cr(III) with collagen increase and the amount of its coordinate covalent bonds with –COO⁻ groups decreases at the equilibrium.
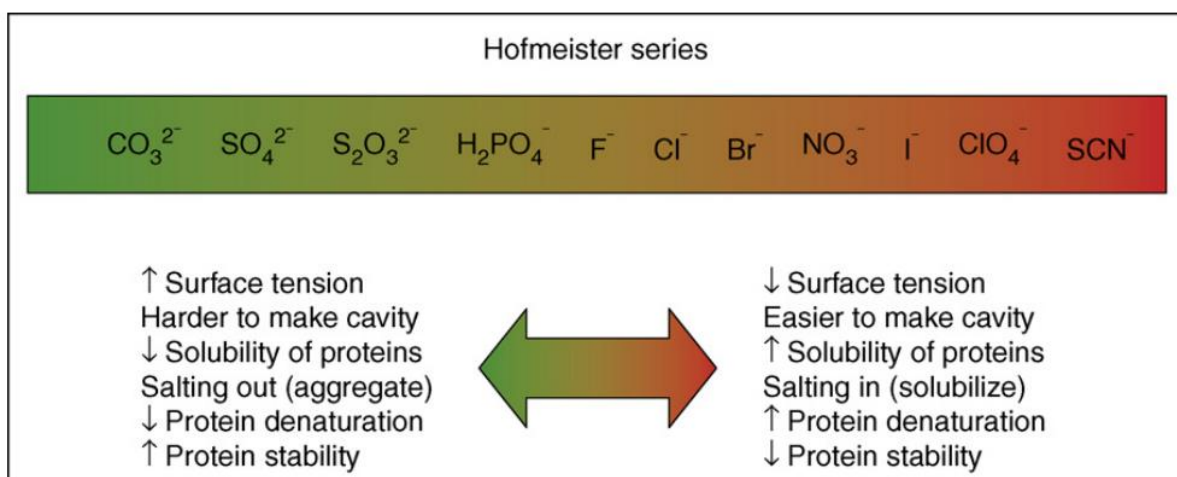
Figure 3.5: The Hofmeister series. (Reprinted from Ref. [179] with permission from Elsevier.)

The anion-regulated mechanism is further highlighted by calculating the relative intensity of the 5th to the 3rd order peak ($R_{5/3}$, Figure 3.6). The two peaks are chosen based on the established knowledge in previous studies. Generally speaking, lower ordered peaks are stronger and can lead to more reliable results. In addition, several studies have shown that even order peaks (6th in particular) are significantly affected by the hydration level of collagen [45, 95, 96], thus not suitable for analysing collagen gone through a drying-rewetting cycle; even if the collagen fibre is "fully" rehydrated after drying, some irreversible structural change will remain in place [183].

The calculation reveals a clear increasing trend in $R_{5/3}$ with the concentration of chromium sulfate, whereas lacking either Cr (as in Coll-4.5-SS), SO_4^{2-} anion (as in Coll-4.5-CC), or a

suitable pH (as in acidic Coll-2.5-CS or Coll-2.5-CC) would not favour the changes, indicating the lack of site-specific (covalent) binding of Cr(III) to collagen.
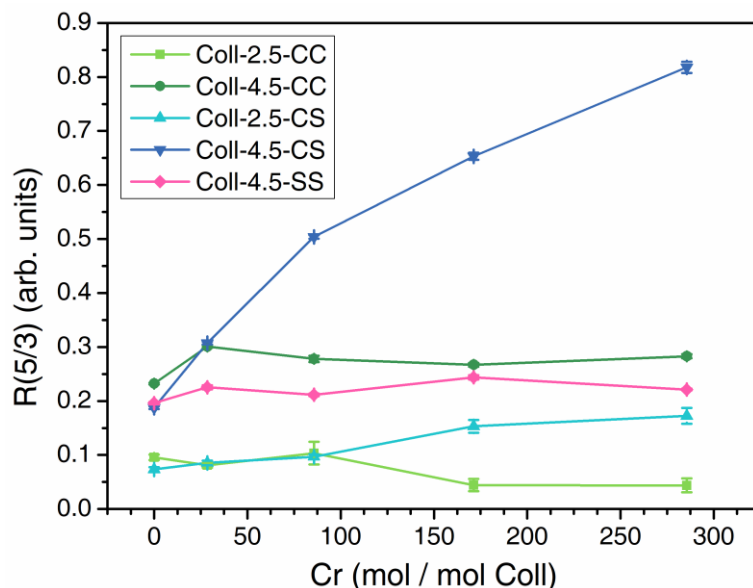
Figure 3.6: Relative peak intensity of the 5th to the 3rd order ($R_{5/3}$) (fitting errors shown) of Coll-4.5-CS, Coll-2.5-CS, Coll-4.5-CC, Coll-2.5-CC, and Coll-4.5-SS. The Cr concentration of Coll-4.5-CS, Coll-2.5-CS, Coll-4.5-CC, and Coll-2.5-CC are displayed as is. The concentrations of Na_2SO_4 in Coll-4.5-SS are converted to the equivalent Cr concentrations by matching the SO_4^{2-} concentrations in Coll-4.5-CS.

3.3.2 Thermal Stability

It is well-known amongst leather makers that chrome tanning provides high thermal stability to the leather [6], while the mechanism is not yet fully explained. The covalent binding of Cr(III) via $-COO^-$ groups, the complexing of Cr(III) with anions (the "link-lock" theory [73]) and the electrostatic interactions and hydrogen bonding could all contribute to the thermal stability of collagen to a various degree.

A series of representative DSC thermograms are displayed in Figure 3.7. It is not surprising to observe a gradual increase in the denaturation temperature (T_d) from 55–60 °C in native collagen fibres to as high as 100 °C with the increasing chromium sulfate concentration; high T_d at 100 °C is commonly observed in excessively chrome-tanned leathers [74].
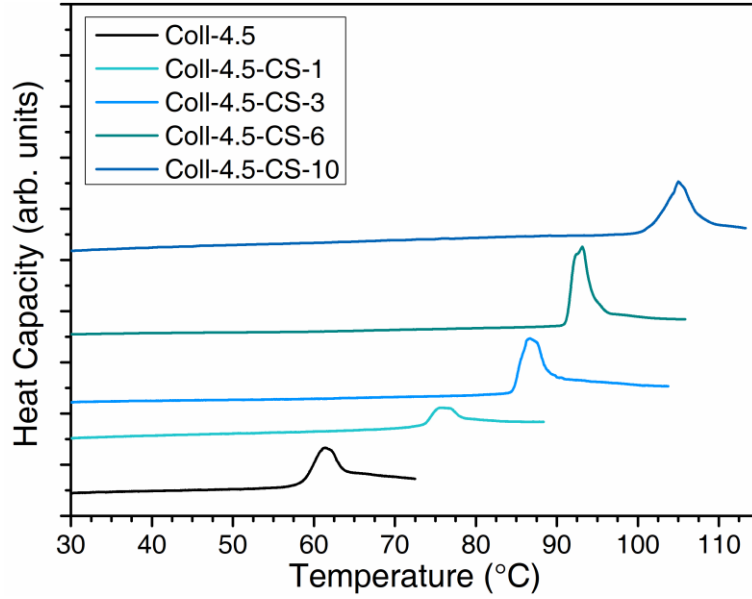
Figure 3.7: Stacked DSC thermograms of Coll-4.5 and Coll-4.5-CS-x ($x = 1, 3, 6, 10$).

However, through a similar investigation by replacing chromium sulfate with other salts, we observe much lower T_d at equivalent Cr or SO_4^{2-} concentrations (Figure 3.8). With Cl^- replacing SO_4^{2-} (Coll-4.5-CC), the collagen samples at all Cr concentrations present a maximum T_d at around only 80 °C. When no Cr(III) is involved (Coll-4.5-SS), a lower T_d of 70 °C is observed. At pH = 2.5 (Coll-2.5-CS or Coll-2.5-CC), collagen samples give medium T_d values between 70 °C and 80 °C.

It is worth noting that the T_d values of our collagen samples match the prediction based on the link-lock tanning theory proposed by Covington [73], but when combined with the SAXS results, the results strongly support the anion-regulated mechanism while conflicting with the link-lock mechanism (which was derived almost solely from thermal data). In the case of chromium sulfate, "linking" may refer to the binding of Cr(III) to collagen, while "locking" may refer to the hydrogen bonding or complexing of SO_4^{2-} with Cr(III) to form a so-called "crosslink". Hence, the "linking" should occur as a separate event regardless of the "locking" reagent. However, our SAXS results indicate the lack of covalent Cr(III)–OOC bonds in Coll-4.5-CC, rejecting the initial "linking" in this scenario. Also, the DSC results show similar T_d from Coll-4.5-CC compared to Coll-2.5-CC; the latter has the same Cl^- anion but a low pH that disfavours the "linking". A similar comparison can be carried out between Coll-4.5-CC and Coll-2.5-CS to achieve the same conclusion.

Therefore, considering the high T_d in Coll-4.5-CS and the minor increases in T_d by Na_2SO_4 in Coll-4.5-SS, the increases in T_d of the rest three series can be attributed to the dominant electrostatic interactions of $Cr(H_2O)_6^{3+}$ and Cl^- or SO_4^{2-} with collagen, possibly in addition to minor covalent binding interactions of Cr(III) with collagen.
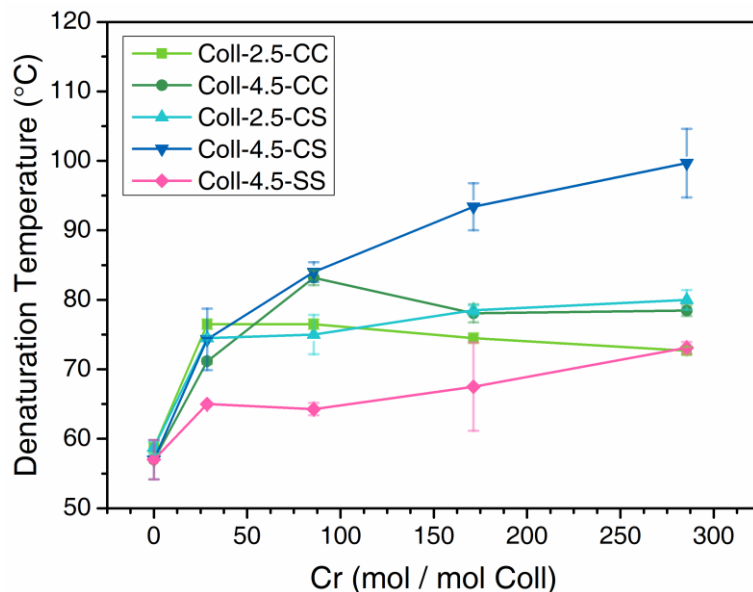
Figure 3.8: T_d of collagen at different Cr or SO_4^{2-} concentrations in Coll-2.5-CS, Coll-2.5-CC, Coll-4.5-CS, Coll-4.5-CC, and Coll-4.5-SS. Error bars represent the standard deviations of the replicates. The Cr concentration of Coll-4.5-CS, Coll-2.5-CS, Coll-4.5-CC, and Coll-2.5-CC are displayed as is. The concentrations of Na_2SO_4 in Coll-4.5-SS were converted to the equivalent Cr concentrations by matching the SO_4^{2-} concentrations in Coll-4.5-CS.

3.3.3 Raman Spectra

The Raman spectroscopy measurements were first conducted under non-SERS conditions. As expected, we observe characteristic Raman spectra from the native collagen samples to compare with the samples with chromium sulfate (Figure 3.9). The peaks are listed and assigned in Table 3.2, including the strong amide I and amide III peaks, the aliphatic CH_2 peak, and the C–C bond-related peaks originating from the collagen backbone or the aliphatic and aromatic rings in Pro, Hyp, Phe, and Tyr. The spectra of Coll-4.5-CS are almost identical to Coll-4.5, apart from the peak at 980 cm^{-1} attributed to the symmetrical stretching of the SO_4^{2-} group. The unchanged amide peaks confirm our previous observations in FT-IR on chrome-tanned leathers [94], indicating that the binding of Cr(III) to the amino acid side chains only subtly changes the collagen secondary structure. These negative findings also highlight the limitation of the non-enhanced Raman spectroscopy in resolving site-specific changes in collagen structure.
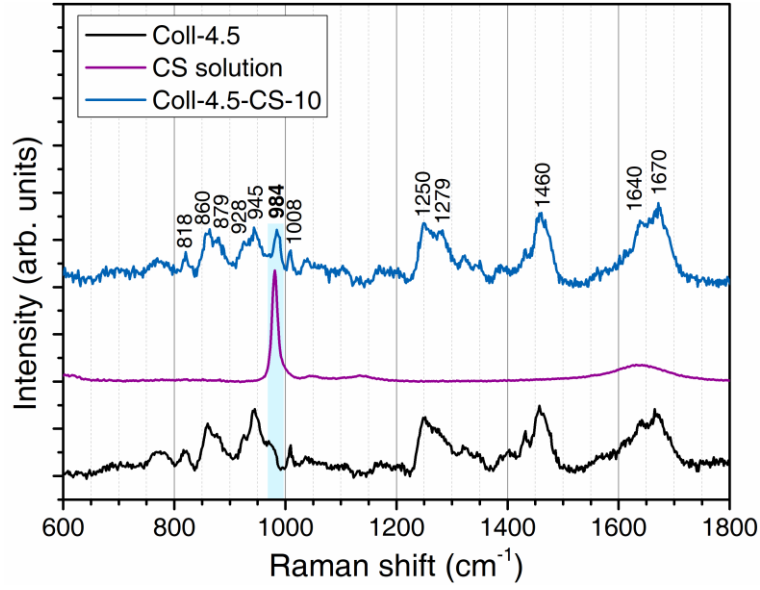
Figure 3.9: Stacked Raman spectra of Coll-4.5, Coll-4.5-CS-10 and a chromium sulfate (CS) solution as a reference.

Table 3.2: Raman peak assignments of Coll-4.5 and Coll-4.5-CS-10. General notations refer to Appendix A.

Raman shift (cm^{-1})	Assignments	References (cm^{-1})
1670	Amide I; [86]	1670; [86]
	Amide I (β-sheet); [103]	1675; [103]
	Amide I (α-helix; β-sheet); [111]	1666–1668; [111]
1640sh	Amide I; [86]	1642; [86]
	Amide I (3_{10}-helix); [103]	1632; [103]
1460	δ(CH$_2$); δ(CH$_3$); [86]	1451–1464; [86]
1279	Amide III; [86]	1271; [86]
	Amide III; *ν_3, Phe; ν_3, Tyr; [103]	1265–1285; [103]
	Amide III, δ(N–H); [109]	1269; [109]
	Amide III, α-helix; [184]	1260–1270; [184]
1250	Amide III; [86]	1248; [86]
	Amide III; Tyr; [103]	1235–1245; [103]
	Amide III, ν(C–N); [109]	1251; [109]
	Amide III, random coil; [184]	1230–1240; [184]
1008	Phe; [86]	1006; [86]
	ν_{12}, Phe; [103]	995; [103]
	ν(C–C), Phe ring; [109]	1001; [109]
984**	ν_1, SO$_4^{2-}$; [185]	980; [185]
945	ν(C–C), backbone; [86]	938; [86]
	ν(C–COO$^-$); ν_{17a}, Phe; ν_{17a}, Tyr; [103]	940–945; [103]
	ν(C–C), α-helix; [109]	934; [109]
928sh	ν(C–C), Pro ring; [86]	921; [86]
879	ν(C–C), Hyp ring; [86]	876; [86]

| 860 | ν(C–C), Pro ring; [86] | 856; [86] |
| 818 | ν(C–C), backbone; [86] | 821; [86] |

*: Wilson's notation for modes of benzene ring vibration [112], same below;

**: Not observed in Coll-4.5.

3.3.4 SERS using AgNPs

To resolve the subtle changes in the side chains of the amino acid residues in collagen affected by Cr(III), we attempt to conduct SERS measurements on collagen fibres. Inspired by the pioneering SERS study by Gullekson *et al.* on dry collagen fibrils [103], we designed a simple approach for measuring SERS on wet collagen samples. The approach involves drop-casting AgNPs onto the collagen samples to achieve an *in situ* aggregation to coat the collagen fibres, though not until our later study was conducted (to be elaborated in Chapter 4) did we fully understand the mechanism behind this successful attempt.

The UV-Vis spectra and the TEM images of AgNPs confirm the spherical morphology and the monodispersity (Figure 3.10). The UV-Vis spectra peak sits at 417 nm, and the average size of AgNPs is around 45 nm, largely matching the referenced method [175]. The solution has a neutral pH, thus not significantly affecting the pH of the samples.
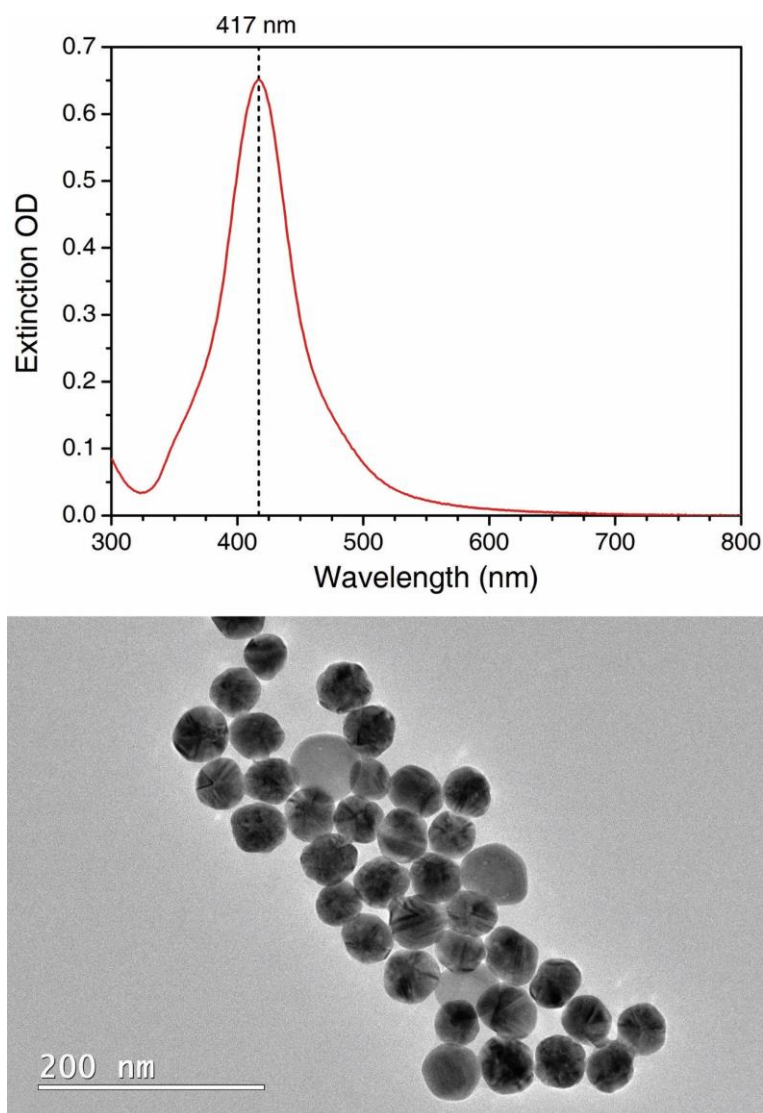
Figure 3.10: A representative UV-Vis extinction spectrum (dilution factor $= 10$) and a TEM image of the AgNPs following the seeded growth method.

Darkening of the colour is observed as a 0.1 mL drop of AgNPs is added to the collagen fibres, which could be recognised as a sign of aggregation of AgNPs. However, the distribution of AgNPs remains inhomogeneous; therefore, efforts are required to identify steady focusing spots and capture the SERS spectra. Applying a more concentrated AgNPs colloid would facilitate this process.

When the exciting laser hits the amino acid side chains in the vicinity of the surface of the AgNPs, the SERS signals from the corresponding functional groups can be observed. Figure 3.11 shows a collection of SERS spectra from collagen samples treated with chromium sulfate. From non-SERS to SERS, a series of extra features from specific amino acid groups are resolved, including but not limited to:

89

(1) The strongest peak at 1389 cm^{-1}, the adjacent small peak at 1424 cm^{-1}, and a shoulder at 1560sh cm^{-1} related to the –COO$^-$ and –COOH groups in Asp and Glu residues, which are assigned to $\nu_s(COO^-)$, $\delta(C–OH)$, and $\nu_{as}(COO^-)$, respectively;

(2) Two distinct peaks at 1586 cm^{-1} and 1494 cm^{-1}, in addition to the 1005 cm^{-1} peak, are attributed to the aromatic ring breathing C–C stretching modes of Phe or Tyr residues.
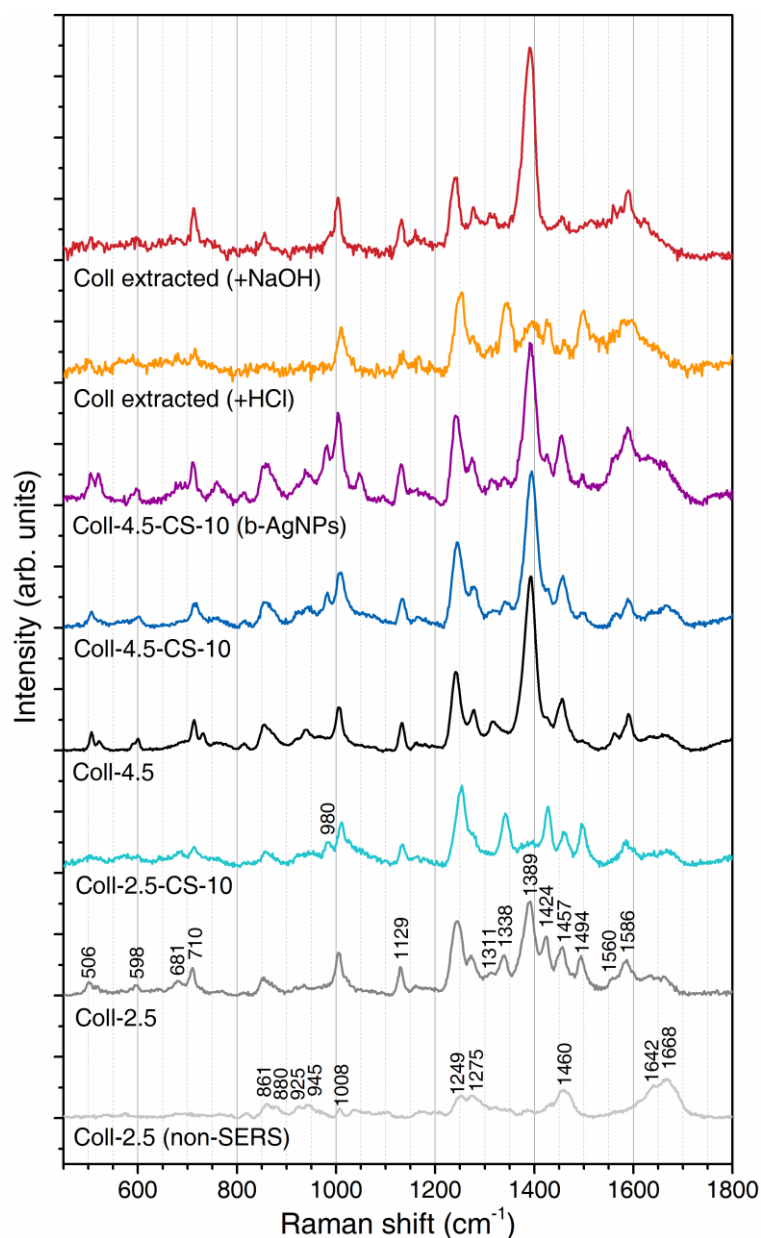
Figure 3.11: Stacked SERS spectra of Coll-2.5, Coll-2.5-CS, Coll-4.5, Coll-4.5-CS, and Coll-4.5-CS collected using borohydride-reduced b-AgNPs, as well as a non-SERS reference of Coll-2.5. Cr concentration = 285 mol/mol Coll. Lyophilised pure collagen sponges (extracted from bovine skins) were also measured using AgNPs at acidified and partially basified conditions.

Detailed peak assignments are listed in Table 3.3. Note that the potential signals from citrate species capping on the surface of the AgNPs are ruled out by the highly consistent SERS

spectrum of collagen enhanced by citrate-free, borohydride-reduced b-AgNPs. Similarly, one can acquire comparable features when replacing the collagen fibres in bovine skins with pure collagen extracted from bovine skins, confirming the origin of the enhanced peaks.

Table 3.3: Raman and SERS peak assignments of Coll-2.5. General notations refer to Appendix A.

Raman shift (cm^{-1})		Assignments	References (cm^{-1})
Raman	SERS		
1668	1662	Amide I; [86] Amide I (β-sheet); [103] Amide I (α-helix; β-sheet); [111]	1670; [86] 1675; [103] 1666–1668; [111]
1642sh	1637	Amide I; [86] Amide I (3_{10}-helix); [103]	1642; [86] 1632; [103]
	1586	ν_{8b}, Phe; ν_{8b}, Tyr; $\nu_{as}(COO^-)$; [103] ν(C–C), Phe ring; [107]	1585; [103] 1580–1585; [107]
	1560sh	Amide II; [103] $\nu_{as}(COO^-)$; [186]	1585; [103] 1562; [186]
	1494	ν_{19a}, Phe; ν_{19a}, Tyr; [103] $\delta(CH_3)$; [104]	1485–1515; [103] 1495; [104]
1460	1457	$\delta(CH_2)$; $\delta(CH_3)$; [86]	1451–1464; [86]
	1424	$\nu_s(COO^-)$; [86] δ(C–OH) in –COOH; [108]	1422; [86] 1415; [108]
	1389	$\nu_s(COO^-)$; [103]	1405-1410; [103]
	1338	$\omega(CH_2)$; $\omega(CH_3)$; [86] $\delta_s(CH_2)$; [109]	1343; [86] 1340; [109]
	1311w	$\tau(CH_2)$; $\tau(CH_3)$; [86]	1314; [86]
1275	1273	Amide III; [86] Amide III; *ν_3, Phe; ν_3, Tyr; [103] Amide III, δ(N–H); [109] Amide III, α-helix; [184]	1271; [86] 1265–1285; [103] 1269; [109] 1260–1270; [184]
1249	1246	Amide III; [86] Amide III; Tyr; [103] Amide III, ν(C–N); [109] Amide III, random coil; [184]	1248; [86] 1235–1245; [103] 1251; [109] 1230–1240; [184]
	1129	$\delta(NH_3^+)$; [107] $\rho(NH_3^+)$; $\rho(CH_3)$; [187]	1136–1143; [107] 1125–1128; [187]
1008	1005	Phe; [86] ν_{12}, Phe; [103] ν(C–C), Phe ring; [109]	1006; [86] 995; [103] 1001; [109]
945	935vw	ν(C–C), backbone; [86] ν(C–COO$^-$); ν_{17a}, Phe; ν_{17a}, Tyr; [103] ν(C–C), α-helix; [109]	938; [86] 940–945; [103] 934; [109]
925	920vw	ν(C–C), Pro ring; [86] ν(C–C); [102]	921; [86] 923; [102]
880		ν(C–C), Hyp ring; [86]	876; [86]

861	855	ν(C–C), Pro ring; [86]	856; [86]
		ν_s(COC); [109]	862; [109]
		Tyr; [102]	857; [102]
818	814vw	ν(C–C), backbone; [86]	821; [86]
		δ(CCN); δ(COC); [109]	810; [109]
	710	δ(COO$^-$); [107]	718–720; [107]
		ν(C–S), Met; [107]	701–703; [107]
	681	δ(COO$^-$); ω(COO$^-$); [186]	670–696; [186]
	598w	ρ(C–O), Pro; [186]	572-593; [186]
	506w	δ(C–C), backbone; [188]	506; [188]

With the SERS enhancement, we could reveal further details in the binding mechanism of Cr(III) with collagen. One of the most distinctive features is the changes in the ν_s(COO$^-$) peak at 1389 cm^{-1} corresponding to the different conditions. The change in pH from 4.5 to 2.5 (Coll-4.5 to Coll-2.5) results in the halving of the ν_s(COO$^-$) peak along with an increase in δ(C–OH) peak at 1424 cm^{-1} [103, 107, 186]. We could recall the estimated deprotonated percentage of the –COOH group at different pH: at pH = 4.5, 65% is deprotonated; at pH = 2.5, only 3% is deprotonated. Hence, the SERS intensity shows a positive but non-linear correlation with the amount of free –COO$^-$ groups.

Now considering the amount of Asp and Glu residues in collagen: in every 1000 residues (a single collagen polypeptide chain), there are 95 Asp and Glu on average, giving 62 mol of –COO$^-$ sites at pH = 4.5 [26, 73]. That converts to 186 mol –COO$^-$ sites in a collagen molecule. Therefore, when we added as high as 285 mol of Cr(III) to each mol of collagen (Coll-4.5-CS-10). It is supposed to occupy (covalently) all the –COO$^-$ groups. However, minor changes are observed in the –COO$^-$ group-related peaks (and the other peaks) comparing Coll-4.5-CS with Coll-4.5. This observation suggests that a sufficient amount of the –COO$^-$ groups in collagen remain unbound to be observed by SERS. This result indicates that, even at the favoured pH = 4.5 for covalent binding, a significant amount of electrostatically binding Cr(III) species present in the collagen matrix (possibly in the form of Cr(H$_2$O)$_6^{3+}$).

Additionally, the SERS spectra also reinforce the presence of the covalent binding mechanism at pH = 4.5. In Coll-4.5, a stronger τ(CH$_2$) peak at 1311 cm^{-1} than the ω(CH$_2$) peak at 1338 cm^{-1} is observed, while the spectra of Coll-2.5 show the opposite. The differences here may indicate that the aliphatic –CH$_2$– groups in protonated Asp and Glu (*i.e.*, covalently bound with protons) favour a conformation for AgNPs to enhance the out-of-plane wagging mode, whilst the deprotonated ones prefer the out-of-plane twisting mode to be enhanced. The pattern of Coll-4.5-CS between 1300–1400 cm^{-1} resembles that of Coll-2.5, confirming the covalent binding of collagen with Cr(III).

Besides that, the minimal covalent binding is also confirmed at pH = 2.5. Comparing Coll-2.5 with Coll-2.5-CS-10, significant decreases in the ν_s(COO$^-$) peak at around 1390 cm^{-1} and the

shoulder $\nu_{as}(COO^-)$ peak at 1560 cm^{-1} are observed when Cr(III) was introduced to the collagen matrix). Last but not least, the amide III peaks (1245 cm^{-1} and 1275 cm^{-1}) are strongly enhanced to evidence the changes in the secondary structure. Much stronger enhancements are found in the 1245 cm^{-1} peak, which seems to shift towards higher wavenumbers when covalent binding occurs at a higher degree.

3.4 Conclusion

In summary, the evidence presented in this study clarifies the long-standing doubt about how Cr(III) binds to collagen molecules in skins during chrome tanning under varying conditions, including concentrations, pH, and anions. Our findings confirm the relationship of the Cr(III) binding mechanisms with pH that protonated –COOH groups disfavour covalent binding. With regards to the anions, however, rather than rejecting the previous understandings, we suggest another crucial role of the anions: regulating the formation of covalent bonds between the Cr(III) and the collagen –COO⁻ groups.

The SO_4^{2-} anion was previously recognised as a "locking" (or bridging) component of the Cr(III) complexes by directly participating in the binding reaction. However, our results reveal that it also indirectly promotes the covalent binding to take a considerable (if not dominant) part in addition to the ever-existing electrostatic binding. With its high kosmotropicity according to the modernised Hofmeister series, SO_4^{2-} anion binds to water molecules to facilitate the formation of Cr(III)–OOC bonds and contributes directly to the thermal stability of collagen. On the contrary, the more chaotropic or neutral Cl^- anion does not perform in the above ways, leading to the limited formation of covalent bonds, resulting in low thermal stabilities of the collagen.

In whichever case above, the results emphasise that both covalent and electrostatic bindings coexist, confirming our previous observations [74] and raising the awareness of the potential leaching of Cr(III) species followed by related health concerns. It also highlights the excessive use of chromium salts during the processing of skins into leathers since the electrostatic mechanism can be achieved by many other metallic salts or polyphenolic natural products at a similar level to the $Cr(H_2O)_6^{3+}$ complex ions. Novel benign processing technologies would benefit the leather industry with an improvement in sustainability metrics both environmentally.

In addition to the implications, this is also the first application of SERS to analyse the binding mechanisms in collagen, which opens a new pathway for researchers to study chemical modifications in collagen-based biomaterials. However, as mentioned earlier, this coincidental success owes to the presence of Cl^- (the residual HCl and NaCl added during pickling) in all samples, leading to the featureless AgNPs background for the clear observation of collagen SERS signals. The mechanism behind the effects of halide anions on AgNPs-enhanced SERS will be discussed in Chapter 4.

Chapter 4   Collagen in Solution: Interference in SERS from Coadsorbed Species on AgNPs

This chapter covers the extensive investigations of the background features observed during our SERS measurements of collagen solutions using AgNPs. Rather than a pre-planned research aim, it was the needs that arose from the initial attempts that have driven the study into its current form. Our initial experimental attempts followed a recognised method in the literature [189] but revealed a set of SERS signals that cannot be explained by simple changes in the orientation of the collagen molecules attached to the AgNPs. Being alerted by these unexpected background signals, we looked into the origin of such SERS results from AgNPs and AuNPs in the literature but, surprisingly, to no avail. The interfering species have been reported but often shunned from detailed identifications. A research aim was then set to investigate these phenomena. Later, our investigations found that the background interference was inconsistent; the signals varied with the pre-treatment methods. If not explicated, the complexity of this scenario would certainly have hindered us from developing a reproducible and reliable SERS detection method for collagen.

In our study, efforts are made to unveil the unexpectedly coadsorbed[11] species on AgNPs and the variations in the binding affinities of those residual species when strong ligands such as halide anions are involved. Based on our SERS results, we proposed a mechanism to explain the variations based on the surface coverage of AgNPs by the capping ligands. Our findings provide a critical patch to the existing theory and methods of SERS analysis in colloidal solutions for proteins. It also highlights the potential pitfalls during the precise surface functionalisation of AgNPs or other plasmonic nanostructures for interfacial properties and applications.

Most of the findings in this chapter have been published in Ref. [2] and are reused with permission (Copyright (2022) American Chemical Society). The narrative is slightly rearranged to interconnect with the rest of the thesis.

4.1   Background

The colloidal solution of choice for many SERS studies is the well-known citrate-reduced Lee-Meisel's AgNPs developed over 40 years ago [190] due to the simplicity of synthesis, the near-optimal size for enhancement (50–60 nm in diameter [191]), and the suitable stability for controlled aggregation that remains in a colloidal form for a reasonably long time [192].

Around the same time, the first attempt of using halide anions (in particular, Cl⁻, Br⁻, and I⁻) to "activate" AgNPs was reported by Hildebrandt *et al.* in measuring the resonance Raman effect of the dye molecule rhodamine 6G (R6G) using SERRS (the extra "R" for resonance)

---

[11] Instead of "adsorb", the term "coadsorb" is used to highlight that the species we discuss in this study do not dominate adsorption to Ag atoms but "coadsorb" together with other major ligands (*e.g.*, halides).

[193]. The mechanism of the "activation" effects by halide anions was explained as the displacement of the original surface ligands (*i.e.*, the citrate anions), thereby allowing the adsorption of R6G onto certain "active sites" for SERS enhancement [194]. The "active sites" are, in fact, the exposed Ag atoms that allow non-specific binding to species, rather than specifically located "sites". Such an effective ligand exchange is facilitated by the stronger binding affinity of the halide anions or the thiol anions than the citrate anions on AgNPs, which is also widely recognised to form a complete coating layer over AgNPs [195-197]. However, experimental evidence contradicting this assumption is not rare, although the opinions emerging from the evidence were rather divergent, showing the lack of comprehensive understanding in this aspect [198-202]. The scattered conclusions are collected and hereby listed as follows:

(1) As an initial attempt, Huang *et al.* [198] gave a tentative assignment of the species on iodide ligand coated AuNPs to polyvinylpyrrolidone (PVP);

(2) Later, Xie *et al.* and Park *et al.* [199, 200] provided another assignment of the same SERS signals to citrate anions based on similar experiments in which they exposed AuNPs to iodide and thiols, respectively;

(3) On the contrary, Perera *et al.* [201] found that halides and thiols can readily eliminate citrate anions but leave unspecified organic cations on AuNPs;

(4) Recently, Wang *et al.* [202] observed unspecified surface anions on bromide ligand coated AgNPs interfering with the target analyte during their study on the trace detection of fentanyl.

The existing evidence is neither comprehensive nor conclusive for us to depict a mechanism of the coadsorption and the relative binding affinities of the coadsorbed species on differently coated AgNPs. A full mechanistic understanding is particularly important for bioanalytical applications, supported by the claims in an inclusive review of the state-of-the-art SERS methods for bioanalysis [91]: the substrate design of a reliable bioanalytical SERS experiment should be "uniform, clean, and anti-interference" as well as "capable of targeting the analytes of interest".

In this study, we investigate the changes in the SERS spectra, aiming to identify the coadsorbed species on citrate-reduced AgNPs when halide ligand exchanges occur. The SERS technique is extremely sensitive for us to acquire information from a trace amount of residual species, yet it could be a double-edged sword which makes it hard to verify the results using a complementary technique. The results strongly suggest the determinative roles of the halide ligands on the binding affinity of the species, which leads to the competitive adsorption on the binding sites between the residual species and the target protein (*i.e.*, collagen). The previous observations are carefully considered when interpreting our results, including some interesting differences highlighting the complexity of bioanalytical scenarios.

4.2 Experimental Details

4.2.1 Extraction of Collagen from Bovine Skins

The collagen solution was prepared following the procedures reported previously by our group [50] while replacing the acetic acid with HCl to avoid interference from its methyl (–CH$_3$) and carboxyl (–COOH) groups. The split bottom layer of the bovine skins, also called the "lime splits" or "corium split"[12] [73], were collected from a local tannery. A "deliming" process was carried out using NH$_4$Cl and HCl to neutralise the corium split to a pH of around 7 to wash off the sulfides. The delimed corium splits were frozen at −20 °C before they were used for collagen extraction. All of the extraction and purification steps were carried out at 4 °C.

Typically, in a batch, 50 g of delimed corium splits were cut into a uniform size of 5 mm × 5 mm (L × W) were soaked in 500 mL of 5 mM HCl with added 1.0% (w/w) pepsin (to the skin weight) and stirred mechanically over 24 h. The viscous crude collagen solution was collected and centrifuged to remove the insoluble pieces at 10000 rpm (a relative centrifugal force (RCF) or g-force at 15317 times gravity (× g)) for 30 min (Heraeus Multifuge X3R, Thermo Scientific). The supernatant was basified using 10 M NaOH to pH = 10 to denature the pepsin and kept for 2 h before being reacidified using 37% (w/w) HCl to pH = 3. It was then mixed with 4 M NaCl solution towards a final concentration of 2 M to precipitate ("salt out") the collagen. The precipitated collagen pieces were centrifuged into sticky pellets and redissolved into 500 mL 5 mM HCl to give a highly viscous solution. The viscous collagen solution was dialysed (D9402, 14 kDa molecular weight cut-off, Sigma-Aldrich) against 5 L of 1 mM HCl at least five times (each round takes 24 h) to remove NaCl until the electroconductivity showed lower than 500 µS.

The as-prepared collagen (Coll) was stored in the solution form in a group of 2.0 mL Eppendorf tubes at −20 °C for long-term storage or 4 °C for short-term storage (no more than 72 h) before further diluting for the SDS-PAGE characterisations and the SERS experiments. For the non-SERS collagen reference spectra, the collagen solution was air-dried in a non-stick petri dish into a dry, dense collagen film.

Chemicals:
Pepsin, 2336 FIP.U/mg, BIP1008, Apollo Scientific Ltd., UK;
Hydrochloric acid (HCl), 37% (w/w), CARLO ERBA Reagents S.r.l., Italy;
Sodium hydroxide (NaOH), CARLO ERBA Reagents S.r.l., Italy;
Sodium chloride (NaCl), Dominion Salt Ltd., New Zealand.

---

[12] "Liming" is a leather processing stage in which the skins are treated with sodium sulfide, sodium hydroxide, and calcium hydroxide ("lime"). At this stage, skins swell due to the strong basic pH, and the increased thickness makes the splitting of thick bovine skins easier for the desired thickness. The removed part is called "lime split" or "corium split" because it is split at the liming stage and composed of the corium layer of the skin.

4.2.2 Synthesis of AgNPs

Lee-Meisel's method [190] was followed for synthesising the citrate-reduced AgNPs. First, a mixture of 3.3 mL of 0.5% (w/v) $AgNO_3$ and 94 mL DI water was heated to boiling. Then, to the boiling mixture, we rapidly added 3.0 mL of 1% (w/v) $Na_3Cit \cdot 2H_2O$ and the mixture was kept boiling under vigorous stirring for 1 h and cooled down to room temperature. The solution was transferred to a Schott bottle and topped up to 100 g with DI water. The as-prepared AgNPs were stored at 4 °C and kept away from light.

For comparison, Leopold's method [203] was followed for synthesizing hydroxylamine-reduced, citrate-free h-AgNPs (prefix "h" for hydroxylamine). An initial mixture of 3.0 mL of 100 mM NaOH, 10.0 mL of 15 mM $NH_2OH \cdot HCl$ and 77 mL of DI water was prepared at room temperature. Then, 10.0 mL of 10 mM $AgNO_3$ was added dropwise to the mixture under vigorous stirring. The dropwise addition took about 2 min to finish, and then the mixture was kept stirring for another 10 min. The solution was transferred to a Schott bottle and topped up to 100 g with DI water. The as-prepared h-AgNPs were stored at 4 °C and kept away from light.

Chemicals:
Silver nitrate ($AgNO_3$), Apollo Scientific Ltd., UK;
Trisodium citrate dihydrate ($Na_3C_6H_5O_7 \cdot 2H_2O$ or $Na_3Cit \cdot 2H_2O$), Pure Science Ltd., New Zealand;
Sodium hydroxide (NaOH), CARLO ERBA Reagents S.r.l., Italy;
Hydroxylamine hydrochloride ($NH_2OH \cdot HCl$), Sigma-Aldrich, USA.

4.2.3 UV-Vis Spectroscopy Measurements

AgNPs and h-AgNPs were measured for the extinction optical densities (OD) using the Cloudspec (Marama Labs), covering wavelengths from 300 nm to 800 nm. Proper dilution using DI water was performed for each sample to achieve an extinction OD from 0.3 to 1.0. DI water was used as the reference for background subtraction.

4.2.4 TEM and SAED Imaging

AgNPs and h-AgNPs were centrifuged and washed using DI water and sonicated for 30 s before being cast onto a formvar/carbon-coated copper grid (200mesh, ProSciTech, Australia). Images were acquired using the JEOL-2100F (JEOL) electron microscope operated at 200 kV, and the SAED patterns were acquired using the Gatan 833J45N camera.

4.2.5 Preparation of the SERS Samples

The preparation of the SERS samples follows:

(1) Centrifugation: In a 1.5 mL Eppendorf tube, 1000 µL of AgNPs or h-AgNPs was centrifuged to concentrate (with a speed and time of 5 krpm for 15 min, 10 krpm for 10

min, or 14.5 krpm for 10 min), and 900 µL was removed from the supernatant, leaving the rest 100 µL to be redispersed using a vortex mixer at a low speed (around 2000 rpm) for 1 sec. Note that a higher vortex speed would splash the liquid drops onto the wall of the Eppendorf tube, giving a less homogeneous overall solution.

(2) Ligand exchange: To the concentrated 100 µL of AgNPs was added 100 µL of a salt solution (KCl, KBr, KI, NaHS, or DI water for the negative control), and the mixture was incubated at room temperature for a set amount of time (5 min, 20 min, or 60 min, for the optimisation of time for the ligand exchange).

Alternatively, when h-AgNPs were used instead of AgNPs, to the equivalently concentrated 100 µL of h-AgNPs was added 100 µL of a salt solution (KCl, Na₃Cit, thermally decomposed Na₃Cit, NaAc, a successive addition of two components, or DI water for the negative control). The mixture was then incubated at room temperature for 5 min.

The thermal decomposition of Na₃Cit was carried out by keeping 1 mL of 2 mM Na₃Cit in a 1.5 mL Eppendorf tube (with its lid closed) at 95 °C for 3 h and cooled down before being used in the experiments.

All the mixing (or addition) operations from this step onwards were performed by pipetting 5 times instead of using a vortex mixer; the latter would accelerate electrostatic aggregation (if the condition suits) and significantly deteriorate the SERS signals.

(3) Aggregation: finally, the 200 µL solution acquired was mixed with 200 µL of an aggregating agent (neutral MgSO₄, MgSO₄ in HCl, or Coll in HCl) to form the 400 µL final aggregated mixture from which the aliquot was withdrawn for the SERS measurements.

Chemicals:

Potassium chloride (KCl), Pure Science Ltd., New Zealand;

Potassium bromide (KBr), Merck KGaA, Germany;

Potassium iodide (KI) Sigma-Aldrich, USA;

Sodium hydrosulfide hydrate (NaHS), ≥60% by Na₂S₂O₃ titration (typically 70%–72%), Sigma-Aldrich, USA;

Trisodium citrate dihydrate (Na₃C₆H₅O₇·2H₂O or Na₃Cit·2H₂O), Pure Science Ltd., New Zealand;

Sodium acetate trihydrate (CH₃COONa·3H₂O, NaAc·3H₂O), Pure Science Ltd., New Zealand;

Magnesium sulfate (MgSO₄), Fisher chemical, UK;

Hydrochloric acid (HCl), 37% (*w/w*), CARLO ERBA Reagents S.r.l., Italy;

Sodium hydroxide (NaOH), CARLO ERBA Reagents S.r.l., Italy.

A summary of the volume changes during the sample preparations is shown in Table 4.1 for clarification. Table 4.2 lists the sample preparation details of all experiments (numbers 1 to 9) in this study, including the three-digit sample numbers (#*x-y-z*), the original NPs used in the experiment and their changes to highlight the major ligands (suffix "@A") and the coadsorbed species ("+B"), followed by the aspects of variations and the specific values of the parameters for all preparation steps. The rationales behind the determinations of the major ligands and the coadsorbed species are covered in the results and discussion section.

Table 4.1: Sample volume at each preparation step and the parameters related to the step.

Preparation steps	*Centrifugation*	*Ligand exchange*	*Aggregation*
$V_{initial}$ (µL)	1000 µL	100 µL	200 µL
ΔV (µL)	− 900 µL	+ 100 µL in total, may be multiple additions, *e.g.*, 65 µL + 35 µL;	+ 200 µL
V_{final} (µL)	= 100 µL	= 200 µL	= 400 µL
Parameters	Rotational speed; Time;	Type of salt; Concentration; Time;	Type of aggregation reagent; Concentration; Acidity;

Table 4.2: Detailed sample preparation methods. Experiments 1, 3, 4, 5, and 7 involved the optimisation of the centrifugation and the ligand exchange conditions, with the optimised parameters highlighted as underlined and bold. Full names of the abbreviated terms that were not noted earlier are shown after asterisk symbols (*).

Sample number	Original NPs →If NPs are modified; @Major ligand; +Coadsorbed species (revealed in this study);	Variations	Preparation steps and parameters		
			Centrifugation	*Ligand exchange (or adding coadsorbed species)*	*Aggregation*
(1) Centrifugation: parameter optimisation					
#1-1-1 #1-1-2 #1-1-3	AgNPs@Cit (*i.e.*, Lee-Meisel's AgNPs)	Rotational speed; Time;	**5 krpm, 15 min;** 10 krpm, 10 min; 14.5 krpm, 10 min;	-	-
(2) Without halide ligand exchange: the adsorption of citrate					
#2-1-1	AgNPs@Cit	-	5 krpm, 15 min;	DI water, 5 min;	5 mM MgSO₄;
(3) Ligand exchange: Cl					

#3-1-1 #3-1-2 #3-1-3 #3-1-4 #3-1-5	AgNPs@Cit →AgNPs@Cl (+AAc) *(AAc = acetoacetate)	KCl concentration;	5 krpm, 15 min;	1 mM KCl, 60 min; 2 mM KCl, 60 min; **5 mM KCl,** 60 min (**$[Cl^-]_{final}$ = 1.25 mM**); 6 mM KCl, 60 min; 10 mM KCl, 60 min;	5 mM $MgSO_4$;
#3-2-1 #3-2-2	AgNPs@Cit →AgNPs@Cl (+AAc)	KCl time;	5 krpm, 15 min;	5 mM KCl, 20 min; **5 mM KCl, 5 min;**	5 mM $MgSO_4$;
(4) Identification of the coadsorbed species on Cl ligand coated AgNPs					
#4-1-1	h-AgNPs@Cl$_{part}$ (*i.e.*, Leopold's h-AgNPs)	-	5 krpm, 15 min;	DI water, 5 min;	5 mM $MgSO_4$;
#4-2-1	h-AgNPs@Cl$_{part}$ →h-AgNPs@Cl	Sufficient KCl;	5 krpm, 15 min;	5 mM KCl, 5 min;	5 mM $MgSO_4$;
#4-3-1 #4-3-2 #4-3-3 #4-3-4	h-AgNPs@Cl$_{part}$ →h-AgNPs@Cl$_{part}$ (+Cit)	Add Na_3Cit;	5 krpm, 15 min;	0.67 mM Na_3Cit, 5 min; 1 mM Na_3Cit, 5 min; 2 mM Na_3Cit, 5 min; 10 mM Na_3Cit, 5 min;	5 mM $MgSO_4$;
#4-4-1	h-AgNPs@Cl$_{part}$ →h-AgNPs@Cl$_{part}$ (+AAc)	Add thermally decomposed Na_3Cit;	5 krpm, 15 min;	Thermally decomposed 2 mM Na_3Cit, 5 min;	5 mM $MgSO_4$;
#4-5-1	h-AgNPs@Cl$_{part}$	Add NaAc;	5 krpm, 15 min;	2 mM NaAc, 5 min;	5 mM $MgSO_4$;
#4-6-1	h-AgNPs@Cl$_{part}$ →h-AgNPs@Cl (+AAc)	Sufficient KCl; Add thermally decomposed Na_3Cit;	5 krpm, 15 min;	65 µL of thermally decomposed 2 mM Na_3Cit and 35 µL of 10 mM KCl, 5 min;	5 mM $MgSO_4$;

#4-7-1 #4-7-2	h-AgNPs@Cl$_{part}$ →h-AgNPs@Cl	Sufficient KCl; Add Na$_3$Cit;	5 krpm, 15 min;	65 µL of 2 mM Na$_3$Cit and 35 µL of 10 mM KCl, 5 min; 50 µL of 10 mM Na$_3$Cit and 50 µL of 7 mM KCl, 5 min;	5 mM MgSO$_4$;
#4-8-1	AgNPs@Cit →AgNPs@Cl	Sufficient KCl; Acidification;	5 krpm, 15 min;	5 mM KCl, 5 min;	5 mM MgSO$_4$ in 2 mM HCl;
(5) Ligand exchange: Br					
#5-1-1 #5-1-2 #5-1-3	AgNPs@Cit →AgNPs@Br (+AS) *(AS = anionic surfactant, residual in water)	KBr concentration;	5 krpm, 15 min;	0.05 mM KBr, 60 min; **1 mM KBr,** 60 min (**[Br⁻]$_{final}$ = 0.25 mM**); 2 mM KBr, 60 min;	5 mM MgSO$_4$;
#5-2-1 #5-2-2	AgNPs@Cit →AgNPs@Br (+AS)	KBr time;	5 krpm, 15 min;	1 mM KBr, 20 min; **1 mM KBr, 5 min;**	5 mM MgSO$_4$;
#5-3-1	AgNPs@Cit →AgNPs@Br (+AS)	Sufficient KBr; Acidification;	5 krpm, 15 min;	1 mM KBr, 5 min;	5 mM MgSO$_4$ in 2 mM HCl;
(6) Ligand exchange: I					
#6-1-1 #6-1-2 #6-1-3	AgNPs@Cit →AgNPs@I (+AS)	KI concentration;	5 krpm, 15 min;	0.05 mM KI, 60 min; **1 mM KI,** 60 min; (**[I⁻]$_{final}$ = 0.25 mM**); 2 mM KI, 60 min;	5 mM MgSO$_4$;
#6-2-1 #6-2-2	AgNPs@Cit →AgNPs@I (+AS)	KI times;	5 krpm, 15 min;	1 mM KI, 20 min; **1 mM KI, 5 min;**	5 mM MgSO$_4$;
#6-3-1	AgNPs@Cit →AgNPs@I (+AS)	Sufficient KI; Acidification;	5 krpm, 15 min;	1 mM KI, 5 min;	5 mM MgSO$_4$ in 2 mM HCl;
(7) Identification of the coadsorbed species on Br or I ligand coated AgNPs					
#7-1-1	h-AgNPs@Cl$_{part}$ →h-AgNPs@Br (+AS)	Sufficient KBr;	5 krpm, 15 min;	1 mM KBr, 5 min;	5 mM MgSO$_4$;

#7-2-1	h-AgNPs@Cl$_{part}$ →h-AgNPs@I (+AS)	Sufficient KI;	5 krpm, 15 min;	1 mM KI, 5 min;	5 mM MgSO$_4$;
#7-3-1	h-AgNPs@Cl$_{part}$ →h-AgNPs@Br (+AS)	Sufficient KBr; D$_2$O exchange;	5 krpm, 15 min;	1 mM KBr (in 90 µL D$_2$O and 10 µL H$_2$O), 5 min;	5 mM MgSO$_4$ (dissolved in 100 µL D$_2$O and 100 µL H$_2$O);
#7-4-1	h-AgNPs@Cl$_{part}$ →h-AgNPs@I (+AS)	Sufficient KI; D$_2$O exchange;	5 krpm, 15 min;	1 mM KI (in 90 µL D$_2$O and 10 µL H$_2$O), 5 min;	5 mM MgSO$_4$ (dissolved in 100 µL D$_2$O and 100 µL H$_2$O);
(8) Ligand exchange: S					
#8-1-1 #8-1-2 #8-1-3	AgNPs@Cit →AgNPs@S	NaHS concentration;	5 krpm, 15 min;	0.05 mM NaHS, 5 min; **0.2 mM NaHS, 5 min ([HS$^-$]$_{eq,\ final}$ = 0.05 mM);** 1 mM NaHS, 5 min;	5 mM MgSO$_4$;
(9) Aggregation with collagen					
#9-1-1 #9-1-2 #9-1-3 #9-1-4 #9-1-5 #9-1-6	AgNPs@Cit →AgNPs@Cl (+Coll)	Sufficient KCl; Add collagen;	5 krpm, 15 min;	5 mM KCl, 5 min;	1 µg/mL collagen in 2 mM HCl; 2 µg/mL collagen in 2 mM HCl; 5 µg/mL collagen in 2 mM HCl; 10 µg/mL collagen in 2 mM HCl; 20 µg/mL collagen in 2 mM HCl; 50 µg/mL collagen in 2 mM HCl;
#9-2-1 #9-2-2 #9-2-3 #9-2-4 #9-2-5 #9-2-6	AgNPs@Cit →AgNPs@Br (+Coll)	Sufficient KBr; Add collagen;	5 krpm, 15 min;	1 mM KBr, 5 min;	1 µg/mL collagen in 2 mM HCl; 2 µg/mL collagen in 2 mM HCl; 5 µg/mL collagen in 2 mM HCl; 10 µg/mL collagen in 2 mM HCl; 20 µg/mL collagen in 2 mM HCl; 50 µg/mL collagen in 2 mM HCl;

#9-3-1	AgNPs@Cit	Sufficient KI;	5 krpm, 15 min;	1 mM KI, 5 min;	1 µg/mL collagen in 2 mM HCl;
#9-3-2	→AgNPs@I (+Coll +AS)	Add collagen;			2 µg/mL collagen in 2 mM HCl;
#9-3-3					5 µg/mL collagen in 2 mM HCl;
#9-3-4					10 µg/mL collagen in 2 mM HCl;
#9-3-5					20 µg/mL collagen in 2 mM HCl;
#9-3-6					50 µg/mL collagen in 2 mM HCl;
#9-4-1	AgNPs@Cit	Sufficient NaHS;	5 krpm, 15 min;	0.2 mM NaHS, 5 min;	50 µg/mL collagen in 2 mM HCl;
	→AgNPs@S (+Coll)	Add collagen;			

4.2.6 Raman and SERS Measurements

The Raman and SERS experiments were conducted using the LabRam HR spectrometer (Horiba-Jobin Yvon) in the Raman Lab at VUW. The laser wavelength was 514 nm, delivered to the sample through an LM Plan FI Olympus air objective ($\times$50, NA = 0.50). The power exiting the objective was approximately 10 mW.

For SERS, each liquid sample has a volume of 150–200 µL and was contained in the cap of the Eppendorf tube of the corresponding sample to avoid cross-contamination. The laser was focused at 300 µm below the air/liquid interface into the solution for an exposure time ranging from 3 s to 10 s with ten accumulations for each spectrum.

The Raman spectra of dry collagen film were measured with the same setup but with the laser focusing around 20 µm above the air/solid interface (*i.e.*, defocused) to reduce the fluorescence from native collagen (see Ref. [204] for more discussion).

The flat-field correction method was applied to minimise the static artificial features from the CCD and the notch filter. The intensity of each Raman spectrum is normalized to count per second and stacked by offsetting (or scaling when indicated).

4.3 Results and Discussion

4.3.1 Characterisations of AgNPs and Type I Collagen

The representative UV-Vis extinction spectra of the AgNPs (Figure 4.1) match the corresponding references, showing peaks at 417 nm for Lee-Meisel's AgNPs (reference value = 420 nm, see Ref. [190]) and at 410 nm for Leopold's h-AgNPs (reference value = 408 nm, see Ref. [203]). TEM images display an expected level of polydispersity and a largely spherical morphology. The polycrystallinity is confirmed by the SAED images showing the characteristic rings from the (111), (200), (220), and (311) lattice planes.
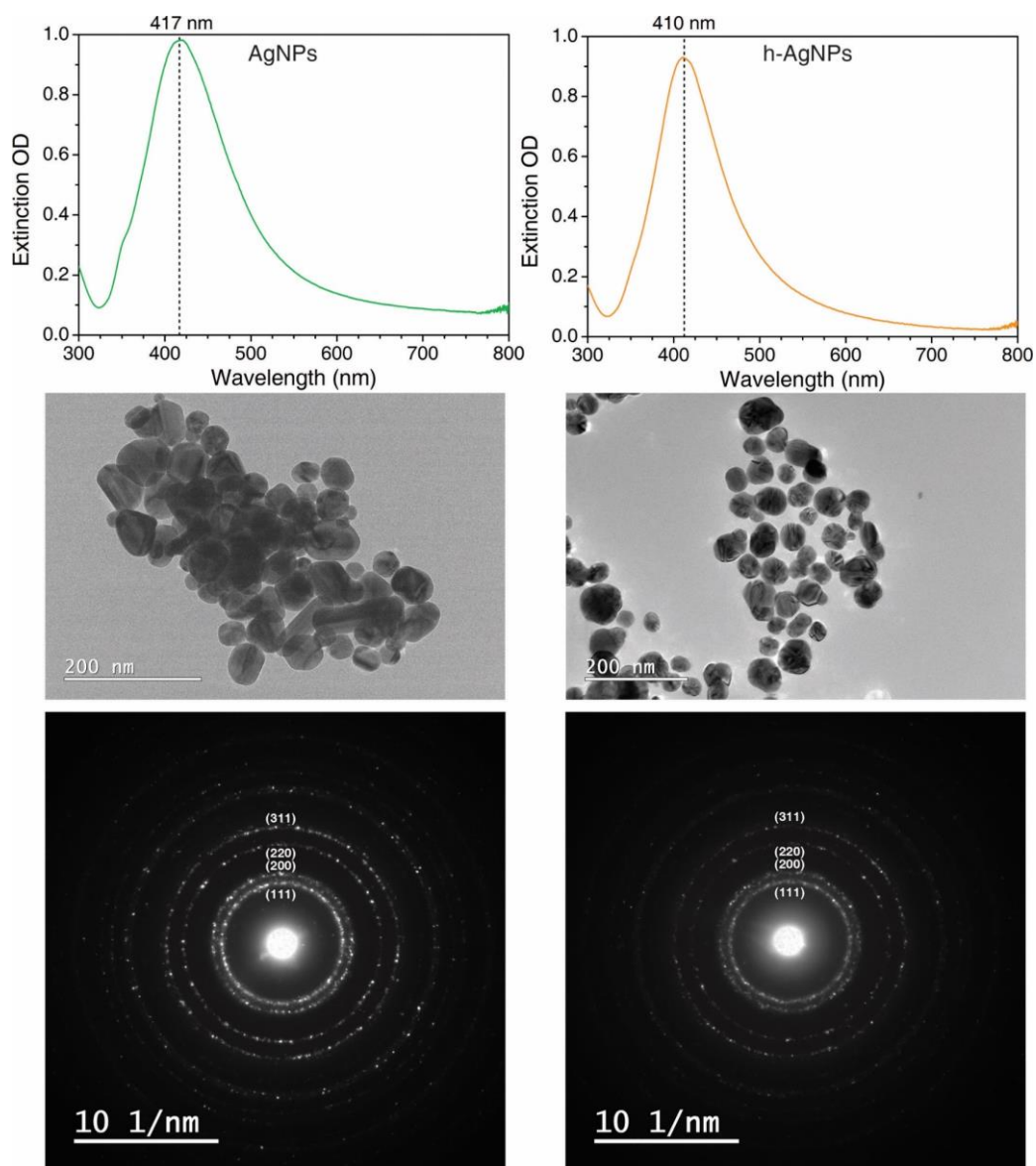
Figure 4.1: The representative UV-Vis extinction spectra, TEM images and SAED patterns of AgNPs following Lee-Meisel's method [190] and h-AgNPs following Leopold's method [203]. AgNPs and h-AgNPs were first concentrated by centrifuging at 5 krpm for 15 min from 1000 µL to 100 µL, then rediluted to proper concentrations to represent the actual SERS samples. For UV-Vis, dilution factor (DF) = 40.

The SDS-PAGE gel of the extracted collagen shows a clear group of bands, including the collagen β bands at around 250 kDa and the two well-resolved collagen α bands between 100 and 150 kDa (Figure 4.2). The absence of hydrolysed bands in low kDa regions indicates satisfactory integrity of the extracted collagen.
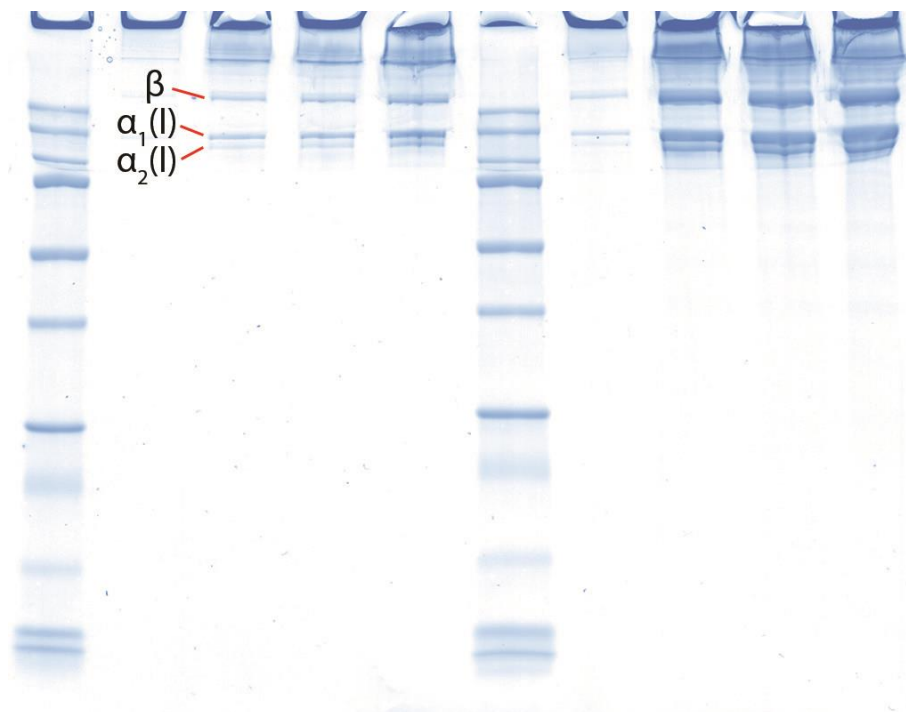
Figure 4.2: An SDS-PAGE gel of the extracted collagen solution. The gel comprises 4% stacking and 12% separating components. Bio-Rad Precision Plus Protein standards were used as the protein ladder. Samples: lane 1, Protein ladder; lanes 2 to 5, 2 µL, 4 µL, 6 µL, and 8 µL collagen solution loads; same for lanes 6 to 10 but heat denatured prior to loading.

4.3.2 The Effect of Centrifugation on AgNPs

One can find in the literature this common practice of centrifuging the NPs before mixing with the protein samples for SERS measurements [189, 205-207], but the effect of centrifugation on the SERS results was not explained clearly. Figure 4.3 shows the SERS spectra of differently centrifuged AgNPs. A consistent set of peaks are identified in the SERS spectra of the AgNPs centrifuged at 14.5 krpm for 10 min without adding $MgSO_4$ or any other aggregating agents (#1-1-3); the origin of the signals will be discussed in a later section. Reducing the centrifugation speed and time minimises the SERS features while maintaining a good AgNPs recovery rate for the SERS experiments. Therefore, a moderated speed and time at 5 krpm for 15 min was chosen for the rest of the study.
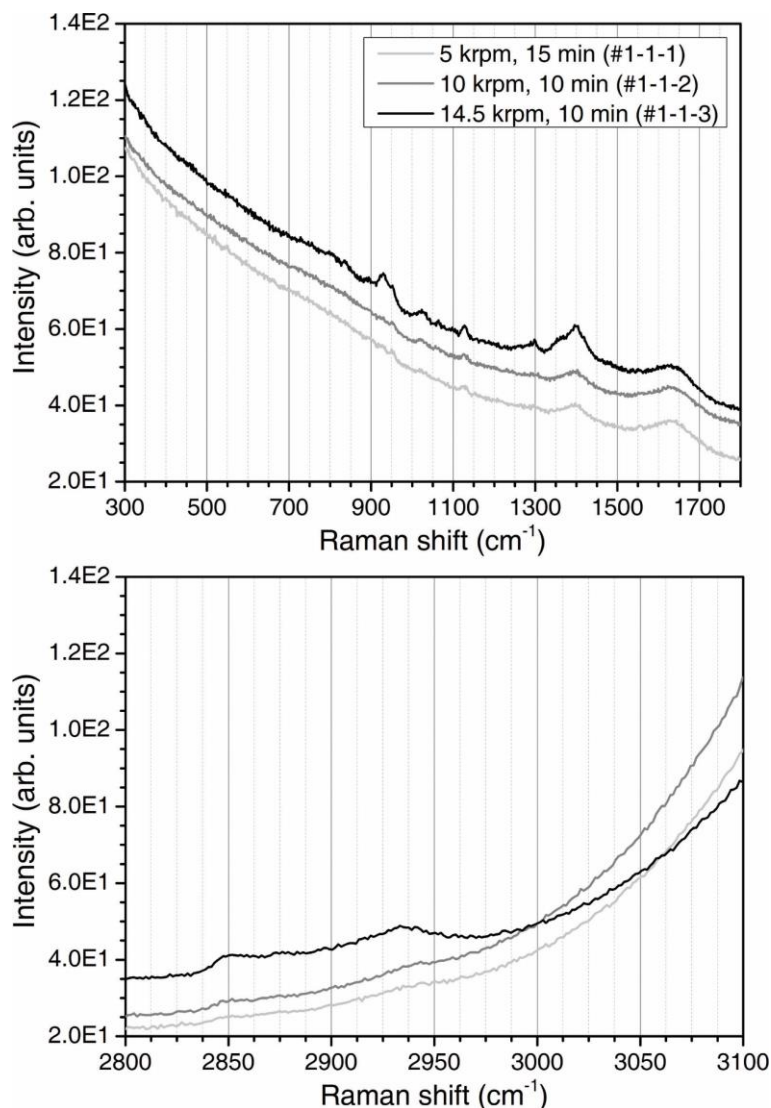
Figure 4.3: Stacked SERS spectra showing aggregation induced by centrifugation of AgNPs: 5 krpm, 15 min (#1-1-1), 10 krpm, 10 min (#1-1-2), 14.5 krpm, 10 min (#1-1-3).

4.3.3 AgNPs@Cit

Without ligand exchange, the as-prepared AgNPs are known to have an adsorbed citrate (Cit) layer and are hereby named "AgNPs@Cit", despite the presence of oxidation and thermal decomposition products of Cit in the final solution, as they were found not to adsorb on the AgNPs [208]. For convenience, the abbreviation "Cit" in this thesis represents not only the fully deprotonated citrate anion (*i.e.*, Cit^{3-}) but also includes the partially protonated $HCit^{2-}$ and H_2Cit^- anions. In such a way, we also highlight the lack of evidence in this study to attribute the SERS features to specific Cit species. The same rule of simplification or abbreviation was followed for other capping ligands (Cl, Br, I, and S) and coadsorbed species for consistency.

A characteristic SERS spectrum of surface-bound Cit is acquired when the AgNPs@Cit are centrifuged and then aggregated using $MgSO_4$ (Figure 4.4). Note that SO_4^{2-} would not displace

the adsorbed Cit from AgNPs@Cit, as SO_4^{2-} has a much weaker binding affinity to Ag atoms than Cit [209]. Here, for discussion and peak assignments, we define each carbon atom in Cit differently with C_x:

(1) x = c, for the carbon atom of the central carboxyl group;
(2) x = t, for the carbon atoms of the terminal carboxyl groups;
(3) x = h, for the carbon atom to which the hydroxyl group attaches;
(4) x = b, for the carbon atoms of the methylene (–CH$_2$–) groups.
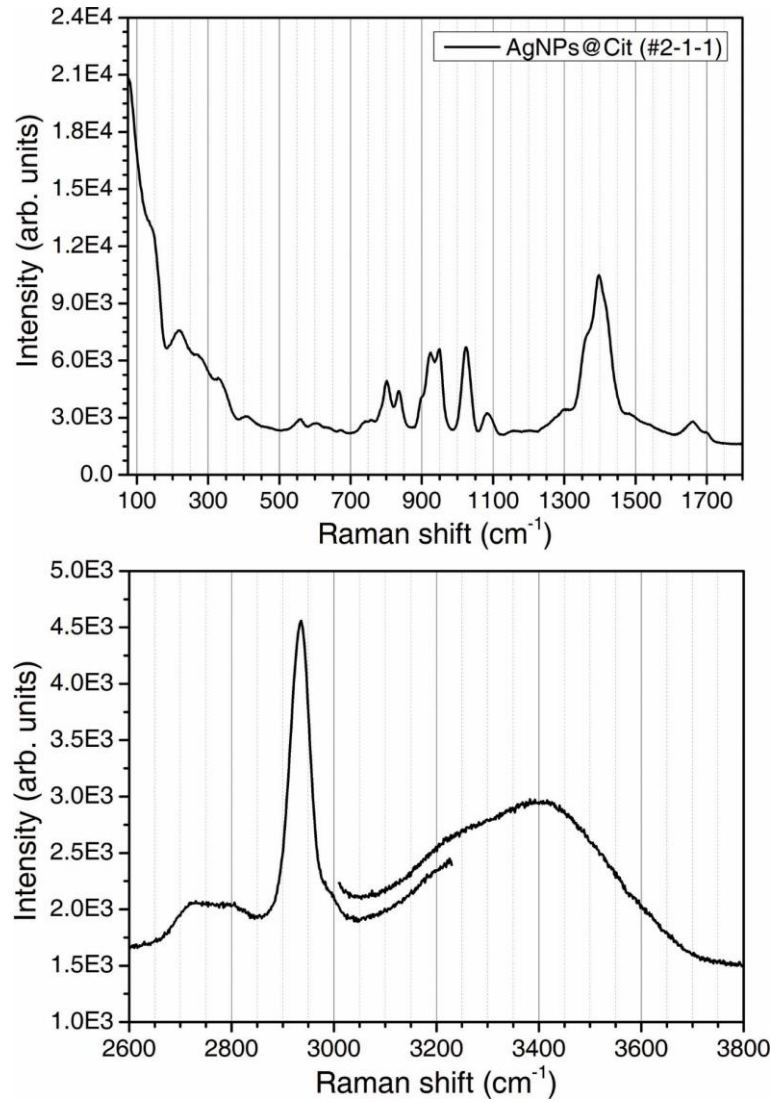
Figure 4.4: The SERS spectra of AgNPs@Cit (#2-1-1). The spectra from 2600 cm^{-1} to 3800 cm^{-1} are not superimposed as they were measured at different grating positions (same for other spectra in this study).

Most of the SERS peaks in the spectrum are assignable to Cit (notations refer to Appendix A), including 2934 cm^{-1} (ν_s(CH$_2$)), 2723 cm^{-1} (ν(O–H), in $\varkappa^1$-COOH), 1700sh cm^{-1} (ν(C$_t$–OH), $\varkappa^1$-C$_t$OOH), 1660 cm^{-1} (ν(C$_t$=O), $\varkappa^1$-C$_t$OO$^-$), 1414sh cm^{-1} (ν_s(COO$^-$), unbound), 1397 cm^{-1} (ν_s(C$_c$OO$^-$), bound), 1360sh cm^{-1} (ν_s(C$_t$OO$^-$), bound), 1297w cm^{-1} (ν(C$_t$–O), $\varkappa^1$-C$_t$OO$^-$ or $\varkappa^1$-C$_t$OOH), 1084 cm^{-1} (ν(C$_b$–C$_h$)), 1024 cm^{-1} (ν(C$_c$–C$_h$), bound), 948 cm^{-1} (ν(C$_t$–C$_b$), unbound), 925 cm^{-1} (ν(C$_t$–C$_b$), bound), 899sh cm^{-1} (ν(C–COO)), and 835 cm^{-1} (ν(C$_h$–O)), in addition to a broad peak at 218 cm^{-1} assigned to ν(COO–Ag) indicating the binding of Cit to Ag atoms via its carboxylate (–COO$^-$) group [208, 210-215]. Detailed peak assignments are listed in Table 4.3 (#2-1-1). The binding coordination of Cit in AgNPs@Cit resembles the Cit on "rough" surfaces of AuNPs with adatoms [213, 216], highlighted by the prominent 1084 cm^{-1} peak of ν(C$_b$–C$_h$), which indicates that the central carboxylate (–C$_c$OO$^-$) group and at least one of the terminal carboxylate (–C$_t$OO$^-$) groups in Cit are bound to Ag atoms (Figure 4.5).
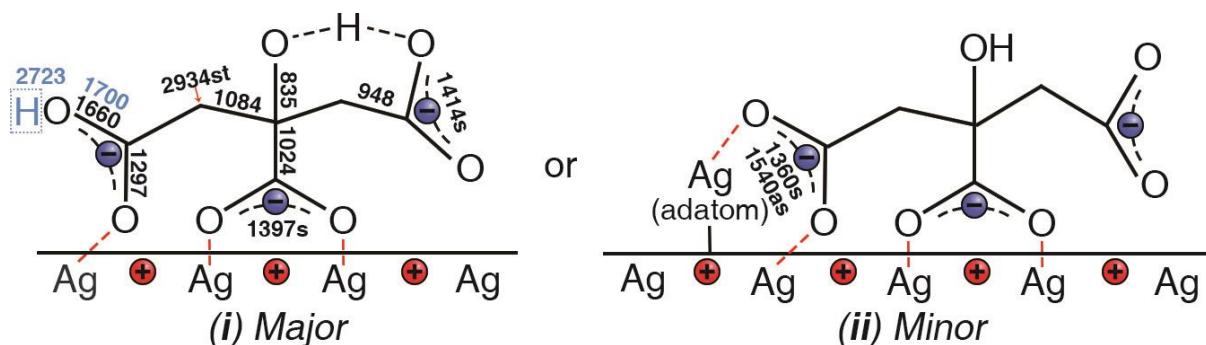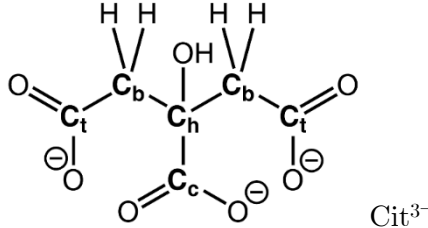
Figure 4.5: Possible binding coordination of Cit with Ag atoms in AgNPs@Cit (#2-1-1). Associated Raman shifts (in the unit of [cm^{-1}]) of the peaks from Cit are labelled next to the corresponding bonds. The red arrow indicates that the peak is assigned to the –CH$_2$– group. The blue-coloured numbers and the hydrogen atom highlight the potential protonation of the –COO$^-$ group into a –COOH group and the associated SERS peaks.

Table 4.3: SERS peak assignments of (1) #2-1-1 and (2) #4-3-3 (discussed in Section 4.3.4, but highly relevant to #2-1-1). The concentrations of species (*e.g.*, [Cl⁻] and [Cit]) are the concentrations in the final mixtures for SERS measurements (same below, unless specified). The species of each vibrational mode is noted based on the information reported in the corresponding reference, apart from the SERS modes originating from Cit or AgNPs. Postulated assignments are highlighted with asterisk symbols (*). General notations refer to Appendix A.

Raman shift (cm⁻¹)		Assignment	Reference (cm⁻¹)
#2-1-1	**#4-3-3**		
AgNPs@Cit **+ MgSO₄** **pH = 8**	**h-AgNPs@Cl_part** **+ Na₃Cit** **+ MgSO₄** **pH = 8** **[Cl⁻] = 0.375 mM** **[Cit] = 0.5 mM**	Cit^{3-}	
3424	3414	ν_{as}(O–H), water, hydrogen-bonded; [217] DA-OH, water; [218]	3435; [217] 3432; [218]
3217sh	3236sh	ν_s(O–H), water, hydrogen-bonded; [217] DDAA-OH, water; [218]	3247; [217] 3226; [218]
2997sh		ν_{as}(CH₂); [210]	3000(DFT); [210]
2934	2937w	ν_s(C–H), in Cu₂(Cit)·2H₂O; [211] ν_s(CH₂); [210]	2929; [211] 2934(DFT); [210]
2804sh			
2723		ν(O–H), in –COOH, bound; [212]	2500–2700; [212]
1700sh		ν(C$_t$–OH), $\varkappa^1$-C$_t$OOH; [213]	1710; [213]
1660		ν(C$_t$=O), $\varkappa^1$-C$_t$OO⁻; [213]	1685; [213]
	1622	ν_{as}(COO⁻); [214]	1624; [214]
1540sh		ν_{as}(COO⁻); [211] ν_{as}(COO⁻); [215] ν_{as}(C$_t$OO⁻), $\varkappa^2$; [213]	1555; [211] 1550; [215] 1535; [213]
1490w			

1414sh	1415sh	$\nu_s(COO^-)$; [214]	1415; [214]
		$\nu_s(COO^-)$, bound; [211]	1415; [211]
		$\nu_s(COO^-)$, unbound; [208]	1412; [208]
		$\nu_s(COO^-)$, Cit(aq); [208]	1417; [208]
		$\nu_s(COO^-)$, Cit(aq); [213]	1410; [213]
1397		$\nu_s(COO^-)$; [214]	1400; [214]
		$\nu_s(COO^-)$; [215]	1392; [215]
		$\nu_s(COO^-)$, bound; [208]	1400; [208]
		$\nu_s(COO^-)$, $\varkappa^2$; [213]	1385; [213]
		*$\nu_s(C_cOO^-)$, bound;	
1360sh	1373	$\nu_s(COO^-)$, bound; [208]	1370; [208]
		$\nu_s(COO^-)$; [214]	1345; [214]
		*$\nu_s(C_tOO^-)$, bound;	
1297w		$\nu(C_t–O)$, $\varkappa^1$-C_tOO^- or $\varkappa^1$-C_tOOH; [213]	1300; [213]
1084	1082vw	$\nu(C_b–C_h)$, c_2t_2 or c_2t_2-t_2; [213]	1080; [213]
1024	1028	$\nu_s(C–C)$; [214]	1026; [214]
		$\nu(C–O)$; [208]	1025; [208]
		$\nu(C_c–C_h)$, c_2; [213]	1030(DFT); [213]
		$\nu(C_c–C_h)$, linked to $\varkappa^2$-C_cOO–Au; [213]	1020; [213]
948	951	$\nu(C–C)$; [214]	956; [214]
		$\nu(C–C)$, Cit(aq); [215]	957; [215]
		$\nu(C–COO)$; [208]	952; [208]
		$\nu(C_t–C_b)$, unbound; [213]	950; [213]
925	923	$\nu(C–C)$, bound; [214]	940; [214]
		$\nu(C–C)$; [215]	933; [215]
		$\nu(C–COO)$; [208]	933; [208]
		*$\nu(C_t–C_b)$, bound;	
899sh	899sh	$\nu(C–COO)$; [208]	903; [208]
835	833w	$\nu(C_h–O)$; [214]	845; [214]
		$\nu(C_h–O)$, Cit(aq); [215]	846; [215]

801			
757w		$\nu(C_t–C_b)$, Cit(aq); [213]	750; [213]
736sh			
673		$\delta(OCO)$; [211] $\delta(COO)$; [208]	680; [211] 670; [208]
641w			
602w		$\delta(COO)$; [208]	596; [208]
557		$\pi(COO)$; [211] $\delta(COO)$; [208]	568; [211] 560; [208]
472w	445sh	$\rho(COO)$; [211] $\nu(Ag–O)$, subsurface; [215]	475; [211] 464; [215]
408		$\rho(COO)$; [219]	
332		$\nu(Ag–O)$, adsorbed; [215] Eclipsing of $–C_cOO^-$ with $–C_tOO^-$; [208]	320; [215] 336; [208]
278sh			
	240	$\nu(Ag–Cl)$; [209] $\nu(Ag–Cl)$; [196] $\nu(Ag–Cl)$; [220]	245; [209] 243; [196] 240; [220]
218		$\nu(COO–Ag)$; [208]	232; [208]
147sh	158sh	Ag lattice vibration; [221]	147; [221]

4.3.4 AgNPs@Cl

The attempts to exchange the surface ligands on the AgNPs to Cl were carried out by treating the as-prepared AgNPs@Cit with various amounts of KCl for different exposure times. The resulting SERS spectra reveal progressive changes as [Cl$^-$] increases (Figure 4.6).

At [Cl$^-$] = 0.25 mM (added [KCl]$_{added}$ = 1 mM, #3-1-1), the most prominent peak appears at 239 cm^{-1} assignable to the ν(Ag–Cl) mode, suggesting the direct binding of Cl ligand to Ag atoms as an indication of its successful adsorption onto the AgNPs. Although the original ν(COO–Ag) peak at 218 cm^{-1} is overwhelmed, the largely diminished fingerprint signals still resemble those of the untreated AgNPs@Cit (#2-1-1), showing the coadsorption of Cit on the AgNPs. Except for the Cit signals, a broad peak shown at around 1600 cm^{-1} can be vaguely resolved as two merged shoulder peaks at 1585 cm^{-1} and 1625 cm^{-1} and assigned to the ν_{as}(C$_t$OO$^-$) and ν_{as}(C$_c$OO$^-$) modes of Cit, respectively [213]. Additionally, a peak emerges at 2849 cm^{-1} as the intensity of the 2935 cm^{-1} peak diminishes, highlighting either an unidentified species bound to the AgNPs or a change in Cit binding coordination due to the interference from the Cl ligands. These emerging peaks are also observed at a slightly increased [Cl$^-$] = 0.5 mM (added [KCl]$_{added}$ = 2 mM, #3-1-2), showing moderate changes in the fingerprint region to resemble less of the AgNPs@Cit spectra.

Increasing [Cl$^-$] to 1.25 mM (#3-1-3) leads to the diminishing of 1585 cm^{-1} and 1625 cm^{-1} peaks corresponding to ν_{as}(COO$^-$), while the 2849 cm^{-1} peak remains prominent. Further increases of [Cl$^-$] up to 1.5 mM (#3-1-4) and 2.5 mM (#3-1-5) show no further changes in the spectra. Similarly, no changes are observed in the SERS spectra when the exposure time is shortened from 60 min (#3-1-3) to 20 min (#3-2-1) and 5 min (#3-2-2). Therefore, despite the opposite claims elsewhere [222, 223], our results imply that sufficient Cl ligands only form a near-complete layer on AgNPs but leave a considerable amount of Ag atoms to remain exposed for direct binding or coadsorption with species. Hereafter, #3-2-2 is denominated as "AgNPs@Cl" to highlight the major ligand rather than exclude the existence of coadsorbed species.

Nevertheless, up till this point, an optimal condition is revealed through our ligand exchange attempts, which could help suppress the etching of the AgNPs over prolonged exposure to unnecessarily high concentrations of halide anions [222, 224]. The optimal condition (#3-2-2) is summarised here: the stock solution of [KCl]$_{added}$ = 5 mM was mixed with the AgNPs in a 1:1 ratio for a controlled exposure for 5 min at a temporary concentration at [Cl$^-$]$_{temp}$ = 2.5 mM, which is then diluted to [Cl$^-$] = 1.25 mM in the aggregated mixture for SERS measurements. The peaks observed in #3-2-2 are summarised in Table 4.4.
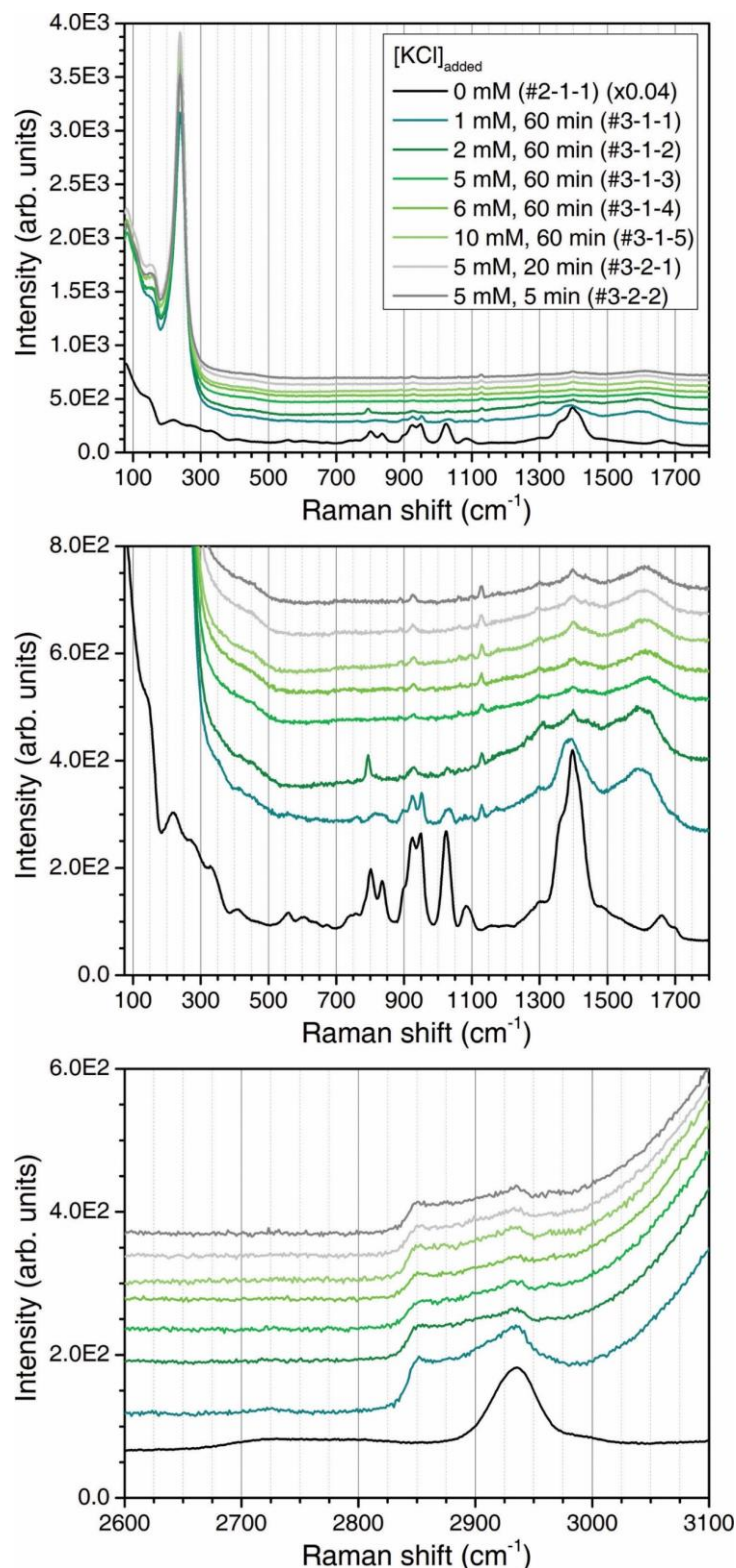
Figure 4.6: Stacked SERS spectra of the KCl ligand exchange series (#3-1-z and #3-2-z). The concentrations of the stock solutions added ([KCl]$_\text{added}$) include 0 mM (#2-1-1) (×0.04), 1 mM (#3-1-1), 2 mM (#3-1-2), 5 mM (#3-1-3, #3-2-1, and #3-2-2), 6 mM (#3-1-4), and 10 mM (#3-1-5). The fingerprint region below 1800 cm^{-1} was plotted twice with differently scaled y-axes to display the weak features and the overwhelmingly strong Ag–X peaks (similar to other spectra in this study).

Upon clarifying the incomplete surface coverage by Cl at the optimal condition and the coadsorption phenomenon, we encounter the question about the coadsorbed species (which, in retrospect, took much more effort to answer than expected).

A straightforward assumption for the coadsorbed species is Cit in different binding coordination due to the similarity in the SERS spectra, but the minor differences are of concern. The immediate doubt comes from the new peak at 2849 cm^{-1}: it coexists with the peak at 2935 cm^{-1} with a fixed relative intensity but is scarcely reported alongside the 2935 cm^{-1} peak to show any association with Cit or disprove its relevance with Cit.

Through detailed comparisons, one seemingly irrelevant sample comes to light which shows both of the above peaks: the high-speed centrifuged AgNPs@Cit (Figure 4.7, #1-1-3). It proves that the species existed before the addition of KCl or MgSO$_4$. In other words, the species is adsorbed on AgNPs@Cit but rather being unearthed instead of triggered to adsorb by the Cl ligand exchange.

Following the method of exclusion, we employ a citrate-free synthesis using hydroxylamine (h-AgNPs) to confirm whether the signals originate from the citrate-based AgNPs synthesis. It must be clarified that the h-AgNPs have an intrinsic layer of Cl introduced during the synthesis by the reducing agent NH$_2$OH·HCl. The Cl$^-$ is carried over into each sample and contributes an extra 0.375 mM to the final [Cl$^-$]. Based on the earlier observations in AgNPs@Cl, we may expect that the surface coverage of Cl ligands on h-AgNPs is insufficient to displace Cit fully (if present), thus named "h-AgNPs@Cl$_{part}$"[13]. Unsurprisingly, the h-AgNPs@Cl$_{part}$ shows clean spectra with no prominent peaks when aggregated using MgSO$_4$, except for the ν(Ag–Cl) and water peaks (Figure 4.7, #4-1-1), narrowing down the candidates for the unidentified species to Cit and Cit-related species during the citrate-based AgNPs synthesis.

---

[13] Here, the subscript "part" means partial. However, later in the discussion (Section 4.3.7), we revealed that this low intrinsic concentration is sufficient for Cl to lead to a near-complete coverage. Cl at low concentrations does not overwhelm Cit due to their comparable affinity to the AgNPs.
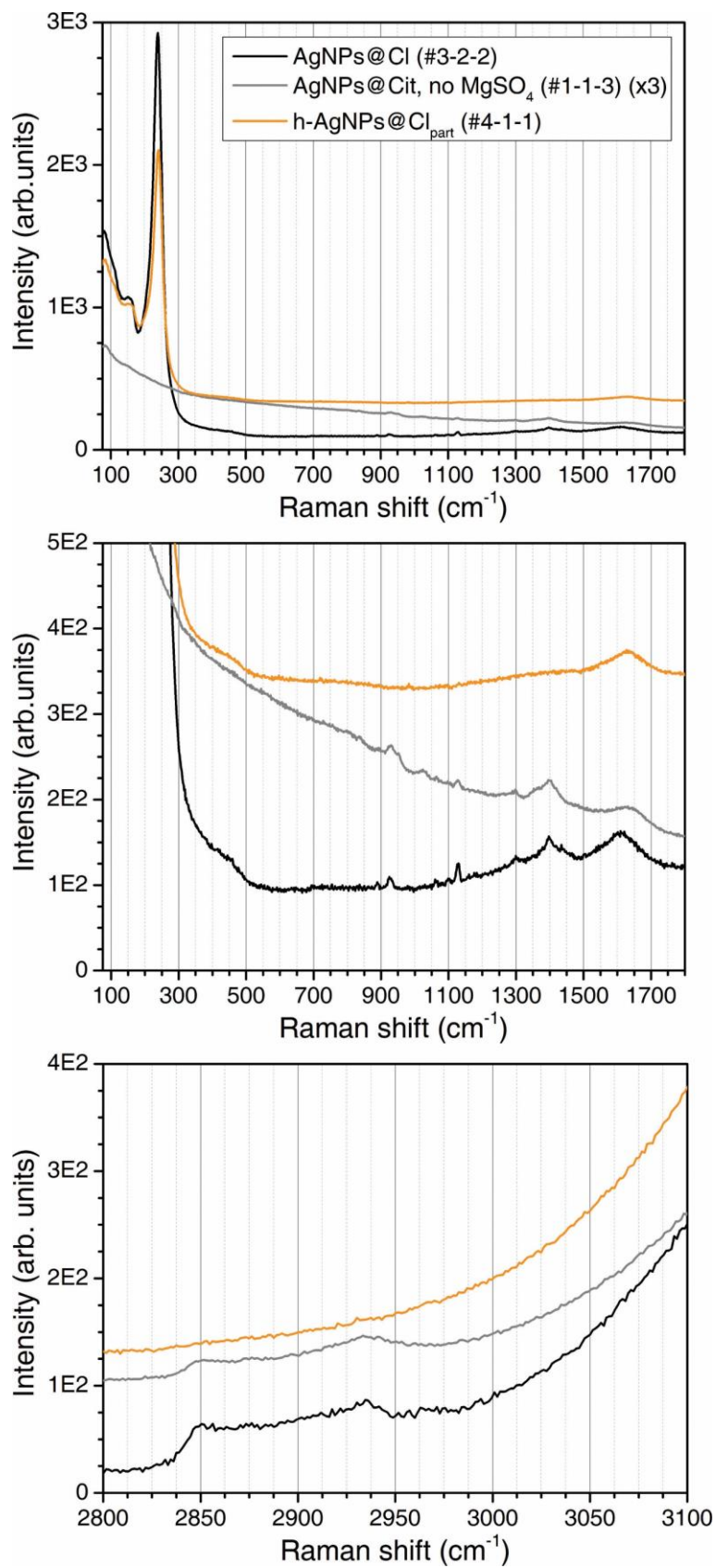
Figure 4.7: Stacked SERS spectra of AgNPs@Cl (#3-2-2), high-speed centrifuged AgNPs@Cit (#1-1-3) (×3), and h-AgNPs@Cl$_{part}$ (#4-1-1).

Knowing the vague origin of the signals is particularly helpful in this scenario. To verify whether the coadsorbed species is Cit, we added fresh Na_3Cit to the h-AgNPs@Cl$_{part}$ at a series of concentrations ([Cit]$_{added}$ = 0.67 to 10 mM), followed by the aggregation using $MgSO_4$ (Figure 4.8).

The SERS spectra of fresh Na_3Cit at the highest concentration ([Cit]$_{added}$ = 10 mM, #4-3-4) with h-AgNPs@Cl$_{part}$ are almost identical to untreated AgNPs@Cit (#2-1-1), apart from the distinct ν(Ag–Cl) signal from the former sample. When less Na_3Cit is added ([Cit]$_{added}$ = 2 mM, #4-3-3), the SERS spectra fall to a comparable intensity to those of AgNPs@Cl (#3-2-2). However, peaks do not match; the spectra of #4-3-3 lack the peaks at 2849 cm^{-1} and 1128 cm^{-1} while having an extra peak at 950 cm^{-1}. On the contrary, all the peaks in #4-3-3 are assignable to Cit at 2937vw cm^{-1} ($\nu_s(CH_2)$), 1622 cm^{-1} ($\nu_{as}(COO^-)$), 1415sh cm^{-1} ($\nu_s(COO^-)$, unbound), 1373 cm^{-1} ($\nu_s(C_tOO^-)$, bound), 1028 cm^{-1} ($\nu(C_c–C_h)$), 951 cm^{-1} ($\nu(C_t–C_b)$, unbound), 923 cm^{-1} ($\nu(C_t–C_b)$, bound), 899sh cm^{-1} ($\nu(C–COO)$), and 833w cm^{-1} ($\nu(C_h–O)$). Detailed peak assignments of #4-3-3 are also listed in Table 4.3 to highlight the similarity with #2-1-1.
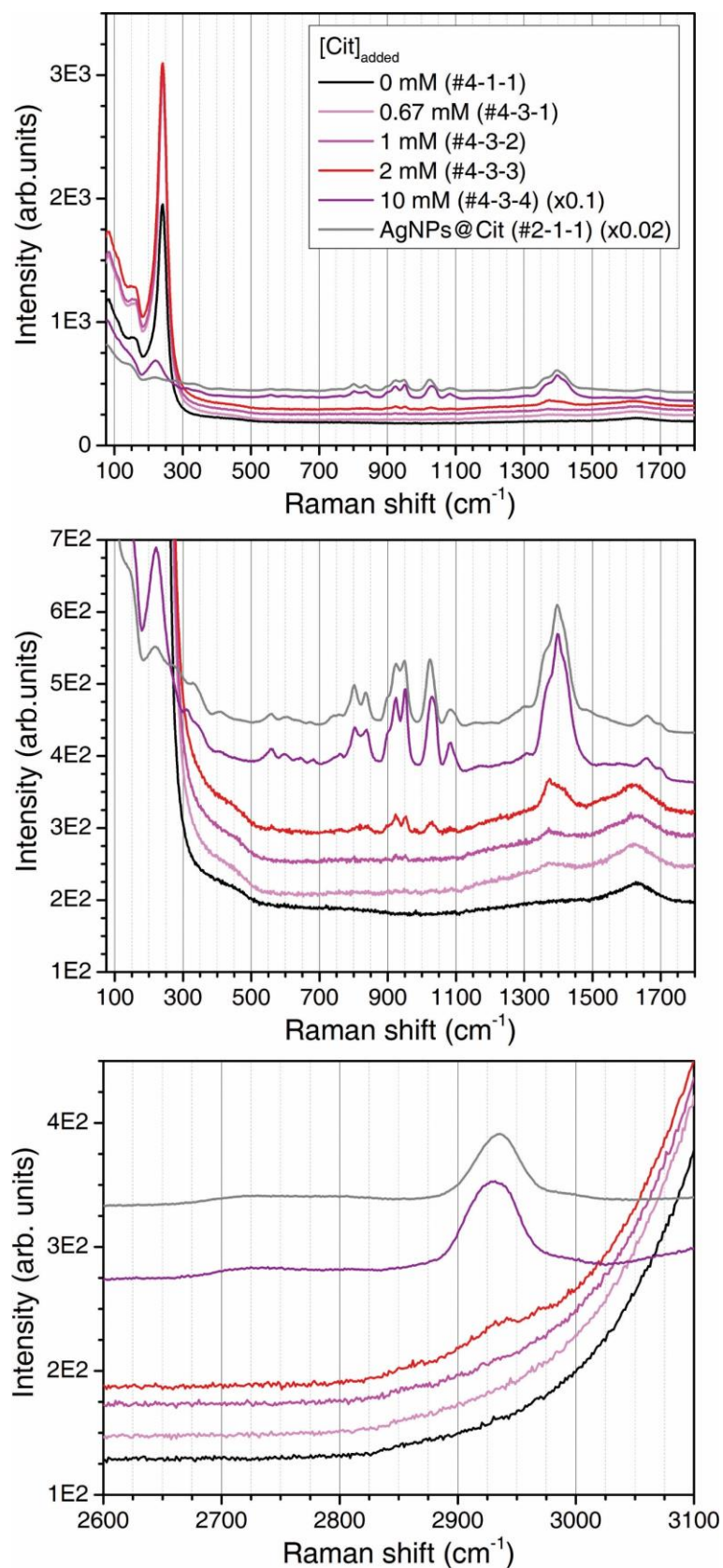
Figure 4.8: Stacked SERS spectra of h-AgNPs@Cl$_{part}$ with a series amount of Cit ([Cit]$_{added}$): 0 mM (#4-1-1), 0.67 mM (#4-3-1), 1 mM (#4-3-2), 2 mM (#4-3-3), and 10 mM (#4-3-4) (×0.1), as well as AgNPs@Cit (#2-1-1) (×0.02) as reference.

On the other hand, when we add a sufficient amount of KCl into the mixture of h-AgNPs@Cl$_{part}$ and Na$_3$Cit to match the [Cl$^-$] in AgNPs@Cl, the above Cit peaks disappear, giving clean spectra except for the ν(Ag–Cl) and water peaks (Figure 4.9, #4-7-1 and #4-7-2). The absence of Cit signals could be attributed to the electrostatic repulsion between the negatively charged Cl ligand and the Cit anions, which counteracts the affinity of Cit to Ag atoms. An additional experiment on adding NaAc to h-AgNPs@Cl$_{part}$ (without sufficient KCl) leads to clean spectra (Figure 4.9, #4-5-1), same as the negative control (#4-1-1).
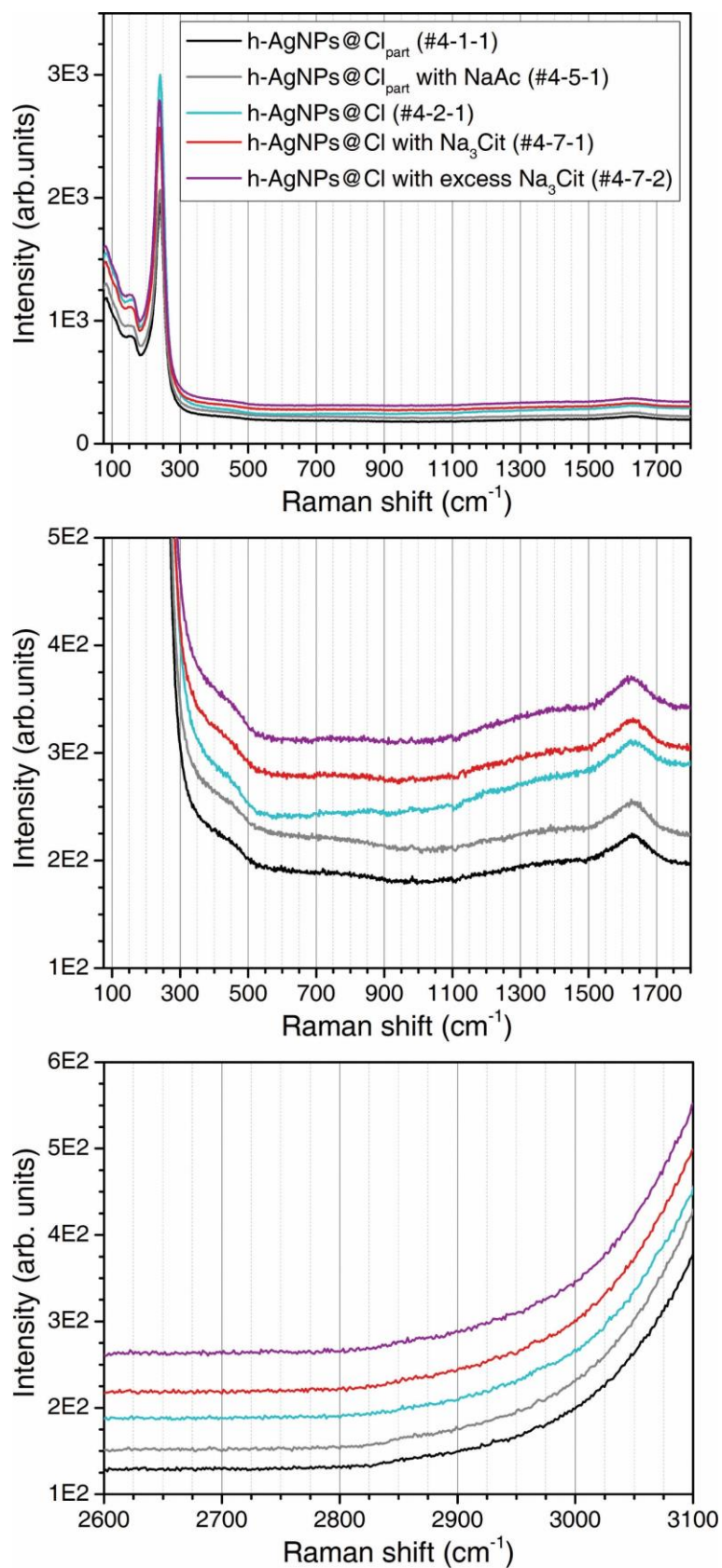
Figure 4.9: Stacked SERS spectra of h-AgNPs@Cl_part (#4-1-1), h-AgNPs@Cl_part with NaAc (#4-5-1), h-AgNPs@Cl (#4-2-1), and h-AgNPs@Cl with Na₃Cit (#4-7-1 and #4-7-2).

We have hitherto investigated and ruled out Cit and Ac, leaving only two possible candidates: acetonedicarboxylate (ADC^{2-}) and acetoacetate (AAc$^-$) or their protonated forms. Both were found during the synthesis of AgNPs@Cit, with ADC likely to undergo decomposition (decarboxylation) at elevated temperature into AAc [208, 213]. Hence, the spectra with the 2849 cm^{-1} and 2935 cm^{-1} peaks are likely to be caused by AAc.

To confirm this, we prepared 2 mM Na$_3$Cit, decomposed a 1.0 mL aliquot in a sealed Eppendorf tube at 95 °C for 3 h, and then added it to the h-AgNPs@Cl$_{part}$ followed by sufficient KCl (for mimicking the near-complete coverage), with a final touch of MgSO$_4$ for the aggregation. Thermal decomposition could partially oxidise Cit into AAc, probably by consuming the dissolved oxygen and the oxygen in the air pocket above the solution; a failed decomposition attempt using the same amount of 10 mM Na$_3$Cit (which resulted in the same spectra as fresh Na$_3$Cit) could support this mechanism.

The resulting SERS spectra (Figure 4.10, #4-6-1) perfectly match the AgNPs@Cl (Figure 4.10, #3-2-2), observing the characteristic features from AAc highlighted as follows:

(1) The presence of peaks at 2851 cm^{-1} and 1437 cm^{-1} from its methyl group (–CH$_3$);
(2) The presence and higher peak intensity at 1399 cm^{-1} in comparison with those at 1370 cm^{-1} or 1410 cm^{-1} (see #4-3-3 in Figure 4.10 for a counterexample);
(3) The absence of peaks at 1028 cm^{-1} and 950 cm^{-1};

The third feature is particularly convincing, as both peaks are distinct in previously reported Cit or ADC SERS spectra [208, 213], whereas our AAc spectra feature a stronger 925 cm^{-1} peak and a slightly weaker 890 cm^{-1}. Detailed peak assignments and the comparisons are listed in Table 4.4 (#4-6-1 versus #3-2-2). Moreover, a mixture of AAc and Cit features can be observed by deliberately not providing sufficient [Cl$^-$] to lessen the electrostatic repulsion, thereby allowing the binding of both AAc and Cit to Ag atoms, as shown in Figure 4.10 (#4-4-1).
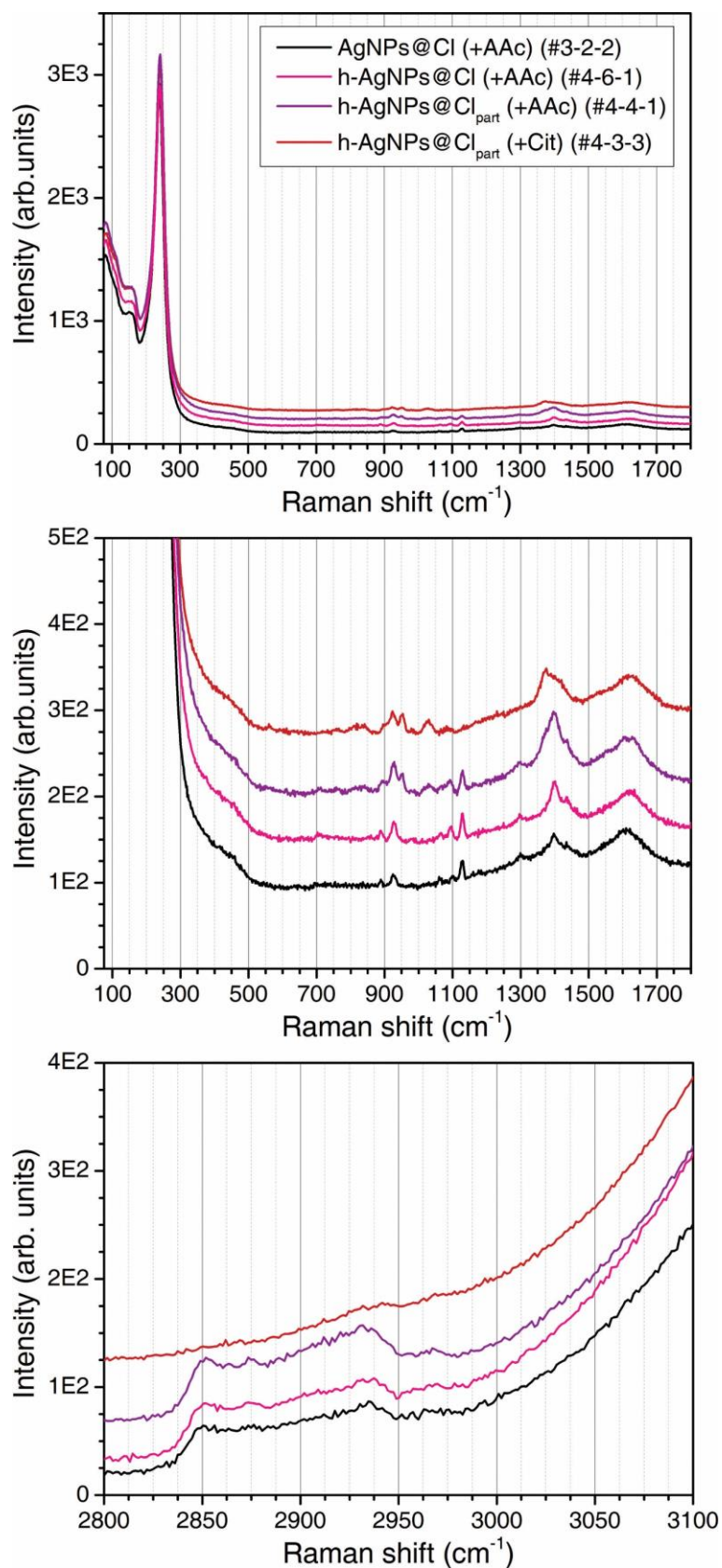
Figure 4.10: Stacked SERS spectra of AgNPs@Cl (+AAc) (#3-2-2), h-AgNPs@Cl (+AAc) (#4-6-1), h-AgNPs@Cl$_{part}$ (+AAc) (#4-4-1), and h-AgNPs@Cl$_{part}$ (+Cit) (#4-3-3).

Last but not least, when the AgNPs@Cl (+AAc) are aggregated using HCl acidified $MgSO_4$ at a final pH = 3 (which inevitably increases [Cl⁻] to 2.25 mM), the AAc peaks are barely identifiable, leaving the ν(Ag–Cl) and water peaks as the only strong features (Figure 4.11, #4-8-1). With its pKa at 3.58, most AAc⁻ anions are protonated to form HAAc, reducing their binding potency to Ag atoms. In addition, HAAc is unstable and may readily decompose into acetone and carbon dioxide [225]; the decomposition could also be accelerated by the localised heat introduced by the focused laser. One shall also recall that the concentration of the Cl⁻ anion is not relevant to the absence of AAc, as was observed earlier at a higher final concentration ([Cl⁻] = 2.5 mM, #3-1-5).
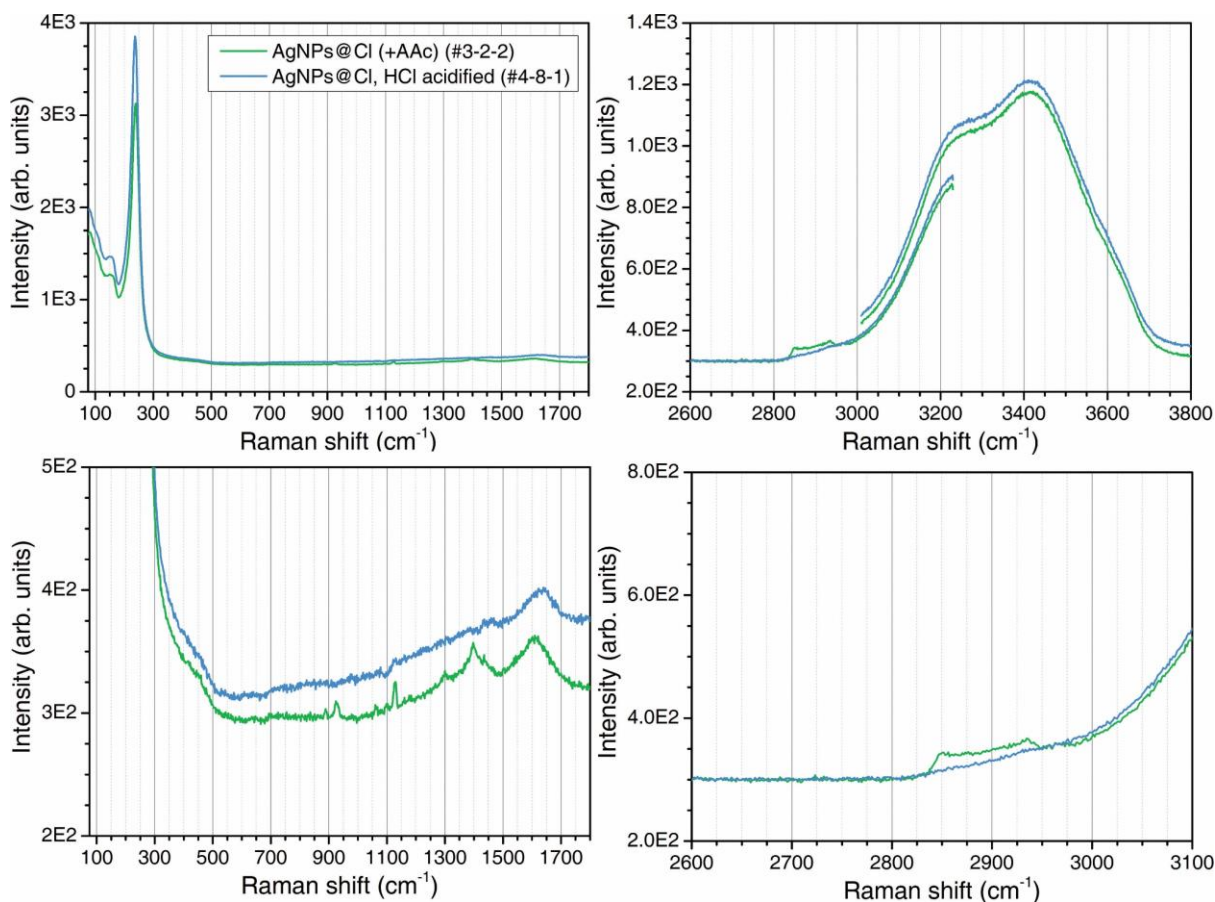
Figure 4.11: Stacked SERS spectra of AgNPs@Cl (+AAc) (#3-2-2) and AgNPs@Cl acidified using HCl (#4-8-1).

Based on the evidence above, we could finally infer that: on the AgNPs after Cl ligand exchange, a near-complete Cl layer forms on the AgNPs, and the negative charge repels Cit anions. The remaining exposed Ag atoms could favour coordinate covalent bonds with the –COO⁻ group in AAc. The resulting coadsorption on the AgNPs can be described more precisely as "AgNPs@Cl/AAc", highlighting the major ligand Cl and the coadsorbed AAc. Figure 4.12 depicts the proposed binding coordination of AAc with exposed Ag atoms on AgNPs@Cl.
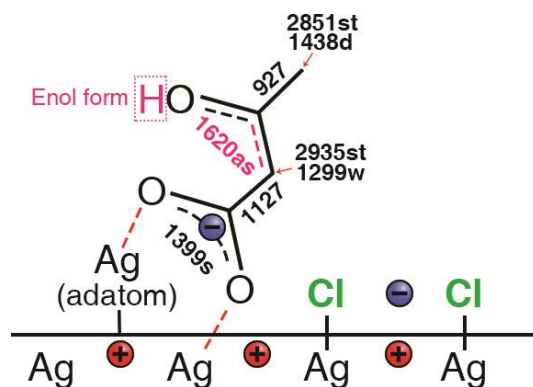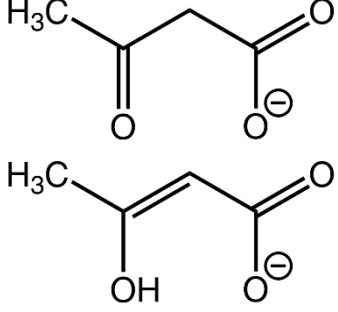
Figure 4.12: Possible binding coordination of AAc with exposed Ag atoms on AgNPs@Cl (#3-2-2). Associated Raman shifts (in the unit of [cm⁻¹]) of the peaks from AAc are labelled next to the corresponding bonds. The red arrow indicates that the peak is assigned to the –CH₂– group. The pink-coloured number, bond, and hydrogen atom highlight the enol form of AAc and the related SERS peak.

Table 4.4: SERS peak assignments of (1) #3-2-2, (2) #4-6-1, and (3) #4-8-1. The species of each vibrational mode is noted based on the information reported in the corresponding reference. Postulated assignments are highlighted with asterisk symbols (*). The SERS modes originating from anionic surfactant (AS) will be explained in Section 4.3.5. General notations refer to Appendix A.

Raman shift (cm^{-1})			Assignment	Reference (cm^{-1})
#3-2-2	#4-6-1	#4-8-1		
AgNPs@Cl + MgSO$_4$ pH = 8 [Cl$^-$] = 1.25 mM	h-AgNPs@Cl + Thermally decomposed Na$_3$Cit + MgSO$_4$ pH = 8 [Cl$^-$] = 1.25 mM [Cit]$_{eq}$ = 0.325 mM	AgNPs@Cl + MgSO$_4$ in 2 mM HCl pH = 3 [Cl$^-$] = 2.25 mM	AAc$^-$, keto form; AAc$^-$, enol form	
3624sh	3619sh	3627sh	ν_s(O–H), water, unbound; [217] Free OH, water; [218]	3627; [217] 3636; [218]
3418	3415	3418	ν_{as}(O–H), water, hydrogen-bonded; [217] DA-OH, water; [218]	3435; [217] 3432; [218]
3228sh	3235sh	3228sh	ν_s(O–H), water, hydrogen-bonded; [217] DDAA-OH, water; [218]	3247; [217] 3226; [218]
2967vw	2968vw		ν_{as}(CH$_3$), methyl acetoacetate; [226]	2962; [226]
2935	2935	2940vw	ν_{as}(CH$_2$), methyl acetoacetate; [226] ν_s(CH$_2$), methyl acetoacetate; [226]	2942; [226] 2930; [226]
2849	2851	2856vw	ν_s(CH$_3$), methyl acetoacetate; [226]	2849; [226]
		1640	δ(HOH), water; [227]	1641; [227]
1610	1620		ν(O–C=C), enol form, methyl acetoacetate; [226]	1627; [226]
		1450vw	*δ(CH$_2$), anionic surfactant (AS);	
1436sh	1437		n.a., acetoacetic acid,; [208] δ_s(CH$_3$), methyl acetoacetate; [226]	1442; [208] 1453; [226]

1398w	1399		n.a., acetoacetic acid; [208] *ν_s(COO⁻);	1400; [208]
1299w	1299		n.a., lithium acetoacetate; [228] ω(CH$_2$), methyl acetoacetate; [226]	1283; [228] 1317; [226]
1128	1127		ν(CCC), methyl acetoacetate; [226] n.a., lithium acetoacetate; [228]	1158; [226] 1158; [228]
1098vw	1095		n.a., acetoacetic acid; [208] n.a., lithium acetoacetate; [228]	1085; [208] 1087; [228]
1062w	1064w			
926w	927		n.a., acetoacetic acid; [208] n.a., lithium acetoacetate; [228] ν(C–CH$_3$), methyl acetoacetate; [226]	935; [208] 928; [228] 903; [226]
889w	889w		n.a., lithium acetoacetate; [228] δ(CCO), methyl acetoacetate; [226]	903; [228] 875; [226]
434sh	448sh		ν(Ag–O), subsurface; [215]	464; [215]
239	240	237	ν(Ag–Cl); [209] ν(Ag–Cl); [196] ν(Ag–Cl); [220]	245; [209] 243; [196] 240; [220]
155sh	160sh	155sh	Ag lattice vibration; [221]	147; [221]

4.3.5 AgNPs@Br and AgNPs@I

In the case of Br ligands, similar attempts were carried out using KBr to achieve the optimal concentration and time for sufficient ligand exchange, and the resulting SERS spectra are displayed in Figure 4.13.

An initial sample was treated at a very low concentration at $[Br^-]$ = 0.0125 mM (added $[KBr]_{added}$ = 0.05 mM, #5-1-1) and shows almost identical fingerprint signals as the untreated AgNPs@Cit (#2-1-1), apart from the emerging shoulder peak at 162 cm^{-1} and the distinct shoulder peak at 2845 cm^{-1}.

Increasing the concentration to $[Br^-]$ = 0.25 mM (added $[KBr]_{added}$ = 1 mM, #5-1-2) leads to dramatic changes in the spectra that are different from either AgNPs@Cit (#2-1-1) or AgNPs@Cl/AAc (#3-2-2). Prominent peaks are observed at 2926 cm^{-1}, 2896 cm^{-1}, 2845 cm^{-1}, 2723 cm^{-1}, 1590 cm^{-1}, 1461 cm^{-1}, 1440 cm^{-1}, 1302 cm^{-1}, 1128 cm^{-1}, and 720 cm^{-1}, as well as the characteristic ν(Ag–Br) peak at 162 cm^{-1}; vaguely resolvable peaks are also observed to centre at 3067w cm^{-1}, 1718w cm^{-1}, and 1253w cm^{-1}. The sharp peak at 162 cm^{-1} gives us confidence that the ligand exchange occurs successfully. It is also confirmed that the above peaks stay unchanged with doubled concentration at $[Br^-]$ = 0.5 mM ($[KBr]$ = 2 mM, #5-1-3), and the exposure time can be reduced to 5 min (#5-2-2) without affecting the ligand exchange.
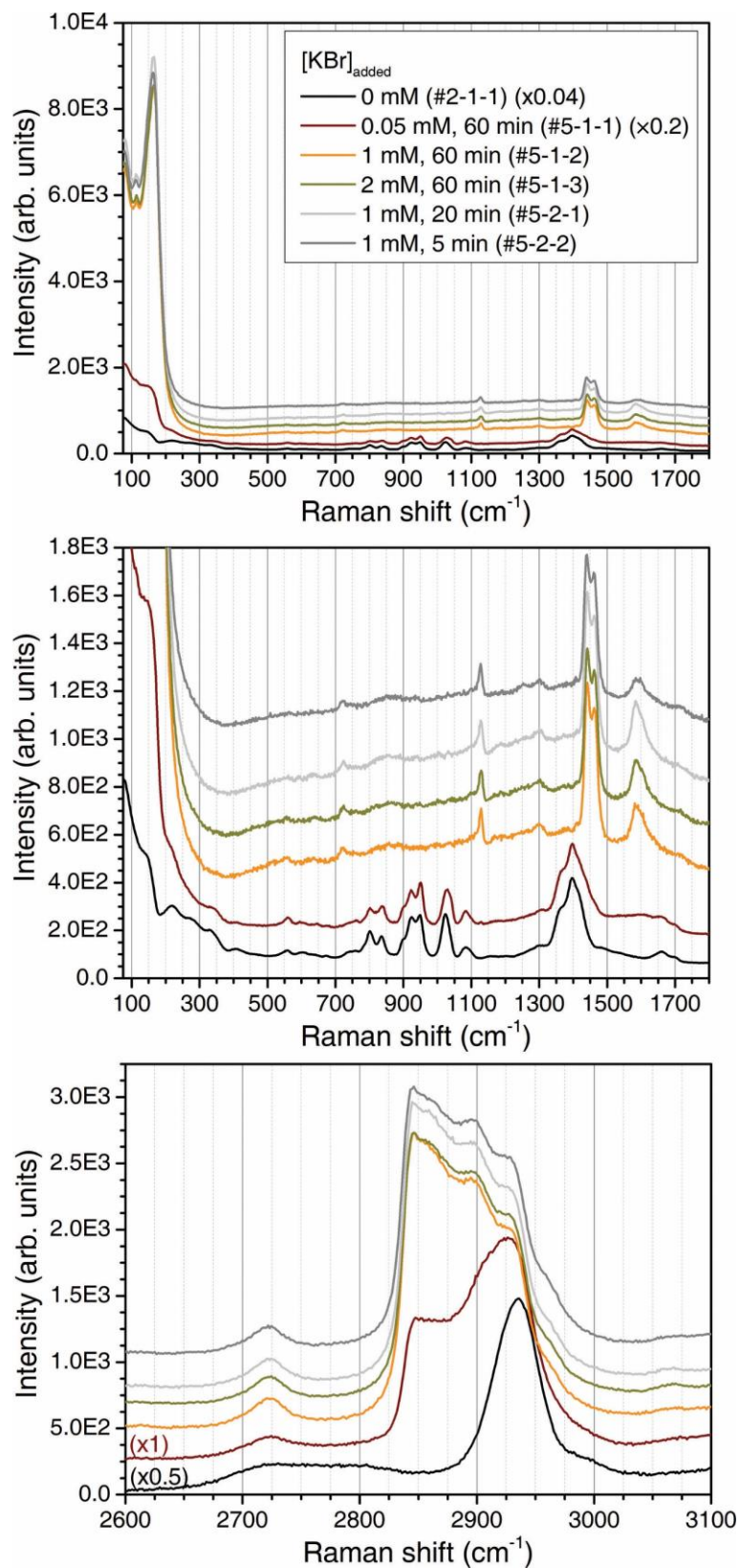
Figure 4.13: Stacked SERS spectra of the KBr ligand exchange series (#5-1-z and #5-2-z). The concentrations of the stock solutions added ([KBr]$_{added}$) include 0 mM (#2-1-1) (×0.04, ×0.04, ×0.5), 0.05 mM (#5-1-1) (×0.2，×0.2，×1), 1 mM (#5-1-2, #5-2-1, and #5-2-2), and 2 mM (#5-1-3).

Upon treatments using KI, we observe a similar trend compared to KBr regarding the concentration and time required to achieve sufficient ligand exchange on the AgNPs (Figure 4.14). Interestingly, most of the peaks from #5-2-2 are also identified upon a sufficient I ligand exchange (#6-2-2), although differences include:

(1) Diminished weak features at 1253w cm^{-1} and 1590 cm^{-1};
(2) Rising peaks at 1650w cm^{-1} and 1165w cm^{-1};
(3) The distinctive peak at 110 cm^{-1} from ν(Ag–I) in replacement of the ν(Ag–Br) peak;

With the strong peaks from ν(Ag–Br) and ν(Ag–I), based on a similar rationale as in the case of KCl, the background SERS signals could be attributed to the incomplete coverage on the Ag surface by Br or I ligands, leaving gaps of suitable sizes for species to coadsorb. Henceforward, #5-2-2 and #6-2-2 are temporarily denominated as "AgNPs@Br" and "AgNPs@I" to highlight the major ligands while pending of identifying the coadsorbed species. Moreover, the prominent residual peaks after Br or I ligand exchange show no resemblance to the AAc peaks in AgNPs@Cl (#3-2-2), suggesting a likely different origin to be studied.

A quick comparison of Br and I ligand exchange with Cl ligand exchange is worthy of giving regarding the concentrations required. At [Cl$^-$] = 0.25 mM (#3-1-1), the spectra remain similar to the AgNPs@Cit (#2-1-1); however, at [Br$^-$] or [I$^-$] = 0.25 mM (#5-2-2 or #6-2-2), the exchange occurs sufficiently. Further, at a low concentration of [I$^-$] = 0.0125 mM (#6-1-1), a very strong peak at 2842 cm^{-1} is observed, while at [Br$^-$] = 0.0125 (#5-1-1), the peak only appears as a shoulder next to the strong 2934 cm^{-1} peak from Cit. The required concentration for ligand exchange accords with the solubility product constants of silver halide salts (K$_{sp}$); the latter inversely reflects the binding affinities of the halides to Ag [229]: Cl < Br < I.

However, the SERS signals in AgNPs@Br or AgNPs@I are considerably stronger than those of AgNPs@Cl/AAc, which seems to contradict the binding affinity sequence above. One possible explanation stands on the possibly larger gaps between Br or I ligands on the Ag surface compared with Cl ligands, suggested by a previous study by Espinoza *et al.* [222], in which they mention that Br or I ligands form a "porous" layer on the AgNPs to provide less of a barrier effect to the diffusion of species during oxidative decomposition of AgNPs.
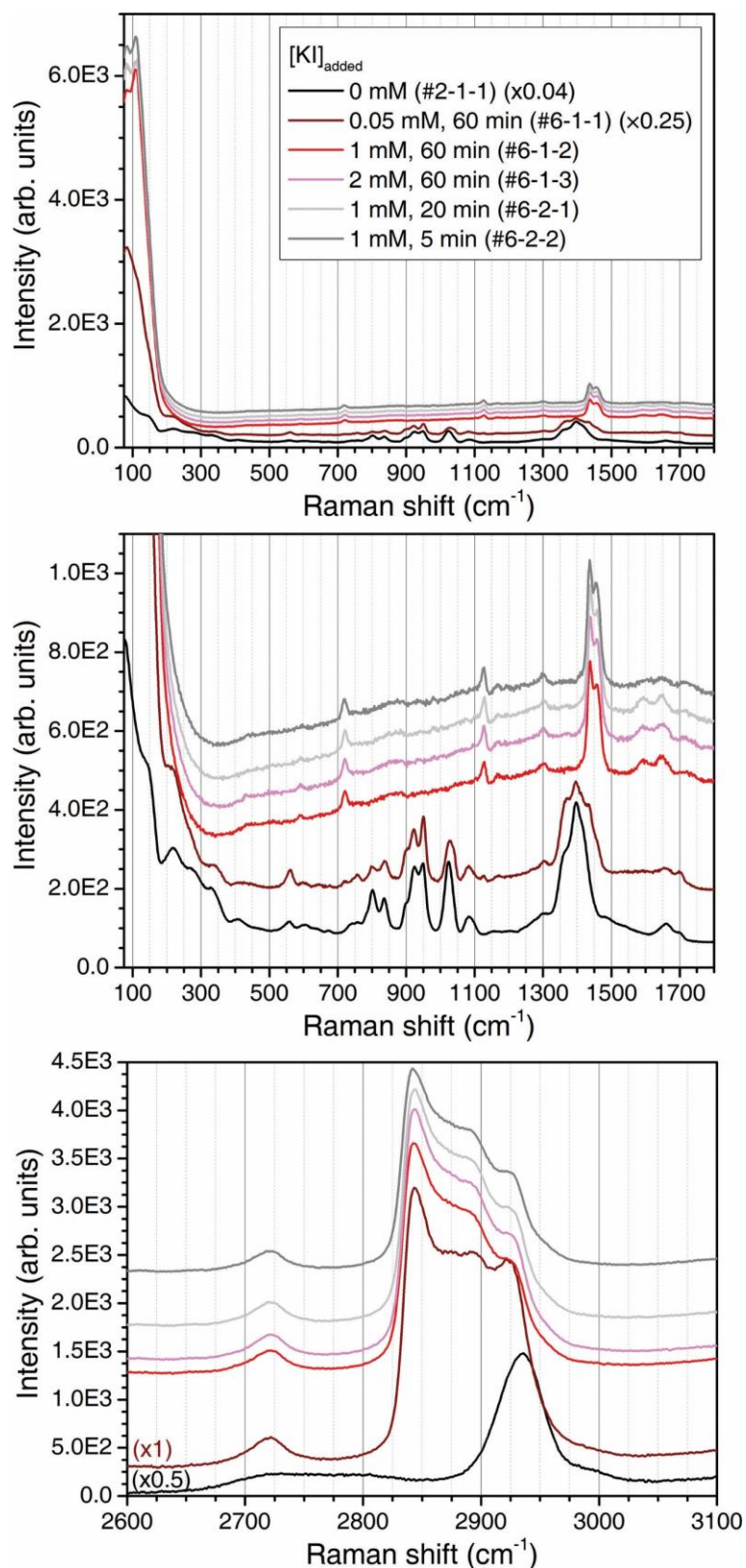
Figure 4.14: Stacked SERS spectra of the KI ligand exchange series (#6-1-z and #6-2-z). The concentrations of the stock solutions added ([KI]$_{added}$) include 0 mM (#2-1-1) (×0.04, ×0.04, ×0.5), 0.05 mM (#6-1-1) (×0.25, ×0.25, ×1), 1 mM (#6-1-2, #6-2-1, and #6-2-2), and 2 mM (#6-1-3).

Now we proceed to the attempts to identify the coadsorbed species on the Br or I ligand layers. Again, the citrate-free h-AgNPs were used to exclude the association with Cit. The intrinsic partial layer of Cl introduced during the synthesis is readily displaced by Br and I ligands, indicated by the arisen ν(Ag–Br) and ν(Ag–I) peaks (Figure 4.15). However, in sharp contrast to h-AgNPs@Cl$_{part}$ (#4-1-1), the spectra of h-AgNPs@Br (#7-1-1) and h-AgNPs@I (#7-2-1) show identical strong features to the ones from citrate-reduced AgNPs (#5-2-2 and #6-2-2). This evidence rules out the relevance of the signals with Cit or its thermal decomposition products.
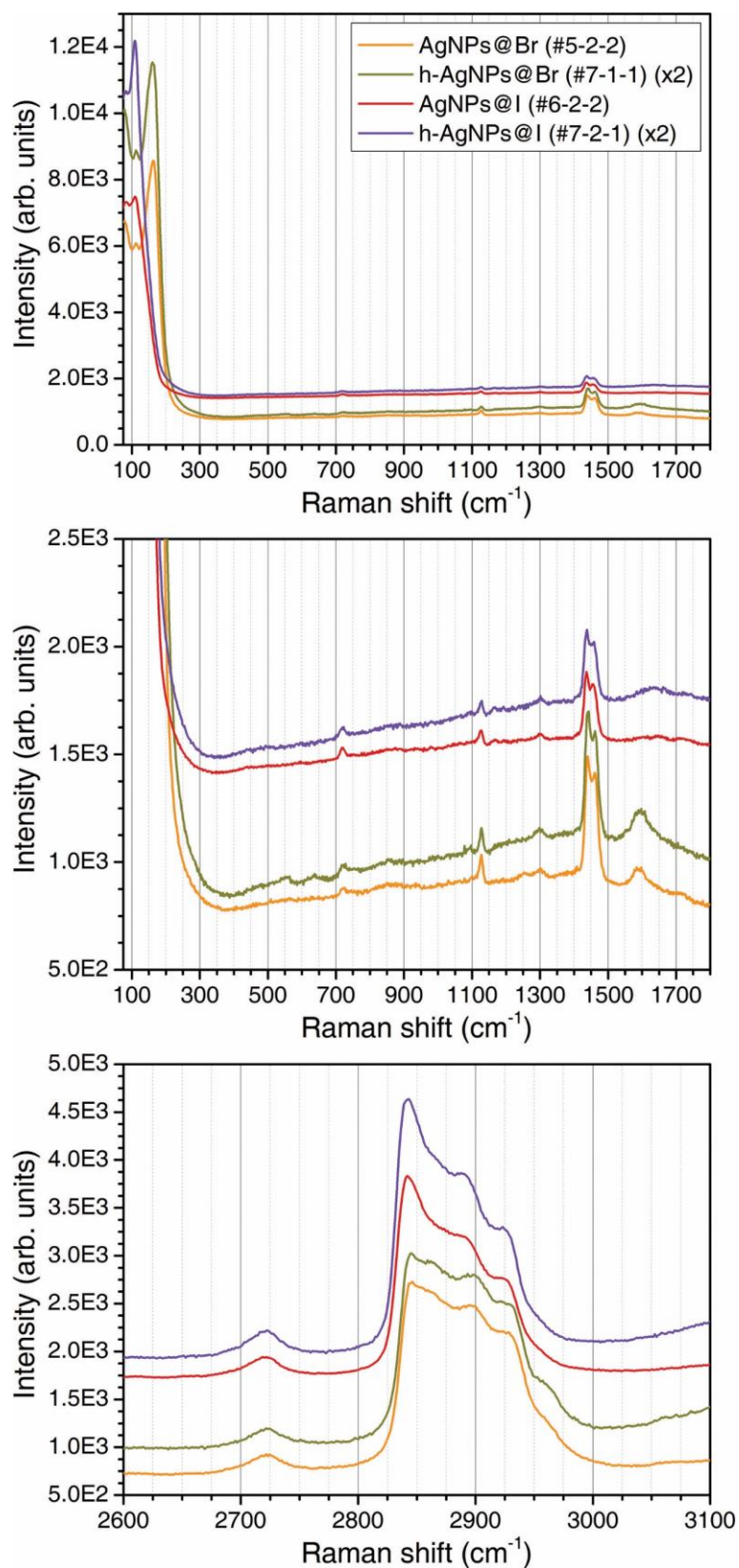
Figure 4.15: Stacked SERS spectra of h-AgNPs@Br (#7-1-1) (×2) and h-AgNPs@I (#7-2-1) (×2) in comparison with AgNPs@Br (#5-2-2) and AgNPs@I (#6-2-2).

Similarly, following the method of exclusion, we referred to the common species introduced during the syntheses of the citrate-reduced AgNPs and the citrate-free h-AgNPs. There are, in fact, only a handful of choices, within which the most plausible ones are NO_3^- [230-232] and CO_3^{2-} [215, 233] (which could exist in low amounts in any basic solutions), but neither of them provides spectra close to our observations. Even the option of bound H_2O molecules being the source of the peaks is also considered. However, the assumption is rejected by the samples prepared in D_2O/H_2O mixture, as shown in Figure 4.16: only the signals from bulk H_2O are changed while all the distinct features are unaffected.
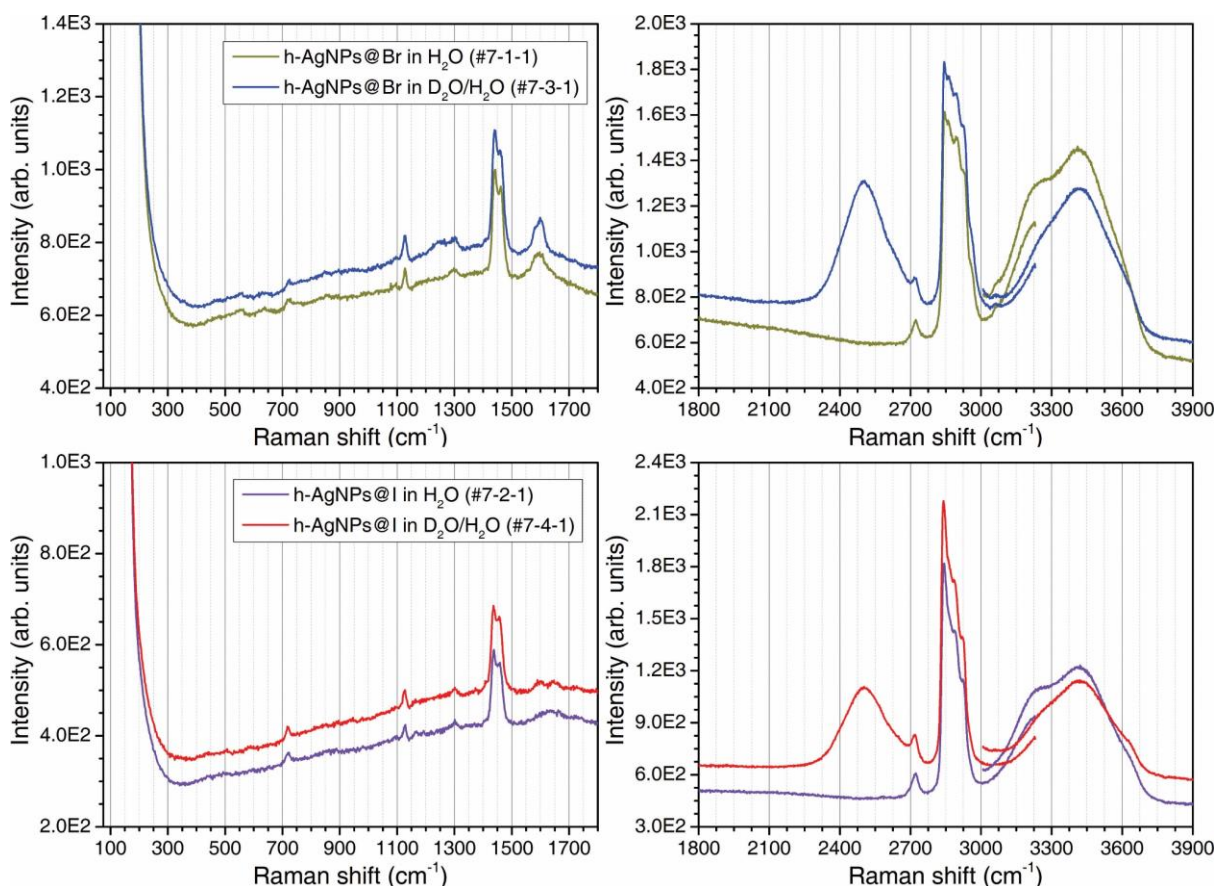
Figure 4.16: Stacked SERS spectra of h-AgNPs@Br and h-AgNPs@I (in D_2O/H_2O mixture) (#7-3-1 and #7-4-1) compared with h-AgNPs@Br and h-AgNPs@I (in H_2O) (#7-1-1 and #7-2-1). D_2O:H_2O = 190:210 ≈ 0.9.

Looking back into the previous studies and comparing them to our results, we discerned some more clues: First, similar sharp doublet peaks at around 1440 cm^{-1} and 1460 cm^{-1} are reported (but not discussed) in several studies on AgNPs or AuNPs with Br or I ligand exchanges [196, 198, 202, 220, 234, 235]. This commonness indicates that the features seem not restricted to a specific experimental condition; in other words, the unidentified species could be largely identical across various aqueous systems.

Secondly, amongst all the studies referred to, only Pepera *et al.* displayed the spectra in the 2800–3000 cm^{-1} region [201]. The multiplet peaks in their KBr or KI treated AuNPs, although

hard to be deconvoluted due to low resolution, are very similar in terms of the intensity ratios compared to our AgNPs@Br and AgNPs@I. Also, in the same study, their KCl-treated AuNPs showed stronger peaks in the 2800–3000 cm^{-1} region, and they used adenine to remove those peaks successfully. Consequently, they suggested that the unknown species are cationic and rich in carbon, oxygen, and sp^3 C–H bonds. In contrast, our h-AgNPs@Cl (Figure 4.9, #4-2-1) show no peaks between 2800 cm^{-1} and 3000 cm^{-1}; hence, we must rule out cations or zwitterions (which would partially bind to the negatively charged surface of h-AgNPs@Cl).

Thirdly, when we aggregate AgNPs@Br or AgNPs@I using HCl acidified MgSO$_4$ at a final pH = 3 (#5-3-1 or #6-3-1), identical spectra are acquired as their neutral counterparts (Figure 4.17). Therefore, the species likely consists of functional groups not sensitive to pH changes to maintain its attachment to the AgNPs upon acidification.
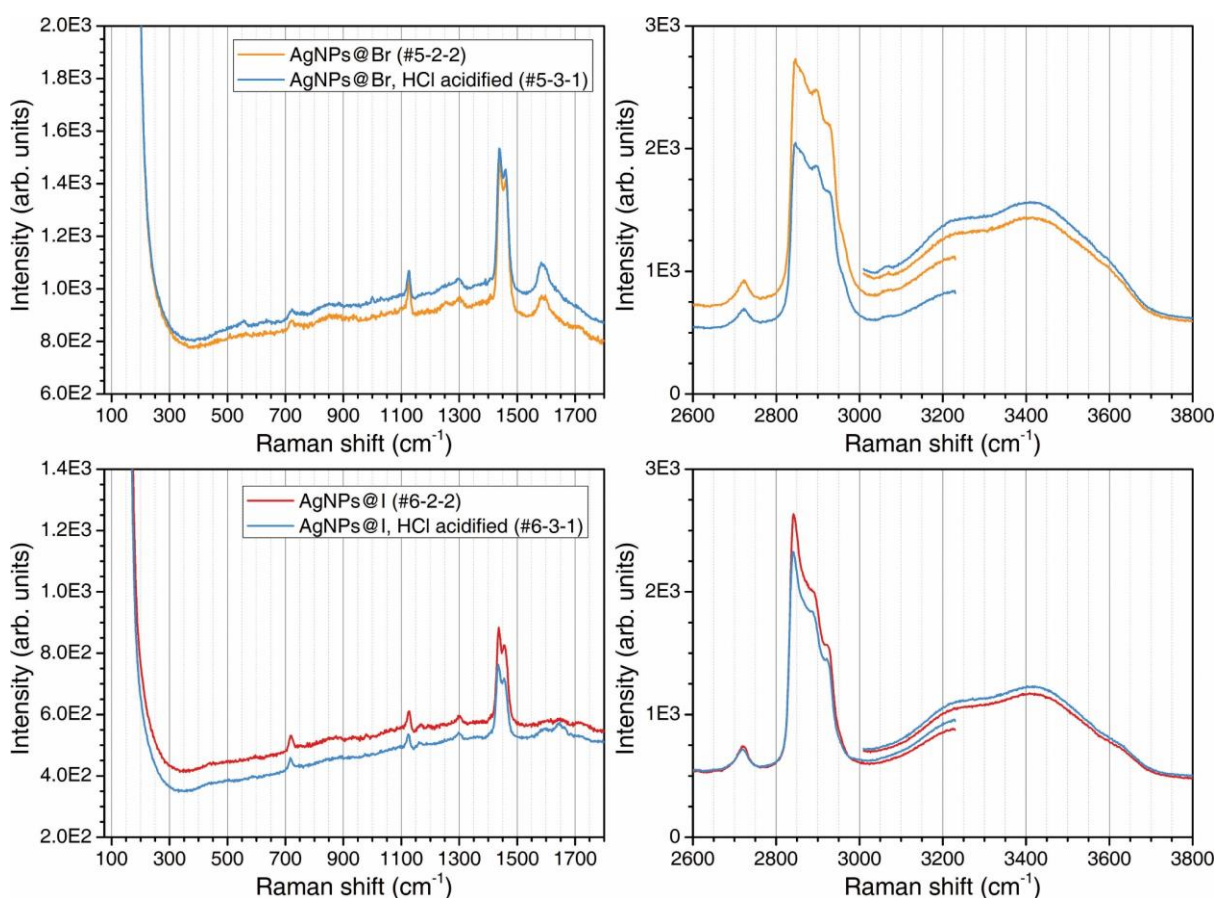
Figure 4.17: Stacked SERS spectra of AgNPs@Br and AgNPs@I (#5-2-2 and #6-2-2) compared to their counterparts acidified using HCl (#5-3-1 and #6-3-1).

As a quick summary, the coadsorbed species need to meet the following criteria:

(1) Universal and soluble in aqueous solutions;
(2) Weakly anionic (otherwise repelled) or non-ionic, but unlikely cationic;
(3) Without many O–H or N–H bonds (otherwise, peaks shift with D_2O exchange);
(4) Structurally simple (*e.g.*, small molecules) or with repetitive units (*e.g.*, polymers) because the spectra only consist of a few distinct peaks instead of many peaks;

Based on these elements and our SERS spectra, we postulate that the species in our system is an anionic surfactant (AS) present as a residue in the water. This postulation was based on the spectral evidence presented in this study that rejects Cit and other potential species being the origin of the signals, as well as the matching results in previous studies that highlight this phenomenon as being universal and could be related to species lower than the detection limit of other techniques [201, 202]. Such an AS should contain ether groups (–C–O–C–) to support coordinative binding to Ag atoms. Polyoxyethylene alkyl ether carboxylic acid could be a suitable candidate [236] with its general structure motif including a hydrophobic alkyl (–CH_2–) chain, several hydrophilic ethylene oxide (–CH_2CH_2O–) units, and a terminating carboxymethyl (–CH_2COOH) group. This type of molecule has a generic molecular formula of $CH_3(CH_2)_iCH_2O(CH_2CH_2O)_jCH_2COOH$ or, in short, $C_iE_jCH_2COOH$, with the i and j being arbitrary integers larger than 4.

Hence, the peaks from AS on AgNPs@Br can be assigned as follows: 2926 cm^{-1} ($\nu_s(CH_3)$), 2896 cm^{-1} ($\nu_{as}(CH_2)$), 2845 cm^{-1} ($\nu_s(CH_2)$), 2723 cm^{-1} ($\tau(CH_2) + \delta(CH_2)$, a combination mode), 1590 cm^{-1} ($\nu_{as}(COO^-)$, $\varkappa^2$), 1461 cm^{-1} ($\delta_s(CH_2)$, ether), 1440 cm^{-1} ($\delta_s(CH_2)$, alkyl), 1302 cm^{-1} ($\tau(CH_2)$), 1128 cm^{-1} ($\nu(C–C)$), and 720 cm^{-1} ($\rho(CH_2)$, alkyl) (Table 4.5, #5-2-2) [237-241]. The different features from AS on AgNPs@I at 1650w cm^{-1} can then be assigned to $\nu(C=O)$ of bound $\varkappa^1$-COO$^-$, whereas the 1165w cm^{-1} peak can be related to the $\nu(C–O)$ in ether units (Table 4.5, #6-2-2).

Furthermore, considering the C–H bond-related peaks at 2925 cm^{-1}, 2891 cm^{-1}, and 2842 cm^{-1}, we found a much higher intensity of 2842 cm^{-1} over the other two peaks in the AS spectra on AgNPs@I compared with AgNPs@Br (Figure 4.18). In addition, blueshifts were identified not only in the above three peaks but also in the doublet at 1461 cm^{-1} and 1440 cm^{-1} ($\Delta = -5$ cm^{-1}) (Figure 4.18). The shifts could indicate the slightly stronger binding affinity of AS to AgNPs@I than AgNPs@Br.
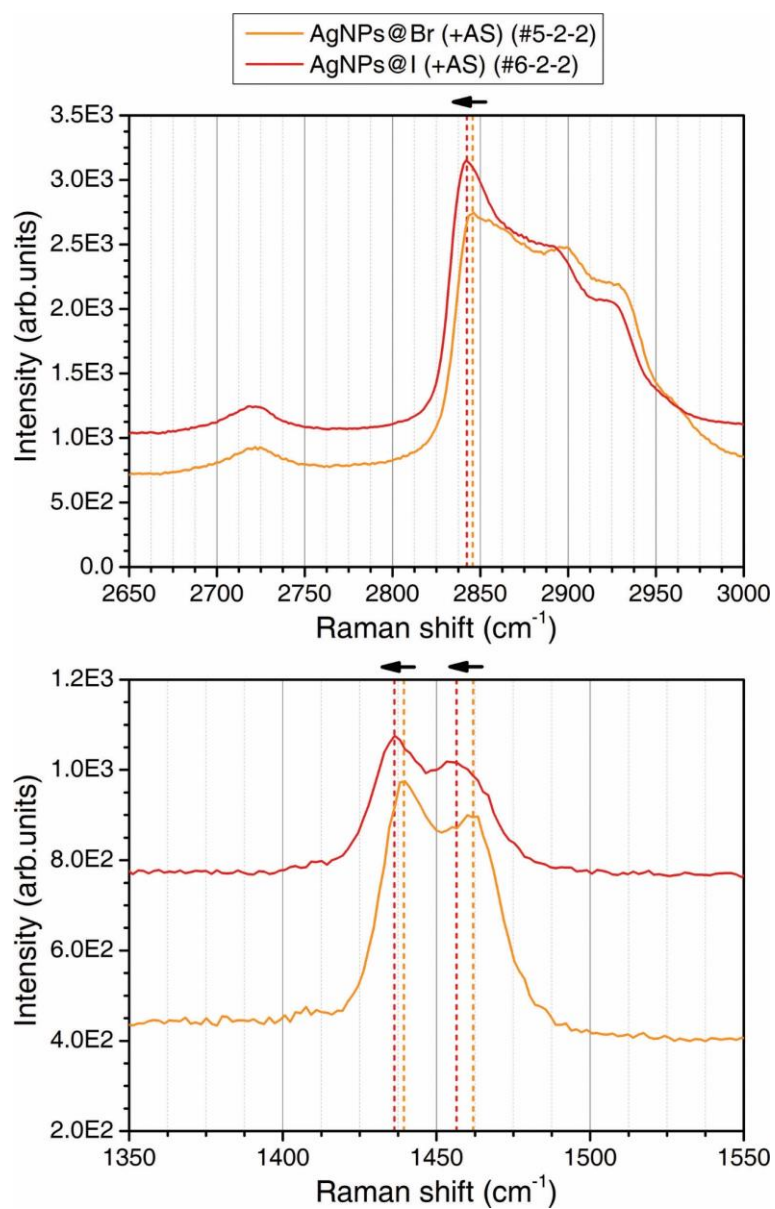
Figure 4.18: Stacked SERS spectra of AgNPs@Br (+AS) (#5-2-2) and AgNPs@I (+AS) (#6-2-2) highlighting the peak shifts.

In summary, we propose that upon Br or I ligand exchange, the adsorption of AS overtakes that of AAc to become the preferred coadsorbed species on the AgNPs, probably due to its lower charge density. The –COO⁻ and –C–O–C– groups can bind to Ag atoms at the presumably larger gaps in the Br or I ligand layer. The resistance to desorption under acidic conditions may be explained by the binding to Ag atoms via the –C–O–C– group. The resulting coadsorption can be described better as "AgNPs@Br/AS" and "AgNPs@I/AS", with their proposed binding coordination with exposed Ag atoms depicted in Figure 4.19.
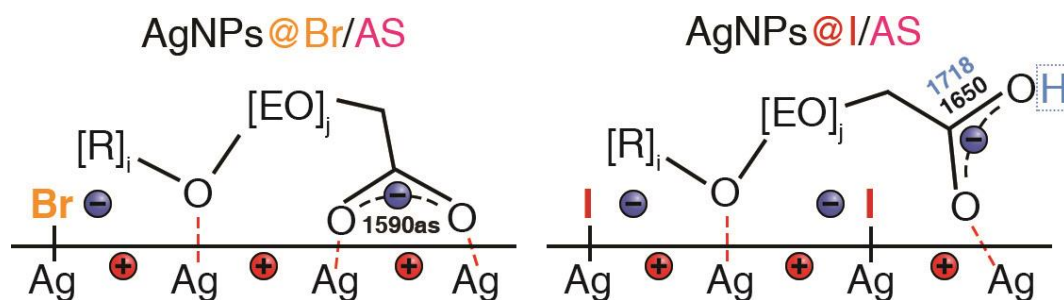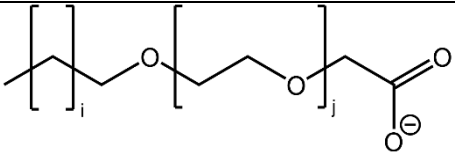
Figure 4.19: Possible binding coordination of AS with exposed Ag atoms on AgNPs@Br and AgNPs@I (#5-2-2 and #6-2-2). The different Raman feature (in the unit of [cm⁻¹]) between AgNPs@Br and AgNPs@I is labelled next to the corresponding C–O bonds. The blue-coloured numbers and the hydrogen atom highlight the potential protonation of the –COO⁻ group into a –COOH group and the associated SERS peak. (EO = ethylene oxide unit; R = alkyl chain.)

Table 4.5: SERS peak assignments of (1) #5-2-2, (2) #5-3-1, (3) #6-2-2, and (4) #6-3-1. The species of each vibrational mode is noted based on the information reported in the corresponding reference. Postulated assignments are highlighted with asterisk symbols (*). General notations refer to Appendix A.

Raman shift (cm^{-1})				Assignment	Reference(cm^{-1})
#5-2-2	**#5-3-1**	**#6-2-2**	**#6-3-1**		
AgNPs@Br + MgSO$_4$ pH = 8	**AgNPs@Br + MgSO$_4$ in 2 mM HCl pH = 3**	**AgNPs@I + MgSO$_4$ pH = 8**	**AgNPs@I + MgSO$_4$ in 2 mM HCl pH = 3**	alkyl chain + ethylene oxide units + carboxylate group in AS	
3612sh	3618sh	3622sh	3622sh	ν_s(O–H), water, unbound; [217] Free OH, water; [218]	3627; [217] 3636; [218]
3416	3412	3420	3421	ν_{as}(O–H), water, hydrogen-bonded; [217] DA-OH, water; [218]	3435; [217] 3432; [218]
3221sh	3219sh	3222sh	3219sh	ν_s(O–H), water, hydrogen-bonded; [217] DDAA-OH, water; [218]	3247; [217] 3226; [218]
3067w	3064w				
2960sh	2960sh			ν_{as}(CH$_3$), polyethylene (PE); [238] ν_{as}(CH$_3$), poly(propylene oxide) (PPO); [239] ν_{as}(CH$_3$), triacylglycerols; [241]	2960–2965; [238] 2970; [239] 2957–2965; [241]
2926	2924	2925sh	2921sh	ν_s(CH$_2$)$_{FR}$, PE; [238] ν_s(CH$_3$), PPO; [239] ν_s(CH$_3$), fatty acids; [241]	2925; [238] 2930; [239] 2909–2937; [241]
2896	2895	2891sh	2886sh	ν_{as}(CH$_2$), PE; [238] ν_{as}(CH$_2$), poly(ethylene oxide) (PEO); [239] ν_{as}(CH$_2$), fatty acids; [241]	2881–2886; [238] 2880; [239] 2870–2895; [241]
2861sh	2860sh			ν_s(CH$_2$), fatty acids; [241]	2852–2862; [241]

2845	2844	2842	2841	$\nu_s(CH_2)$, PE; [238] $\nu_s(CH_2)$, PEO; [239] $\nu_s(CH_2)$, fatty acids; [241]	2847–2852; [238] 2850; [239] 2832–2845; [241]
2723	2721	2720	2719	*Combination mode of $(\tau(CH_2) + \delta(CH_2))$;	*1300 + 1440 = 2740;
1718w	1714vw	1718vw	1722vw	$\nu(C=O)$, –COOH, triacylglycerols; [241] *$\nu(C-OH)$, –COOH;	1727–1730; [241]
		1650w	1646	$\nu(C=C)$, unsaturated fatty acid; [241] *$\nu(C=O)$, $\varkappa^1$-COO$^-$;	1653–1672; [241]
1590	1587	1596w	1591sh	$\nu_{as}(COO^-)$, potassium n-alkyl carboxylate; [237] *$\nu_{as}(COO^-)$, $\varkappa^2$;	1580–1600; [237]
1461	1460	1455	1456	$\delta_s(CH_2)$, potassium n-alkyl carboxylate; [237] $\delta_{as}(CH_3)$, PE; [238] $\delta_s(CH_2)$, PEO; [239] $\delta(CH_2)$, $\delta(CH_3)$, fatty acids; [241]	1450–1465; [237] 1445–1450; [238] 1470; [239] 1457–1464; [241]
1440	1439	1436	1434	$\delta(CH_2)$, PE; [238] $\delta_s(CH_2)$, PEO; [239] $\delta_s(CH_2)$, fatty acids; [241]	1440–1441; [238] 1448; [239] 1433–1445; [241]
1302	1299	1300	1299	$\nu(CH_2-CH_2)$, potassium n-alkyl carboxylate; [237] $\tau(CH_2)$, PE; [238] $\tau(CH_2)$, fatty acids; [241]	1290–1300; [237] 1295–1302; [238] 1294–1306; [241]
1253w	1251w			$\tau(CH_2)$, PEO; [239] $\delta(=C-H)$, fatty acid; [241]	1232; [239] 1260–1265; [241]
		1166w	1165w	$\nu(C-O)$, PEO; [239] $\nu(C-C)$, fatty acid; [241]	1141; [239] 1166–1179; [241]
1128	1126	1125	1124	$\nu(C-C)_T$, PE; [238] $\nu(C-C)$, $\omega(CH_2)$, PEO; [239] $\nu(C-C)$, fatty acid; [241]	1124–1128; [238] 1125; [239] 1118–1133; [241]
	1000vw				
720	720	719	719	$\rho(CH_2)$, aliphatic polyester; [240]	720; [240]

563vw	559w			δ(OCC), PEO; [239]	536; [239]
162	160			ν(Ag–Br); [221] ν(Ag–Br); [196] ν(Ag–Br); [220]	175; [221] 162; [196] 166; [220]
111w	111w				
		110	106	ν(Ag–I), A$_1$ transition in β-AgI polymorph; [221] ν(Ag–I); [196] ν(Ag–I); [220]	103; [221] 118; [196] 127; [220]

141

4.3.6 An Additional Case: AgNPs@S

As was mentioned in the previous section, the SERS signals from AS on AgNPs@Br (#5-2-2) or AgNPs@I (#6-2-2) are stronger than AAc on AgNPs@Cl. Based on this observation, the sequence of surface coverage of the halide ligands is described as Cl > Br ≈ I. We also mentioned that a much larger amount of Cl is required for its best coverage over the AgNPs (*i.e.*, lowest possible SERS intensity from the coadsorbed species) compared to Br or I, giving the same sequence as the binding affinity Cl < Br < I. The common feature here seems to be the halide-induced oxidative decomposition of the AgNPs (the so-called "etching", as halide binding causes decreases in the oxidative potential of Ag^+/Ag redox couple) that creates the porous structure on the surface of the AgNPs.

An additional set of ligand exchange experiments were investigated to validate the assumption that by mixing NaHS with the AgNPs@Cit, the Ag–S bond is formed stronger than all the Ag–X bonds (X = Cl, Br, I) [229]. Stronger etching generates more pores than the AgNPs@I for a stronger SERS signal from (if existing) coadsorbed species. However, the resulting SERS spectra on AgNPs@S stand for the opposite (Figure 4.20): at an optimal final concentration of $[HS^-]$ = 0.05 mM (added $[NaHS]_{added}$ = 0.2 mM), the signal is very weak with only a broad feature at 225 cm^{-1} assignable to $\nu(Ag–S)$ [242], suggesting that no species is coadsorbed with the S ligand layer on the AgNPs. The potential of over-etching leading to the weakening of the SERS effect is also considered and verified using a successful SERS enhancement of collagen using AgNPs@S (Figure 4.20). However, it is also worth mentioning that the overall SERS signals from AgNPs@S generally decrease much more rapidly than AgNPs@X (X = Cl, Br, I), probably indicating its stronger etching effect.
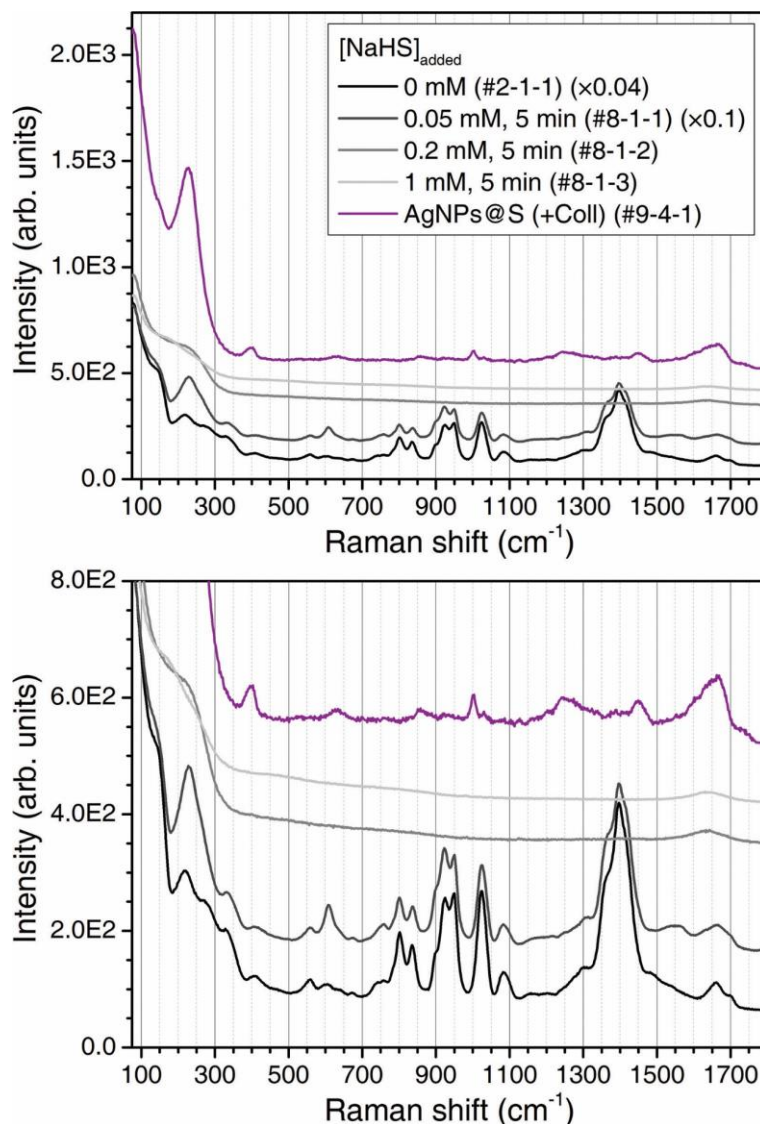
Figure 4.20: Stacked SERS spectra of the NaHS ligand exchange series (#8-1-z). The concentrations of the stock solutions added ([NaHS]$_{added}$) include 0 mM (#2-1-1) (×0.04), 0.05 mM (#8-1-1) (×0.1), 0.2 mM (#8-1-2), and 1 mM (#8-1-3). A collagen-induced aggregation of AgNPs@S (#9-4-1) is also shown to verify its ability on SERS enhancement.

We propose that a synergistic effect of two mechanisms drives the clean SERS background of AgNPs@S. The first is the smaller radius of HS$^-$ (or S^{2-}, 160–170 pm) than Br$^-$ (182 pm) and I$^-$ (206 pm), leading to the better coverage of small gaps, similar to the case of Cl$^-$ (167 pm) [243]. The second is the stronger binding of HS$^-$ (or S^{2-}) with Ag atoms than halides to outperform most of the organic species in this system; a study on thiol-coated AuNPs also observed a complete removal of Cit from the surface [201]. Accordingly, the surface coverage estimation can be expanded as (Cl, S) > (Br, I) (within the brackets are the ligands of the same group with similar surface coverage).

4.3.7 A Quick Revisit: AgNPs@Cl vs h-AgNPs@Cl$_{part}$

Upon revealing the existence of AS in all mixtures, it is important to revisit AgNPs@Cl and h-AgNPs@Cl$_{part}$ to answer a question: why is AS unfavoured to coadsorb to "insufficiently" treated h-AgNPs@Cl$_{part}$?

We mentioned that in AgNPs@Cl, the Cl ligands form a near-complete layer over the Ag surface. If the intrinsically Cl ligand coated h-AgNPs give an inadequate coverage, AS should be favoured to coadsorb as in the cases of Br or I ligand covered h-AgNPs@Br or h-AgNPs@I. The opposite results thus imply that the intrinsic surface coverage of Cl ligands on h-AgNPs is not "partial" (as in the temporary name "h-AgNPs@Cl$_{part}$") but is closer to a near-complete coverage as in AgNPs@Cl.

Considering stoichiometry, the halide ligands required to cover the Ag surface should not vary significantly across Cl, Br, and I; the amount required to form a complete monolayer is much lower than our usage [209]. However, it is the competition with Cit in AgNPs that resulted in a higher [Cl$^-$] needed to give a maximum (near-complete) surface coverage compared to h-AgNPs. Further comparisons of [Cit] with [Cl$^-$], [Br$^-$], and [I$^-$] reveal that Cit has a comparable affinity to Ag atoms as Cl, while the affinity of either Cit or Cl is much lower than Br or I.

4.3.8 Collagen vs Residual Species: Competitive Coadsorption

Now, with a comprehensive understanding of the coadsorbed species on halide-coated AgNPs, we can confidently analyse the SERS spectra of collagen even if interfered with by the background signals.

To acquire the SERS spectra of collagen in a solution, we need to aggregate the AgNPs to the collagen molecules. Due to the positive charge of the collagen molecules in HCl solution at pH = 3 [244, 245], mixing the collagen solution with the negatively charged AgNPs@X (X = Cl, Br, I, S) will immediately trigger the aggregation of AgNPs@X. It is worthy of emphasising at this point that, for ligand exchange, the results can be adversely affected if the added salt concentration is overly high to trigger a localised aggregation. Therefore, we carefully determined the added salt concentrations and followed a 1:1 mixing (half-half dilution) method to mitigate this potential adverse effect [246]. The same practice was strictly carried out when triggering the charge-driven aggregation between AgNPs@X and collagen for mitigating inhomogeneity in SERS enhancement.

The aggregation of AgNPs@X with collagen follows a similar mechanism as a previously reported nanoparticle/protein system, AuNPs@Cit/Hb (Hb = haemoglobin) [247]. When the mixing volumes are controlled (in our study, 200 µL + 200 µL), the resulting size of the aggregates is dependent on the concentration ratio [Coll]/[AgNPs] in the final mixture. With the [AgNPs] fixed, we applied six different [Coll] covering a wide range, with each two representing one aggregation mechanism to include all possible states. Figure 4.21 shows the

UV-Vis spectra of AgNPs@Cl before and after aggregations triggered by collagen at a series of final concentrations.

At [Coll] = 0.5 µg/mL or 1 µg/mL, each collagen molecule is surrounded by the maximum number of AgNPs allowed, named "maximum aggregation", while excess AgNPs stay around to contribute to the negative-negative charge repulsion, ensuring the stability of the new heterogeneous colloidal solution (*i.e.*, the mixture of AgNPs/Coll clusters and excessive discrete AgNPs). In this scenario, the original yellow solution will turn to slightly darker yellow, observed in UV-Vis spectra as the decreases in the original LSPR peak and the moderate increases in the long wavelength region. The heterogeneous colloidal solution will stay stable for a sufficiently long period for the SERS measurements.

At [Coll] = 2.5 µg/mL or 5 µg/mL, the AgNPs and collagen aggregate rapidly, and the unstable clusters continue to grow until all the NPs or collagen are consumed, referred to as "infinite clustering". The clusters formed in such a way generally have large and non-uniform sizes [247], observed as a significant decrease in the original LSPR peak while showing a broad peak centring at around 700 nm. The metastable state during the progressive aggregation before the equilibrium can still be captured using SERS for good spectral resolution and excellent initial enhancement, while the signal intensity constantly decreases and often disappears within 1 h. Therefore, this concentration range is the least suitable for the SERS analyses of collagen.

At [Coll] = 10 µg/mL or 25 µg/mL, collagen triggers "self-terminated aggregation" of the AgNPs, resulting in finite-sized clusters surrounding the collagen molecules. The excess collagen molecules stabilise the clusters by providing sufficient positive-positive charge repulsion in the solution. Such aggregation is observed in the UV-Vis spectra as moderate decreases in the LSPR peak, increasing mainly in the 500–600 nm region but less in longer wavelength regions. The clusters are at the highest stability in this scenario among all the three, yet the aggregation would not be as uniform as the lowest concentration, as it is kinetically driven by the instant capturing of the AgNPs when they encounter the introduced collagen molecules. Hence, the amount of AgNPs attaching to each collagen molecule decreases as the [Coll] increases (compare #9-1-5 with #9-1-6 in Figure 4.21), leading to poor or no aggregation at excessively high concentrations.
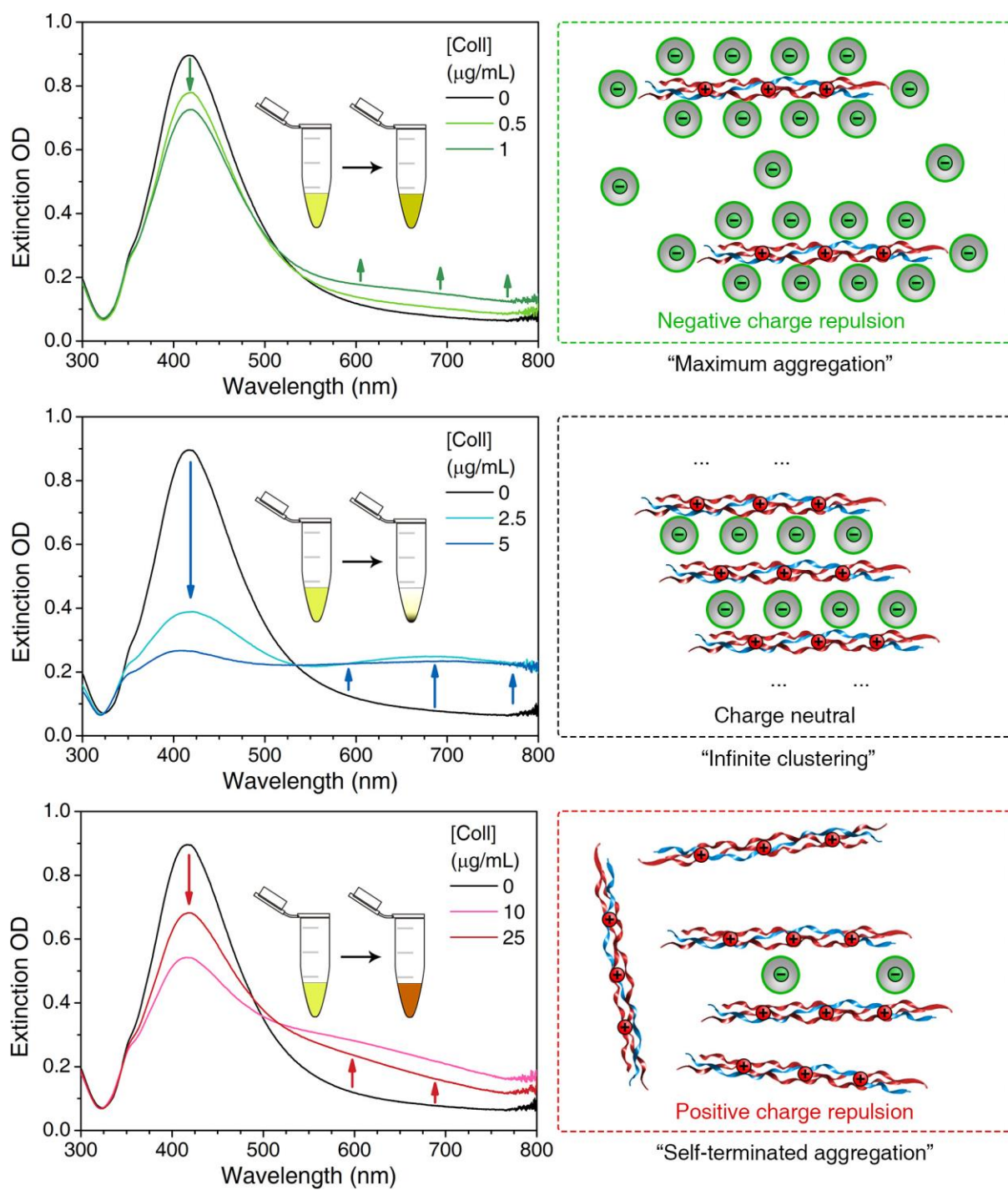
Figure 4.21: UV-Vis extinction spectra before and after the aggregation of AgNPs@Cl with collagen. Insets demonstrate expected colour changes on aggregation. The schematic illustrations for the proposed aggregation mechanisms are shown next to the spectra.

Note that changing the ligand from AgNPs@Cl to AgNPs@Br or AgNPs@I would not affect the mechanisms, yet the degree of aggregation could be slightly different due to the varied negative charge on a unit surface [248-250].

Regardless of the aggregation state, we observe distinct features in the SERS spectra of AgNPs@Cl, AgNPs@Br and AgNPs@I when they mix with collagen (temporarily denominated as "AgNPs@X/Coll", X = Cl, Br, I), highlighting the binding competition between collagen and the existing coadsorbed species.

In AgNPs@Cl/Coll, no residual SERS peaks are observed in addition to the collagen signals (Figure 4.22), consistent with the similarly acidified $MgSO_4$ aggregated AgNPs@Cl (#4-8-1). Changes in concentration (although leading to dramatically different aggregation) do not affect the binding of collagen to AgNPs@Cl nor the SERS spectra. For instance, the observed SERS peaks at the highest [Coll] = 25 µg/mL (Table 4.6, #9-1-6) are assignable based on dry collagen Raman spectra: 2934 cm^{-1} ($\nu(CH_3)$; $\nu(CH_2)$), 2877 cm^{-1} ($\nu_s(CH_3)$), 1731 cm^{-1} ($\nu(C=O)$, in –COOH of Asp or Glu), 1670 cm^{-1} (Amide I ($\nu(C=O)$, β-sheet); $\nu_{as}(COO^-)$), 1636 cm^{-1} (Amide I ($\nu(C=O)$, 3_{10}-helix); $\nu_{as}(COO^-)$), 1444 cm^{-1} ($\delta(CH_3)$; $\delta(CH_2)$), 1410 cm^{-1} ($\nu_s(COO^-)$), 1384 cm^{-1} ($\nu_s(COO^-)$), 1321 cm^{-1} ($\tau(CH_3)$; $\tau(CH_2)$), 1264 cm^{-1} (Amide III, $\delta(N–H)$), 1244 cm^{-1} (Amide III, $\nu(C–N)$), 1027 cm^{-1} (ν_{18a}, Phe or Tyr), 934 cm^{-1} ($\nu(C–C)$, backbone), and 854 cm^{-1} ($\nu(C–C)$, Pro ring). Here, we highlight the enhanced $\nu_s(COO^-)$ peak at 1410 cm^{-1}, which is not usually resolvable in non-SERS collagen spectra; it could indicate the formation of direct coordinative binding of collagen through the –COO$^-$ group with Ag atoms.
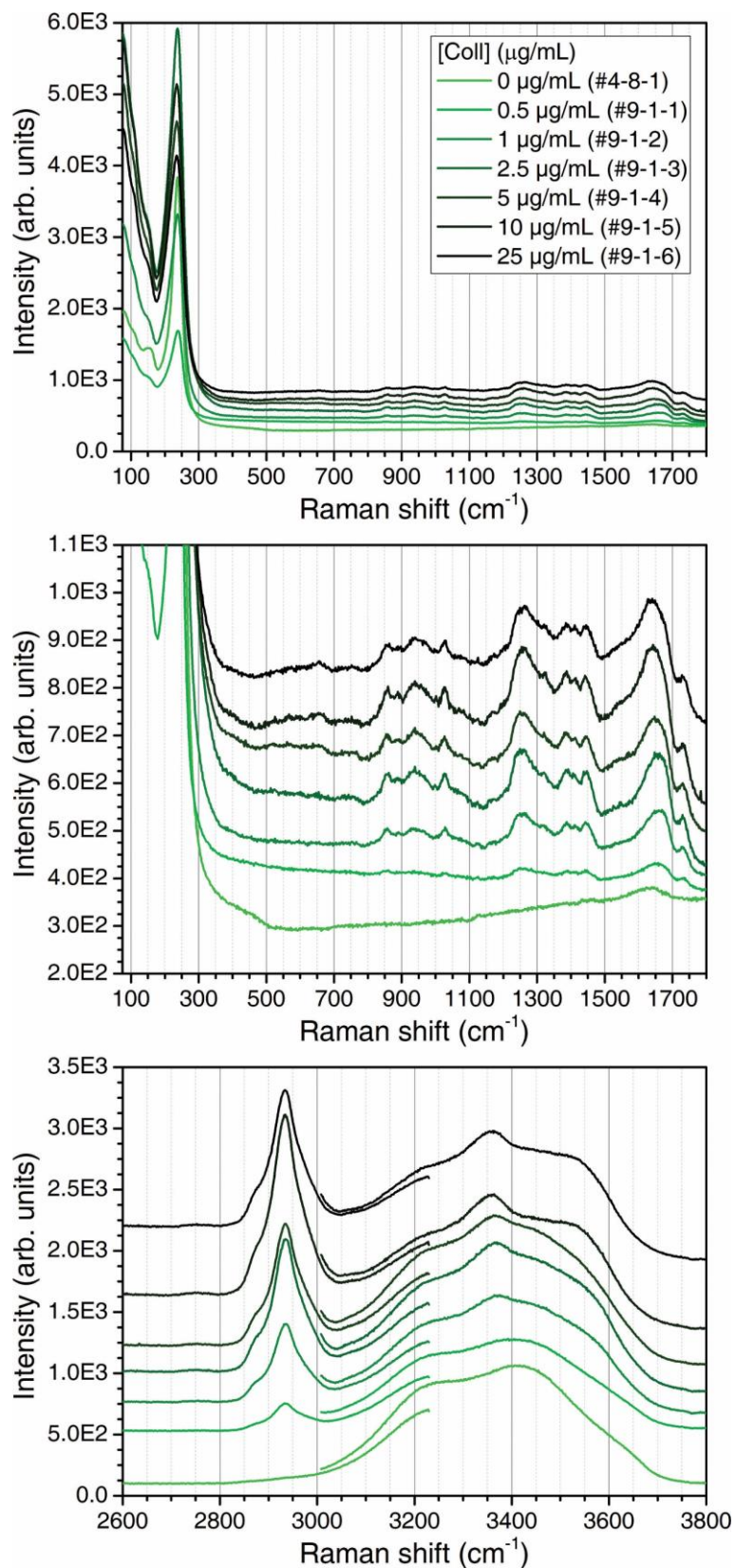
Figure 4.22: Stacked SERS spectra of the collagen concentration series on AgNPs@Cl (#9-1-z). The final concentrations in the mixture ([Coll]) include 0 µg/mL (#4-8-1), 0.5 µg/mL (#9-1-1), 1 µg/mL (#9-1-2), 2.5 µg/mL (#9-1-3), 5 µg/mL (#9-1-4), 10 µg/mL (#9-1-5), and 25 µg/mL (#9-1-6).

However, In AgNPs@Br/Coll, we observe significant decreases in the AS-related peaks at 2844 cm^{-1}, 2721 cm^{-1}, 1587 cm^{-1}, 1460 cm^{-1}, 1439 cm^{-1}, and 1126 cm^{-1} concurrently with the presence of strong collagen peaks (Figure 4.23), indicating the absence of AS near the surface of AgNPs@Br/Coll. However, much weaker 1410 cm^{-1} peaks are observed from AgNPs@Br/Coll to show a diminishing direct binding of collagen to the Ag atoms.

In sharp contrast, when mixing AgNPs@I with collagen, the AS peaks are untouched, highlighted by the strong C–H peaks at 2844 cm^{-1} and 1438 cm^{-1}, even at the highest [Coll] (Figure 4.24). The SERS spectra from AgNPs@I/Coll at all collagen concentrations show clear superpositions of AS and collagen features.
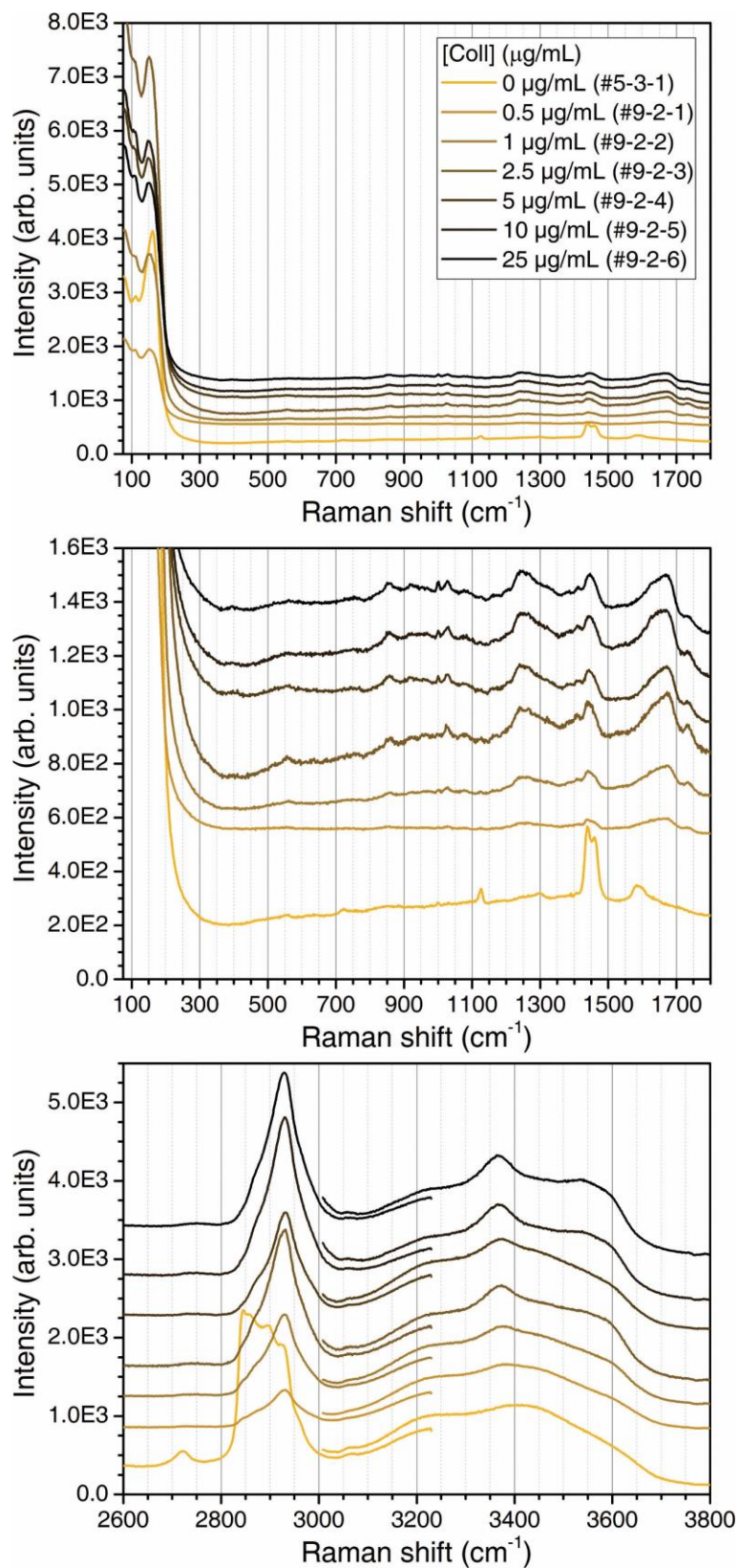
Figure 4.23: Stacked SERS spectra of the collagen concentration series on AgNPs@Br (#9-2-*z*). The final concentrations in the mixture ([Coll]) include 0 µg/mL (#5-3-1), 0.5 µg/mL (#9-2-1), 1 µg/mL (#9-2-2), 2.5 µg/mL (#9-2-3), 5 µg/mL (#9-2-4), 10 µg/mL (#9-2-5), and 25 µg/mL (#9-2-6).
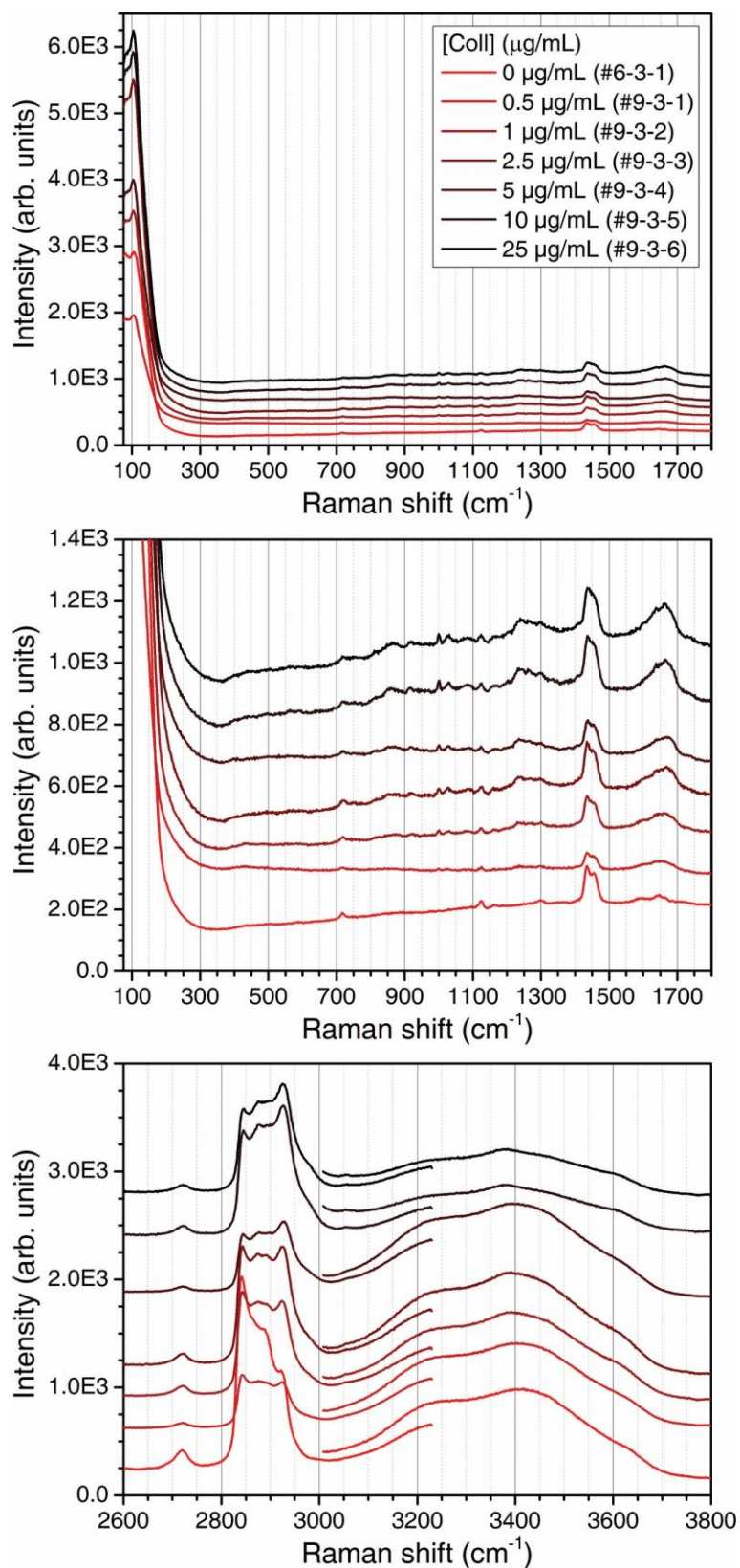
Figure 4.24: Stacked SERS spectra of the collagen concentration series on AgNPs@I (#9-3-*z*). The final concentrations in the mixture ([Coll]) include 0 µg/mL (#6-3-1), 0.5 µg/mL (#9-3-1), 1 µg/mL (#9-3-2), 2.5 µg/mL (#9-3-3), 5 µg/mL (#9-3-4), 10 µg/mL (#9-3-5), and 25 µg/mL (#9-3-6).

Additionally, a peak was found to be present at around 3360 cm^{-1} in all three AgNPs@X/Coll (X = Cl, Br, I) and is assigned to ν_s(N–H) in –NH$_2$ or –NH$_3^+$ groups. Its charge-driven adsorption onto the AgNPs may result in the blueshift to 3360 cm^{-1} from 3320 cm^{-1} in non-SERS conditions [109]. Closer analysis of the shifts of the ν(N–H) peak and the ν(C–H) peak (2940 cm^{-1}) show monotonic changes (Cl < Br < I) in the blueshifts from the non-SERS spectra of collagen to the SERS enhanced spectra (Figure 4.25). It may indicate that the electrostatic interaction of the NH$_3^+$ group with the I ligand layer is the strongest of the three, followed by the Br ligand layer and is the weakest with the Cl ligand layer.
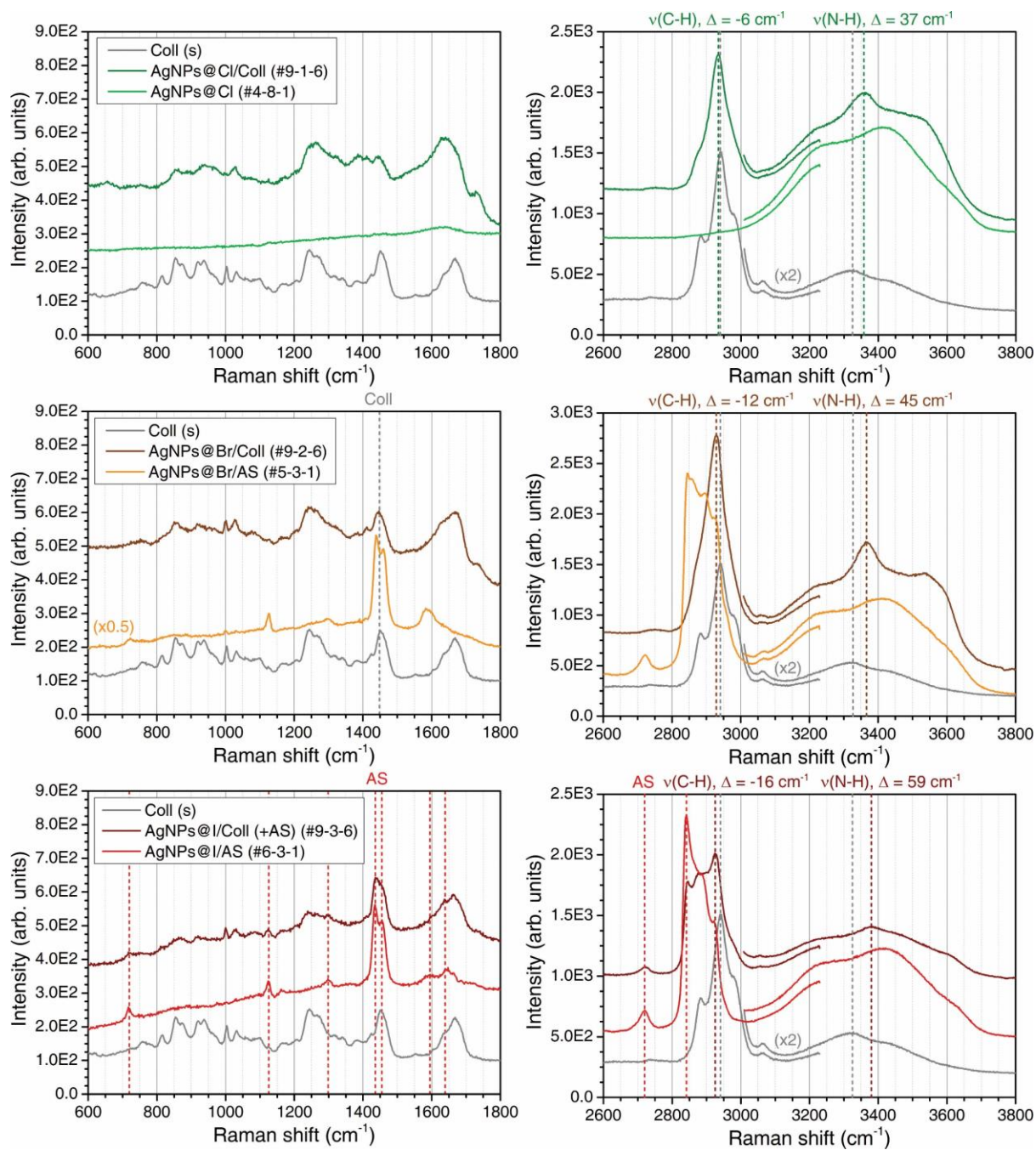
Figure 4.25: Stacked SERS spectra at [Coll] = 25 µg/mL of AgNPs@Cl/Coll (#9-1-6), AgNPs@Br/Coll (#9-2-6), and AgNPs@I/Coll (+AS) (#9-3-6) compared with the Raman spectra of dry collagen and the corresponding control samples AgNPs@Cl (#4-8-1), AgNPs@Br/AS (#5-3-1), and AgNPs@I/AS (#6-3-1).

Based on the observations of the functional groups in collagen identified in the SERS spectra, we can elucidate the competitive coadsorption between collagen and AS with the Br or I ligand layers on the surface of AgNPs. Here is a quick recap covering the related amino acid residues in collagen [26], highlighting their functions in binding to AgNPs:

(1) The $-NH_x^+$ groups can electrostatically attach to the negatively charged surface of AgNPs@X (X = Cl, Br, I). N−H bonds in $-NH_x^+$ (x = 2, 3) groups are mainly present as part of the amide bonds in the backbone, yet hard to attach to NPs due to steric hindrance [251]). Dangling side chains are generally exposed to the surface of proteins, including Arg and Lys residues (major proportion) and His residues (minor proportion). N-terminals of the polypeptide chains also contribute to the attachment with a minor proportion of N−H.

(2) The $-COO^-$ or $-COOH$ groups are apt to form coordinate bonds with Ag atoms and are found in Asp and Glu residues (major proportion) and on the C-terminals of the polypeptide chains (minor proportion);

(3) The C−OH bonds may also assist in binding to Ag atoms as supportive electron donors. This type of bond is commonly found in side chains like Ser or Hyp, which are generally shorter than the $-NH_x^+$ and $-COO^-$ side chains.

Hence, we could see that AS shares similar Ag−O coordinative covalent binding mechanisms to collagen via the $-COO^-$ or $-COOH$ and $-C-O-C-$ groups yet lacks the electrostatic attractions via the $-NH_x^+$ groups. This affinity comparison based on the intrinsic properties of the molecules gives AS < Coll, which could explain the detachment of AS from AgNPs@Br when collagen is introduced. However, on AgNPs@I, the SERS spectra support an opposite overall affinity (AS > Coll). This opposite trend advises us to compare the surface properties of AgNPs@I with AgNPs@Br for the differences.

A closer comparison of the spectra in Figure 4.25 leads us to an interesting finding on the peak intensities: whilst the spectra suggest an increasing binding affinity of collagen via the $-NH_3^+$ group following Cl < Br < I, the other collagen peaks showed no significant shifts but a weakening covalent binding according to the decreasing $\nu_s(COO^-)$ peak. In contrast, the above-mentioned blueshifts of the C−H bond-related peaks of AS (Figure 4.18) show its stronger direct binding to the Ag atoms. We can thus speculate that a strong "shielding effect" due to the increasing radius of halide ions (Cl < Br < I) increasingly repels the "advantageous" $-COO^-$ group in collagen, whereas facilitating the binding to Ag in the ligand gaps via the spatially narrow non-ionic groups (such as $-C-O-C-$). The overall effect leads to AS outperforming its overall binding affinity to AgNPs@I over collagen.

Finally, based on the above discussions and evidence, we can elucidate the binding in the coadsorbing layer, which can now be more accurately described as AgNPs@[(A/B)/C], with A representing the strong ligands (that dominate the binding to Ag atoms), B also directly binding to Ag atoms but filling the presumed gaps of A, and C weakly attaching to AgNPs indirectly over the layer of A and B through electrostatic interactions. With Cl ligands and S ligands, the coverage is near-complete with minor gaps, and when forming clusters with

collagen, they form AgNPs@Cl/Coll and AgNPs@S/Coll. AgNPs@Cl/Coll, in particular, could also be written as AgNPs@[(Cl/Coll)/Coll] to emphasise the possible covalent binding of collagen with exposed Ag atoms in the minor gaps. With Br ligands, the adsorption of collagen causes AS to desorb from the AgNPs; however, it also lacks direct binding of collagen with the Ag atoms, giving AgNPs@[(Br/gap)/Coll]. With I ligands, AS are shielded by the deeper gaps between I ligands (due to its largest radius amongst the three halides). The exposed Ag atoms would be hardly accessible by collagen side chains, and the resulting coadsorption can be described as AgNPs@[(I/AS)/Coll]. The coadsorption mechanism may also apply to other proteins with adequate amounts of $-COO^-$, $-NH_3^+$ and $-C-OH$ groups in the amino acid side chains.

Table 4.6: SERS peak assignments of (1) #9-1-2, (2) #9-1-6, (3) #9-2-2, (4) #9-2-6, (5) #9-3-2, (6) #9-3-6, and (7) dry collagen. The species of each vibrational mode is noted based on the information reported in the corresponding reference. Peaks that potentially originate from AS are underlined and bold. Postulated assignments are highlighted with asterisk symbols (*). General notations refer to Appendix A.

Raman shift (cm^{-1})							Assignment	Reference (cm^{-1})
#9-1-2	#9-1-6	#9-2-2	#9-2-6	#9-3-2	#9-3-6	-		
AgNPs@Cl + Coll in 2 mM HCl pH = 3		AgNPs@Br + Coll in 2 mM HCl pH = 3		AgNPs@I + Coll in 2 mM HCl pH = 3		Dry collagen		
1 µg/mL	25 µg/mL	1 µg/mL	25 µg/mL	1 µg/mL	25 µg/mL	-		
		3580sh	3580sh	3589sh	3595sh		ν_s(O–H), water, unbound; [217] ν_{as}(O–H), water, unbound; [217]	3627; [217] 3531; [217]
3556sh	3529sh		3534				*ν_{as}(N–H), bound to NPs;	
3447sh		3455sh		3454sh	3458sh	3438sh	ν_{as}(O–H), water, hydrogen-bonded; [217]	3435; [217]
3367	3357	3374	3365	3390	3379		*ν_s(N–H), bound to NPs;	
						3320	ν(N–H), in amide bond or side chains; [109] ν(N–H); [102] ν(N–H), amide; [252]	3324; [109] 3300; [102] 3329; [252]
3220sh	3228sh	3222sh	3221sh	3228sh	3236sh		ν_s(O–H), water, hydrogen-bonded; [217]	3247; [217]
		3063vw	3059w	3054w	3063		*ν(O–H), in hydrogen-bonded –COOH in collagen;	
				2974sh	2980sh		ν_{as}(CH$_3$); [102]	2977; [102]

2934	2934	2930	2928	2923	2924	2940	ν(CH₃); ν(CH₂); [103] ν(CH₂); [102]	2928–2938; [103] 2937; [102]
				2892sh			**νₐₛ(CH₂), AS;**	
2876sh	2877sh	2868sh	2870sh	2874	2875	2882	νₛ(CH₃); [102]	2880; [102]
				2843	**2844**		**νₛ(CH₂), AS;**	
		2736w		**2721**	**2722**		ν(O–H), in bonded –COOH; [212] **τ(CH₂) + δ(CH₂), AS;**	2500–2700; [212]
1732	1731	1736	1734	1730vw			ν(C=O), in –COOH of Asp or Glu in collagen; [113]	1700–1750; [113]
1660	1670sh	1673	1670	1662	1664	1666	Amide I; [86] νₐₛ(COO⁻) or Amide I (β-sheet); [103]	1670; [86] 1675; [103]
1630sh	1636	1626sh	1632sh	1636sh	1638sh	1637sh	Amide I; [86] νₐₛ(COO⁻) or Amide I (3₁₀-helix); [103]	1642; [86] 1632; [103]
				1594sh		1605sh	νₐₛ(COO⁻) or ν₈ₐ** (Phe or Tyr); [103] δ(N–H); [102]	1605; [103] 1594; [102]
						1554w	Amide II; [103] νₐₛ(COO⁻); [186]	1565; [103] 1562; [186]
						1464sh	δ(CH₃); δ(CH₂); [86]	1464; [86]
				1456	**1457sh**		**δ(CH₂), AS;**	
1445	1444	1444	1446			1453	δ(CH₃); δ(CH₂); [86] C–H; ν₁₉ᵦ, Phe; [103]	1451; [86] 1445; [103]
				1435	**1438**		**δ(CH₂), AS;**	

1413	1410	1410w	1410	1406vw		1424sh	ν_s(COO⁻); [86] δ(C–OH) in –COOH; [108]	1422; [86] 1415; [108]
1386	1384	1382vw	1380w			1380	ν_s(COO⁻); [103] δ_s(CH$_2$); [109]	1405-1410; [103] 1391; [109]
						1340w	ω(CH$_3$); ω(CH$_2$); [86] δ_s(CH$_2$); [109]	1343; [86] 1340; [109]
1323w	1321w	1324sh	1320sh			1318w	τ(CH$_3$); τ(CH$_2$); [86]	1314; [86]
				1300w	**1301w**		**τ(CH$_2$), AS;**	
1263	1264	1265	1263	1269w	1268	1270	Amide III ; [86] Amide III; C–H; ν_3, Phe; ν_3, Tyr ; [103] δ(N–H), Amide III; [109]	1271; [86] 1265–1285; [103] 1269; [109]
1242	1244	1238	1241	1240w	1239	1245	Amide III; [86] Amide III; Tyr; [103] ν(C–N), Amide III; [109] Amide III; [102]	1248; [86] 1235–1245; [103] 1251; [109] 1234–1252; [102]
		1206sh	1199sh		1204sh	1205w	Hyp; Tyr; [86] Phe; Tyr; [103]	1211; [86] 1215; [103]
	1169vw	1166vw	1162vw	1162w	1167vw	1172w	Tyr; [86] ν_{9a}, Phe; [103] δ(NH⁺), Pro; [107]	1178; [86] 1175–1195; [103] 1174; [107]
1124vw		1126vw	1128vw	**1124**	**1123**	1126w	δ(NH$_3^+$); [107] **ν(C–C), ω(CH$_2$), AS;**	1136–1143; [107]
						1100	ν_{as}(COC); [109]	1094; [109]

		1079vw	1082vw	1084vw		1062vw	ν_{18b}, Phe; [103]	1065; [103]
1027	1026	1027	1028	1028	1028	1031	*ν(C–C), Pro; [86] ν_{18a}, Phe; ν_{18a}, Tyr; [103] Phe; [102]	1037; [86] 1025; [103] 1032; [102]
		1001	1001	1000	1001	1003	Phe; [86] ν_{12}, Phe; [103] ν(C–C), Phe ring; [109] Phe; [102]	1006; [86] 995; [103] 1001; [109] 1004; [102]
	966sh	966vw	966vw			969sh	Amide III'; [86]	966; [86]
940w	934					939	ν(C–C), backbone; [86] ν(C–COO$^-$); ν_{17a}, Phe; ν_{17a}, Tyr; [103] ν(C–C), α-helix; [109]	938; [86] 940–945; [103] 934; [109]
						920	ν(C–C), Pro ring; [86] ν(C–C); [102]	921; [86] 923; [102]
892w								
				875vw	874w	875	ν(C–C), Hyp ring; [86]	876; [86]
856	854	858w	855	855vw	854sh	855	ν(C–C), Pro ring; [86] ν_s(COC); [109] Tyr; [102]	856; [86] 862; [109] 857; [102]
				815vw		815	ν(C–C), backbone; [86] δ(CCN); δ(COC); [109]	821; [86] 810; [109]
						757w		
				718	**719w**		**ϱ(CH$_2$), AS;**	
	658w						ω(COO$^-$); ν_{6b}, Tyr; [103]	645–665; [103]
		559w	560vw			566w		
						531w		
				433		424sh		
		395vw				392w		
						301w		

238	235						ν(Ag–Cl); [209] ν(Ag–Cl); [196] ν(Ag–Cl); [220]	245; [209] 243; [196] 240; [220]
		153	149				ν(Ag–Br); [221] ν(Ag–Br); [196] ν(Ag–Br); [220]	175; [221] 162; [196] 166; [220]
153sh	152sh						Ag lattice vibration; [221]	147; [221]
		111w	109w					
				104	104		ν(Ag–I), A$_1$ transition in β-AgI polymorph; [221] ν(Ag–I); [196] ν(Ag–I); [220]	103; [221] 118; [196] 127; [220]

4.4 Conclusion

Through this study, we investigated the coadsorbed species that consist of the fingerprint signals in the SERS spectra of halide-coated AgNPs and explicated their different coadsorption affinities under competition with collagen. Table 4.7 summarises the estimated sequences of the binding affinity of all the present species (*i.e.*, Cit, AAc, AS, Coll) over bare or halide-coated Ag surfaces at neutral and acidic pH.

Table 4.7: A comparison of the binding affinity of species over Ag surface under different conditions. The species with similar surface binding affinities are categorised within brackets.

Major ligands on Ag surface	Affinity	
	Neutral	Acidic (+Coll)
Bare Ag	Cit > (AAc, AS);	-
Cl	AAc > (Cit, AS) ≈ 0;	Coll > (Cit, AAc, AS) ≈ 0;
Br	AS > (Cit, AAc);	Coll > AS > (Cit, AAc);
I	AS > (Cit, AAc);	AS > Coll > (Cit, AAc);

If the mixture contains Cit (*e.g.*, citrate-reduced AgNPs) but no halides, Cit dominates the binding to Ag atoms via the COO–Ag bond, while other species, such as AAc and AS, are not allowed to coadsorb. Note that, rather than unresolved (overwhelmed by the strong signals of Cit), they are more likely unbound, indicated by the absence of the 2850 cm^{-1} peak.

When Cl ligands coat the Ag surface, Cit is no longer favoured to adsorb due to its strong negative charge. Instead, AAc can coadsorb with Cl to the few exposed Ag atoms in the minor gaps. AS is not as favoured probably for its bulkiness. Acidification destabilises the AAc (or its binding), leaving a clean SERS background without interfering with collagen.

Changing from Cl ligands to bulkier Br ligands, gaps are left and favour the coadsorption with AS more than the smaller species such as Cit or AAc. The thicker negatively charged ligand layer increasingly repels the small but densely charged anions (Cit or AAc) and prevents the species from approaching the exposed Ag atoms in the relatively deeper gaps. However, AS is detachable when encounters collagen indicated by the disappearance of the 2850 cm^{-1} peak, thus not interfering with the analyses.

Comparing the bulkiest I ligands with Br ligands, the affinity of AS further increase and prevail in the competitive coadsorption with collagen. The increase in the affinity of AS could be explained by a "shielding effect" again due to the thickening negatively charged layer of halides from Br to I, leading to the deepening of the presumed gaps to suit better for the AS to be embedded within.

From a bioanalysis point of view, it is worth noting that the spectra of AgNPs@[(Br/gap)/Coll] match the best to the dry collagen in relative peak intensities (Figure 4.25) while giving the

strongest ν(N–H) peak (around 3370 cm^{-1}) amongst the three (although not the greatest blueshift). This observation is attributed to the combination of the following aspects:

(1) The direct binding via coordinative covalent bonds is scarce due to the thickness of the Br ligand layer, leading to negligible chemical enhancement component via charge-transfer bonding with Ag atoms (which could distort protein structure [189]);

(2) The arbitrary positioning of the –NH$_x^+$ groups in collagen allows uniform attachment of the long molecule in the near-field of AgNPs for electromagnetic enhancement;

(3) The weaker binding affinity of AS excludes the concerns around background interference with collagen, which could be a reason for Br to be a common option for ligand exchange on AgNPs for bioanalytical applications.

To this point, our success in the SERS attempts on collagen fibres in Chapter 3 can be explained based on the mechanistic understanding of the halide ligands. The citrate-capped AgNPs were not treated with halide beforehand but concomitantly with the mixing step due to the residual HCl and NaCl in the collagen fibres carried over from the pickling solution. The Cl ligand exchange and acidification (at pH = 2.5 and 4.5) leads to the desorption of Cit and AAc from the surface of AgNPs. The same exchange occurred on borohydride-reduced b-AgNPs, thus giving the same SERS spectra of collagen in fibres.

In a broader context, understanding the coadsorption mechanism on AgNPs provided through this study can benefit a wider range of applications than bioanalyses, such as photocatalysis [253] and therapeutics [254]. For instance, in a catalysed reaction, the bond activation via direct coordinative bonds with the Ag atoms can be affected by any unwanted coadsorbed species or by the surface coverage of the AgNPs by ligands [220]. Also, the surface coadsorption phenomena on other plasmonic nanostructures (*e.g.*, AuNPs) can be investigated similarly using SERS to extend the knowledge.

Chapter 5   Collagen in Bovine Pericardium: Effects of Organic Crosslinkers on Structure and Stability

This chapter presents our study on the effects of organic crosslinkers on collagen structure during the reactions and the corresponding stability of the crosslinked materials. This choice of focus originates from the growing need for developing efficient processes to stabilise and give desired functionalities to collagen-based biomaterials. Enormous efforts have been made in this field, yet clear guidance from mechanistic understandings of the structure-stability relationship is lacking. Here, we employed SAXS as the tool to monitor the structural changes in bovine pericardia in combination with the conventional stability assessment methods. Results indicate that crosslinking reactions contribute more efficiently to the structural changes and stabilities at low concentrations via telopeptidyl-helical intermolecular linkages; adding the excessive amount gives minor improvements in the required properties via less specific reactions. The findings could support the development of benign and efficient crosslinking strategies to mitigate adverse effects on biomaterials for medical applications.

Also, this study extended our knowledge of collagen structural changes from a niche focus on metallic species (*e.g.*, chrome tanning) to cover a broader interest in organic crosslinkers; the latter is used both in and outside of the leather industry and can have more variations in terms of the properties they can impart to the materials. The discussion in this chapter is concentrated towards the end, as the organic crosslinkers gave much subtler changes than Cr(III) in Chapter 3, hence, not until most of the results were collected could we postulate the mechanism behind the effects on structure and stability.

Major findings in this chapter have been published in Ref. [3] and are reused with permission.

5.1   Background

Bovine pericardium (BP) has been involved in clinical practice since around 50 years ago [255-257]. It has since been developed progressively and applied widely as a material for surgical operations, including but not limited to bioprosthetic heart valve leaflets, vascular, pericardial and abdominal patches, and ligament substitutes [258]. The known advantages of using BP include its biocompatibility, flexibility, durability, and consistency, with potential benefit in supporting cellular ingrowth [257, 258]

At about the same time when BP was introduced as bioprosthesis, two aims were set for designing the biochemical treatments on BP required for the applications [259]. The first is to prevent inflammatory and immunological reactions, which can be achieved by eliminating antigens such as glycoproteins in cells. Therefore, a common decellularisation practice is conducted on BPs to produce acellular bovine pericardia (ABPs). The second is to suppress collagen degradation via chemical crosslinking, amongst which the most popular choice is glutaraldehyde (GA) [257].

However, drawbacks of GA-crosslinked ABPs were revealed during the past two decades. Prominent ones include structural degradation, calcification and immune responses after implantation, of which most were suggested to be related to GA crosslinking [69, 260-263]. Hence, many researchers endeavoured to mitigate these issues through various strategies that can be generally categorised into three:

(1) Replacing GA with other types of crosslinkers, including 1-ethyl-3-(3-dimethylaminopropyl) carbodiimide coupled with N-hydroxysuccinimide (EDC/NHS), diphenylphosphorylazide, and modified polysaccharides [264-268];

(2) Applying post-treatments on GA-crosslinked ABPs to suppress adverse effects using, for example, chitosan, heparin, hyaluronic acid, organophosphates, polypeptides, polyol, SDS, Triton X-100, deoxycholate [269-276];

(3) Altering GA crosslinking conditions to reduce its usage [277-279];

The findings under these three categories were established based on common indicators and criteria for assessing the effects of crosslinking on the performances of the ABPs; the focus could vary amongst enzymatic, thermal, and mechanical properties and cell responses (including calcification). However, discrepancies in these criteria were often found, especially with varying crosslinking chemistries, revealing the lack of mechanistic understanding behind these indicators [266, 267]. Complementary techniques such as spectroscopies and colourimetric assays (e.g., degree of crosslinking) were often employed [280-282], yet none provided sufficient information for establishing coherent mechanisms behind the properties.

Since ABPs are mostly composed of collagen[14], the macroscopic properties of ABPs are largely determined by the units at various structural hierarchies, especially at the levels of collagen molecules which react with the crosslinkers [283, 284]. In the past 20 years, SAXS has been used to inspect the effects of chemical crosslinking on BPs or ABPs to study the structure-property relationship [98, 99, 285].

Through this study, we aim to build a bridge between the structure and the enzymatic and thermal stability of chemically crosslinked ABPs using SAXS as the main tool. The crosslinkers of choice in this study include GA and EDC/NHS, highlighting differences in the reaction chemistry between long-chain and zero-length crosslinks. Crosslinker concentrations from the conventional usage to 1:50 dilution were investigated to differentiate the multiplexing roles of each crosslinker in inducing structural changes in collagen to associate with the properties.

---

[14] A native BP includes three layers: (1) the serosa, the thin inner layer consisting of mesothelial cells; (2) the fibrosa, the thicker layer containing collagen and elastin; (3) the epipericardial connective tissue layer, the outer layer that is partly continuous with the pericardiosternal ligaments. In this thesis, "ABP" refers to the fibrosa layer rich in collagen.

5.2 Experimental Details

5.2.1 Decellularisation of Fresh BPs to ABPs

Freshly harvested BPs were received from a local meat processor sourced from two individual animals slaughtered in the same batch. BPs were decellularised to ABPs following a modified method based on Ref. [286].

First, blood was rinsed off and the adipose tissues and fats were removed from the surface of the BPs. The cleaned BPs were then rinsed in phosphate-buffered saline (PBS) at 4 °C before sampling. Homogeneous areas in the BPs away from the ligaments were chosen for the studies. Around 100 g of the BPs were soaked and stirred gently in 2 L of the decellularisation solution at 4 °C for 24 h. After that, the now named ABPs were washed using PBS three times over 1 h to remove residual chemicals and stored at 4 °C before crosslinking.

Chemicals:
Ethylenediaminetetraacetic acid disodium salt dihydrate ($Na_2EDTA \cdot 2H_2O$), Pure Science Ltd., New Zealand;
Triton X-100 (t-Octylphenoxypolyethoxyethanol), Merck KGaA, Germany;
Antibiotic-Antimycotic 100X, ThermoFisher Scientific, USA;
Sodium chloride (NaCl), Dominion Salt Ltd., New Zealand;
Potassium chloride (KCl), Pure Science Ltd., New Zealand;
Disodium hydrogen phosphate dihydrate ($Na_2HPO_4 \cdot 2H_2O$), Panreac Química SLU, Spain;
Potassium dihydrogen phosphate (KH_2PO_4), Pure Science Ltd., New Zealand;
Sodium hydroxide (NaOH), CARLO ERBA Reagents S.r.l., Italy;
Hydrochloric acid (HCl), 37% (w/w), CARLO ERBA Reagents S.r.l., Italy.

Solutions:
PBS (buffer): Dissolve 137 mM NaCl, 2.7 mM KCl, 10 mM Na_2HPO_4, and 1.8 mM KH_2PO_4 in DI water and use HCl or NaOH to adjust pH to 7.4;
Decellularisation solution: 1% (w/v) Triton X-100, 0.02% (w/v) EDTA, and 1X Antibiotic-Antimycotic, all dissolved in PBS.

5.2.2 Crosslinking of ABPs

The ABPs were cut into a uniform size of around 40 mm × 40 mm (L × W) with an intrinsic thickness of 0.4 mm. Each piece was transferred into a Petri dish (∅ = 55 mm) and flattened. We then added 10 mL of a freshly prepared crosslinker solution to each Petri dish to immerse the ABP. The Petri dishes were sealed using Parafilm and were agitated on an orbital shaker at 20 °C for 24 h. Uncrosslinked negative controls (UN-ABPs) were soaked in PBS without GA at 4 °C for 24 h. After the agitation, GA-crosslinked ABPs (GA-ABPs) were treated with 0.2 M glycine solution for 24 h, while the EDC-crosslinked ABPs (EN-ABPs) were washed using PBS for 24 h. Both groups of ABPs were rinsed and soaked in PBS with 1X Antibiotic-Antimycotic at 4 °C before the SAXS measurements. A portion of each sample was

cut off, rinsed with DI water and lyophilised for other analyses. Each crosslinking condition and the corresponding measurements were repeated on two biological replicates.

Chemicals:

Glutaraldehyde (GA), Grade II, 25% (w/v) in H_2O, Sigma-Aldrich, USA;

1-Ethyl-3-(3-dimethylaminopropyl)carbodiimide (EDC), Sigma-Aldrich, USA;

N-Hydroxysuccinimide (NHS), Sigma-Aldrich, USA;

Glycine (Gly), Sigma-Aldrich, USA;

Sodium chloride (NaCl), Dominion Salt Ltd., New Zealand;

Potassium chloride (KCl), Pure Science Ltd., New Zealand;

Disodium hydrogen phosphate dihydrate ($Na_2HPO_4 \cdot 2H_2O$), Panreac Química SLU, Spain;

Potassium dihydrogen phosphate (KH_2PO_4), Pure Science Ltd., New Zealand;

Sodium hydroxide (NaOH), CARLO ERBA Reagents S.r.l., Italy;

Hydrochloric acid (HCl), 37% (w/w), CARLO ERBA Reagents S.r.l., Italy;

4-Morpholineethanesulfonic acid (MES), Sigma-Aldrich, USA.

Solutions:

PBS (buffer): 137 mM NaCl, 2.7 mM KCl, 10 mM Na_2HPO_4, and 1.8 mM KH_2PO_4 at pH = 7.4 (adjusted using HCl or NaOH solutions if needed);

MES (buffer): 100 mM MES at pH = 5.5 (adjusted using HCl or NaOH solutions if needed);

GA crosslinker solution: The prepared stock solution contained 0.625% (w/v) GA diluted using PBS and was further diluted in PBS to a dilution factor (DF) of 1 (no dilution), 5, 10, and 50;

The corresponding samples were named "GA-ABP-DFx", where x = 1, 5, 10, 50;

EDC/NHS crosslinker solution: The prepared stock solution contained 50 mM EDC and 20 mM NHS (EDC:NHS = 2.5:1) that were freshly dissolved in MES and were further diluted in MES to a dilution factor (DF) of 1 (no dilution), 5, 10, and 50;

The corresponding samples were named "EN-ABP-DFx", where x = 1, 5, 10, 50.

5.2.3 Synchrotron SAXS Measurements

The SAXS measurements were conducted on beamline I22 at Diamond in Didcot, UK. From each ABP sample, a small disc ($\varnothing$ = 10 mm) was cut off, mounted onto the I22 sample grid, and then sealed with Kapton tape on both sides to prevent dehydration. All the samples were orientated with the surface perpendicular to the X-ray beam. The samples were kept at room temperature and were exposed to X-ray at an energy of 12.4 keV for 1 s. The q range is from 0.0155 nm^{-1} to 0.179 Å^{-1} captured by a Pilatus P3-2M detector. Mapping was conducted over 2.5 mm $\times$ 2.5 mm on each sample, giving a 6×6 data matrix. The SAXS profiles were presented as $I(q)$ versus q plots. The 3rd order peak positions were fitted and converted to the D-period. The 3rd, 5th, and 6th order peak areas were fitted for calculating the 5th to 3rd and the 6th to 5th peak area ratios ($R_{5/3}$ and $R_{6/5}$).

Fitting q range for peaks (note: the unit of raw data was [Å^{-1}] when processed in DAWN):
The 3rd order peak, from 0.24 nm^{-1} to 0.33 nm^{-1};

The 5th order peak, from 0.43 nm^{-1} to 0.52 nm^{-1};
The 6th order peak, from 0.54 nm^{-1} to 0.61 nm^{-1}.

5.2.4 DSC Measurements

The DSC measurements were performed on the Q2000 DSC (TA Instruments). For each measurement, around 1.5 mg of lyophilised ABP sample was loaded into a Tzero aluminium pan and rehydrated using DI water (weight ratio of sample to water = 1:6). The pans were then sealed hermetically and kept at 4 °C for 16 h before the measurements. The measurements were carried out at a ramp rate of 5 °C/min from 20 °C to 100 °C under N$_2$ purge. The onset temperature of each thermogram was calculated to represent the denaturation temperature of collagen (T$_d$), and the integrated peak area was used to estimate the enthalpy of the denaturation (ΔH).

5.2.5 Enzymatic Resistance and Hydroxyproline Assay

The enzymatic resistance assay was conducted following a reported method [287]. For each assay, around 15 mg of lyophilised ABP sample was soaked in 1.5 mL of the collagenase solution or the digestion buffer (negative control), followed by incubation at 37 °C for 24 h. The digestion mixture after incubation was centrifuged at 12000 × g for 10 min at 4 °C, and an aliquot of 1 mL was taken from the supernatant for hydroxyproline (Hyp) assay.

The Hyp assay was conducted using a chloramine-T method [80]. The 1 mL supernatant was mixed with 1 mL of 37% (w/w) HCl in a PYREX glass tube (Corning Life Sciences) closed with a polytetrafluoroethylene (PTFE) liner screw cap. The mixture was hydrolysed at 108 °C for 20 h. The hydrolysate was transferred to a 10 mL volumetric flask, neutralised with NaOH solution, and made up to volume with DI water. A 0.4 mL aliquot of the neutralised hydrolysate was taken from the 10 mL stock solution and mixed with 0.2 mL of the chloramine-T reagent. The mixture was incubated at room temperature for 20 min. Then, 0.2 mL of 20% (w/w) perchloric acid was added to the mixture and incubated at room temperature for 5 min. Lastly, 0.2 mL of 10% (w/v) 4-(dimethylamino)benzaldehyde (p-DMAB) (in 2-propanol) was added to the mixture, which was further incubated at 60 °C for 20 min. After cooling down, a 0.2 mL aliquot was transferred to a 96-well plate, and the absorbance was measured using a BioTek ELx800 microplate reader (Agilent Technologies) at 550 nm. The absorbance was compared with the calibration curve based on standard solutions containing 1–5 µg of Hyp (dissolved in 0.4 mL DI water). When the sample was oversaturated, less volume was taken from the neutralised hydrolysate, topped up with DI water to 0.4 mL, and repeated.

Chemicals:
Sodium chloride (NaCl), Dominion Salt Ltd., New Zealand;
Calcium chloride (CaCl$_2$), Sigma-Aldrich, USA;
2-[(2-Hydroxy-1,1-bis(hydroxymethyl)ethyl)amino]ethanesulfonic acid (TES), Sigma-Aldrich, USA;
Collagenase from *Clostridium histolyticum*, C9891, 499 unit/mg, Sigma-Aldrich, USA;

Sodium hydroxide (NaOH), CARLO ERBA Reagents S.r.l., Italy;

Hydrochloric acid (HCl), 37% (w/w), CARLO ERBA Reagents S.r.l., Italy.

Sodium acetate trihydrate ($CH_3COONa \cdot 3H_2O$, $NaAc \cdot 3H_2O$), Pure Science Ltd., New Zealand;

Trisodium citrate dihydrate ($Na_3C_6H_5O_7 \cdot 2H_2O$ or $Na_3Cit \cdot 2H_2O$), Pure Science Ltd., New Zealand;

Citric acid ($H_3C_6H_5O_7$ or H_3Cit), Panreac Química SLU, Spain;

2-Propanol (($CH_3)_2CHOH$), Sigma-Aldrich, USA;

Perchloric acid ($HClO_4$), 60% (w/w), Merck KGaA, Germany;

Chloramine-T trihydrate ($C_7H_7ClNNaO_2S \cdot 3H_2O$), 98% ($w/w$), Alfa Aesar, USA;

4-Dimethylaminobenzaldehyde (p-DMAB), Alfa Aesar, USA.

Solutions:

Digestion buffer: Dissolve 134 mM NaCl, 20 mM TES, and 0.5 mM $CaCl_2$ in DI water and adjust to pH = 7.4 using HCl or NaOH;

Collagenase solution: Dissolve 1 mg/mL collagenase in the digestion buffer;

Citrate buffer: 28.5g of $NaAc \cdot 3H_2O$, 18.75g of $Na_3Cit \cdot 2H_2O$, and 2.75g of H_3Cit are dissolved in 200 mL of DI water, then add 200 mL of 2-propanol, mix well and top up with DI water to 500 mL;

Chloramine-T reagent: 0.175g of chloramine-T dissolve in 15 mL of the citrate buffer.

5.2.6 Ninhydrin Assay

A ninhydrin assay was carried out following previous methods with slight modifications [288, 289]. For each assay, about 5 mg of lyophilised ABP sample was soaked in 1 mL of the ninhydrin reagent and sealed in a 1.5 mL Eppendorf tube, followed by heating at 100 °C for 20 min. The reaction mixture was cooled down, and 40 µL of the supernatant was diluted with 160 µL of 2-propanol in a 96-well plate. The absorbance was measured using a BioTek ELx800 microplate reader (Agilent Technologies) at 550 nm. Two internal replicates were analysed on each biological replicate for better accuracy. Gly was used as the calibration standard.

The degree of crosslinking and the number of covalently linked sites are calculated as:

$$\text{Degree of crosslinking (\%)} = \left(1 - \frac{N_X}{N_{UN}}\right) \times 100\%$$

$$\text{Number of covalently linked sites} = (N_{UN} - N_X) \times MW_{Coll} \times n$$

where N_{UN} and N_X are the free amino (–NH_2) group content of uncrosslinked and crosslinked ABP samples (unit: [µmol/g Coll]), MW_{Coll} is the molecular weight of collagen (around 300 kDa [290]), and n is the number of sites that are covalently linked on collagen per –NH_2 group involved. For GA, each –NH_2 group involved in crosslinking results in one site (the –NH_2 group itself) being covalently linked, *i.e.*, $n = 1$. For EDC, each –NH_2 group involved in crosslinking results in two sites (an –NH_2 group and a –COOH group) being covalently linked, *i.e.*, $n = 2$.

Chemicals:

Sodium hydroxide (NaOH), CARLO ERBA Reagents S.r.l., Italy;

Hydrochloric acid (HCl), 37% (w/w), CARLO ERBA Reagents S.r.l., Italy;

Citric acid ($H_3C_6H_5O_7$ or H_3Cit), Panreac Química SLU, Spain;

Stannous chloride dihydrate ($SnCl_2 \cdot 2H_2O$), Riedel-de Haën, Germany;

Ninhydrin ($C_9H_6O_4$), Sigma-Aldrich, USA;

Ethylene glycol anhydrous ($HOCH_2CH_2OH$), Sigma-Aldrich, USA;

2-Propanol ((CH_3)$_2$CHOH), Sigma-Aldrich, USA.

Solutions:

Reducing buffer: 2.1 g of H_3Cit, 0.8 g of NaOH and 25 mg of $SnCl_2 \cdot 2H_2O$ were dissolved in 50 mL of DI water and adjusted to pH = 5;

Ninhydrin solution: 4% (w/v) ninhydrin dissolved in ethylene glycol;

Ninhydrin reagent: 1:1 (v/v) mixture of the ninhydrin solution and the reducing buffer.

5.3　Results and Discussion

5.3.1　SAXS Profiles

The SAXS profiles of all ABP samples show characteristic features of collagen fibrils (Figure 5.1) [98, 291]. With a logarithmic scale on both axes, the broad peaks low q region shows the form factor demonstrating the morphology of the collagen fibrils. The concave at $q \approx 0.03$ nm^{-1} may originate from the structure factor that indicates the interfibrillar interference [291, 292]. The weakening interfibrillar interference upon crosslinking seems to match the widening interfibrillar gaps found in another recent SAXS study of ours (Ref. [78], not part of this thesis), yet this is not the focus of this study.

On the other hand, the sharp diffraction peaks are attributed to the well-known axial D-periodic packing of the collagen molecules within a fibril. The D-period is calculated based on the 3rd order diffraction peak due to the overlapping of the form factor features with the 1st order peak and the unresolved 2nd order peak. Note here that the changes in peak intensity are hardly identifiable when visually comparing UN-ABP to GA-ABP-DF1. The peak intensity changes are not as prominent as in our previous SAXS studies on the binding with metallic species (*e.g.*, Cr(III), Zr(IV) [74, 76]), probably due to the lesser electron density contributed by GA in this study.
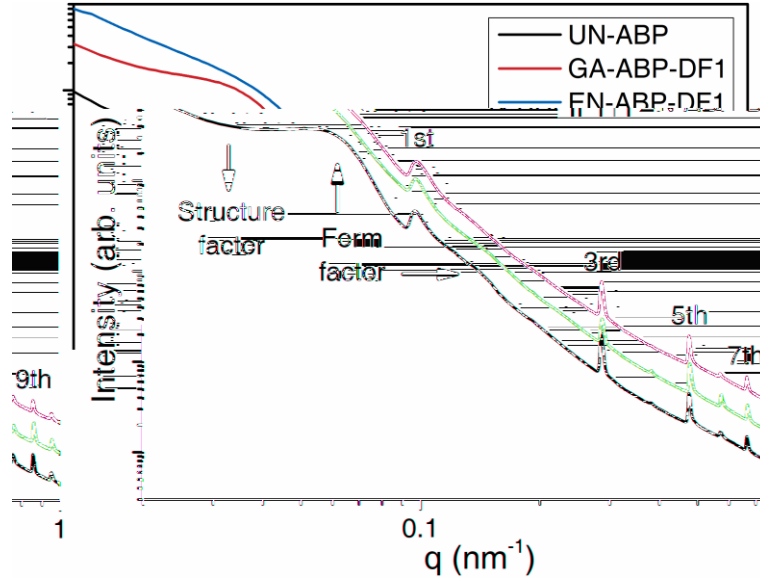
Figure 5.1: Stacked SAXS profiles of UN-ABP, GA-ABP-DF1 and EN-ABP-DF1 in logarithmic scale (left) and linear scale (right) in the q range from 0.02 nm^{-1} to 1 nm^{-1}. Resolvable peaks are denoted according to the peak orders.

Mapping over each sample across an area of 2.5 mm × 2.5 mm with 36 data points shows the uniformity of the D-period within each ABP, displayed by the bar charts of a representative UN-ABP, GA-ABP-DF1 and EN-ABP-DF1 (Figure 5.2). It indicates the homogeneity of the crosslinking reaction. The D-period decreases upon GA crosslinking by around 0.2–0.3 nm and EDC crosslinking but to a lesser extent of around 0.1 nm.
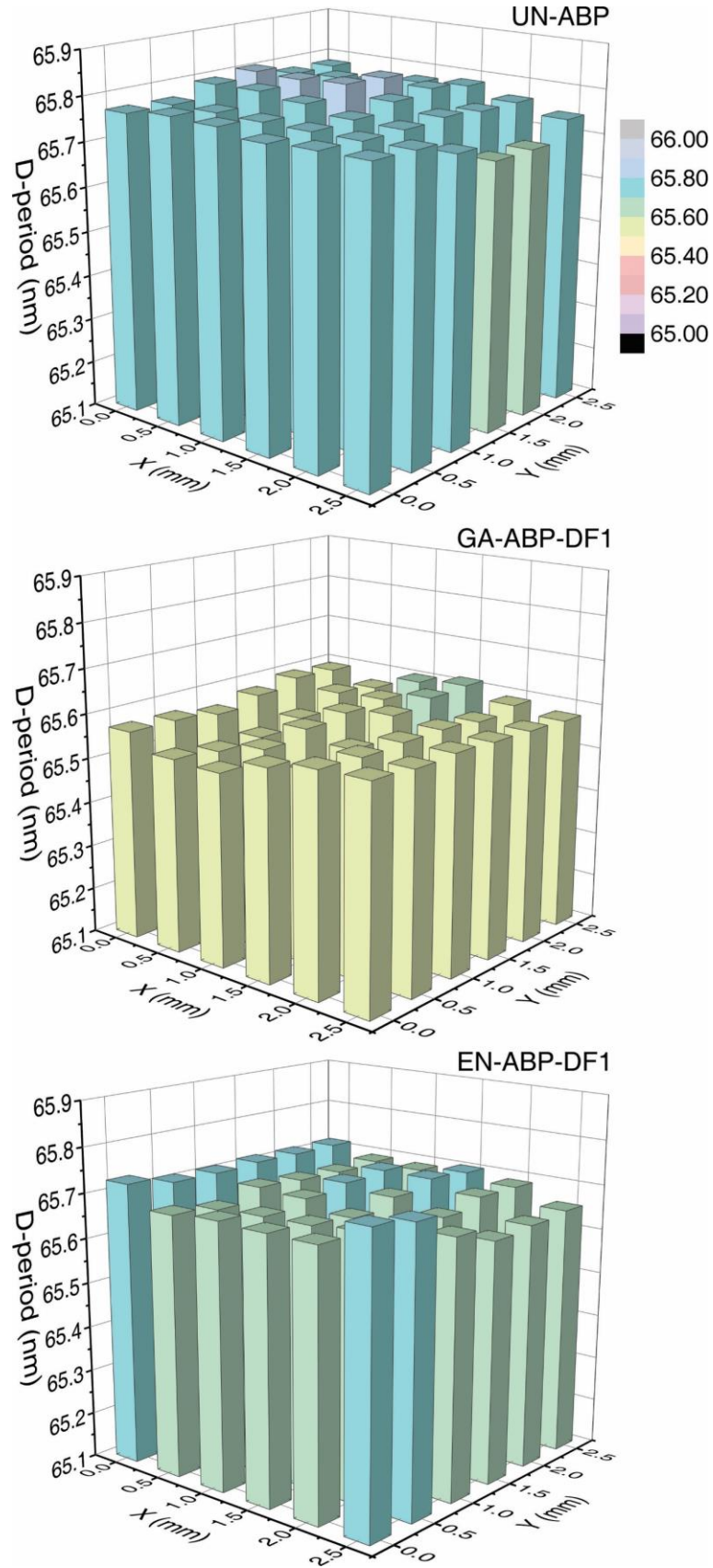
Figure 5.2: The *D*-period of UN-ABP, GA-ABP-DF1 and EN-ABP-DF1 mapped in an area of 2.5 mm × 2.5 mm (6 × 6 data matrix).

The investigation over a series of concentrations reveals more details about the decrease in D-period during crosslinking, shown as stacked SAXS profiles in Figure 5.3. When the GA stock solution (DF1) is diluted to DF5 (or DF10), the peaks shift towards higher q, giving a further decrease in the D-period of collagen of GA-ABP-DF5 (or DF10) compared to DF1. When the GA solution is further diluted to DF50, the decreases in D-period lessened to become closer to the uncrosslinked control (UN-ABP). A similar trend of peak shift is found in EDC crosslinked EN-ABPs, with the dilutions of crosslinker stock solution leading to a further decrease in the D-period of the collagen followed by a rebound after hitting bottom.
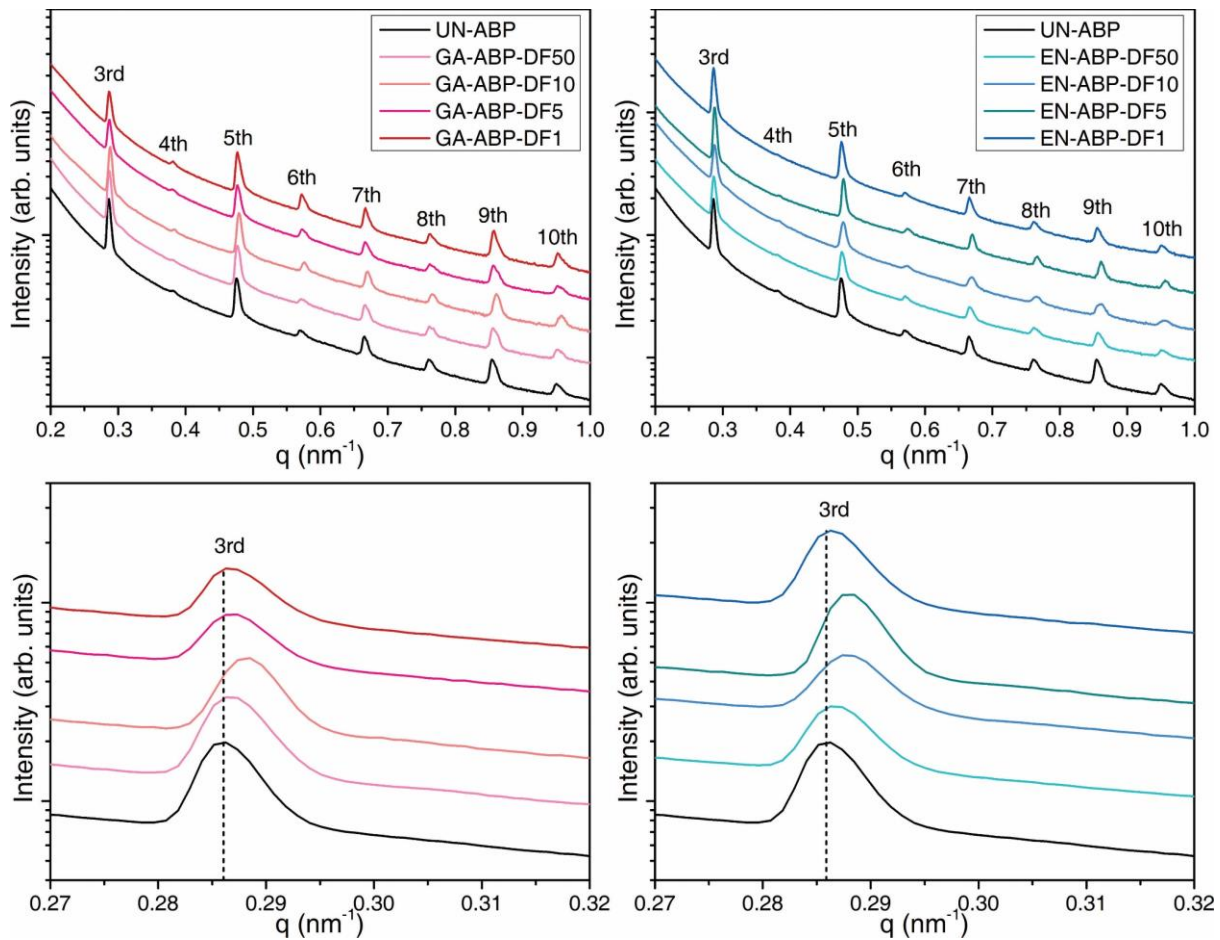
Figure 5.3: Stacked SAXS profiles of GA-ABP-DFx or EN-ABP-DFx ($x = 1, 5, 10, 50$) in the q range from 0.2 nm^{-1} to 1.0 nm^{-1}. The UN-ABP from the corresponding biological replicate is also plotted in each stack as the reference. The rescaled figures highlight the shifts of the 3rd order peak with dashed lines indicating the peak position in UN-ABP. Resolvable peaks are denoted according to the peak orders.

A rescaled x-axis to focus on the 3rd order peak of both the GA and the EDC concentration series show a clear reciprocation of the peak positions. The average D-period changes are shown in a bar chart (Figure 5.4). Unlike the skin powder[15] used in Chapter 3, the harvested pieces of ABPs we use in this study retain their organised structure and give changes in a consistent trend in the D-period with acceptable error values.
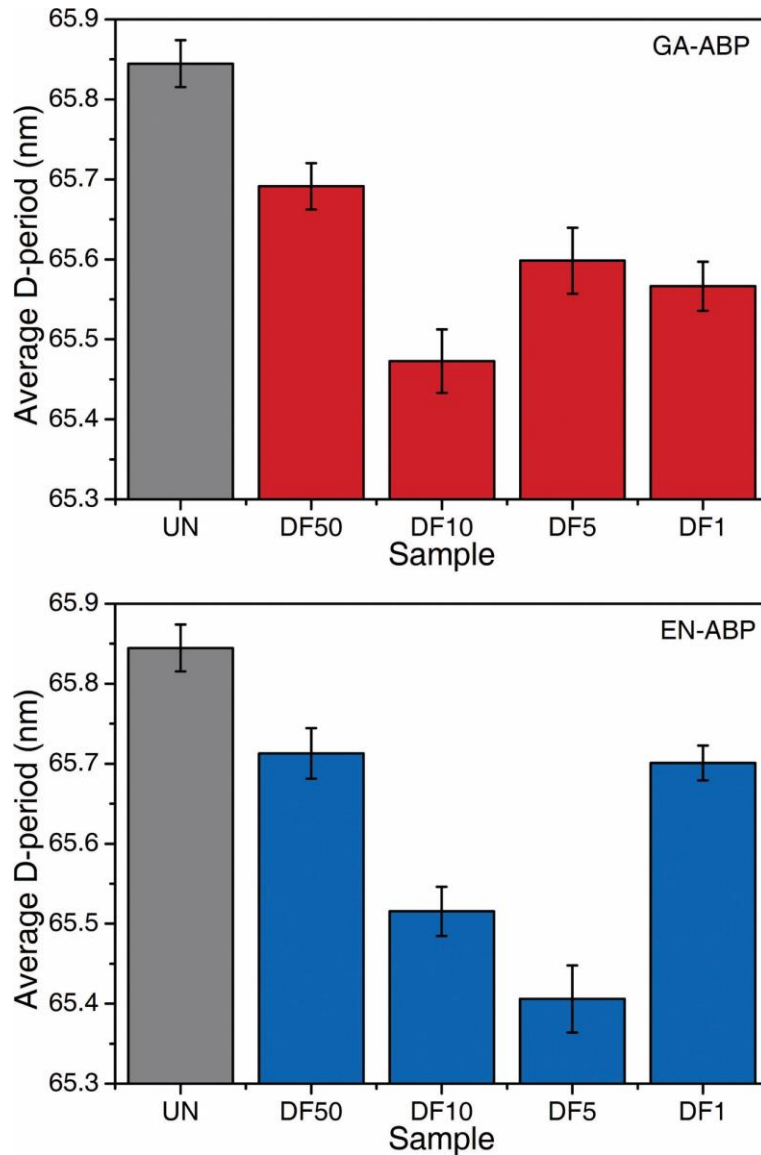
Figure 5.4: The average D-period across the mapped area of two replicates of UN-ABP, GA-ABP-DFx and EN-ABP-DFx ($x = 1, 5, 10, 50$).

---

[15] ABPs are much thinner than bovine skins (0.4 mm vs 3–8 mm). Therefore, the latter has to be ground into powder for uniform penetration at low chemical concentrations, yet leading to randomness in the D-period.

Apart from the *D*-period, the raw peak intensities fluctuate slightly across the measured area and vary substantially between replicates (Figure 5.5). Similar observations were shown in Section 3.3.1 and attributed to variations in the amount of collagen along the beam path; the same rationale could apply to the variations across the individual animals from which we source the BPs. The variations within the area of interest in the same piece of ABP sample could be attributed to the fluctuation in the density of the interwoven fibre network.

As was introduced earlier in Section 1.3.1, many studies on the crosslinking of collagenous tissues (including BPs) have employed the peak ratios to reflect the structural changes in collagen. The two particularly useful peaks are the 3rd and the 6th, leading to the area ratios of the 5th to 3rd ($R_{5/3}$) and the 6th to 5th ($R_{6/5}$); replacing the 5th with other odd order peaks may give similar trends but less accurate as the raw intensity decrease with increasing diffraction order. The increases in $R_{5/3}$ were used to represent the binding of metallic species to collagen molecules; our group recently observed similar phenomena using a polysaccharide organic crosslinker [78]. The $R_{6/5}$ was used to indicate the unbound water in the collagen matrix. It can be sensitive to the localised hydration level at the measured spot (especially if the spot is sufficiently small).
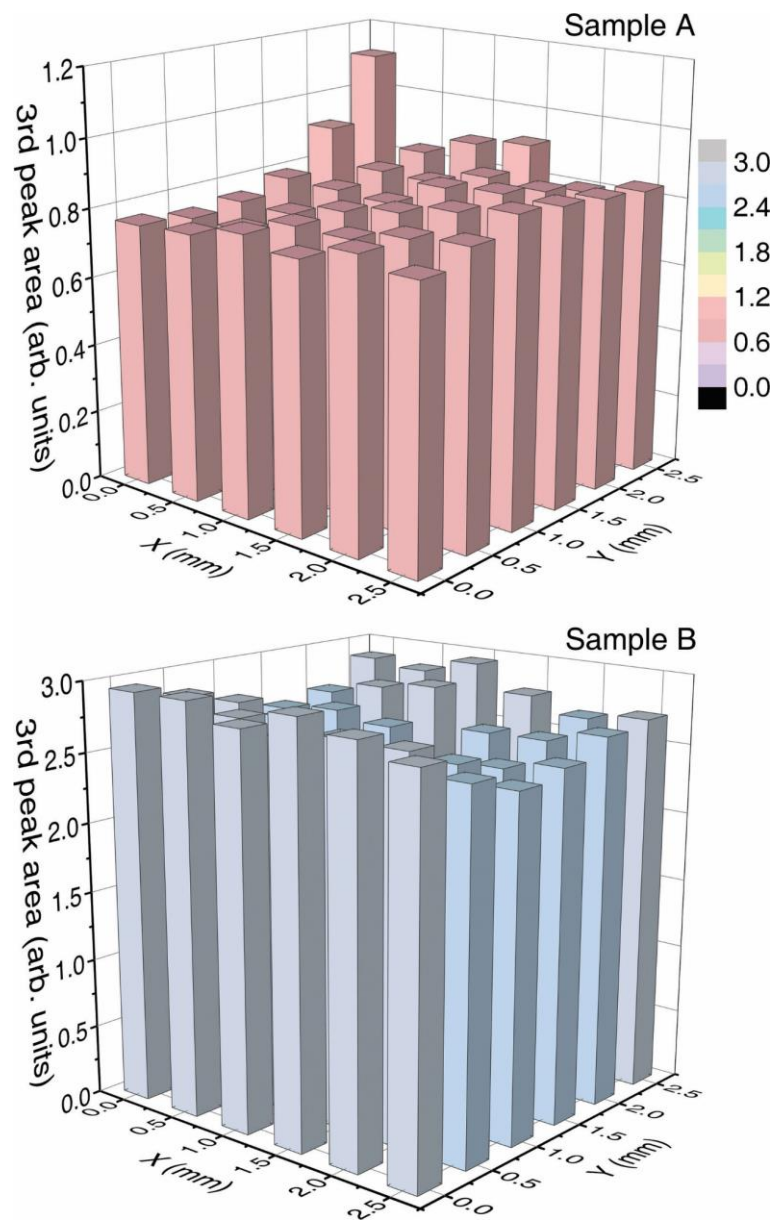
Figure 5.5: Raw integrated area of the 3rd order diffraction peaks in the 1D SAXS profiles of two UN-ABPs, highlighting the variations between biological replicates.

The calculated $R_{5/3}$ and $R_{6/5}$ show consistent values in two biological replicates (Figure 5.6), highlighting a successful exclusion of the irrelevant variations in raw intensity. The $R_{5/3}$ value lies around 0.22 for both UN-ABPs, closely matching the findings in uncrosslinked bovine collagen in skins [1, 78]. The value of $R_{6/5}$ fluctuates more than $R_{5/3}$ across the same area showing an average value between 0.09–0.10, different from the values in bovine skins that are pickled (*i.e.*, salted and acidified, which makes the tissues less hydrated than at physiological conditions). Again we confirm the consistency of $R_{5/3}$ across different types of collagenous tissues and the sensitivity of $R_{6/5}$ to the hydration level.
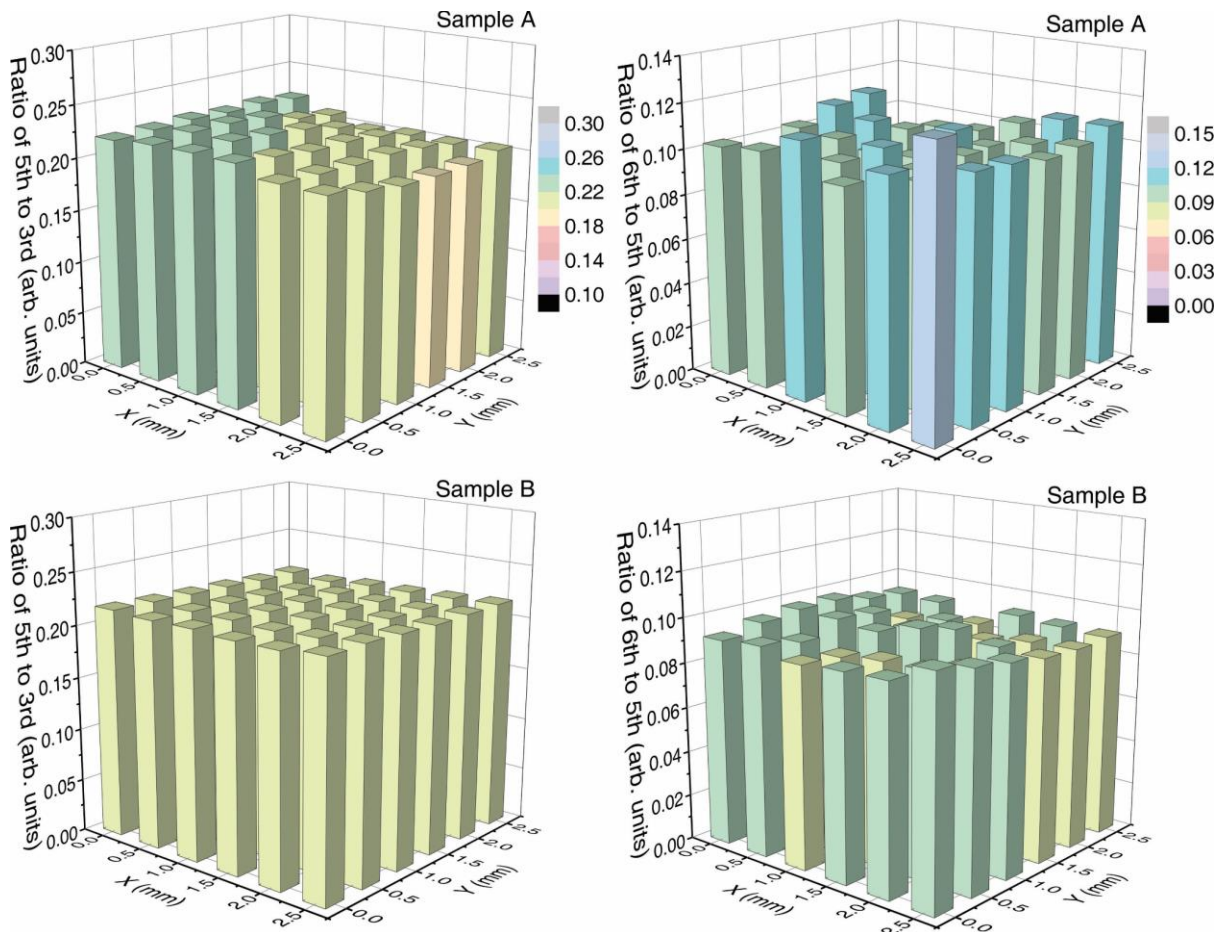
Figure 5.6: The ratios of the peak areas 5th to 3rd ($R_{5/3}$) and 6th to 5th ($R_{6/5}$) of two UN-ABPs.

The average values of the $R_{5/3}$ and $R_{6/5}$ from two biological replicates across the mapped area are calculated and plotted in Figure 5.7, including the full concentration series of GA and EDC. When we introduce GA crosslinking to the ABPs, the $R_{5/3}$ observes a monotonous increase along with GA concentration from 0.215 ± 0.009 in UN-ABP to 0.382 ± 0.008 in GA-ABP-DF1. The $R_{6/5}$ decreases from 0.097 ± 0.008 in UN-ABP to 0.075 ± 0.009 at the lowest GA concentration (DF50). However, it increases at higher GA concentrations (DF10, DF5, and DF1), with its value more than doubled to reach 0.242 ± 0.011 for DF1.

On the other hand, EDC crosslinking leads to only minor fluctuations in $R_{5/3}$ around the initial value within a range of 0.21–0.23 but gradually decreases in $R_{6/5}$ from 0.097 ± 0.008 to 0.071 ± 0.016 while seeing larger errors.
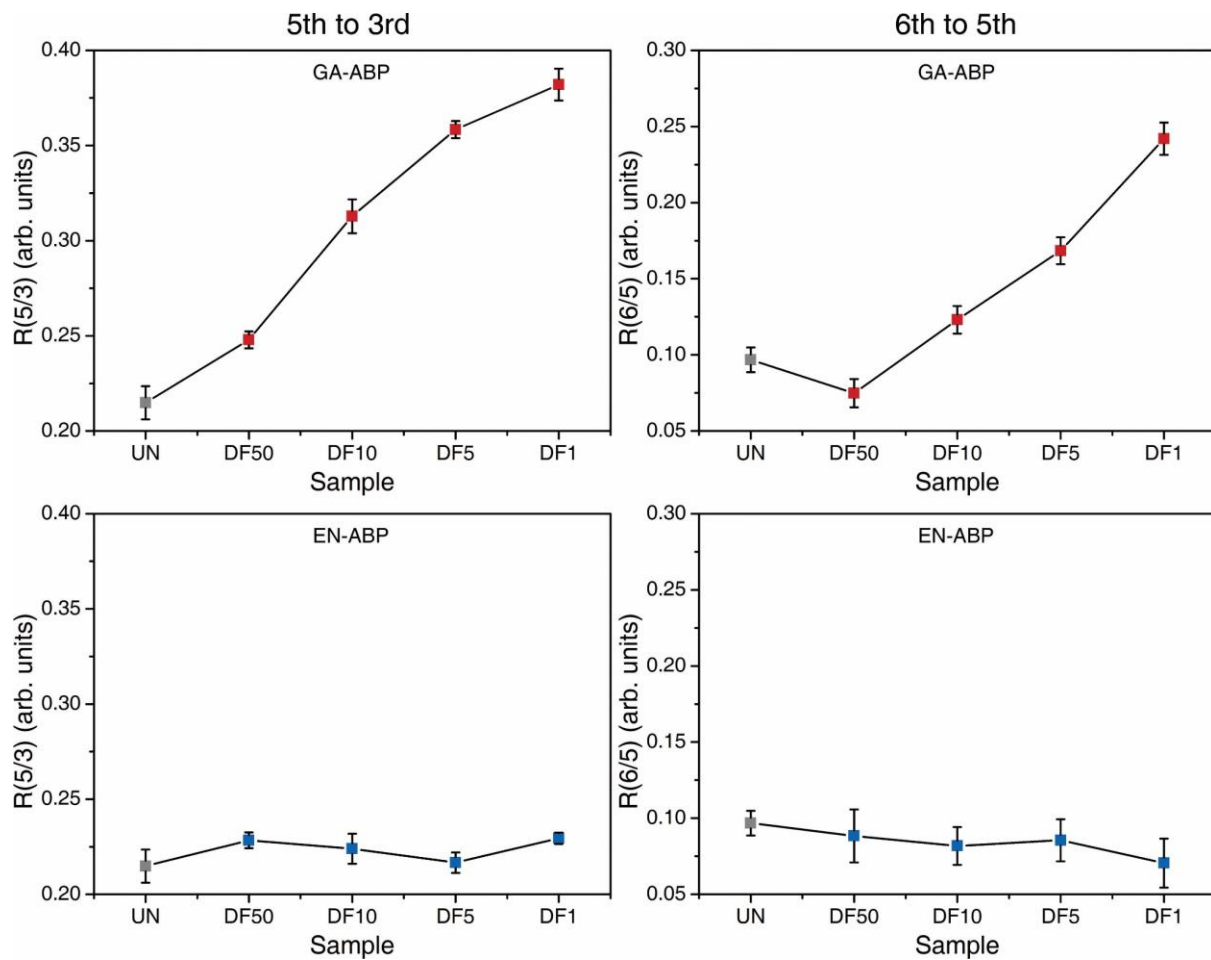
Figure 5.7: The average $R_{5/3}$ and $R_{6/5}$ values across the mapped area of two replicates of UN-ABP, GA-ABP-DFx and EN-ABP-DFx ($x = 1, 5, 10, 50$).

5.3.2 Thermal Stability

Characteristic DSC thermograms are acquired from the ABPs (Figure 5.8), showing well-resolved endothermic peaks followed by shifted baselines commonly observed during protein unfolding [152].
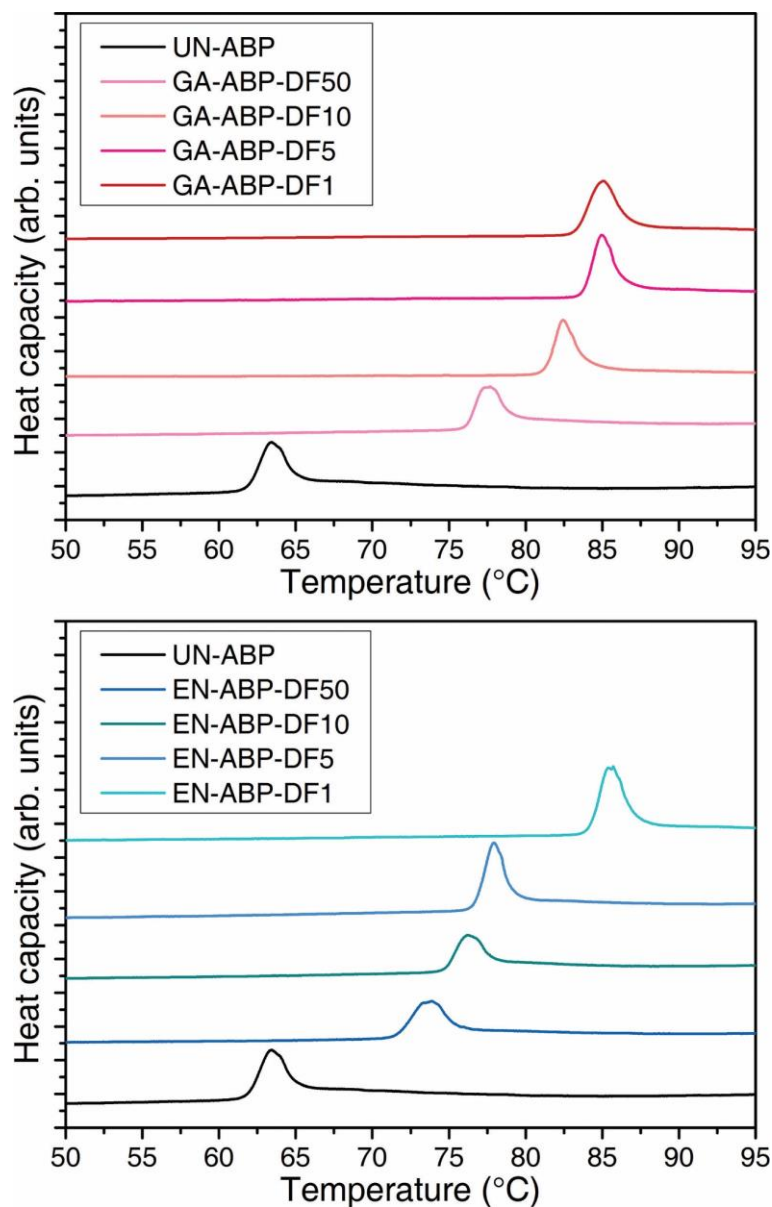
Figure 5.8: Stacked representative DSC thermograms of UN-ABP, GA-ABP-DFx and EN-ABP-DFx ($x = 1, 5, 10, 50$).

When crosslinked by GA or EDC, the peaks shift to higher temperatures to various extents, giving higher onset temperatures (T_d) that indicate increased thermal stability. This increment in thermal stability is commonly used as a convenient criterion by comparing it to a target value to assess whether or not the tissue is sufficiently crosslinked. The averaged results are displayed in Figure 5.9.

The uncrosslinked collagen in UN-ABP has the lowest average T_d at 64.2 ± 2.0 °C, which increases with GA crosslinking to 75.6 ± 1.6 °C at DF50. An increase in GA concentration to DF10 results in a large increment to 81.9 ± 0.8 °C. However, when GA concentration increases towards higher levels at DF5 and DF1, the changes in T_d are not statistically significant (p > 0.05, Student's t-test, same below), giving a plateau at around 84 °C. The unchanged T_d from DF5 to DF1 clearly stated the excess usage of GA in the conventional practice (DF1).

In the case of EN-ABPs, steady increments in T_d are observed at all concentrations studied. Starting from UN-ABP, T_d increases to 71.2 ± 0.7 °C at DF50, followed by 75.5 ± 1.2 °C at DF10, 77.6 ± 1.1 °C at DF5, and finally to the highest value at 84.7 ± 1.0 °C in EN-ABP-DF1.
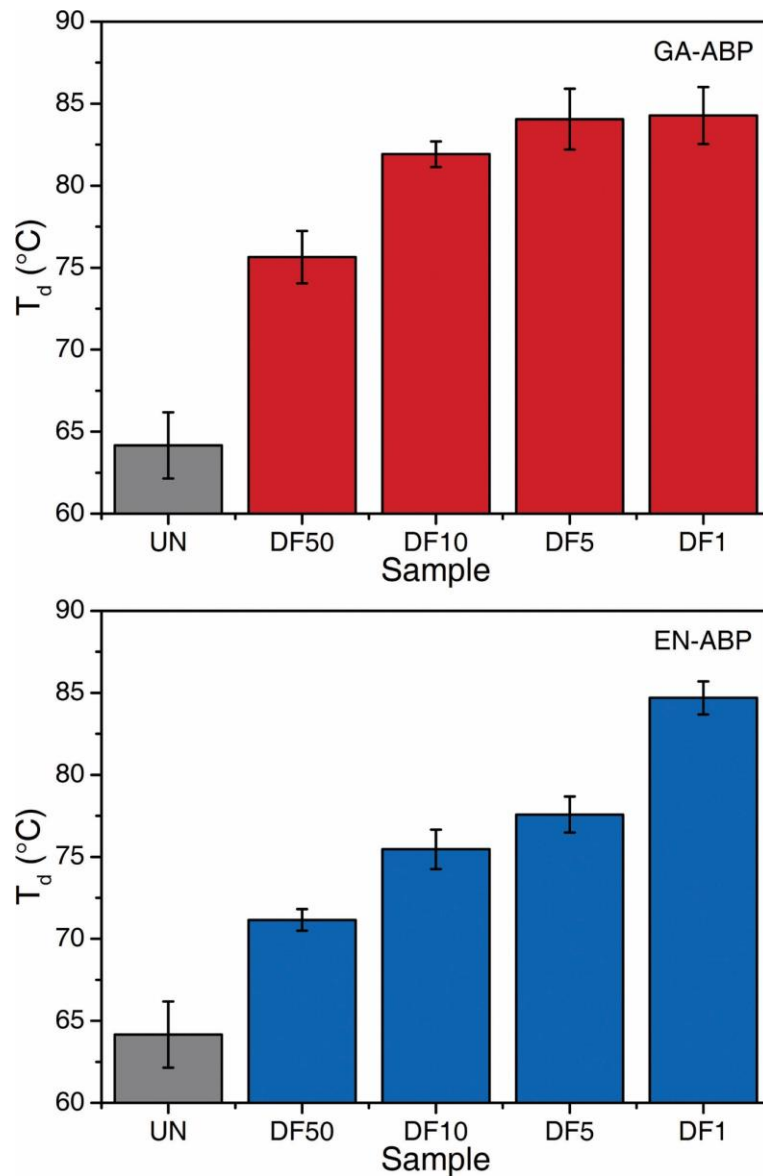
Figure 5.9: Average denaturation temperatures (T_d) of UN-ABP, GA-ABP-DFx and EN-ABP-DFx ($x = 1, 5, 10, 50$).

The peak area integration gives the calorimetric ΔH and is normalised to the amount of collagen (on average, 81.9% (w/w) in dry ABPs) (Figure 5.10). Large variations were found across replicated samples, leading to an insignificant result with the average values ranging from 30 to 40 J/g Coll. Similar ΔH values can be found in previous reports on chemically and physically crosslinked collagen [67, 293, 294], which also involve considerable variations. The large variations could be related to the integration method and the imperfections in the baselines. The method we use is exemplified in Section 2.4.2 as an iterated curvy baseline representing the heat capacity change during collagen denaturation. If a flat baseline were drawn for integration (when the thermogram is rough), it might lead to a higher value of ΔH, although giving similar unvarying ΔH upon crosslinking [67, 77].
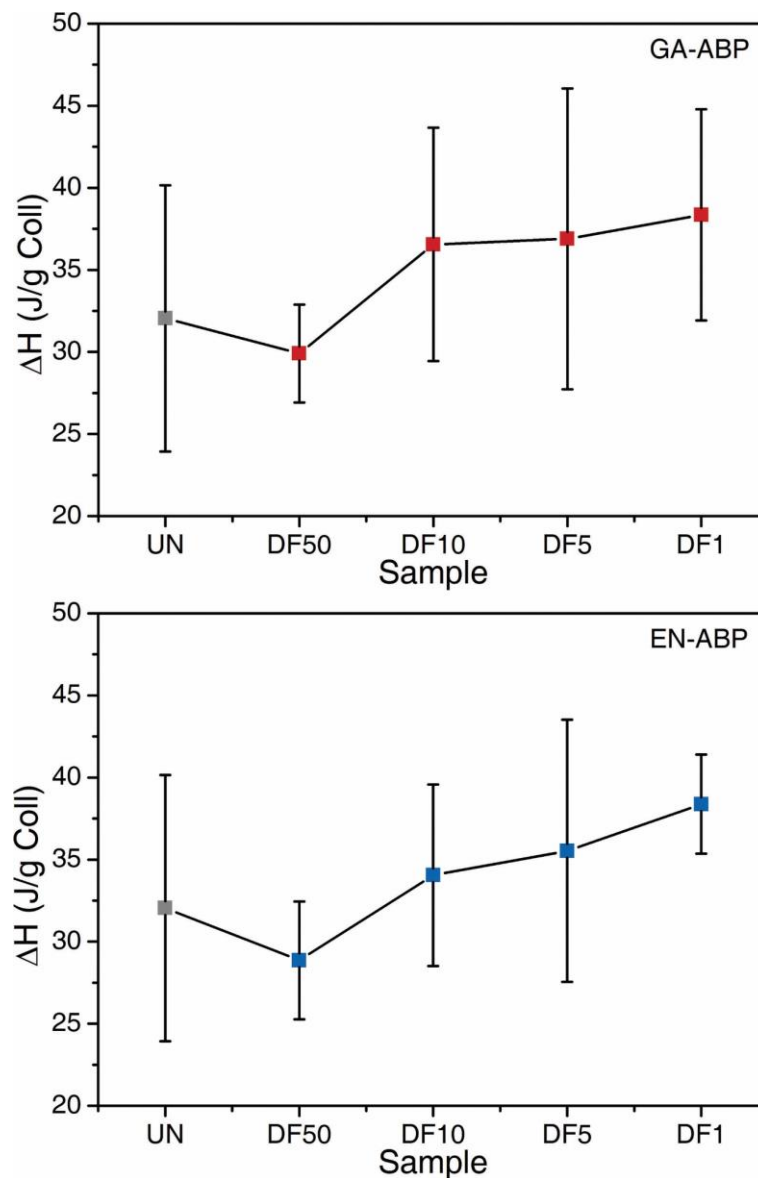
Figure 5.10: Average enthalpy changes of collagen denaturation (ΔH) of UN-ABP, GA-ABP-DFx and EN-ABP-DFx (x = 1, 5, 10, 50).

5.3.3 Enzymatic Resistance

Another important criterion of the stability of ABPs upon crosslinking is the enzymatic resistance. Although the enzymatic degradation process is kinetically relevant, prolonged exposure should not promote degradation if a suitable digestion site is inapproachable. This study set a 24-hour exposure time for all samples to compare the dramatic differences between the uncrosslinked and crosslinked ABPs at different concentrations. The results are listed in Table 5.1.

Table 5.1: Collagenase solubilised Hyp from GA-ABP-DFx and EN-ABP-DFx ($x = 1, 5, 10, 50$) shown as percentage values normalised to the uncrosslinked control samples (UN-ABPs).

Sample	DF50	DF10	DF5	DF1
GA	21.5% ± 12.4%	1.1% ± 0.5%	1.2% ± 0.6%	1.2% ± 0.7%
EDC	94.2% ± 1.7%	30.5% ± 11.6%	1.8% ± 1.0%	1.2% ± 0.5%

Even with the lowest concentration studied, GA can impart a substantial level of resistance to collagenase degradation, with only 21.5% of the collagen being solubilised; yet this is far from sufficient. However, at higher concentrations (DF10 and DF5), full resistances can be achieved with negligible solubilisation levels and are comparable to the ABPs crosslinked at the conventional GA concentration (DF1).

Similarly, EDC crosslinking at DF5 and DF1 provided full resistance against collagenase during the experiment. However, the stabilisation effect weakens at DF10 and further at DF50, with the latter having only minor differences from the completely dissolved uncrosslinked UN-ABPs.

5.3.4 Free Amino Group Content

The last criterion employed in this study is the free amino ($-NH_2$) group content quantified based on the renowned ninhydrin reaction. Results are shown in Figure 5.11. The average free $-NH_2$ group content value (unit: [µmol/g Coll]) shows gradual decreases upon being consumed by GA crosslinking from 155 ± 11 µmol/g Coll to 62.6 ± 1.3 µmol/g Coll at the highest concentration (DF1). On the other hand, EDC occupies fewer $-NH_2$ groups than GA, observing a moderate decrease toward 101 ± 4 µmol/g Coll.
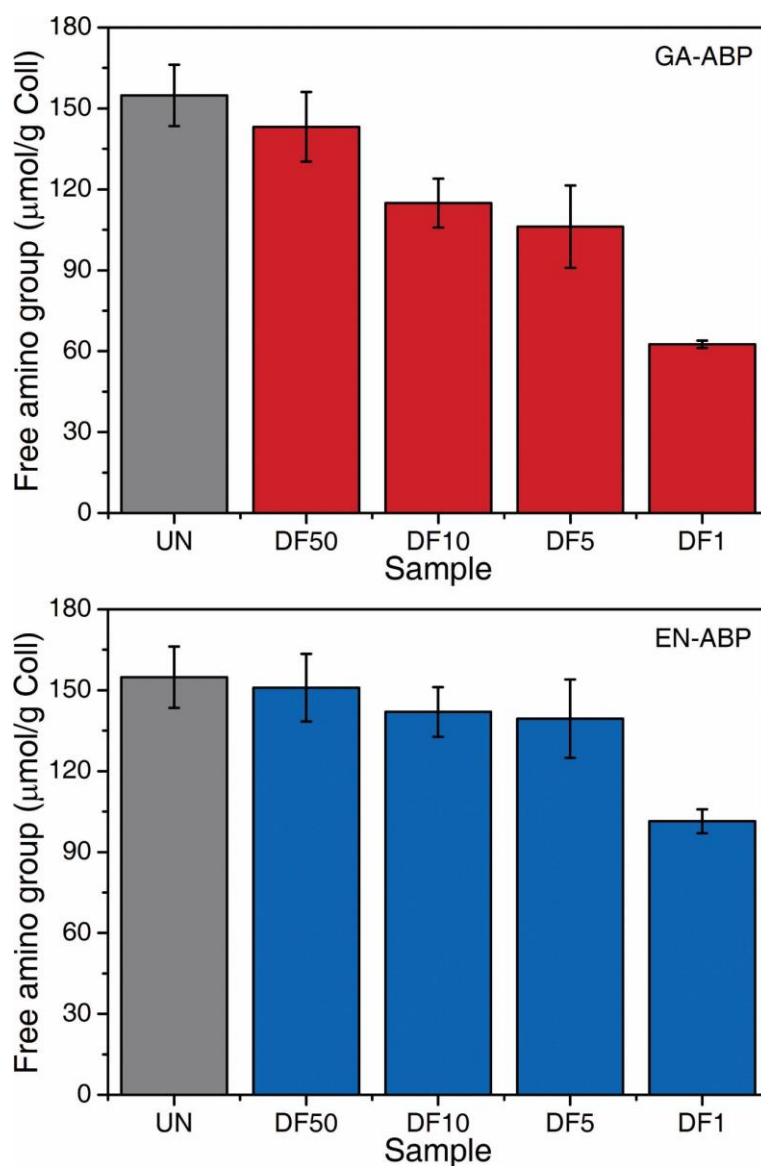
Figure 5.11: The average content of free $-NH_2$ groups in UN-ABP, GA-ABP-DFx and EN-ABP-DFx ($x = 1, 5, 10, 50$).

The free –NH₂ group content values are commonly calculated to the degree of crosslinking (Figure 5.12) to represent the performance of the crosslinker. In GA-ABPs, the degree of crosslinking shows steady increments with GA concentrations. At DF1, it gives the highest value amongst all samples at 59.4% ± 3.0%. When diluted to DF5 and DF10, the value halves to around 31.3% ± 9.5% and 25.5% ± 8.0%, respectively, and the difference between the two concentrations is insignificant (p > 0.05). At the lowest concentration at DF50, the value decreases to 7.4% ± 6.7%, showing a substantial error across the replicates.

A similar trend was observed in EN-ABPs: the value is at 34.0% ± 8.0% at DF1 which decreases significantly to 12.8% ± 4.1% at DF5, and then vaguely halves to DF10 and DF50 $(0.05 < p_{\text{one-tailed}} < 0.25)$. The larger errors could be attributed to the less uniform reaction with EDC than GA.
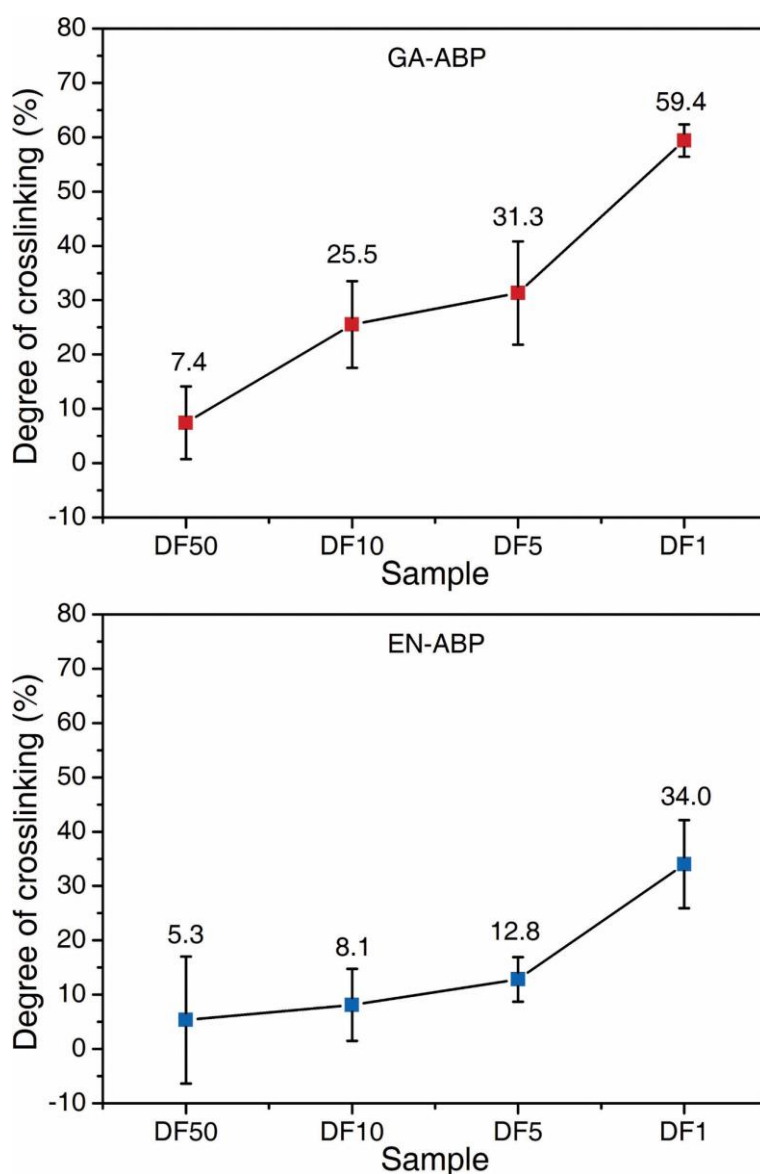
Figure 5.12: The average degree of crosslinking of GA-ABP-DFx and EN-ABP-DFx ($x = 1$, 5, 10, 50) calculated based on the free –NH₂ group contents.

The "degree" or "extent" of crosslinking solely based on the free –NH₂ group content is straightforward for dialdehyde crosslinkers but can be confusing when comparing crosslinkers undergoing different mechanisms. Here, a factor n (number of covalently linked sites per –NH₂ involved, see Section 5.2.6) was introduced to consider the different occupancy of sites between GA and EDC. The resulting value, the number of covalently linked sites, allows us to direct percept the number of "blockages" that the crosslinkers created in the collagen matrix.

Results show that GA occupies about 4 sites per collagen molecule at DF50, increasing to 12 at DF10, 14.6 at DF5, and 27.6 at DF1. The EDC samples also show a vague increasing trend at low concentrations, followed by a significant increase from DF5 to DF1. With the number of occupied sites, we can now intuitively see that the GA-ABP-DF1 and EN-ABP-DF1 have similar performances (around 30 sites occupied per collagen molecule) regarding the occupancy or "blockage" of reactive sites in collagen.
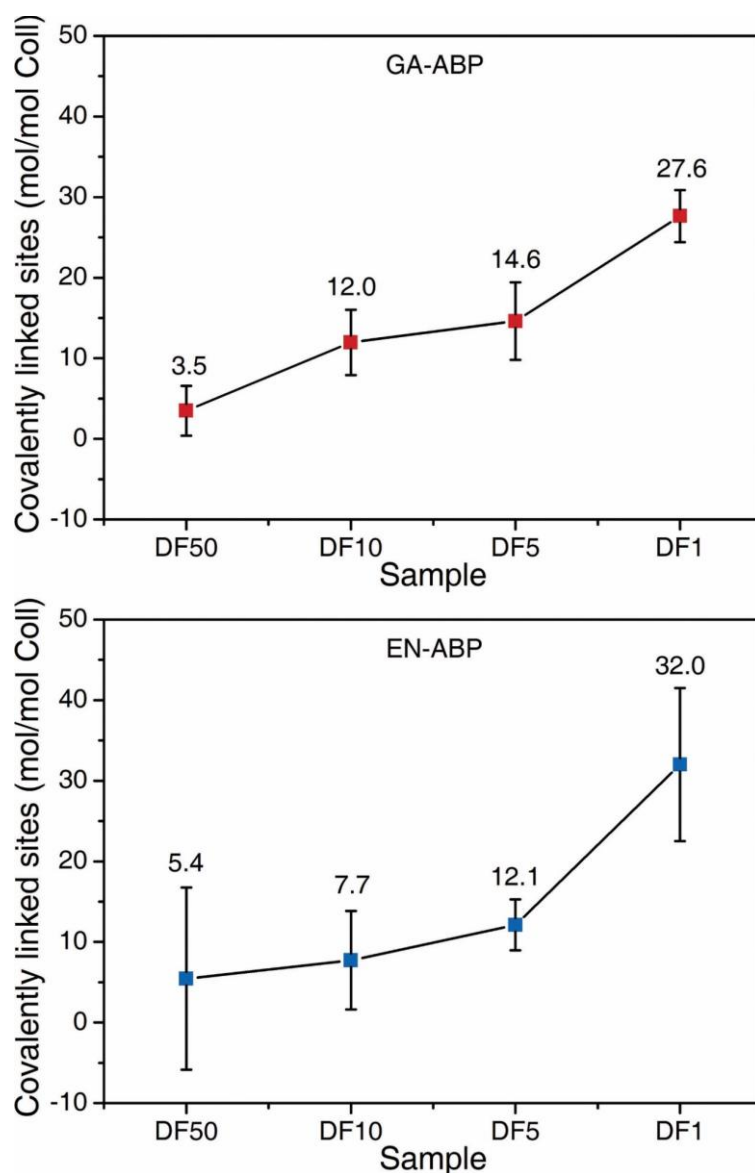
Figure 5.13: The average number of covalently linked sites in GA-ABP-DFx and EN-ABP-DFx (x = 1, 5, 10, 50) calculated based on the free –NH₂ group contents.

5.3.5 GA vs EDC: Crosslinking Mechanisms

A brief recap of GA and EDC crosslinking reaction mechanisms is given to facilitate the following discussion [62, 295]. The reaction of GA with collagen starts from the formation of a Schiff base intermediate between an aldehyde (–CHO) group of GA and an amino (–NH$_2$) group in collagen. The dangling –CHO group on the other end of the GA molecule then links with another –NH$_2$ group or self-polymerise to form longer chains before being terminated. In contrast, "zero-length" crosslinks form between a carboxyl (–COOH) group and a –NH$_2$ group induced by EDC. First, EDC converts a –COOH group in collagen into an O-acylisourea to trigger the linkage with a –NH$_2$ group to form a peptide bond.

Now, with the results covering the structural changes and the set of stability criteria, one can distinguish the multiple events that could occur at different crosslinking conditions. Here are the possible types of (divalent) crosslinks that can form in the collagen matrix by GA or EDC, with a schematic illustrated in Figure 5.14:

(1) Telopeptidyl-helical intermolecular linkage;
(2) Telopeptidyl-telopeptidyl intramolecular (interchain) linkage;
(3) Helical-helical intermolecular linkage;
(4) Helical-helical intramolecular (interchain) linkage;

/ = telopeptidyl-helical, intermolecular
❬ = telopeptidyl-telopeptidyl, intramolecular
⫶ = helical-helical, intermolecular
•-• = helical-helical, intramolecular
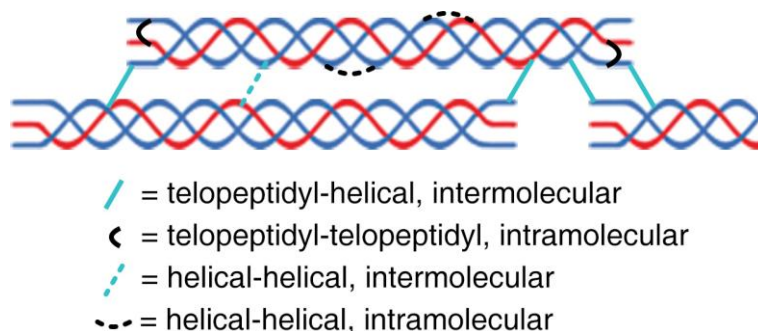
Figure 5.14: A schematic illustration of the possible types of crosslinks in the collagen matrix formed by GA or EDC. The lengths of the telopeptides are exaggerated to be visible at this scale.

At low concentrations, because of the insufficiency of the crosslinker, we expect a preference in the reaction sites to initiate the crosslinking reaction. Due to better chain flexibility, the functional groups in the telopeptidyl region of collagen are more favoured when binding with the crosslinkers than those in the helical region. In our case, GA initiates on –NH$_2$ groups, while EDC initiates on –COOH groups.

Then, a linkage toward an adjacent functional group is formed. Here, in theory, we have four different scenarios depending on whether the functional group is in another collagen molecule or another polypeptide chain within the same molecule and whether it is in the telopeptidyl or helical region.

The large gap between the telopeptide of one collagen molecule and that of another makes the formation of telopeptidyl-telopeptidyl intermolecular linkages impossible. Figure 5.15 shows that a Lys residue at position 17 is linkable to the hydroxylysine (Hyl) residue at position 87 in an adjacent molecule [100]; a telopeptide in collagen contains less than 25 residues. Thus, we could exclude the formation of telopeptidyl-telopeptidyl intramolecular linkages. For a similar reason, telopeptidyl-helical intramolecular linkages are excluded.
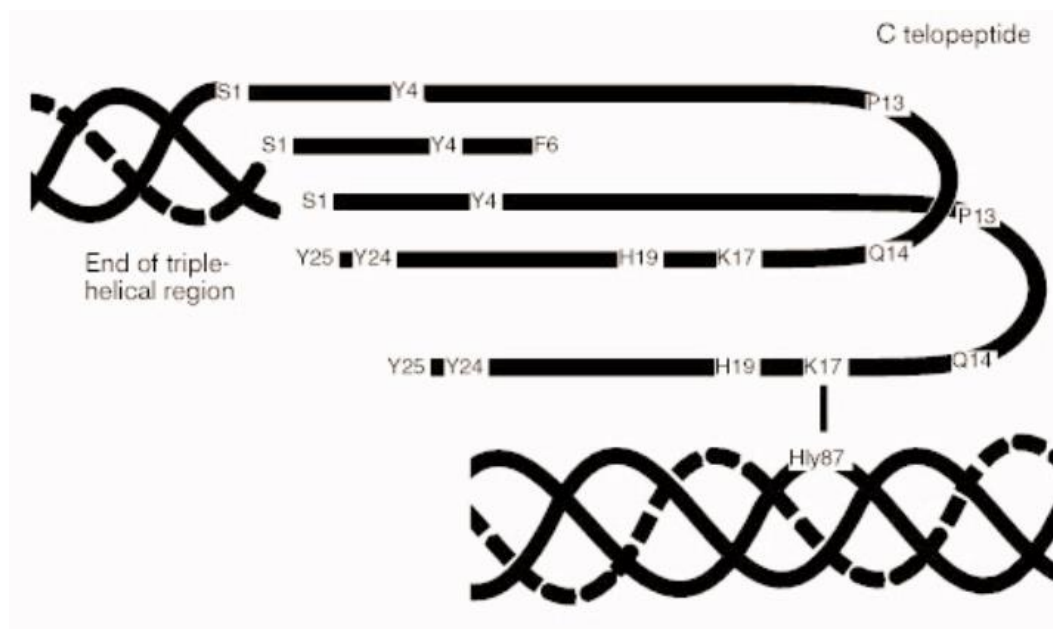
Figure 5.15: A expanded view of the C-telopeptides and their relative positioning with the adjacent helical region. (Reprinted from Ref. [100] with permission from Elsevier.)

The telopeptidyl-helical intermolecular linkage leads to conformational changes in the telopeptides to a more contracted or folded form, as shown in Figure 5.15. The changes lead to a rearrangement via side-by-side gliding of collagen molecules along the fibril axis, resulting in decreased *D*-period; the gliding model was applied to explain the rearrangement of collagen molecules during drying rat tail tendon (RTT) [47]. They also considered the lack of water as a lubricant during drying to prevent gliding, which is not a concern in our fully hydrated ABPs. Other studies also found that covalent crosslinking cause decreases in the *D*-period in collagenous tissues [45, 78, 296]. On the contrary, the telopeptidyl-telopeptidyl intramolecular linkages would have minor impacts on the intermolecular spacing since no gliding or repositioning is required to form the crosslinks. Therefore, the observed *D*-period changes indicate the dominant formation of telopeptidyl-helical intermolecular linkages at low concentrations. Either GA or EDC causes the *D*-period to decrease by around 0.3 nm at suitable low concentrations.

At high concentrations, the crosslinkers would have exhausted the available sites in the telopeptides. Therefore, the larger number of $-NH_2$ and $-COOH$ groups in the helical region could be initiated to form crosslinks by GA and EDC, respectively, leading to helical-helical linkages. The electron density mapping by Orgel's group showed the lateral gap size of around

0.3 nm between the surfaces of the triple helical collagen molecules in the overlap region [11], allowing helical-helical intermolecular linkages. It was introduced earlier in Section 1.1.2 that collagen molecules are tilted in the overlap region, resulting in a pleated structure along the fibril [32]. The formation of helical-helical intermolecular crosslinks between the lateral gaps of collagen molecules could lead to a more compact packing of collagen molecules in the radial direction of the fibrils. This heterogenous dimensional change could straighten or elongate the fibrils and cause the D-period to rebound.

Following the same rationale, we may deduce that helical-helical intramolecular linkages would lead to fewer impacts in the intermolecular packing of collagen, thereby giving minor effects to the D-period. However, due to the comparable interchain distances (helical rise, 0.28 nm) to the intermolecular lateral distances (0.3 nm) [11, 39], both types of crosslinks can form to an equivalent extent. This conclusion applies to both GA and EDC crosslinking.

It is interesting to note that, despite the completely different crosslinking chemistry and binding sites, GA and EDC affect the D-period in very similar ways at all concentrations. However, the other evidence will extend the understanding of the structural impacts and differentiate GA from EDC.

The site-specific binding of GA to $-NH_2$ containing residues leads to prominent increments in $R_{5/3}$ because it contributes to the electron density contrast in the repeating units. The increments in $R_{5/3}$ to a maximum of 0.4 match those imparted by polysaccharide crosslinkers (0.4–0.6) [78] but are less than those by bound Cr(III) species (0.8) [1]. The molecular hydration level indicated by $R_{6/5}$ shows an interesting decrease at only the lowest GA concentration, followed by steep increases at high GA concentrations. This unexpected decrease could be explained by considering the additional strain introduced by GA crosslinks that can disrupt the native interdigitation of collagen molecular segments in one microfibril with its neighbours, leading to a mismatch which opens more gaps between the microfibrils. At high concentrations, GA crosslinks take up part of the intermolecular spaces and displace water from the collagen matrix to cause dehydration and increases in $R_{6/5}$.

In contrast, the fact that no foreign species is involved in the zero-length linkages by EDC leads to a similar collagen structure to the native state, showing unchanged $R_{5/3}$. Regarding the hydration level changes, a similar rationale as GA at low concentration could apply: the peptide linkages disrupt the interdigitation of collagen molecules and open gaps, thereby containing more water. However, adding more EDC further sets the structure with peptide crosslinks in the intermolecular structure but does not introduce foreign species to displace water molecules in the collagen matrix, resulting in a continuing decrease in $R_{6/5}$.

We can now employ the proposed mechanism based on structural characterisations to explain the interesting discrepancies amongst the stability criteria.

The improved thermal stability (T_d) of collagen by chemical crosslinking was previously recognised as nothing more than a result of molecular dehydration [77]. However, we observe

a plateau in GA crosslinked ABPs over DF5, conflicting with the hydration level represented by $R_{6/5}$. Increasing GA up to DF1 is confirmed to form more crosslinks and displace water but stop contributing to T_d. EDC also gives a mismatch between the increased T_d across all concentrations and the opposite trend in molecular hydration. The above evidence highlights the potential oversimplification in the explanation solely based on dehydration.

Here, we postulate a mechanism for the increased T_d based on the types of crosslinking and binding in collagen. At low concentrations, either GA or EDC forms divalent crosslinks that increase the structural rigidity and spatial confinement to hinder the uncoiling of the collagen triple helices when heated. Excess GA molecules attach to collagen only monovalently to $-NH_2$ groups or self-polymerising at high concentrations due to insufficient binding sites to be paired. With monovalent binding, GA behaves similarly to monoaldehydes which may not contribute to the T_d of collagen if overwhelmed by the divalent crosslinks [62, 293]. The continued increase in the degree of crosslinking confirms the formation of direct monovalent binding. On the other hand, the potential self-polymerising only provides steric hindrance effects by occupying intermolecular spaces, whose contribution could also be overshadowed by the major divalent crosslinks.

Instead, EDC may continue to form divalent crosslinks at high concentrations because of its halved consumption of $-NH_2$ compared with GA; note that Asp and Glu ($-COOH$ groups) are more abundant than Lys and Arg ($-NH_2$ groups). The increment in T_d thus progressively increases with concentrations.

This observation also highlights the limitations of evaluating the GA-stabilised ABPs based on the degree of crosslinking or the number of covalently linked sites. These criteria give good representation at low GA concentrations but deviate from reality at high GA concentrations.

Also, as is observed, the trend in enzymatic resistance differs largely from the other two criteria. However, we can further extend the proposed mechanism to include the effects of GA or EDC crosslinking on the resistance to enzymatic degradation. The collagenase from *Clostridium histolyticum* has a molecular weight of 116 kDa and approximately 10 nm in diameter that is too bulky to penetrate through lateral molecular gaps [11, 297, 298], so the digestion would mostly occur from the surface of collagen fibrils. It cleaves specifically at the X–Gly bond in a –R–Pro–X–Gly–Pro–R– peptide sequence, where X is mostly a neutral amino acid residue which is not reactive with GA or EDC. Hence, the way that GA or EDC imparts collagenase resistance to the ABPs is unlikely via direct blockage on the X sites.

However, the indirect contribution of GA crosslinking to collagenase resistance is mechanistically different from EDC crosslinking. GA binds to collagen and forms a coating to spatially occupy a certain volume, blocking the suitable positions for collagenase to attach to the surface of collagen fibrils. Instead, EDC could not coat the collagen molecule, but due to its zero-length characteristics, it tightens the gaps between chains and molecules, thereby blocking the path for collagenase. Overall, the number of covalently linked sites and the enzymatic resistance follow similar trends in both GA and EDC cases.

The variation of the resistance at different concentrations can be explained when we consider all aspects, including the number of covalently linked sites, the length of collagen molecule (around 300 nm) [31] and the quasi-hexagonal lattice structure. The average gap size to allow the collagenase to attach to collagen is $(300/x)$ nm, where x is the number of covalently linked sites. Sizes above 35 nm (less than 8 occupied sites) can be found at DF50 for GA and DF50 and DF10 for EDC. The gaps may remain sufficiently large for collagenase to attach and cut the specific peptide bonds.

When over 12 sites are occupied per collagen molecule, we could estimate a distance smaller than 25 nm, which may be even narrower considering the higher reactivity with surface molecules than the embedded molecules. The probability of the collagenase fitting into the gaps minimises, resulting in the observed full resistance. A higher degree of crosslinking increases blockages, but as mentioned earlier, they may not further improve the resistance if a suitable digestion site is already inapproachable to the collagenase.

5.4 Conclusion

Through the insightful structural characterisations, a mechanism was proposed for how chemical crosslinking affects collagen structure in ABPs, and explicate the relationship and discrepancies between the stability indicators. The importance of considering structural aspects is highlighted in providing essential complements to the existing stability criteria for assessing processing strategies to produce biomaterials from collagenous tissues.

The mechanism proposes the prioritised formation of telopeptidyl-helical intermolecular linkages, which leads to the following changes:

(1) Decreases in the D-period. The folded telopeptides disrupt the intermolecular packing leading to a side-by-side gliding between collagen molecules for a smaller D-period. Also, when species (*e.g.*, GA) attach to collagen in a certain pattern of specificity, the electron density changes, and so do the diffraction peak intensities.
(2) Increases in T_d. The divalent crosslinks restrain the uncoiling of collagen under heat.
(3) Improvements in collagenase resistance. Gaps for the enzyme to approach specific sites are blocked due to the increased steric effects (for GA) or packing compactness (for EDC).

As the available telopeptidyl sites decrease, helical-helical linkages gradually become dominant in the crosslinking events. Upon the exhaustion of telopeptidyl sites, partial formation of helical-helical linkages would have occurred, with the majority remaining uncrosslinked. At this point, the following changes (or unvarying aspects) are expected:

(1) Increases in the D-period. The linkages draw collagen molecules closer together in the radial direction of the fibrils. It could lead to heterogenous dimensional changes to straighten the kinks in the tilted packing, resulting in the D-periods increments.
(2) Further increases in T_d via the same mechanisms.
(3) Additional linkages do not further improve collagenase resistance.

With a clear mechanism established, we could now apply this mechanism to predict the optimal reaction conditions (without specifying the crosslinker) and estimate the stability criteria accordingly. An optimal condition should maximise the telopeptidyl-helical linkages[16] rather than fulfilling all the possible helical-helical linkages via excess usage of crosslinkers. If that were achieved, it would result in a minimum D-period, at which point the T_d may give around 80 °C, and the number of covalently linked sites is about 12 per collagen molecule.

It is worth highlighting that the overall efficiency of GA or EDC crosslinking decreases with increasing crosslinker concentration regarding the outcomes per crosslinker added, including the occupancy of free amino groups, the increments in T_d and the already maximised enzymatic resistance. These are probably due to the occurrence of side reactions, namely, more monovalent binding and self-polymerisation of GA and more hydrolysis of the

---

[16] It is also preferred *in vivo* when forming natural crosslinks, which are initially divalent but progressively develop into trivalent for better stability as the animal ages.

activated –COOH intermediate (O-acylisourea) in the case of EDC. It highlights the drawback of excess usage and suggests that extra functionalities, when needed for targeted applications, are better imparted by components other than chemical crosslinkers to maximise crosslinking efficiency and minimise the adverse effects.

Chapter 6   Summary and Future Work

A group of niche aspects of extensive interest to scientist peers in this interdisciplinary research field was covered in this work. It is manifested following the trajectory of my growing knowledge in chemistry to support the three pillars of the project (*i.e.*, collagen, SERS, and SAXS), from coordination chemistry to physical chemistry and, at last, materials chemistry. All these aspects are coherent through an internal logic: the binding of materials or chemicals to collagen that alters its native structure. This focus has been pursued since my first publication on collagen in 2017 but has been greatly empowered during this PhD project since 2019, through which various forms of bovine collagen were investigated, including skin, extracted solution, and pericardium. The main findings are re-emphasised here with potential future research to highlight the role of the two advanced techniques in accomplishing this work to provide us with mechanistic findings.

Using the SERS technique, the successful attempts in Chapter 3 and Chapter 4 provided molecular-level information on collagen binding to Cr(III) and Ag atoms on the surface of nanoparticles. The near-field electromagnetic enhancement allowed weak Raman bands to be observed, *e.g.*, the –COO⁻ groups. Some bands are visible in IR spectroscopy yet are limited to the dry state, which is far from ideal for biological samples. The –COO⁻ or –COOH group is vital for the binding to metallic species, and the changes it could result in would lead to persistent doubt in interpreting SERS spectra of proteins if the mechanism of its variations in binding affinity were not understood. From this perspective, the findings through the SERS studies (especially Chapter 4) have made a significant step forward. It also highlights that, although SERS has been a mature technique with its fundamental research questions answered much earlier than this work, many aspects remain to be rounded out for practical applications.

Amongst the many natural extensions from this part of the work, the formation of well-defined colloids via controllable aggregation could be of prime importance. In principle, the half-half dilution method would give an evenly adsorbed target analyte to the nanoparticles and stable SERS events in the colloidal solution. However, the bulkiness of protein molecules could make the reality far from ideal. Additionally, to monitor chemical crosslinking reactions or electrostatic binding with other biomolecules, concerns over the competitive binding of collagen with the other species need to be resolved for correct data interpretations. Future work on protein analysis using SERS may be focused on this aspect.

Another potentially interesting focus for future research comes from the preliminary comparison in the studies on collagen samples in solution and as solid in fibres. The SERS measurements on lyophilised extracted collagen sponges gave an intermediate example, with the spectra largely resembling those of collagen in fibres. The similarity in the concentration of the sponges with the fibres probably results in the resemblance. However, the differences in the SERS spectra of lyophilised collagen from collagen solution may lead to the further differentiation of the affinity of functional groups on collagen to AgNPs. Such an aspect may

be extended to region-specific monitoring of collagen during binding with other biomolecules that comprise an ongoing interest of our group from a materials point of view.

On the other hand, using the SAXS technique, stepping stones for developing processing methods of collagen materials were constituted by revealing the binding and/or crosslinking mechanism of Cr(III), GA, and EDC when added to collagen at different concentrations, as discussed in Chapter 3 and Chapter 5. The new insights on Cr(III) highlight the selectivity in its preferred binding mechanisms to collagen regulated by the anions in the system. The findings on GA and EDC point out the inefficiency when telopeptidyl collagen side chains are exhausted. The distinctive roles of the "binders" (a term to include all three chemicals) are explicated based on the rich information from SAXS diffraction peaks. While the renowned axial D-periodicity of collagen could be accurately measured yet vary across different types of tissues or even biological replicates, the ratios of the peak areas are highly consistent and indicative of the interactions of collagen with extrinsic species.

However, as much as we would like to think SAXS has allowed us (and the pioneer researchers) to understand a wealth of phenomena via numerous chemical treatments, several natural extensions of this work should be considered in future studies. One direct extension comes from the wide variety of organic crosslinkers. As the fundamental principle tells, only changes in the electron density contrast in the regularly packed collagen repeating units would lead to diffraction peak intensity changes; this was briefly confirmed in the case of EDC. If the crosslinker happens to have a very similar electron density to the collagen molecules, the changes will be hardly assessable using SAXS; this is highly possible if we continue to investigate the increasing number of novel organic crosslinkers developed for benign crosslinking strategies as potential alternatives to the conventional GA or Cr(III). Therefore, *in situ* approaches based on individual pieces of tissue to give accurate comparisons of the D-period to support the subtle peak intensity changes is an ongoing work of our group.

Another extension could add to the intricacy. As most of the drying studies stated, the peak intensity changes could not only be caused via binding on specific sites by extrinsic species but also by shifts in relative positioning. The pioneer studies used a model built based on type I collagen for the subject of rat tail tendon. However, in skins, for example, the majority is indeed composed of type I collagen, but a non-negligible minor part is composed of type III collagen; heterotypic fibril assembly is common in collagenous tissues [15]. So here is a dilemma. A simple metric like the "asymmetry value" or the peak ratios could be convenient for investigating the binding species that modify native collagenous tissues but may hit the barrier when interpreting the outcomes of fibrillogenesis due to many variables in the system. Using crude models considering the gap and overlap as blocks is an alternative approach which ignores molecular binding but can add an extra piece of information on the D-periodic packing of collagen. In contrast, perfecting the model on which SAXS electron density mapping work was established significantly increases accuracy; however, it may add enormous complexity as each tissue has a different composition of multiple types of collagen. Nonetheless, this may be

the ultimate but tedious solution for studies in the future aiming to reconstruct native collagen structures *in vitro* to mimic the heterotypic fibril assembly *in vivo*.

At last, a general conclusion is given from the collagen perspective, with the overarching aim to reveal the structure of this complicated biomacromolecule from its precisely organised structural hierarchy from molecule, cluster, fibre, and network in a tissue. The SERS and SAXS techniques enable an attractive sensitivity and specificity level to investigate the changes in collagen. While exploring only two of the above forms (cluster and fibre) through this thesis, the fundamental understanding of the techniques was extended and the methodologies were improved. The work paves the way for further advancing the applications of the techniques and expanding their potential in protein structural studies.

Appendix A Notations

A.1 Vibrational Mode in Peak Assignment Tables

ν, stretching;

ν_s, symmetric stretching;

ν_{as}, asymmetric stretching;

δ, bending (undefined);

in. pl., in-plane bending;

δ_s, in-plane scissoring;

ρ, in-plane rocking;

o. pl., out-of-plane bending;

ω (or γ_w), out-of-plane wagging;

τ (or γ_t), out-of-plane twisting;

n.a., not assigned by the reference;

FR, Fermi resonance;

G, gauche conformation;

T, trans conformation;

DFT, reference peak position calculated using the density functional theory;

Cit(aq), the aqueous solution of trisodium citrate (measured at non-SERS conditions);

A.2 Vibrational Mode in Binding Coordination Illustrations

s, symmetric stretching;

as, asymmetric stretching;

st, stretching;

d, scissoring;

w, wagging;

A.3 Peak Shape and Intensity

s, strong;

m, medium;

w, weak (when peak maximum is identifiable but have a poorly defined shape);

vw, very weak (when peak centre is hardly identifiable, usually assigned based on the difference or similarity with control samples);

sh, shoulder (when an adjacent peak covers the centre of the proposed peak);

A.4 Citrate Binding Coordination with Ag Atoms

$\varkappa$, non-bridging ligand (binding to multiple metal atoms through non-continuous atoms);

n, denticity;

c, bound via central carboxyl [213];

t, bound via terminal carboxyl [213];

Bibliography

1.   Zhang, Y.; Mehta, M.; Mansel, B. W.; Ng, H. W.; Liu, Y.; Holmes, G.; Le Ru, E. C.; Prabakar, S., Anion-regulated binding selectivity of Cr (III) in collagen. *Biopolymers* 2020, e23406.

2.   Zhang, Y.; Prabakar, S.; Le Ru, E. C., Coadsorbed Species with Halide Ligands on Silver Nanoparticles with Different Binding Affinities. *The Journal of Physical Chemistry C* 2022, *126* (20), 8692-8702.

3.   Zhang, Y.; Zhang, W.; Snow, T.; Ju, Y.; Liu, Y.; Smith, A. J.; Prabakar, S., Minimising Chemical Crosslinking for Stabilising Collagen in Acellular Bovine Pericardium: Mechanistic Insights via Structural Characterisations. *Acta Biomaterialia* 2022.

4.   Fratzl, P., *Collagen: structure and mechanics*. Springer Science & Business Media: New York, 2008.

5.   Shoulders, M. D.; Raines, R. T., Collagen structure and stability. *Annual Review of Biochemistry* 2009, *78*, 929-958.

6.   Meyer, M., Processing of collagen based biomaterials and the resulting materials properties. *Biomedical Engineering Online* 2019, *18* (1), 24.

7.   Okuyama, K., Revisiting the molecular structure of collagen. *Connective Tissue Research* 2008, *49* (5), 299-310.

8.   Ramachandran, G. N., Stereochemistry of collagen. *International Journal of Peptide and Protein Research* 1988, *31* (1), 1-16.

9.   Pauling, L.; Corey, R. B., The structure of fibrous proteins of the collagen-gelatin group. *Proceedings of the National Academy of Sciences* 1951, *37* (5), 272.

10.   Hodge, A. J., Recent studies with the electron microscope on ordered aggregates of the tropocollagen macromolecule. *Aspects of Protein Structure* 1963, 289-300.

11.   Xu, Y.; Nudelman, F.; Eren, E. D.; Wirix, M. J. M.; Cantaert, B.; Nijhuis, W. H.; Hermida-Merino, D.; Portale, G.; Bomans, P. H. H.; Ottmann, C.; Friedrich, H.; Bras, W.; Akiva, A.; Orgel, J. P. R. O.; Meldrum, F. C.; Sommerdijk, N., Intermolecular channels direct crystal orientation in mineralized collagen. *Nature Communications* 2020, *11* (1), 5068.

12.   Kong, W.; Lyu, C.; Liao, H.; Du, Y., Collagen crosslinking: effect on structure, mechanics and fibrosis progression. *Biomedical Materials* 2021, *16* (6), 062005.

13.   Bielajew, B. J.; Hu, J. C.; Athanasiou, K. A., Collagen: quantification, biomechanics and role of minor subtypes in cartilage. *Nature Reviews Materials* 2020, *5* (10), 730-747.

14.   Bella, J., Collagen structure: new tricks from a very old dog. *Biochemical Journal* 2016, *473* (8), 1001-1025.

15.   Hulmes, D. J. S., Collagen diversity, synthesis and assembly. In *Collagen: Structure and Mechanics*, Fratzl, P., Ed. Springer: Boston, MA, 2008; pp 15-47.

16.   Gautieri, A.; Vesentini, S.; Redaelli, A.; Buehler, M. J., Hierarchical structure and nanomechanics of collagen microfibrils from the atomistic scale up. *Nano Letters* 2011, *11* (2), 757-766.

17.   Fang, M.; Goldstein, E. L.; Turner, A. S.; Les, C. M.; Orr, B. G.; Fisher, G. J.; Welch, K. B.; Rothman, E. D.; Banaszak Holl, M. M., Type I collagen D-spacing in fibril bundles of dermis, tendon, and bone: bridging between nano-and micro-level tissue hierarchy. *ACS Nano* 2012, *6* (11), 9503-9514.

18.   Bella, J.; Brodsky, B.; Berman, H. M., Hydration structure of a collagen peptide. *Structure* 1995, *3* (9), 893-906.

19.   Canty, E. G.; Kadler, K. E., Procollagen trafficking, processing and fibrillogenesis. *Journal of Cell Science* 2005, *118* (Pt 7), 1341-53.

20.   Beck, K.; Brodsky, B., Supercoiled protein motifs: The collagen triple-helix and the α-helical coiled coil. *Journal of Structural Biology* 1998, *122* (1-2), 17-29.

21.   Porter, S.; Clark, I. M.; Kevorkian, L.; Edwards, D. R., The ADAMTS metalloproteinases. *Biochemical Journal* 2005, *386* (Pt 1), 15-27.

22.   Hopkins, D. R.; Keles, S.; Greenspan, D. S., The bone morphogenetic protein 1/Tolloid-like metalloproteinases. *Matrix Biology* 2007, *26* (7), 508-523.

23.   Seidah, N. G.; Prat, A., Precursor convertases in the secretory pathway, cytosol and extracellular milieu. *Essays in Biochemistry* 2002, *38*, 79-94.

24.   Ramshaw, J. A. M.; Shah, N. K.; Brodsky, B., Gly-X-Y tripeptide frequencies in collagen: A context for host-guest triple-helical peptides. *Journal of Structural Biology* 1998, *122* (1-2), 86-91.

25.   Wess, T. J., Collagen fibrillar structure and hierarchies. In *Collagen*, Springer: 2008; pp 49-80.

26.   Bowes, J. H.; Elliott, R. G.; Moss, J. A., The composition of collagen and acid-soluble collagen of bovine skin. *Biochemical Journal* 1955, *61* (1), 143-150.

27.   Cram, D. J., The Design of Molecular Hosts, Guests, and Their Complexes. *Angewandte Chemie International Edition in English* 1988, *27* (8), 1009-1020.

28.   Boudko, S. P.; Engel, J.; Okuyama, K.; Mizuno, K.; Bächinger, H. P.; Schumacher, M. A., Crystal structure of human type III collagen Gly991-Gly1032 cystine knot-containing peptide shows both 7/2 and 10/3 triple helical symmetries. *Journal of Biological Chemistry* 2008, *283* (47), 32580-9.

29.   Orgel, J. P. R. O.; Persikov, A. V.; Antipova, O., Variation in the helical structure of native collagen. *PLOS ONE* 2014, *9* (2), e89519.

30.   Boudko, S. P.; Engel, J.; Okuyama, K.; Mizuno, K.; Bächinger, H. P.; Schumacher, M. A., Crystal structure of human type III collagen Gly991–Gly1032 cystine knot-containing peptide shows both 7/2 and 10/3 triple helical symmetries. *Journal of Biological Chemistry* 2008, *283* (47), 32580-32589.

31.   Orgel, J. P. R. O.; Miller, A.; Irving, T. C.; Fischetti, R. F.; Hammersley, A. P.; Wess, T. J., The in situ supermolecular structure of type I collagen. *Structure* 2001, *9* (11), 1061-1069.

32.   Orgel, J. P. R. O.; Irving, T. C.; Miller, A.; Wess, T. J., Microfibrillar structure of type I collagen in situ. *Proceedings of the National Academy of Sciences* 2006, *103* (24), 9001-9005.

33.   Canty, E. G.; Lu, Y.; Meadows, R. S.; Shaw, M. K.; Holmes, D. F.; Kadler, K. E., Coalignment of plasma membrane channels and protrusions (fibripositors) specifies the parallelism of tendon. *Journal of Cell Biology* 2004, *165* (4), 553-63.

34.   Streeter, I.; de Leeuw, N. H., A molecular dynamics study of the interprotein interactions in collagen fibrils. *Soft Matter* 2011, *7* (7), 3373-3382.

35.   Kadler, K. E.; Holmes, D. F.; Trotter, J. A.; Chapman, J. A., Collagen fibril formation. *Biochemical Journal* 1996, *11*, 1-11.

36.   Hulmes, D. J. S.; Miller, A.; Parry, D. A. D.; Piez, K. A.; Woodhead-Galloway, J., Analysis of the primary structure of collagen for the origins of molecular packing. *Journal of Molecular Biology* 1973, *79* (1), 137-148.

37.   Ward, N. P.; Hulmes, D. J. S.; Chapman, J. A., Collagen self-assembly in vitro: electron microscopy of initial aggregates formed during the lag phase. *Journal of Molecular Biology* 1986, *190* (1), 107-112.

38.   Hulmes, D. J., Building collagen molecules, fibrils, and suprafibrillar structures. *Journal of Structural Biology* 2002, *137* (1-2), 2-10.

39.   Maxwell, C. A.; Wess, T. J.; Kennedy, C. J., X-ray diffraction study into the effects of liming on the structure of collagen. *Biomacromolecules* 2006, *7* (8), 2321-2326.

40.   Naffa, R.; Zhang, Y.; Mansel, B.; Zhang, W.; Maidment, C.; Deb-Choudhury, S.; Holmes, G.; Shehadi, I. A.; Prabakar, S., Chemical and Structural Composition of Alpaca (Vicugna pacos) Skin with a Focus on Collagen Crosslinks. *Small Ruminant Research* 2020, *190* (April), 106144-106144.

41.   Avery, N. C.; Bailey, A. J., Restraining cross-links responsible for the mechanical properties of collagen fibers: natural and artificial. In *Collagen*, Springer: 2008; pp 81-110.

42.   Ottani, V.; Raspanti, M.; Ruggeri, A., Collagen structure and functional implications. *ACS NanoMicron* 2001, *32* (3), 251-260.

43.   Birk, D. E.; Fitch, J. M.; Babiarz, J. P.; Doane, K. J.; Linsenmayer, T. F., Collagen fibrillogenesis in vitro: Interaction of types I and V collagen regulates fibril diameter. *Journal of Cell Science* 1990, *95* (4), 649-657.

44.   Birk, D. E.; Mayne, R., Localization of collagen types I, III and V during tendon development. Changes in collagen types I and III are correlated with changes in fibril diameter. *European Journal of Cell Biology* 1997, *72* (4), 352-352.

45.   Buchanan, J. K.; Zhang, Y.; Holmes, G.; Covington, A. D.; Prabakar, S., Role of X-ray   Scattering   Techniques   in   Understanding   the   Collagen   Structure   of   Leather. *ChemistrySelect* 2019, *4* (48), 14091-14102.

46.   Buehler, M. J., Nature designs tough collagen: Explaining the nanostructure of collagen fibrils. *Proceedings of the National Academy of Sciences* 2006, *103* (33), 12285-12290.

47.   Masic, A.; Bertinetti, L.; Schuetz, R.; Chang, S.-W.; Metzger, T. H.; Buehler, M. J.; Fratzl, P., Osmotic pressure induced tensile forces in tendon collagen. *Nature Communications* 2015, *6*, 5942.

48.   Price, R. I.; Lees, S.; Kirschner, D. A., X-ray diffraction analysis of tendon collagen at ambient and cryogenic temperatures: Role of hydration. *International Journal of Biological Macromolecules* 1997, *20* (1), 23-33.

49.   Sui, T.; Salvati, E.; Harper, R. A.; Zhang, H.; Shelton, R. M.; Landini, G.; Korsunsky, A. M., In situ monitoring and analysis of enamel demineralisation using synchrotron X-ray scattering. *Acta Biomaterialia* 2018, *77*, 333-341.

50.   Ng, H. W.; Zhang, Y.; Naffa, R.; Prabakar, S., Monitoring the Degradation of Collagen Hydrogels by Collagenase Clostridium histolyticum. *Gels* 2020, *6* (4), 46-46.

51.   Nomura, S.; Hiltner, A.; Lando, J. B.; Baer, E., Interaction of water with native collagen. *Biopolymers* 1977, *16* (2), 231-246.

52.   Holmgren, S. K.; Taylor, K. M.; Bretscher, L. E.; Raines, R. T., Code for collagen's stability deciphered. *Nature* 1998, *392* (6677), 666-667.

53.   Mogilner, I. G.; Ruderman, G.; Grigera, J. R., Collagen stability, hydration and native state. *Journal of Molecular Graphics and Modelling* 2002, *21* (3), 209-213.

54.   Fullerton, G. D.; Nes, E.; Amurao, M.; Rahal, A.; Krasnosselskaia, L.; Cameron, I., An NMR method to characterize multiple water compartments on mammalian collagen. *Cell Biology International* 2006, *30* (1), 66-73.

55.   Fratzl, P.; Misof, K.; Zizak, I.; Rapp, G.; Amenitsch, H.; Bernstorff, S., Fibrillar structure and mechanical properties of collagen. *Journal of Structural Biology* 1998, *122* (1-2), 119-122.

56.   Wess, T. J.; Purslow, P. P.; Kielty, C. M., X-ray diffraction studies of fibrillin-rich microfibrils: effects of tissue extension on axial and lateral packing. *Journal of Structural Biology* 1998, *122* (1-2), 123-127.

57.   Yang, W.; Sherman, V. R.; Gludovatz, B.; Schaible, E.; Stewart, P.; Ritchie, R. O.; Meyers, M. A., On the tear resistance of skin. *Nature Communications* 2015, *6* (1), 1-10.

58.   Sasaki, N.; Odajima, S., Elongation mechanism of collagen fibrils and force-strain relations of tendon at each level of structural hierarchy. *Journal of Biomechanics* 1996, *29* (9), 1131-1136.

59.   Schmidt, M. M.; Dornelles, R. C. P.; Mello, R. O.; Kubota, E. H.; Mazutti, M. A.; Kempka, A. P.; Demiate, I. M., Collagen extraction process. *International Food Research Journal* 2016, *23* (3), 913.

60.   Lynn, A. K.; Yannas, I. V.; Bonfield, W., Antigenicity and immunogenicity of collagen. *Journal of Biomedical Materials Research Part B: Applied Biomaterials* 2004, *71* (2), 343-354.

61.   Adamiak, K.; Sionkowska, A., Current methods of collagen cross-linking: Review. *International Journal of Biological Macromolecules* 2020, *161*, 550-560.

62.   Damink, L. H. H. O.; Dijkstra, P. J.; Van Luyn, M. J. A.; Van Wachem, P. B.; Nieuwenhuis, P.; Feijen, J., Glutaraldehyde as a crosslinking agent for collagen-based biomaterials. *Journal of Materials Science: Materials in Medicine* 1995, *6* (8), 460-472.

63.   Migneault, I.; Dartiguenave, C.; Bertrand, M. J.; Waldron, K. C., Glutaraldehyde: behavior in aqueous solution, reaction with proteins, and application to enzyme crosslinking. *Biotechniques* 2004, *37* (5), 790-802.

64.   Avrameas, S.; Ternynck, T., The cross-linking of proteins with glutaraldehyde and its use for the preparation of immunoadsorbents. *Immunochemistry* 1969, *6* (1), 53-66.

65.   Salem, M.; Mauguen, Y.; Prangé, T., Revisiting glutaraldehyde cross-linking: the case of the Arg–Lys intermolecular doublet. *Acta Crystallographica Section F: Structural Biology and Crystallization Communications* 2010, *66* (3), 225-228.

66.   Udhayakumar, S.; Shankar, K. G.; Sowndarya, S.; Venkatesh, S.; Muralidharan, C.; Rose, C., l-Arginine intercedes bio-crosslinking of a collagen–chitosan 3D-hybrid scaffold for tissue engineering and regeneration: in silico, in vitro, and in vivo studies. *RSC Advances* 2017, *7* (40), 25070-25088.

67.   Schroepfer, M.; Meyer, M., DSC investigation of bovine hide collagen at varying degrees of crosslinking and humidities. *International Journal of Biological Macromolecules* 2017, *103*, 120-128.

68.   Samouillan, V.; Dandurand, J.; Lacabanne, C.; Thoma, R. J.; Adams, A.; Moore, M., Comparison of chemical treatments on the chain dynamics and thermal stability of bovine pericardium collagen. *Journal of Biomedical Materials Research Part A* 2003, *64* (2), 330-338.

69.   Williams, D. F.; Bezuidenhout, D.; De Villiers, J.; Human, P.; Zilla, P., Long-Term Stability and Biocompatibility of Pericardial Bioprosthetic Heart Valves. *Frontiers in Cardiovascular Medicine* 2021, *8*.

70.   Rýglová, Š.; Braun, M.; Suchý, T., Collagen and its modifications—crucial aspects with concern to its processing and analysis. *Macromolecular Materials and Engineering* 2017, *302* (6), 1600460.

71.   Wissink, M. J. B.; Beernink, R.; Pieper, J. S.; Poot, A. A.; Engbers, G. H. M.; Beugeling, T.; Van Aken, W. G.; Feijen, J., Immobilization of heparin to EDC/NHS-crosslinked collagen. Characterization and in vitro evaluation. *Biomaterials* 2001, *22* (2), 151-163.

72.   Yang, C., Enhanced physicochemical properties of collagen by using EDC/NHS-crosslinking. *Bulletin of Materials Science* 2012, *35* (5), 913-918.

73.   Covington, A. D., *Tanning chemistry: the science of leather.* Royal Society of Chemistry: Cambridge, 2009.

74.   Zhang, Y.; Mansel, B. W.; Naffa, R.; Cheong, S.; Yao, Y.; Holmes, G.; Chen, H.-L.; Prabakar, S., Revealing Molecular Level Indicators of Collagen Stability: Minimizing

Chrome Usage in Leather Processing. *ACS Sustainable Chemistry & Engineering* 2018, *6* (5), 7096-7104.

75.   Hedberg, Y. S., Chromium and leather: a review on the chemistry of relevance for allergic contact dermatitis to chromium. *Journal of Leather Science and Engineering* 2020, *2* (1), 1-15.

76.   Zhang, Y.; Ingham, B.; Cheong, S.; Ariotti, N.; Tilley, R. D.; Naffa, R.; Holmes, G.; Clarke, D. J.; Prabakar, S., Real-Time Synchrotron Small-Angle X-ray Scattering Studies of Collagen Structure during Leather Processing. *Industrial & Engineering Chemistry Research* 2018, *57* (1), 63-69.

77.   Miles, C. A.; Avery, N. C.; Rodin, V. V.; Bailey, A. J., The increase in denaturation temperature following cross-linking of collagen is caused by dehydration of the fibres. *Journal of Molecular Biology* 2005, *346* (2), 551-556.

78.   Yi, Y.; Zhang, Y.; Mansel, B.; Wang, Y.-n.; Prabakar, S.; Shi, B., Effect of Dialdehyde Carboxymethyl Cellulose Cross-Linking on the Porous Structure of the Collagen Matrix. *Biomacromolecules* 2022, *23* (4), 1723-1732.

79.   Abraham, L. C.; Zuena, E.; Perez-Ramirez, B.; Kaplan, D. L., Guide to collagen characterization for biomaterial studies. *Journal of Biomedical Materials Research Part B: Applied Biomaterials* 2008, *87* (1), 264-285.

80.   Capella-Monsonís, H.; Coentro, J. Q.; Graceffa, V.; Wu, Z.; Zeugolis, D. I., An experimental toolbox for characterization of mammalian collagen type I in biological specimens. *Nature Protocols* 2018, *13* (3), 507.

81.   Martinez, M. G.; Bullock, A. J.; MacNeil, S.; Rehman, I. U., Characterisation of structural changes in collagen with Raman spectroscopy. *Applied Spectroscopy Reviews* 2019, *54* (6), 509-542.

82.   Lo, S.; Fauzi, M. B., Current update of collagen nanomaterials—fabrication, characterisation and its applications: A review. *Pharmaceutics* 2021, *13* (3), 316.

83.   Bear, R. S., X-ray diffraction studies on protein fibers. I. The large fiber-axis period of collagen. *Journal of the American Chemical Society* 1944, *66* (8), 1297-1305.

84.   Herzog, R. O.; Jancke, W., Über den physikalischen Aufbau einiger hochmolekularer organischer Verbindungen.(1. vorläufige Mitteilung.). *Berichte der deutschen chemischen Gesellschaft (A and B Series)* 1920, *53* (10), 2162-2164.

85.   Okuyama, K.; Takayanagi, M.; Ashida, T.; Kakudo, M., A new structural model for collagen. *Polymer Journal* 1977, *9* (3), 341-343.

86.   Frushour, B. G.; Koenig, J. L., Raman scattering of collagen, gelatin, and elastin. *Biopolymers* 1975, *14* (2), 379-391.

87.   Lopes, C. d. C. A.; Limirio, P. H. J. O.; Novais, V. R.; Dechichi, P., Fourier transform infrared spectroscopy (FTIR) application chemical characterization of enamel, dentin and bone. *Applied Spectroscopy Reviews* 2018, *53* (9), 747-769.

88.   Bergholt, M. S.; Serio, A.; Albro, M. B., Raman spectroscopy: guiding light for the extracellular matrix. *Frontiers in Bioengineering and Biotechnology* 2019, *7*, 303.

89.   Langer, J.; de Aberasturi, D. J.; Aizpurua, J.; Alvarez-Puebla, R. A.; Auguié, B.; Baumberg, J. J.; Bazan, G. C.; Bell, S. E. J.; Boisen, A.; Brolo, A. G.; Choo, J.; Cialla-May, D.; Deckert, V.; Fabris, L.; Faulds, K.; Javier García de Abajo, F.; Goodacre, R.; Graham, D.; Haes, A. J.; Haynes, C. L.; Huck, C.; Itoh, T.; Käll, M.; Kneipp, J.; Kotov, N. A.; Kuang, H.; Le Ru, E. C.; Lee, H. K.; Li, J. F.; Ling, X. Y.; Maier, S. A.; Mayerhöfer, T.; Moskovits, M.; Murakoshi, K.; Nam, J. M.; Nie, S.; Ozaki, Y.; Pastoriza-Santos, I.; Perez-Juste, J.; Popp, J.; Pucci, A.; Reich, S.; Ren, B.; Schatz, G. C.; Shegai, T.; Schlücker, S.; Tay, L. L.; George Thomas, K.; Tian, Z. Q.; van Duyne, R. P.; Vo-Dinh, T.; Wang, Y.; Willets, K. A.; Xu, C.; Xu, H.; Xu, Y.; Yamamoto, Y. S.; Zhao, B.; Liz-Marzán, L. M., Present and future of surface-enhanced Raman scattering. *ACS Nano* 2020, *14* (1), 28-117.

90.   Laing, S.; Gracie, K.; Faulds, K., Multiplex in vitro detection using SERS. *Chemical Society Reviews* 2016, *45* (7), 1901-1918.

91.   Zong, C.; Xu, M.; Xu, L. J.; Wei, T.; Ma, X.; Zheng, X. S.; Hu, R.; Ren, B., Surface-Enhanced Raman Spectroscopy for Bioanalysis: Reliability and Challenges. *Chemical Reviews* 2018, *118* (10), 4946-4980.

92.   Ramachandran, G. N.; Kartha, G., Structure of collagen. *Nature* 1954, *174* (4423), 269-270.

93.   Okuyama, K.; Xu, X.; Iguchi, M.; Noguchi, K., Revision of collagen molecular structure. *Peptide Science* 2006, *84* (2), 181-191.

94.   Zhang, Y.; Ingham, B.; Leveneur, J.; Cheong, S.; Yao, Y.; Clarke, D. J.; Holmes, G.; Kennedy, J.; Prabakar, S., Can sodium silicates affect collagen structure during tanning? Insights from small angle X-ray scattering (SAXS) studies. *RSC Advances* 2017, *7* (19), 11665-11671.

95.   Tomlin, S. G.; Worthington, C. R. In *Low-angle X-ray diffraction patterns of collagen*, Proceedings of the Royal Society of London A: Mathematical, Physical and Engineering Sciences, The Royal Society: 1956; pp 189-201.

96.   Fratzl, P.; Daxer, A., Structural transformation of collagen fibrils in corneal stroma during drying. An x-ray scattering study. *Biophysical Journal* 1993, *64* (4), 1210-1214.

97.   Sasaki, N.; Shukunami, N.; Matsushima, N.; Izumi, Y., Time-resolved X-ray diffraction from tendon collagen during creep using synchrotron radiation. *Journal of Biomechanics* 1999, *32* (3), 285-292.

98.   Giannini, C.; De Caro, L.; Terzi, A.; Fusaro, L.; Altamura, D.; Diaz, A.; Lassandro, R.; Boccafoschi, F.; Bunk, O., Decellularized pericardium tissues at increasing glucose, galactose and ribose concentrations and at different time points studied using scanning X-ray microscopy. *IUCrJ* 2021, *8* (4).

99.   De Caro, L.; Terzi, A.; Fusaro, L.; Altamura, D.; Boccafoschi, F.; Bunk, O.; Giannini, C., Time scale of glycation in collagen of bovine pericardium-derived bio-tissues. *IUCrJ* 2021, *8* (6).

100.	Orgel, J. P.; Wess, T. J.; Miller, A., The in situ conformation and axial location of the intermolecular cross-linked non-helical telopeptides of type I collagen. *Structure* 2000, *8* (2), 137-142.

101.	Cotton, T. M.; Kim, J. H.; Chumanov, G. D., Application of surface-enhanced Raman spectroscopy to biological systems. *Journal of Raman spectroscopy* 1991, *22* (12), 729-742.

102.	Brown, G. M.; Hope, G. A., SERS study of the adsorption of gelatin at a copper electrode in sulfuric acid solution. *Journal of Electroanalytical Chemistry* 1995, *397* (1-2), 293-300.

103.	Gullekson, C.; Lucas, L.; Hewitt, K.; Kreplak, L., Surface-sensitive Raman spectroscopy of collagen I fibrils. *Biophysical Journal* 2011, *100* (7), 1837-1845.

104.	Cárcamo, J. J.; Aliaga, A. E.; Clavijo, E.; Brañes, M.; Campos-Vallette, M. M., Raman and surface-enhanced Raman scattering in the study of human rotator cuff tissues after shock wave treatment. *Journal of Raman Spectroscopy* 2012, *43* (2), 248-254.

105.	France, C. A. M.; Thomas, D. B.; Doney, C. R.; Madden, O., FT-Raman spectroscopy as a method for screening collagen diagenesis in bone. *Journal of Archaeological Science* 2014, *42*, 346-355.

106.	Gasior-Głogowska, M.; Komorowska, M.; Hanuza, J.; Maczka, M.; Zajac, A.; Ptak, M.; Bedziński, R.; Kobielarz, M.; Maksymowicz, K.; Kuropka, P.; Szotek, S., FT-Raman spectroscopic study of human skin subjected to uniaxial stress. *Journal of the Mechanical Behavior of Biomedical Materials* 2013, *18*, 240-252.

107.	Stewart, S.; Fredericks, P. M., Surface-enhanced Raman spectroscopy of peptides and proteins adsorbed on an electrochemically prepared silver surface. *Spectrochimica Acta Part A: Molecular and Biomolecular Spectroscopy* 1999, *55* (7-8), 1615-1640.

108.	Bazylewski, P.; Divigalpitiya, R.; Fanchini, G., In situ Raman spectroscopy distinguishes between reversible and irreversible thiol modifications in l-cysteine. *RSC Advances* 2017, *7* (5), 2964-2970.

109.	Jastrzebska, M.; Wrzalik, R.; Kocot, A.; Zalewska-Rejdak, J.; Cwalina, B., Raman spectroscopic study of glutaraldehyde-stabilized collagen and pericardium tissue. *Journal of Biomaterials Science, Polymer Edition* 2003, *14* (2), 185-197.

110.	Van Gulick, L.; Saby, C.; Morjani, H.; Beljebbar, A., Age-related changes in molecular organization of type I collagen in tendon as probed by polarized SHG and Raman microspectroscopy. *Scientific Reports* 2019, *9* (1), 1-12.

111.	Rygula, A.; Majzner, K.; Marzec, K. M.; Kaczor, A.; Pilarczyk, M.; Baranska, M., Raman spectroscopy of proteins: a review. *Journal of Raman Spectroscopy* 2013, *44* (8), 1061-1076.

112.	Wilson Jr, E. B., The normal modes and frequencies of vibration of the regular plane hexagon model of the benzene molecule. *Physical Review* 1934, *45* (10), 706.

113.	Movasaghi, Z.; Rehman, S.; Rehman, I. U., Raman spectroscopy of biological tissues. *Applied Spectroscopy Reviews* 2007, *42* (5), 493-541.

114.   Wang, Y.-N.; Galiotis, C.; Bader, D. L., Determination of molecular changes in soft tissues under strain using laser Raman microscopy. *Journal of Biomechanics* 2000, *33* (4), 483-486.

115.   Janko, M.; Davydovskaya, P.; Bauer, M.; Zink, A.; Stark, R. W., Anisotropic Raman scattering in collagen bundles. *Optics Letters* 2010, *35* (16), 2765-2767.

116.   Galvis, L.; Dunlop, J. W. C.; Duda, G.; Fratzl, P.; Masic, A., Polarized Raman Anisotropic Response of Collagen in Tendon: Towards 3D Orientation Mapping of Collagen in Tissues. *PLOS ONE* 2013, *8* (5), 1-9.

117.   Keskin, S.; Çulha, M., Label-free detection of proteins from dried-suspended droplets using surface enhanced Raman scattering. *Analyst* 2012, *137* (11), 2651-2657.

118.   Yang, L.; Li, P.; Liu, H.; Tang, X.; Liu, J., A dynamic surface enhanced Raman spectroscopy method for ultra-sensitive detection: from the wet state to the dry state. *Chemical Society Reviews* 2015, *44* (10), 2837-2848.

119.   Moisoiu, V.; Iancu, S. D.; Stefancu, A.; Moisoiu, T.; Pardini, B.; Dragomir, M. P.; Crisan, N.; Avram, L.; Crisan, D.; Andras, I.; Fodor, D.; Leopold, L. F.; Socaciu, C.; Bálint, Z.; Tomuleasa, C.; Elec, F.; Leopold, N., SERS liquid biopsy: An emerging tool for medical diagnosis. *Colloids and Surfaces B: Biointerfaces* 2021, *208*, 112064.

120.   Gliemann, H.; Nickel, U.; Schneider, S., Application of Gelatin-Stabilized Silver Colloids for SERS Measurements. *Journal of Raman Spectroscopy* 1998, *29* (2), 89-96.

121.   Hankus, M. E.; Li, H.; Gibson, G. J.; Cullum, B. M., Surface-enhanced Raman scattering-based nanoprobe for high-resolution, non-scanning chemical imaging. *Analytical Chemistry* 2006, *78* (21), 7535-7546.

122.   Le Ru, E.; Etchegoin, P., *Principles of Surface-Enhanced Raman Spectroscopy: and related plasmonic effects.* Elsevier: 2008.

123.   Long, D. A., *The Raman effect: a unified treatment of the theory of Raman scattering by molecules.* Wiley Chichester: 2002.

124.   Raman, C. V.; Krishnan, K. S., A new type of secondary radiation. *Nature* 1928, *121* (3048), 501-502.

125.   Rousseau, D. L.; Bauman, R. P.; Porto, S. P. S., Normal mode determination in crystals. *Journal of Raman Spectroscopy* 1981, *10* (1), 253-290.

126.   Hayes, W.; Loudon, R.; Birman, J. L., Scattering of light by crystals. *Physics Today* 1980, *33* (4), 55.

127.   Poulet, H.; Mathieu, J. P., *Vibration spectra and symmetry of crystals.* Gordon and Breach New York: 1976.

128.   Fox, M., *Optical properties of solids.* American Association of Physics Teachers: 2002.

129.   Auguié, B.; Reigue, A.; Le Ru, E. C.; Etchegoin, P. G., Tiny Peaks vs Mega Backgrounds: A General Spectroscopic Method with Applications in Resonant Raman Scattering and Atmospheric Absorptions. *Analytical Chemistry* 2012, *84* (18), 7938-7945.

130.   Guinier, A., *X-ray diffraction in crystals, imperfect crystals, and amorphous bodies.* Courier Corporation: 1994.

131.   Feigin, L. A.; Svergun, D. I., *Structure analysis by small-angle X-ray and neutron scattering.* Springer: 1987.

132.   Warren, B. E., *X-ray Diffraction.* Courier Corporation: 1990.

133.   De Jeu, W. H., *Basic X-ray scattering for soft matter.* Oxford University Press: 2016.

134.   Willmott, P., *An introduction to synchrotron radiation: techniques and applications.* John Wiley & Sons: 2019.

135.   Pedersen, J. S., Analysis of small-angle scattering data from colloids and polymer solutions: modeling and least-squares fitting. *Advances in Colloid and Interface Science* 1997, *70*, 171-210.

136.   Chao, A. W.; Mess, K. H., *Handbook of accelerator physics and engineering.* World scientific: 2013.

137.   Ingham, B.; Li, H.; Allen, E. L.; Toney, M. F., SAXSFit: A program for fitting small-angle X-ray and neutron scattering data. *arXiv:0901.4782* 2009, 1-5.

138.   Basham, M.; Filik, J.; Wharmby, M. T.; Chang, P. C. Y.; El Kassaby, B.; Gerring, M.; Aishima, J.; Levik, K.; Pulford, B. C. A.; Sikharulidze, I.; Sneddon, D.; Webber, M.; Dhesi, S. S.; Maccherozzi, F.; Svensson, O.; Brockhauser, S.; Náray, G.; Ashton, A. W., Data Analysis WorkbeNch (DAWN). *J Synchrotron Radiat* 2015, *22* (3), 853-858.

139.   Pauw, B. R.; Smith, A. J.; Snow, T.; Terrill, N. J.; Thünemann, A. F., The modular small-angle X-ray scattering data correction sequence. *J Appl Crystallogr* 2017, *50* (Pt 6), 1800-1811.

140.   Kreibig, U.; Vollmer, M., *Optical properties of metal clusters.* Springer Science & Business Media: 2013.

141.   Quinten, M.; Kreibig, U., Optical properties of aggregates of small metal particles. *Surface Science* 1986, *172* (3), 557-577.

142.   Etchegoin, P. G.; Le Ru, E. C., Basic Electromagnetic Theory of SERS. In *Surface Enhanced Raman Spectroscopy*, 2010; pp 1-37.

143.   Grand, J.; Auguié, B.; Le Ru, E. C., Combined extinction and absorption UV–visible spectroscopy as a method for revealing shape imperfections of metallic nanoparticles. *Analytical Chemistry* 2019, *91* (22), 14639-14648.

144.   Xia, Y.; Xiong, Y.; Lim, B.; Skrabalak, S. E., Shape-Controlled Synthesis of Metal Nanocrystals: Simple Chemistry Meets Complex Physics? *Angewandte Chemie International Edition* 2009, *48* (1), 60-103.

145.   Zhang, Q.; Li, N.; Goebl, J.; Lu, Z.; Yin, Y., A systematic study of the synthesis of silver nanoplates: is citrate a "magic" reagent? *Journal of the American Chemical Society* 2011, *133* (46), 18931-18939.

146.   Stamplecoskie, K. G.; Scaiano, J. C., Light emitting diode irradiation can control the morphology and optical properties of silver nanoparticles. *Journal of the American Chemical Society* 2010, *132* (6), 1825-1827.

147.   Wiley, B. J.; Im, S. H.; Li, Z.-Y.; McLellan, J.; Siekkinen, A.; Xia, Y., Maneuvering the surface plasmon resonance of silver nanostructures through shape-controlled synthesis. *The Journal of Physical Chemistry B* 2006, *110* (32), 15666-15675.

148.   Le Ru, E. C.; Galloway, C.; Etchegoin, P. G., On the connection between optical absorption/extinction and SERS enhancements. *Physical Chemistry Chemical Physics* 2006, *8* (26), 3083-3087.

149.   Wang, H.; Brandl, D. W.; Nordlander, P.; Halas, N. J., Plasmonic nanostructures: artificial molecules. *Accounts of Chemical Research* 2007, *40* (1), 53-62.

150.   Gill, R.; Tian, L.; Somerville, W. R. C.; Le Ru, E. C.; van Amerongen, H.; Subramaniam, V., Silver nanoparticle aggregates as highly efficient plasmonic antennas for fluorescence enhancement. *The Journal of Physical Chemistry C* 2012, *116* (31), 16687-16693.

151.   Höhne, G.; McNaughton, J. L.; Hemminger, W.; Flammersheim, H.-J.; Flammersheim, H.-J., *Differential scanning calorimetry*. Springer Science & Business Media: 2003.

152.   Seelig, J.; Schönfeld, H.-J., Thermal protein unfolding by differential scanning calorimetry and circular dichroism spectroscopy Two-state model versus sequential unfolding. *Quarterly Reviews of Biophysics* 2016, *49*, e9.

153.   Johnson, C. M., Differential scanning calorimetry as a tool for protein folding and stability. *Archives of Biochemistry and Biophysics* 2013, *531* (1-2), 100-109.

154.   Sterpone, F.; Melchionna, S., Thermophilic proteins: insight and perspective from in silico experiments. *Chemical Society Reviews* 2012, *41* (5), 1665-1676.

155.   Clas, S.-D.; Dalton, C. R.; Hancock, B. C., Differential scanning calorimetry: applications in drug development. *Pharmaceutical Science & Technology Today* 1999, *2* (8), 311-320.

156.   Djabourov, M.; Leblond, J.; Papon, P., Gelation of aqueous gelatin solutions. I. Structural investigation. *Journal de Physique* 1988, *49* (2), 319-332.

157.   Liu, W.; Tian, Z.; Li, C.; Li, G., Thermal denaturation of fish collagen in solution: a calorimetric and kinetic analysis. *Thermochimica Acta* 2014, *581*, 32-40.

158.   Guo, L.; Colby, R. H.; Lusignan, C. P.; Whitesides, T. H., Kinetics of triple helix formation in semidilute gelatin solutions. *Macromolecules* 2003, *36* (26), 9999-10008.

159.   Williams, D. B.; Carter, C. B., The transmission electron microscope. In *Transmission Electron Microscopy*, Springer: 1996; pp 3-17.

160.   Walker, J. M., *The protein protocols handbook*. Springer Science & Business Media: 1996.

161.   Walker, J. M., SDS Polyacrylamide Gel Electrophoresis of Proteins. In *The Protein Protocols Handbook*, Walker, J. M., Ed. Humana Press: Totowa, NJ, 2002; pp 61-67.

162. Kliment, C. R.; Englert, J. M.; Crum, L. P.; Oury, T. D., A novel method for accurate collagen and biochemical assessment of pulmonary tissue utilizing one animal. *International Journal of Clinical and Experimental Pathology* 2011, *4* (4), 349.

163. Maynes, R., *Structure and function of collagen types.* Elsevier: 2012.

164. Cissell, D. D.; Link, J. M.; Hu, J. C.; Athanasiou, K. A., A modified hydroxyproline assay based on hydrochloric acid in Ehrlich's solution accurately measures tissue collagen content. *Tissue Engineering Part C: Methods* 2017, *23* (4), 243-250.

165. Woessner Jr, J. F., The determination of hydroxyproline in tissue and protein samples containing small proportions of this imino acid. *Archives of Biochemistry and Biophysics* 1961, *93* (2), 440-447.

166. Stegemann, H.; Stalder, K., Determination of hydroxyproline. *Clinica Chimica Acta* 1967, *18* (2), 267-273.

167. Friedman, M., Applications of the ninhydrin reaction for analysis of amino acids, peptides, and proteins to agricultural and biomedical sciences. *Journal of Agricultural and Food Chemistry* 2004, *52* (3), 385-406.

168. Knapp, F., *Natur und Wesen der Gerberei und des Leders.* Cotta: 1858.

169. Gustavson, K. H., The Nature of the Neutral Salt Effect in Chrome Tanning: I. The Effect of Addition of Sodium Sulfate to Solutions of Basic Chromic Sulfates on their Composition and Tanning Potency. *Journal of the American Leather Chemists Association* 1950, *45* (8), 536-558.

170. Gustavson, K. H., The effect of esterification of the carboxyl groups of collagen upon its combination with chromium compounds. *Journal of the American Chemical Society* 1952, *74* (18), 4608-4611.

171. Covington, A. D.; Lampard, G. S.; Menderes, O.; Chadwick, A. V.; Rafeletos, G.; O'Brien, P., Extended X-ray absorption fine structure studies of the role of chromium in leather tanning. *Polyhedron* 2001, *20* (5), 461-466.

172. Covington, A. D., Modern tanning chemistry. *Chemical Society Reviews* 1997, *26* (2), 111-126.

173. Wu, B.; Mu, C.; Zhang, G.; Lin, W., Effects of Cr3+ on the structure of collagen fiber. *Langmuir* 2009, *25* (19), 11905-11910.

174. Sykes, R. L., Modification of some reactive groups of collagen and the effect on the fixation of tervalent chromium salts. *Journal of the American Leather Chemists Association* 1956, *51* (5), 235-244.

175. Wan, Y.; Guo, Z.; Jiang, X.; Fang, K.; Lu, X.; Zhang, Y.; Gu, N., Quasi-spherical silver nanoparticles: Aqueous synthesis and size control by the seed-mediated Lee-Meisel method. *Journal of Colloid and Interface Science* 2013, *394* (1), 263-268.

176. Mulfinger, L.; Solomon, S. D.; Bahadory, M.; Jeyarajasingam, A. V.; Rutkowsky, S. A.; Boritz, C., Synthesis and study of silver nanoparticles. *Journal of Chemical Education* 2007, *84* (2), 322.

177.   Hémonnot, C. m. Y.; Köster, S., Imaging of biological materials and cells by X-ray scattering and diffraction. *ACS Nano* 2017, *11* (9), 8542-8559.

178.   Chapman, J. A.; Tzaphlidou, M.; Meek, K. M.; Kadler, K. E., The collagen fibril—a model system for studying the staining and fixation of a protein. *Electron Microscopy Reviews* 1990, *3* (1), 143-182.

179.   Zhang, Y.; Cremer, P. S., Interactions between macromolecules and ions: the Hofmeister series. *Current Opinion in Chemical Biology* 2006, *10* (6), 658-663.

180.   Okur, H. I.; Hladílková, J.; Rembert, K. B.; Cho, Y.; Heyda, J.; Dzubiella, J.; Cremer, P. S.; Jungwirth, P., Beyond the Hofmeister series: Ion-specific effects on proteins and their biological functions. *The Journal of Physical Chemistry B* 2017, *121* (9), 1997-2014.

181.   Ahmed, M.; Namboodiri, V.; Singh, A. K.; Mondal, J. A., On the intermolecular vibrational coupling, hydrogen bonding, and librational freedom of water in the hydration shell of mono-and bivalent anions. *The Journal of Chemical Physics* 2014, *141* (16), 164708.

182.   Metrick II, M. A.; MacDonald, G., Hofmeister ion effects on the solvation and thermal stability of model proteins lysozyme and myoglobin. *Colloids and Surfaces A: Physicochemical and Engineering Aspects* 2015, *469*, 242-251.

183.   North, A. C. T.; Cowan, P. M.; Randall, J. T., Structural Units in Collagen Fibrils. *Nature* 1954, *174* (4442), 1142-1143.

184.   Dehring, K. A.; Smukler, A. R.; Roessler, B. J.; Morris, M. D., Correlating changes in collagen secondary structure with aging and defective type II collagen by Raman spectroscopy. *Applied Spectroscopy* 2006, *60* (4), 366-372.

185.   Michota, A.; Kudelski, A.; Bukowska, J., Influence of electrolytes on the structure of cysteamine monolayer on silver studied by surface-enhanced Raman scattering. *Journal of Raman Spectroscopy* 2001, *32* (5), 345-350.

186.   Cárcamo, J. J.; Aliaga, A. E.; Clavijo, E.; Garrido, C.; Gómez-Jeria, J. S.; Campos-Vallette, M. M., Proline and hydroxyproline deposited on silver nanoparticles. A Raman, SERS and theoretical study. *Journal of Raman Spectroscopy* 2012, *43* (6), 750-755.

187.   Freire, P. T. C.; Barboza, F. M.; Lima, J. A.; Melo, F. E.; Mendes Filho, J., Raman spectroscopy of amino acid crystals. *Raman Spectroscopy and Applications* 2017, 201.

188.   Cárcamo, J. J.; Aliaga, A. E.; Clavijo, R. E.; Brañes, M. R.; Campos-Vallette, M. M., Raman study of the shockwave effect on collagens. *Spectrochimica Acta Part A: Molecular and Biomolecular Spectroscopy* 2012, *86*, 360-365.

189.   Xu, L. J.; Zong, C.; Zheng, X. S.; Hu, P.; Feng, J. M.; Ren, B., Label-free detection of native proteins by surface-enhanced Raman spectroscopy using iodide-modified nanoparticles. *Analytical Chemistry* 2014, *86* (4), 2238-2245.

190.   Lee, P. C.; Meisel, D., Adsorption and surface-enhanced Raman of dyes on silver and gold sols. *The Journal of Physical Chemistry* 1982, *86* (17), 3391-3395.

191.   Stamplecoskie, K. G.; Scaiano, J. C.; Tiwari, V. S.; Anis, H., Optimal size of silver nanoparticles for surface-enhanced raman spectroscopy. *The Journal of Physical Chemistry C* 2011, *115* (5), 1403-1409.

192.   Meyer, M.; Le Ru, E. C.; Etchegoin, P. G., Self-limiting aggregation leads to long-lived metastable clusters in colloidal solutions. *The Journal of Physical Chemistry B* 2006, *110* (12), 6040-6047.

193.   Hildebrandt, P.; Stockburger, M., Surface-enhanced resonance Raman spectroscopy of Rhodamine 6G adsorbed on colloidal silver. *The Journal of Physical Chemistry* 1984, *88* (24), 5935-5944.

194.   Qian, X.-M.; Nie, S. M., Single-molecule and single-nanoparticle SERS: from fundamental mechanisms to biomedical applications. *Chemical Society Reviews* 2008, *37* (5), 912-920.

195.   Xu, L.-J.; Lei, Z.-C.; Li, J.; Zong, C.; Yang, C. J.; Ren, B., Label-free surface-enhanced Raman spectroscopy detection of DNA with single-base sensitivity. *Journal of the American Chemical Society* 2015, *137* (15), 5149-5154.

196.   Torres-Nuñez, A.; Faulds, K.; Graham, D.; Alvarez-Puebla, R. A.; Guerrini, L., Silver colloids as plasmonic substrates for direct label-free surface-enhanced Raman scattering analysis of DNA. *Analyst* 2016, *141* (17), 5170-5180.

197.   Dai, X.; Fu, W.; Chi, H.; Mesias, V. S. D.; Zhu, H.; Leung, C. W.; Liu, W.; Huang, J., Optical tweezers-controlled hotspot for sensitive and reproducible surface-enhanced Raman spectroscopy characterization of native protein structures. *Nature Communications* 2021, *12* (1), 1-9.

198.   Huang, J.-Y.; Zong, C.; Xu, L.-J.; Cui, Y.; Ren, B., Clean and modified substrates for direct detection of living cells by surface-enhanced Raman spectroscopy. *Chemical Communications* 2011, *47* (20), 5738-5740.

199.   Xie, L.; Lu, J.; Liu, T.; Chen, G.; Liu, G.; Ren, B.; Tian, Z., Key role of direct adsorption on SERS sensitivity: synergistic effect among target, aggregating agent, and surface with au or Ag colloid as surface-enhanced Raman spectroscopy substrate. *The Journal of Physical Chemistry Letters* 2020, *11* (3), 1022-1029.

200.   Park, J.-W.; Shumaker-Parry, J. S., Strong resistance of citrate anions on metal nanoparticles to desorption under thiol functionalization. *ACS Nano* 2015, *9* (2), 1665-1682.

201.   Perera, G. S.; Athukorale, S. A.; Perez, F.; Pittman Jr, C. U.; Zhang, D., Facile displacement of citrate residues from gold nanoparticle surfaces. *Journal of Colloid and Interface Science* 2018, *511*, 335-343.

202.   Wang, H.; Xue, Z.; Wu, Y.; Gilmore, J.; Wang, L.; Fabris, L., Rapid SERS Quantification of Trace Fentanyl Laced in Recreational Drugs with a Portable Raman Module. *Analytical Chemistry* 2021, *93* (27), 9373-9382.

203.   Leopold, N.; Lendl, B., A new method for fast preparation of highly surface-enhanced raman scattering (SERS) active silver colloids at room temperature by reduction of silver nitrate with hydroxylamine hydrochloride. *The Journal of Physical Chemistry B* 2003, *107* (24), 5723-5727.

204.   Lin, X.-M.; Cui, Y.; Xu, Y.-H.; Ren, B.; Tian, Z.-Q., Surface-enhanced Raman spectroscopy: substrate-related issues. *Analytical and Bioanalytical Chemistry* 2009, *394* (7), 1729-1745.

205.   Kim, H.; Kim, E.; Choi, E.; Baek, C. S.; Song, B.; Cho, C.-H.; Jeong, S. W., Label-free C-reactive protein SERS detection with silver nanoparticle aggregates. *RSC Advances* 2015, *5* (44), 34720-34729.

206.   Bao, Y.; Li, Y.; Ling, L.; Xiang, X.; Han, X.; Zhao, B.; Guo, X., Label-Free and Highly Sensitive Detection of Native Proteins by Ag IANPs via Surface-Enhanced Raman Spectroscopy. *Analytical Chemistry* 2020, *92* (21), 14325-14329.

207.   Wang, X.; Zeng, J.; Sun, Q.; Yang, J.; Xiao, Y.; Zhu, Z.; Yan, B.; Li, Y., An effective method towards label-free detection of antibiotics by surface-enhanced Raman spectroscopy in human serum. *Sensors and Actuators B: Chemical* 2021, *343*, 130084.

208.   Munro, C. H.; Smith, W. E.; Garner, M.; Clarkson, J. W. P. C.; White, P. C., Characterization of the surface of a citrate-reduced colloid optimized for use as a substrate for surface-enhanced resonance Raman scattering. *Langmuir* 1995, *11* (10), 3712-3720.

209.   Bell, S. E. J.; Sirimuthu, N. M. S., Surface-enhanced Raman spectroscopy as a probe of competitive binding by anions to citrate-reduced silver colloids. *The Journal of Physical Chemistry A* 2005, *109* (33), 7405-7410.

210.   Bichara, L. C.; Lanús, H. E.; Ferrer, E. G.; Gramajo, M. B.; Brandán, S. A., Vibrational study and force field of the citric acid dimer based on the SQM methodology. *Advances in Physical Chemistry* 2011, *2011*.

211.   Siiman, O.; Bumm, L. A.; Callaghan, R.; Blatchford, C. G.; Kerker, M., Surface-enhanced Raman scattering by citrate on colloidal silver. *The Journal of Physical Chemistry* 1983, *87* (6), 1014-1023.

212.   Bellamy, L. J., Carboxylic Acids. In *The Infra-red Spectra of Complex Molecules*, Springer Netherlands: Dordrecht, 1975; pp 183-202.

213.   Grys, D.-B.; de Nijs, B.; Salmon, A. R.; Huang, J.; Wang, W.; Chen, W.-H.; Scherman, O. A.; Baumberg, J. J., Citrate Coordination and Bridging of Gold Nanoparticles: The Role of Gold Adatoms in AuNP Aging. *ACS Nano* 2020, *14* (7), 8689-8696.

214.   Kerker, M.; Siiman, O.; Bumm, L. A.; Wang, D. S., Surface enhanced Raman scattering (SERS) of citrate ion adsorbed on colloidal silver. *Applied Optics* 1980, *19* (19), 3253-3255.

215.   Tada, H.; Bronkema, J.; Bell, A. T., Application of in situ surface-enhanced Raman spectroscopy (SERS) to the study of citrate oxidation on silica-supported silver nanoparticles. *Catalysis Letters* 2004, *92* (3), 93-99.

216.   Park, J.-W.; Shumaker-Parry, J. S., Structural study of citrate layers on gold nanoparticles: role of intermolecular interactions in stabilizing nanoparticles. *Journal of the American Chemical Society* 2014, *136* (5), 1907-1921.

217.   Walrafen, G. E., Raman spectral studies of the effects of temperature on water structure. *The Journal of Chemical Physics* 1967, *47* (1), 114-126.

218.   Sun, Q., The Raman OH stretching bands of liquid water. *Vibrational Spectroscopy* 2009, *51* (2), 213-217.

219.   Bickley, R. I.; Edwards, H. G. M.; Gustar, R.; Rose, S. J., A vibrational spectroscopic study of nickel (II) citrate Ni3 (C6H5O7) 2 and its aqueous solutions. *Journal of Molecular Structure* 1991, *246* (3-4), 217-228.

220.   Stefancu, A.; Lee, S.; Zhu, L.; Liu, M.; Lucacel, R. C.; Cortés, E.; Leopold, N., Fermi Level Equilibration at the Metal–Molecule Interface in Plasmonic Systems. *Nano Letters* 2021, *21* (15), 6592-6599.

221.   Assis, M.; Groppo Filho, F. C.; Pimentel, D. S.; Robeldo, T.; Gouveia, A. F.; Castro, T. F.; Fukushima, H. C.; de Foggi, C. C.; da Costa, J. P.; Borra, R. C., Ag nanoparticles/AgX (X= Cl, Br and I) composites with enhanced photocatalytic activity and low toxicological effects. *ChemistrySelect* 2020, *5* (15), 4655-4673.

222.   Espinoza, M. G.; Hinks, M. L.; Mendoza, A. M.; Pullman, D. P.; Peterson, K. I., Kinetics of halide-induced decomposition and aggregation of silver nanoparticles. *The Journal of Physical Chemistry C* 2012, *116* (14), 8305-8313.

223.   Hasi, W.-L.-J.; Lin, X.; Lou, X.-T.; Lin, S.; Yang, F.; Lin, D.-Y.; Lu, Z.-W., Chloride ion-assisted self-assembly of silver nanoparticles on filter paper as SERS substrate. *Applied Physics A* 2015, *118* (3), 799-807.

224.   Tang, B.; Xu, S.; An, J.; Zhao, B.; Xu, W.; Lombardi, J. R., Kinetic effects of halide ions on the morphological evolution of silver nanoplates. *Physical Chemistry Chemical Physics* 2009, *11* (44), 10286-10292.

225.   Hay, R. W.; Bond, M. A., Kinetics of the decarboxylation of acetoacetic acid. *Australian Journal of Chemistry* 1967, *20* (9), 1823-1828.

226.   Schiavoni, M. M.; Di Loreto, H. E.; Hermann, A.; Mack, H. G.; Ulic, S. E.; Della Védova, C. O., Keto–enol tautomerism in β-ketoesters: CH3C (O) CHXC (O) OY (X= H, Cl; Y= CH3, C2H5). Vibrational analyses, NMR spectra and quantum chemical calculations. *Journal of Raman Spectroscopy* 2001, *32* (5), 319-329.

227.   Carey, D. M.; Korenowski, G. M., Measurement of the Raman spectrum of liquid water. *The Journal of Chemical Physics* 1998, *108* (7), 2669-2675.

228.   De Gelder, J.; De Gussem, K.; Vandenabeele, P.; Moens, L., Reference database of Raman spectra of biological molecules. *Journal of Raman Spectroscopy* 2007, *38* (9), 1133-1147.

229.   Li, H.; Xia, H.; Ding, W.; Li, Y.; Shi, Q.; Wang, D.; Tao, X., Synthesis of monodisperse, quasi-spherical silver nanoparticles with sizes defined by the nature of silver precursors. *Langmuir* 2014, *30* (9), 2498-2504.

230.   Volod'Ko, L.; Huoah, L. T., The vibrational spectra of aqueous nitrate solutions. *Journal of Applied Spectroscopy* 1968, *9* (4), 1100-1104.

231.   Shi, Y.-e.; Wang, W.; Zhan, J., A positively charged silver nanowire membrane for rapid on-site swabbing extraction and detection of trace inorganic explosives using a portable Raman spectrometer. *Nano Research* 2016, *9* (8), 2487-2497.

232.	Zhou, Z.; Huang, G. G.; Kato, T.; Ozaki, Y., Experimental parameters for the SERS of nitrate ion for label-free semi-quantitative detection of proteins and mechanism for proteins to form SERS hot sites: a SERS study. *Journal of Raman Spectroscopy* 2011, *42* (9), 1713-1721.

233.	Shah, F. A., Towards refining Raman spectroscopy-based assessment of bone composition. *Scientific Reports* 2020, *10* (1), 1-8.

234.	Li, M. D.; Cui, Y.; Gao, M. X.; Luo, J.; Ren, B.; Tian, Z. Q., Clean substrates prepared by chemical adsorption of iodide followed by electrochemical oxidation for surface-enhanced raman spectroscopic study of cell membrane. *Analytical Chemistry* 2008, *80* (13), 5118-5125.

235.	Dong, X.; Gu, H.; Liu, F., Study of the surface-enhanced Raman spectroscopy of residual impurities in hydroxylamine-reduced silver colloid and the effects of anions on the colloid activity. *Spectrochimica Acta Part A: Molecular and Biomolecular Spectroscopy* 2012, *88*, 97-101.

236.	Chiappisi, L., Polyoxyethylene alkyl ether carboxylic acids: An overview of a neglected class of surfactants with multiresponsive properties. *Advances in Colloid and Interface Science* 2017, *250*, 79-94.

237.	Okabayashi, H.; Okuyama, M.; Kitagawa, T., The Raman spectra of surfactants and the concentration dependence of their molecular conformations in aqueous solutions. *Bulletin of the Chemical Society of Japan* 1975, *48* (8), 2264-2269.

238.	Orendorff, C. J.; Ducey Jr, M. W.; Pemberton, J. E., Quantitative correlation of Raman spectral indicators in determining conformational order in alkyl chains. *The Journal of Physical Chemistry A* 2002, *106* (30), 6991-6998.

239.	Guo, C.; Liu, H.; Wang, J.; Chen, J., Conformational structure of triblock copolymers by FT-Raman and FTIR spectroscopy. *Journal of Colloid and Interface Science* 1999, *209* (2), 368-373.

240.	Holland-Moritz, K.; Hummel, D.-O., Structural studies on linear aliphatic polyesters by electron diffraction, infrared, and Raman spectroscopy. *Journal of Molecular Structure* 1973, *19*, 289-300.

241.	Czamara, K.; Majzner, K.; Pacia, M. Z.; Kochan, K.; Kaczor, A.; Baranska, M., Raman spectroscopy of lipids: a review. *Journal of Raman Spectroscopy* 2015, *46* (1), 4-20.

242.	Joo, T. H.; Kim, M. S.; Kim, K., Surface-enhanced Raman scattering of benzenethiol in silver sol. *Journal of Raman spectroscopy* 1987, *18* (1), 57-60.

243.	Shannon, R. D., Revised effective ionic radii and systematic studies of interatomic distances in halides and chalcogenides. *Acta Crystallographica Section A: Crystal Physics, Diffraction, Theoretical and General Crystallography* 1976, *32* (5), 751-767.

244.	Highberger, J. H., The isoelectric point of collagen. *Journal of the American Chemical Society* 1939, *61* (9), 2302-2303.

245. Zhang, Z.; Li, G.; Shi, B., Physicochemical properties of collagen, gelatin and collagen hydrolysate derived from bovine limed split wastes. *Journal of the Society of Leather Technologists and Chemists* 2006, *90* (1), 23.

246. Darby, B. L.; Le Ru, E. C., Competition between molecular adsorption and diffusion: Dramatic consequences for SERS in colloidal solutions. *Journal of the American Chemical Society* 2014, *136* (31), 10965-10973.

247. Moerz, S. T.; Kraegeloh, A.; Chanana, M.; Kraus, T., Formation mechanism for stable hybrid clusters of proteins and nanoparticles. *ACS Nano* 2015, *9* (7), 6696-6705.

248. Song, X.; Ren, X.; Tang, D.; Li, X., Specific iodide effect on surface-enhanced Raman scattering for ultra-sensitive detection of organic contaminants in water. *Spectrochimica Acta Part A: Molecular and Biomolecular Spectroscopy* 2022, *272*, 120950.

249. Perera, G. S.; Nettles, C. B.; Zhou, Y.; Zou, S.; Hollis, T. K.; Zhang, D., Direct observation of ion pairing at the liquid/solid interfaces by surface enhanced raman spectroscopy. *Langmuir* 2015, *31* (33), 8998-9005.

250. Singh, S.; Agarwal, A.; Avni, A.; Mukhopadhyay, S., Ultrasensitive Characterization of the Prion Protein by Surface-Enhanced Raman Scattering: Selective Enhancement via Electrostatic Tethering of the Intrinsically Disordered Domain with Functionalized Silver Nanoparticles. *The Journal of Physical Chemistry Letters* 2021, *12* (12), 3187-3194.

251. Rose, G. D.; Geselowitz, A. R.; Lesser, G. J.; Lee, R. H.; Zehfus, M. H., Hydrophobicity of amino acid residues in globular proteins. *Science* 1985, *229* (4716), 834-838.

252. Leikin, S.; Parsegian, V. A.; Yang, W. H.; Walrafen, G. E., Raman spectral evidence for hydration forces between collagen triple helices. *Proceedings of the National Academy of Sciences* 1997, *94* (21), 11312-11317.

253. Sarina, S.; Waclawik, E. R.; Zhu, H., Photocatalysis on supported gold and silver nanoparticles under ultraviolet and visible light irradiation. *Green Chemistry* 2013, *15* (7), 1814-1833.

254. Wei, L.; Lu, J.; Xu, H.; Patel, A.; Chen, Z.-S.; Chen, G., Silver nanoparticles: synthesis, properties, and therapeutic applications. *Drug Discovery Today* 2015, *20* (5), 595-601.

255. Swales, P. D.; Holden, M. P.; Dowson, D.; Ionescu, M. I., Some experiments on tissue heart valve prostheses. *Engineering in Medicine* 1973, *2* (2), 27-31.

256. Agishi, T.; Nakazono, M.; Kiraly, R. J.; Picha, G.; Nosé, Y., Biodegradable material for bladder reconstruction. *Journal of Biomedical Materials Research* 1975, *9* (4), 119-131.

257. Jayakrishnan, A.; Jameela, S. R., Glutaraldehyde as a fixative in bioprostheses and drug delivery matrices. *Biomaterials* 1996, *17* (5), 471-484.

258. Li, X.; Guo, Y.; Ziegler, K. R.; Model, L. S.; Eghbalieh, S. D. D.; Brenes, R. A.; Kim, S. T.; Shu, C.; Dardik, A., Current usage and future directions for the bovine pericardial patch. *Annals of Vascular Surgery* 2011, *25* (4), 561-568.

259.   Carpentier, A., The concept of bioprosthesis. *Thorac Cardiovasc Surg* 1971, *19* (05), 379-383.

260.   Schoen, F. J.; Tsao, J. W.; Levy, R. J., Calcification of bovine pericardium used in cardiac valve bioprostheses. Implications for the mechanisms of bioprosthetic tissue mineralization. *The American Journal of Pathology* 1986, *123* (1), 134.

261.   Golomb, G.; Schoen, F. J.; Smith, M. S.; Linden, J.; Dixon, M.; Levy, R. J., The role of glutaraldehyde-induced cross-links in calcification of bovine pericardium used in cardiac valve bioprostheses. *The American Journal of Pathology* 1987, *127* (1), 122.

262.   Dahm, M.; Lyman, W. D.; Schwell, A. B.; Factor, S. M.; Frater, R. W. M., Immunogenicity of glutaraldehyde-tanned bovine pericardium. *The Journal of Thoracic and Cardiovascular Surgery* 1990, *99* (6), 1082-1090.

263.   Grabenwöger, M.; Sider, J.; Fitzal, F.; Zelenka, C.; Windberger, U.; Grimm, M.; Moritz, A.; Böck, P.; Wolner, E., Impact of glutaraldehyde on calcification of pericardial bioprosthetic heart valve material. *The Annals of Thoracic Surgery* 1996, *62* (3), 772-777.

264.   Lee, J. M.; Edwards, H. H. L.; Pereira, C. A.; Samii, S. I., Crosslinking of tissue-derived biomaterials in 1-ethyl-3-(3-dimethylaminopropyl)-carbodiimide (EDC). *Journal of Materials Science: Materials in Medicine* 1996, *7* (9), 531-541.

265.   Jorge-Herrero, E.; Fernandez, P.; Turnay, J.; Olmo, N.; Calero, P.; García, R.; Freile, I.; Castillo-Olivares, J. L., Influence of different chemical cross-linking treatments on the properties of bovine pericardium and collagen. *Biomaterials* 1999, *20* (6), 539-545.

266.   Liu, J.; Jing, H.; Qin, Y.; Li, B.; Sun, Z.; Kong, D.; Leng, X.; Wang, Z., Nonglutaraldehyde fixation for off the shelf decellularized bovine pericardium in anticalcification cardiac valve applications. *ACS Biomaterials Science & Engineering* 2019, *5* (3), 1452-1461.

267.   Sun, Z.; Liu, J.; Wang, X.; Jing, H.; Li, B.; Kong, D.; Leng, X.; Wang, Z., Epoxy Chitosan-Crosslinked Acellular Bovine Pericardium with Improved Anti-calcification and Biological Properties. *ACS Applied Bio Materials* 2020, *3* (4), 2275-2283.

268.   Zhao, Y.; Li, Y.; Peng, X.; Yu, X.; Cheng, C.; Yu, X., Feasibility study of oxidized hyaluronic acid cross-linking acellular bovine pericardium with potential application for abdominal wall repair. *International Journal of Biological Macromolecules* 2021, *184*, 831-842.

269.   Chanda, J., Anticalcification treatment of pericardial prostheses. *Biomaterials* 1994, *15* (6), 465-469.

270.   Chanda, J.; Kuribayashi, R.; Abe, T., Heparin in calcification prevention of porcine pericardial bioprostheses. *Biomaterials* 1997, *18* (16), 1109-1113.

271.   Lee, W. K.; Park, K. D.; Han, D. K.; Suh, H.; Park, J.-C.; Kim, Y. H., Heparinized bovine pericardium as a novel cardiovascular bioprosthesis. *Biomaterials* 2000, *21* (22), 2323-2330.

272.   Ohri, R.; Hahn, S. K.; Hoffman, A. S.; Stayton, P. S.; Giachelli, C. M., Hyaluronic acid grafting mitigates calcification of glutaraldehyde-fixed bovine pericardium. *Journal of Biomedical Materials Research Part A* 2004, *70* (2), 328-334.

273.   Grases, F.; Sanchis, P.; Costa-Bauzá, A.; Bonnin, O.; Isern, B.; Perelló, J.; Prieto, R. M., Phytate inhibits bovine pericardium calcification in vitro. *Cardiovasc Pathol* 2008, *17* (3), 139-45.

274.   Dong, X.; Wei, X.; Yi, W.; Gu, C.; Kang, X.; Liu, Y.; Li, Q.; Yi, D., RGD-modified acellular bovine pericardium as a bioprosthetic scaffold for tissue engineering. *Journal of Materials Science: Materials in Medicine* 2009, *20* (11), 2327-2336.

275.   van den Heever, J. J.; Neethling, W. M.; Smit, F. E.; Litthauer, D.; Joubert, G., The effect of different treatment modalities on the calcification potential and cross-linking stability of bovine pericardium. *Cell Tissue Bank* 2013, *14* (1), 53-63.

276.   Mathapati, S.; Bishi, D. K.; Guhathakurta, S.; Cherian, K. M.; Venugopal, J. R.; Ramakrishna, S.; Verma, R. S., Biomimetic acellular detoxified glutaraldehyde cross-linked bovine pericardium for tissue engineering. *Materials Science and Engineering: C* 2013, *33* (3), 1561-72.

277.   Umashankar, P. R.; Arun, T.; Kumari, T. V., Short duration gluteraldehyde cross linking of decellularized bovine pericardium improves biological response. *Journal of Biomedical Materials Research Part A* 2011, *97* (3), 311-320.

278.   Sinha, P.; Zurakowski, D.; Kumar, T. S.; He, D.; Rossi, C.; Jonas, R. A., Effects of glutaraldehyde concentration, pretreatment time, and type of tissue (porcine versus bovine) on postimplantation calcification. *The Journal of Thoracic and Cardiovascular Surgery* 2012, *143* (1), 224-227.

279.   Lee, C.; Lim, H.-G.; Lee, C.-H.; Kim, Y. J., Effects of glutaraldehyde concentration and fixation time on material characteristics and calcification of bovine pericardium: implications for the optimal method of fixation of autologous pericardium used for cardiovascular surgery. *Interactive Cardiovascular and Thoracic Surgery* 2017, *24* (3), 402-406.

280.   Liang, H.-C.; Chang, Y.; Hsu, C.-K.; Lee, M.-H.; Sung, H.-W., Effects of crosslinking degree of an acellular biological tissue on its tissue regeneration pattern. *Biomaterials* 2004, *25* (17), 3541-3552.

281.   Shaik, T. A.; Alfonso-García, A.; Zhou, X.; Arnold, K. M.; Haudenschild, A. K.; Krafft, C.; Griffiths, L. G.; Popp, J. r.; Marcu, L., FLIm-guided Raman imaging to study cross-linking and calcification of bovine pericardium. *Analytical Chemistry* 2020, *92* (15), 10659-10667.

282.   Jastrzebska, M.; Zalewska-Rejdak, J.; Wrzalik, R.; Kocot, A.; Mroz, I.; Barwinski, B.; Turek, A.; Cwalina, B., Tannic acid-stabilized pericardium tissue: IR spectroscopy, atomic force microscopy, and dielectric spectroscopy investigations. *Journal of Biomedical Materials Research Part A* 2006, *78* (1), 148-156.

283.   Zioupos, P.; Barbenel, J. C., Mechanics of native bovine pericardium: II. A structure based model for the anisotropic mechanical behaviour of the tissue. *Biomaterials* 1994, *15* (5), 374-382.

284.   Ellsmere, J. C.; Khanna, R. A.; Lee, J. M., Mechanical loading of bovine pericardium accelerates enzymatic degradation. *Biomaterials* 1999, *20* (12), 1143-1150.

285.   Liao, J.; Yang, L.; Grashow, J.; Sacks, M. S., Molecular orientation of collagen in intact planar connective tissues under biaxial stretch. *Acta Biomaterialia* 2005, *1* (1), 45-54.

286.   Yang, M.; Chen, C. Z.; Wang, X. N.; Zhu, Y. B.; Gu, Y. J., Favorable effects of the detergent and enzyme extraction method for preparing decellularized bovine pericardium scaffold for tissue engineered heart valves. *Journal of Biomedical Materials Research Part B: Applied Biomaterials* 2009, *91* (1), 354-361.

287.   Han, B.; Jaurequi, J.; Tang, B. W.; Nimni, M. E., Proanthocyanidin: a natural crosslinking reagent for stabilizing collagen matrices. *Journal of Biomedical Materials Research Part A* 2003, *65* (1), 118-124.

288.   Starcher, B., A Ninhydrin-Based Assay to Quantitate the Total Protein Content of Tissue Samples. *Analytical Biochemistry* 2001, *292* (1), 125-129.

289.   Moore, S.; Stein, W. H., Photometric ninhydrin method for use in the chromatography of amino acids. *Journal of Biological Chemistry* 1948, *176* (1), 367-88.

290.   Pei, Y.; Wang, L.; Tang, K.; Kaplan, D. L., Biopolymer nanoscale assemblies as building blocks for new materials: A review. *Advanced Functional Materials* 2021, *31* (15), 2008552.

291.   Goh, K. L.; Hiller, J.; Haston, J. L.; Holmes, D. F.; Kadler, K. E.; Murdoch, A.; Meakin, J. R.; Wess, T. J., Analysis of collagen fibril diameter distribution in connective tissues using small-angle X-ray scattering. *Biochimica et Biophysica Acta - General Subjects* 2005, *1722* (2), 183-188.

292.   Lombardo, D.; Calandra, P.; Kiselev, M. A., Structural Characterization of Biomaterials by Means of Small Angle X-rays and Neutron Scattering (SAXS and SANS), and Light Scattering Experiments. *Molecules* 2020, *25* (23).

293.   Fathima, N. N.; Madhan, B.; Rao, J. R.; Nair, B. U.; Ramasami, T., Interaction of aldehydes with collagen: effect on thermal, enzymatic and conformational stability. *International Journal of Biological Macromolecules* 2004, *34* (4), 241-247.

294.   Madaghiele, M.; Calò, E.; Salvatore, L.; Bonfrate, V.; Pedone, D.; Frigione, M.; Sannino, A., Assessment of collagen crosslinking and denaturation for the design of regenerative scaffolds. *Journal of Biomedical Materials Research Part A* 2016, *104* (1), 186-194.

295.   Damink, L. H. H. O.; Dijkstra, P. J.; Van Luyn, M. J. A.; Van Wachem, P. B.; Nieuwenhuis, P.; Feijen, J., Cross-linking of dermal sheep collagen using a water-soluble carbodiimide. *Biomaterials* 1996, *17* (8), 765-773.

296.   Gautieri, A.; Passini, F. S.; Silván, U.; Guizar-Sicairos, M.; Carimati, G.; Volpi, P.; Moretti, M.; Schoenhuber, H.; Redaelli, A.; Berli, M., Advanced glycation end-products: Mechanics of aged collagen from molecule to tissue. *Matrix Biology* 2017, *59*, 95-108.

297.   Matsushita, O.; Jung, C. M.; Minami, J.; Katayama, S.; Nishi, N.; Okabe, A., A study of the collagen-binding domain of a 116-kDa Clostridium histolyticum collagenase. *Journal of Biological Chemistry* 1998, *273* (6), 3643-8.

298.   Ohbayashi, N.; Yamagata, N.; Goto, M.; Watanabe, K.; Yamagata, Y.; Murayama, K., Enhancement of the Structural Stability of Full-Length Clostridial Collagenase by Calcium Ions. *Applied and Environmental Microbiology* 2012, *78* (16), 5839-5844.